X-ray spectra, variability and pair wind models of Seyfert 1 nuclei
by Karen Marie Leighly

A thesis submitted in partial fulfillment of the requirements for the degree of Doctor of Philosophy in Physics
Montana State University

Abstract:
Previously, iron features were not known to be a common feature of the X-ray spectra of Active Galactic Nuclei (AGN). The data from a long observation of NGC 5506 performed by EXOSAT were reanalyzed, and an emission line and an absorption edge were found. Subsequently, 47 X-ray spectra from a sample of 40 AGN observed with EXOSAT were reanalyzed. Evidence for line emission was found in 13 spectra from 12 sources; however, the line intensities were not well determined.

X-ray variability is an interesting feature of some low luminosity Seyfert 1 galaxies. As part of Tsuruta's simultaneous multi-frequency campaign, the Seyfert I nuclei NGC 7469. and NGC 6814 were observed with the LAC onboard Ginga. These data were analyzed along with a second Ginga observation of NGC 6814. The flux level of NGC 7469 was low and the satellite pointing was not stable, making detailed analysis difficult. The flux level was seen to decrease during the second day of observation with a halving time scale of 25,000 seconds. The photon index was remarkably flat.

From the two observations of NGC 6814, a wealth of interesting results emerged. The rapid flux variability with time scale of ~ 300 seconds and the 12000 second periodicity characteristic of this unusual source were confirmed in both observations. During the first observation, periodic dips were found, in which the flux fell to nearly zero. Spectral variability was confirmed during these dips, as well as a decrease in line emission. During the second observation, periods of rapid flux increase and decrease were found, and spectral variability was again found. Well defined energy delays were also discovered. A variable absorption model was explicitly fit to the delay data. This model could successfully though qualitatively explain the spectral variability during the regions of fastest variability.

In the intense radiation field of an AGN, the motion of particles is influenced by the gravitational and radiation fields. To explore the motion of such particles, a spherically symmetric model by Abramowicz et al. 1990 was extended to a more realistic case by using a modified radiation stress energy tensor. This modification produced a significant change in the character of the critical point solutions.

X-RAY SPECTRA, VARIABILITY AND PAIR WIND MODELS OF SEYFERT 1 NUCLEI

by

Karen Marie Leighly

A thesis submitted in partial fulfillment
of the requirements for the degree

of

Doctor of Philosophy

in

Physics

MONTANA STATE UNIVERSITY
Bozeman, Montana

November 1991

APPROVAL

of a thesis submitted by

Karen Marie Leighly

This thesis has been read by each member of the thesis committee and has been found to be satisfactory regarding content, English usage, format, citations, bibliographic style and consistency, and is ready for submission to the College of Graduate Studies.

11-8-91
Date

Chairperson, Graduate Committee

Approved for the Major Department

11-8-91
Date

John Hermanson
Head, Major Department

Approved for the College of Graduate Studies

November 11, 1991
Date

Henry L Parsons
Graduate Dean

STATEMENT OF PERMISSION TO USE

ACKNOWLEDGEMENTS

Primary acknowledgement and thanks must go to Sachiko Tsuruta for her patience and help during my years as her student. Her support, both financial through NASA grants, and otherwise, has gone far beyond that expected from a research advisor.

Thanks are due to Ken Pounds and the rest of the Leicester group for their hospitality during my two visits for EXOSAT data analysis. Special thanks are due to T. Jane Turner, Tahir Yaqoob, Ian George and Paul Nandra.

Many thanks are due to Hideyo Kunieda and the rest of the Nagoya group for their hospitality during my two visits for *Ginga* data analysis. Particular thanks go to Hisamitsu Awaki for his extensive help and friendship.

Acknowledgement and thanks go to Christine Done for allowing me to use her time series analysis software.

The people who have helped me at Montana State University are innumerable. Matthew Benacquista must be thanked for helping me to understand general relativity at least a little. All of the graduate students must be thanked for their friendship, especially Stuart Hutton, Rand Swanson, Brad Tritz and Hideyuki Umeda. The faculty have been helpful, and must be thanked for their patience and support. Particular thanks go to John Hermanson and Georgeanne Caughlan.

Many thanks are due to my parents, Hollis P. Leighly and Elizabeth P. Leighly, and my brother, David P. Leighly. Their support and confidence have helped me an immeasurable amount. Last but certainly not least, more than thanks must go to Corin L. Dreykus, without whom I could have never done it.

The work in this thesis would not have been possible without the help of many people, and it is impossible to thank them all individually here.

TABLE OF CONTENTS

TABLE OF CONTENTS—Continued

TABLE OF CONTENTS—Continued

TABLE OF CONTENTS—Continued

LIST OF TABLES

LIST OF FIGURES

LIST OF FIGURES—Continued

LIST OF FIGURES—Continued

LIST OF FIGURES—Continued

LIST OF FIGURES—Continued

LIST OF FIGURES—Continued

ABSTRACT

Previously, iron features were not known to be a common feature of the X-ray spectra of Active Galactic Nuclei (AGN). The data from a long observation of NGC 5506 performed by EXOSAT were reanalyzed, and an emission line and an absorption edge were found. Subsequently, 47 X-ray spectra from a sample of 40 AGN observed with EXOSAT were reanalyzed. Evidence for line emission was found in 13 spectra from 12 sources; however, the line intensities were not well determined.

X-ray variability is an interesting feature of some low luminosity Seyfert 1 galaxies. As part of Tsuruta's simultaneous multi-frequency campaign, the Seyfert 1 nuclei NGC 7469 and NGC 6814 were observed with the LAC on-board *Ginga*. These data were analyzed along with a second *Ginga* observation of NGC 6814. The flux level of NGC 7469 was low and the satellite pointing was not stable, making detailed analysis difficult. The flux level was seen to decrease during the second day of observation with a halving time scale of 25,000 seconds. The photon index was remarkably flat.

From the two observations of NGC 6814, a wealth of interesting results emerged. The rapid flux variability with time scale of $\sim$ 300 seconds and the 12000 second periodicity characteristic of this unusual source were confirmed in both observations. During the first observation, periodic dips were found, in which the flux fell to nearly zero. Spectral variability was confirmed during these dips, as well as a decrease in line emission. During the second observation, periods of rapid flux increase and decrease were found, and spectral variability was again found. Well defined energy delays were also discovered. A variable absorption model was explicitly fit to the delay data. This model could successfully though qualitatively explain the spectral variability during the regions of fastest variability.

In the intense radiation field of an AGN, the motion of particles is influenced by the gravitational and radiation fields. To explore the motion of such particles, a spherically symmetric model by Abramowicz et al. 1990 was extended to a more realistic case by using a modified radiation stress energy tensor. This modification produced a significant change in the character of the critical point solutions.

CHAPTER 1

INTRODUCTION

General

Active Galactic Nuclei (AGNs) are the bright nuclei of some galaxies. They are some of the most energetic objects in the universe. Their energy spectra are characteristically non-thermal; that is, the energy spectrum cannot be adequately described by a sum of stellar spectra. They emit nearly equal amounts of energy in all wave bands, and are a strong source of X-rays. There are many different kinds of AGN, and because they are so well studied in the optical wave band, the classification generally depends on their optical properties.

In this thesis, Seyfert 1 nuclei are the predominant type of AGN studied. These are characterized by a strong non-thermal infrared to X-ray continuum and broad optical emission lines from a wide range of ionizations. Generally the host galaxy can be optically resolved. However, Quasi-stellar Objects (QSOs), Seyfert type 2 nuclei, Narrow Emission Line Galaxies (NELGs), and Low Ionization Nuclear Emission Line Regions (LINERS) are also included, as well as a variety of Seyferts whose type are somewhere in between 1 and 2 (1.2, 1.9, for example) depending on the relative strength of the broad and narrow components of their emission lines (Turner 1988). In general many of the differences between these types are in their optical properties. Some differ in luminosity. For example, QSOs are more luminous than Seyfert 1 nuclei, having a typical bolometric luminosity of $10^{44-47}\mathrm{erg\,s^{-1}}$ compared with $10^{41-44}\mathrm{erg\,s^{-1}}$ for Seyfert 1s. However, many of these AGN objects seem to have quite similar X-ray properties, perhaps indicating that the primary emission mechanism is the same.

It has been pointed out that the largest amount of energy from many AGN is emitted from the central region. Since the discovery of this fact, the source of power for this emission has been debated. The currently most popular idea for the predominant source of power is the accretion of material onto a supermassive black hole having a mass from 10^6–10^9 solar masses. The form of the accretion flow is generally thought to depend on the accretion rate (e.g. Rees 1984). Rapid X-ray variability from a fraction of low luminosity Seyfert 1 nuclei implies that the X-rays may be produced in a small central region, from 5 to 100 r_s, where r_s is the Schwartzschild radius appropriate for the supermassive black hole. The broad emission lines are in general thought to come from a region larger than $100r_s$, from clouds which have been photoionized by the strong high energy continuum from further inside.

Many AGN, and in particular, Seyfert 1 nuclei have been detected in X-rays. Recent analysis of maneuvering data from the Japanese *Ginga* X-ray satellite from 3 years of operation found 93 Seyfert galaxies detected (Awaki 1991). In this study, it was estimated that 139 optically identified Seyfert 1 galaxies came into the field of view. Pointing observation data from 75 Seyfert galaxies from the *Einstein Observatory* Imagining Proportional Counter has been recently analyzed by Kruper, Urry and Canizares (1990). Many more detections in X-rays are expected from more sensitive detectors such as those used by the X-ray satellite *ROSAT* in the recently completed All Sky Survey. X-ray emission from at least a portion of Seyfert galaxies has been frequently observed.

As will be discussed in Chapter 2, the primary X-ray radiation from Seyfert 1 galaxies seems to be non-thermal. However, there are spectral features imprinted on the non-thermal primary spectrum which may be thermal, or which come from reprocessing of X-rays in cold material. Therefore, the careful study of the X-ray spectra from Seyfert 1 galaxies can give information about both the nature of the primary spectrum and the material surrounding the emission region.

A fraction of Seyfert 1 nuclei have been found to be rapidly variable, with a doubling time scale of as small as 100 seconds. There is some evidence that the time scale of variability is characteristic of the primary emission process, since luminosity and the time scale of variability have been found to be correlated (Barr and Mushotzky 1986; McHardy 1989). The most naive estimation of the size of the X-ray emission region comes from the light crossing time scale, and can be found from the relation $R = c\Delta T$. In many of the fastest variable AGN, this region is found to be as small as 10^{12} cm. Much information about the nature of the emission process and the material around the Seyfert 1 can be gained by studying in detail the variability of AGN. Of particular interest is spectral variability, because of the strong constraints which can be placed on models of the emission region.

Coupled with the observations of Seyfert 1 nuclei are the theories of the emission region and of the material surrounding the emission region. As mentioned above, copious X-rays have been observed from many Seyfert 1 galaxies, and the rapid variability implies that the emission region must be very small. Therefore, close to the emission region, the flux of radiation will be very intense. Under such radiation flux, some particles may not be gravitationally bound to AGN, and so particle winds may result. Therefore, it is interesting to investigate the nature of such a wind.

Plan of the Thesis

The remainder of this thesis is divided into nine chapters. Two of these chapters, Chapters 2 and 5, provide review of spectra and variability of Seyfert 1 nuclei. Two others, Chapters 3 and 6 provide descriptions of the instrumentation and satellites used to obtain the data under investigation. Three of the chapters, Chapters 4, 7 and 8 describe details of the data analysis conducted by the author, and interpretation of the results. One chapter, Chapter 9, describes her purely theoretical calculation describing the motion of particles in a radiation field. The final chapter is the conclusion.

Chapter 2 gives a partial review of the form of the X-ray spectral components found in Seyfert 1 nuclei. At least five separate spectral components have been identified. This chapter was written from the observer's point of view. Some theories of emission are briefly discussed.

Chapter 3 describes the European X-ray Observatory Satellite, and particularly the Medium Energy instrument. This description of the instrumentation is included for several reasons. The main reason is that it is unwise to use X-ray data without understanding the limitations of the instrument which collected it. Such use can lead to over-interpretation of results. But also, the understanding of the instrument provides a depth and richness to the data analysis. Also included in this chapter are details of the background subtraction for future reference, and also a short review of the statistics involved in fitting X-ray spectra.

Chapter 4 describes all of the EXOSAT data analysis done by the author. The first part describes the analysis and results of a long observation of NGC 5506. The purpose of this analysis was a search for iron emission and absorption features at $\sim 7\,\mathrm{keV}$. The long observation was used because of the better statistics which it could provide. A comparison with a *Ginga* observation was also included, and some discussion of possible models is given.

The second part of Chapter 4 describes the reanalysis of the EXOSAT spectral survey sources. Again the intent of the reanalysis was the search for iron features. Since these observations were in general shorter in duration, the criteria for detection were necessarily statistical. A comparison with recent *Ginga* data from Awaki 1990 is also given. Some statistical correlations are performed on the sample of iron line detections.

Chapter 5 gives a review of X-ray variability of Seyfert 1 nuclei. First the description and nature of the flux variability is described. Several possible models for the most common kind of variability found are briefly discussed. The remainder of the chapter discusses spectral variability. This review was included for reference, because all three of the *Ginga* observations described in subsequent chapters indicated spectral variability. The most common type of spectral variability found is flux correlated. That is, in general, the X-ray spectra are usually observed to become softer as the X-ray flux increases. Thus this section describes models of spectral variability and shows how they can result in apparent flux correlated spectral variability. Diagnostics are described which can ideally decide which model of spectral variability is appropriate.

Chapter 6 describes the Japanese X-ray observatory satellite *Ginga*, as well as the Large Area Counter, the main instrument on-board *Ginga*. Data selection, and background subtraction and modeling are discussed in some detail, since there was a background subtraction problem in one of the *Ginga* observations. Finally in this chapter are described some relatively new methods, not yet widely used, for time series analysis of data with gaps.

In Chapter 7 the analysis, results and interpretation by the author of an observation of NGC 7469 are discussed. This observation found the source in a low flux state. Also there were pointing problems of the satellite further decreasing the flux. Because of the low flux, a background subtraction problem was encountered. The analysis of this problem and two possible solutions are described. Finally, the results of the time series and spectral analysis are compared with previous observations of this source, and a possible model is described.

Chapter 8, the longest chapter of the thesis, also describes the most significant and important work of this thesis. Results from detailed time series and spectral analysis of two *Ginga* observations of NGC 6814 are given. New results, never observed before from Seyfert 1 nuclei, or from this source, were found. Specifically, the hardness ratio from one of the observations was found to have 12,000 periodicity. Periodic dips to nearly zero flux from the other observation were observed. In addition, fast spectral variability, within a few hundred seconds, was discovered during both observations. Also, during one of the observations, energy lags were found, in the sense that the hard flux lagged the soft flux during flux decreases, while the soft flux lagged the hard flux during flux increases. Also shown are calculations from a new variation of the partial covering model explicitly fit to the time series results which successfully though qualitatively describes the spectral fitting results. Extensions of this simple model to explain the rest of the new observations are described.

Chapter 9 describes briefly the author's calculation of wind velocity profiles from AGN. In this calculation the particle approach has been taken; that is, the motion of the wind is interpreted to be the motion of non-interacting particles. Work has been done extending this to the fluid approach, in which the particles are assumed to be coupled by a magnetic field; however, a description of this work is not included in this thesis. A derivation of the radial motion of the particle in the intense radiation field is given, including special and general relativity. This derivation is quite similar to that given by Abramowicz, Ellis and Lanza 1990. Next the solution of the wind equation under two different radiation stress energy tensors is shown. One of these cases was also used by Abramowicz, Ellis and Lanza 1990, and is presented for comparison with the other, new stress energy tensor devised by the author. A small change in the form of the stress energy tensor is shown to completely change the nature of the critical point solutions.

Finally, Chapter 10 describes the major results and conclusions of the thesis. The work which has not yet been done is also described here. Finally, the future prospects of X-ray astronomy are briefly described.

CHAPTER 2

X-RAY SPECTRA OF SEYFERT GALAXIES

General

As discussed in the previous chapter, many Seyfert galaxies and other emission line galaxies are observed in X-rays, and in fact emit a substantial fraction of their energy in X-rays. It has been found that the X-ray spectra from these galaxies have many similarities, and to date, at least five components have been identified which are common to the spectra of many Seyfert 1 nuclei. These are: (1) a power law continuum, (2) low energy absorption, (3) a soft excess component, (4) iron emission and absorption features around 7 keV, and (5) a hard tail. These features, the current state of observation and some theoretical models are reviewed in this chapter.

X-ray Power Law Emission

It has been found that the medium energy X-ray spectra of Seyfert 1 galaxies is generally well described by a power law. An early study by Mushotzky et al. (1980) performed with the A–2 experiment on-board *HEAO 1* found that the spectra of seven Seyfert 1 galaxies from 5–60 keV was well described by power laws with energy indices in the range 0.3 to 1.0, with the most common index found being 0.7. However, because of poor energy resolution, he found that most of these spectra could also be adequately fit with a high temperature thermal bremsstrahlung model. A more sensitive survey of 48 Seyfert type AGN provided by EXOSAT showed that generally power law models provided better fits to the data than thermal bremsstrahlung models (see Chapter 3 for a description of the EXOSAT mission). The weighted mean index in this study was found to be 0.70, with 1 σ dispersion of 0.17. It was noted also that there was a significant spread in the values of the index, beyond that expected for only statistical reasons (Turner and Pounds 1989). Another survey of *Ginga* data from 22 Seyfert 1 galaxies analyzed by Awaki (1991), found the average energy index to be 0.68 with the 1 σ dispersion being 0.15 (see Chapter 6 for a description of the *Ginga* mission). Another sample of 29 *Ginga* spectra from 20 Seyferts found the mean index to be 0.722 with a standard deviation of 0.25 (Pounds, Nandra and Stewart 1990). Other surveys in medium energies (2–10 keV) seem to find a similar result (Turner et al. 1991). These results consistently show that the most common energy index is 0.7; however, the spread in values is too large to be entirely due to statistics, so there must be an intrinsic spread in the value of the energy index from object to object. This intrinsic spread may be due to differing emission mechanisms, or as discussed later in this chapter, could be due to the influence of additional broad spectral components.

The theory of the production of the power law X-ray emission is a topic of intense debate. Several mechanisms have been proposed.

A naturally promising mechanism involves synchrotron radiation, since it is a well known fact that an electron population with a power law energy distribution in a uniform magnetic field will produce a power law photon distribution. One particular model proposed is the synchrotron self-Compton model (Urry and Mushotzky 1982). In this process, radio to soft X-ray emission is synchrotron while the harder X-ray tail is due to Comptonization of the same synchrotron emission.

Another possibility is the Compton model. In this model, primary IR–O–UV soft photons are scattered by higher energy electrons to produce a power law spectrum. In some cases, the X-ray source shows high luminosity as well as fast variability. This implies that the source has a large compactness; in this case it is reasonable to expect that a significant population of electron–positron pairs would be present (e.g., Guilbert, Fabian and Rees 1983). Because of this expectation, many groups of theorists have investigated the spectrum of the radiation due to Comptonization in such electron–positron pair plasmas (e.g., Fabian et al. 1986; Lightman and Zdziarski 1987; Svensson 1987; Done and Fabian 1989). Their results in general indicate that an X-ray power law with an energy index of 0.7 might indeed be produced. However, a general concern with these models is that for a large region of parameter space, more γ-ray photons are produced than is consistent with the observed γ-ray background. This situation is particularly true if the observed energy index is to be 0.7. A way out of this dilemma may be the choice of realistic geometries. Recently, Tritz and Tsuruta (1991) have investigated a model in which the soft thermal emission is confined to a thin disk, and the reprocessing by Comptonization occurs in an electron-positron pair corona above the disk. Preliminary results indicate that indeed a power law with energy index of 0.7 might be produced without an over-abundance of γ-rays. Another way may be the addition of another hard X-ray spectral component with a harder spectrum to the steeper primary spectrum, modifying the measured power law index (Zdziarski et al. 1991). This point will be discussed later in this chapter.

Low Energy Absorption

The hard limit of the X-ray band pass measured depends usually on the detector used; that is, hard X-rays can in general be detected if the optical depth of the detector is large enough. On the other hand, low energy photons are cut off due to an astronomical reason: they are easily photo-electrically absorbed by interstellar hydrogen, as well as heavier elements. A significant column density of interstellar material is present in our Galaxy. Column densities of this origin have been measured by their 21–cm hydrogen emission (Heiles 1975). The column number densities typically range from $1.0 \times 10^{20}\ \mathrm{cm}^{-2}$ to $3.0 \times 10^{21}\ \mathrm{cm}^{-2}$ in our line of sight to Seyfert galaxies considered in this thesis (Turner and Pounds 1989). In spectral fitting, the energy dependent absorption cross section is taken from Morrison and McCammon 1983, who include the effects of neutral heavy elements at cosmic abundances.

Many Seyfert 1 galaxies are not intrinsically heavily absorbed, and the absorption column as measured by spectral fitting is no larger than that due to our Galaxy. However, the results of a recent survey from EXOSAT showed that about half of 35 sources in which the absorption column could be measured showed significant absorption beyond that due to our Galaxy (Turner and Pounds 1989). Note that EXOSAT was a particularly good instrument to measure low energy absorption intrinsic to the host galaxy; because of its extended low energy detection, absorption columns down to $10^{20}\ \mathrm{cm}^{-2}$ could be measured. There is also some evidence that, in general, high absorption columns are more common in low luminosity AGN (Reichert et al. 1985; Turner and Pounds 1989; Turner et al. 1991).

To clearly see the effect of the energy dependent absorption on the measured spectrum, in Figure 1 is shown the ideal spectra for various absorption columns. The dashed line shows the input spectrum with energy index of 0.7, while the solid lines show the emergent spectra. The numbers next to the emergent spectra give

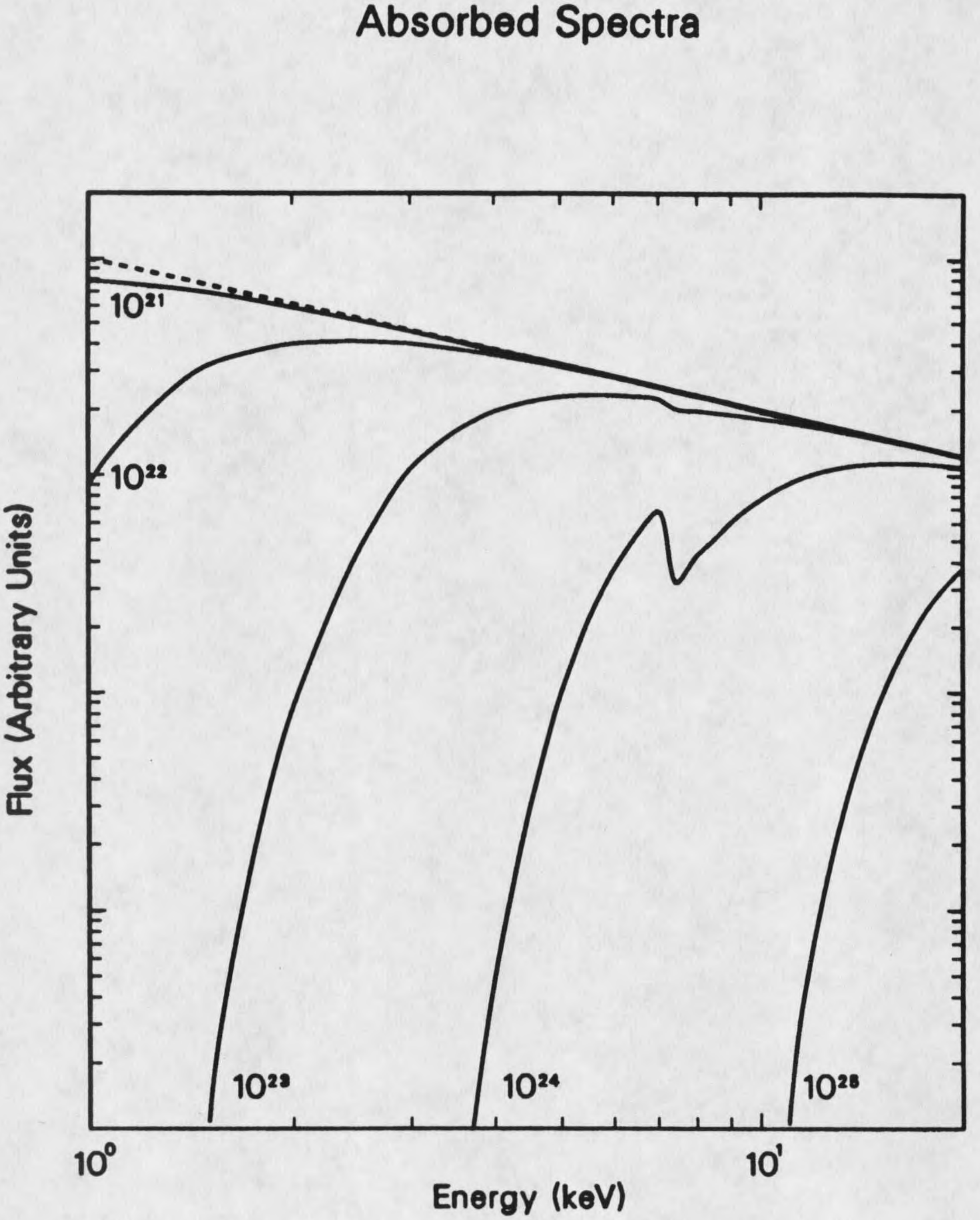

Figure 1. Absorbed spectra. Here the dashed line is the input spectrum with energy index 0.7, while the solid lines show the absorbed spectra. The figures by the solid lines give the absorption column densities in units of cm^{-2}.

the column density in units of cm^{-2}. As this figure illustrates, for columns above about $10^{23}\,cm^{-2}$, the spectrum is quite heavily cut off at low energies.

In some cases there is evidence that the covering material is not uniform over the source, or that it is ionized and the ionization state is changing. These points will be discussed in Chapter 5.

Soft Excess Emission

Surveys performed with instruments having a band pass constrained to low energies have tended to measure steeper energy indices for power law models than those performed in the medium energy band. For example, a survey from the Imaging Proportional Counter on-board *Einstein* in the energy band from 0.2 to 4 keV finds an average index of 0.81 (Kruper, Urry and Canizares 1990). The steeper index may be the result of an additional soft X-ray component, known as the soft excess. The EXOSAT spectral survey, taking advantage of the coverage of low and medium energy X-rays provided by the combination of the LE and ME experiments, found evidence for soft excess emission in approximately half of the unabsorbed sources (Turner and Pounds 1989). Because of the poor energy resolution of the LE instrument, these soft excess components could generally be fit with either an additional power law having an energy index in the range from 2 to 7, or with a thermal bremsstrahlung spectrum with kT of 0.15–0.4 keV. The detailed shape of the soft excess emission could not be determined.

The possibility that this excess is due to thermal emission has been investigated by theorists. It has been noted that excess emission known as the 'blue bump' is also found in the short wavelength ultraviolet continuum. Note that information from the extreme ultraviolet is not available due to interstellar photoelectric absorption, to the extent that the implied EUV excess cannot be directly measured. However, in order to estimate the size of the excess, the two excesses have been fit by a variety of thermal models. For example, for Mkn 841, a single temperature blackbody fit to these excesses gives a luminosity of $2 \times 10^{46}\,\mathrm{erg\,s^{-1}}$ (Arnaud et al. 1985). This is an extremely large luminosity, and it would be super-Eddington for the range of black hole masses relevant for a Seyfert nucleus. Such a radiation field should cause the thin disk to blow up, making the argument inconsistent. Other theorists have proposed more realistic emission models (e.g. Sun and Malkan 1987; Czerny and Elvis 1987; Elvis, Czerny and Wilkes 1987) which may make this type of model more favorable.

Recently the data from the Solid State Spectrometer was re-analyzed simultaneously with data from the Monitor Proportional Counter on-board *Einstein*, and further evidence for soft excess emission was found. In fact, soft excesses were discovered in 46% of 26 sources studied (Turner et al. 1991). The higher resolution of the SSS and its low band pass (0.6–4 keV) combined with the wider band pass (1.2–20 keV) of the MPC made the measurement of the shape of the soft excess possible. The interesting result is that, in some cases, the soft excess measured was well fit by line emission rather than an additional power law or thermal bremsstrahlung. The interpretation was that the soft excess may be a blend of soft X-ray lines, rather than being thermal emission (Turner et al. 1991). This is an interesting result for several reasons. First, if the soft excess is not thermal in origin, the previously discussed problems with super-Eddington emission may be solved. Secondly, if this emission is due to soft X-ray lines, then the source of these lines, and the ionization state of the material emitting them must be identified.

Iron Emission and Absorption

For iron K-shell emission and absorption features to be observed in the hard X-ray spectra of Seyfert 1 galaxies, material in a relatively low state of ionization must exist which is illuminated by a substantial fraction of the continuum emission. The emission energy of the iron fluorescence line is not extremely sensitive to the ionization state for low states of ionization; however, the iron absorption edge energy is very sensitive (Makishima 1986). The least that must be true is that iron cannot be fully ionized, unless the iron line is due to recombination. However, the observed iron line energy from the better energy resolution data from *Ginga* indicates that the iron is not extremely ionized; in general, the iron must be more recombined than XVII. Such relatively recombined iron may be difficult to attain in the central region of an AGN unless the absorbing material is very dense. This is due to the extremely intense primary X-ray spectrum, which can completely ionize any iron atoms available, by photo-ionization. For example, a typical Seyfert galaxy may have an intrinsic luminosity of $10^{43}\,\mathrm{erg\,s^{-1}}$ in the X-ray band from 2–10 keV. Therefore, the flux available for photo-ionization may be at least an order of magnitude larger. Assuming a black hole mass of 10^7 solar masses, based on variability arguments, the Schwartzschild radius is $r_s \sim 3 \times 10^{12}$ cm. At least in one object (NGC 6814), the iron line flux has been found to vary in phase with the continuum X-ray flux (Kunieda et al. 1990). Therefore both the continuum and the line flux must be coming from the region of the central engine, taken for compactness arguments to be $\sim 10 - 100\, r_s$. The ionization state of optically thin gas can be described by the ionization parameter ξ defined to be (Kallman and McCray 1982)

$$\xi = \frac{L}{nR_s} \cong \frac{10^{15}}{n} \tag{2.1}$$

where n is the number density. Now ξ must be less than ~ 1000 for iron not to be heavily ionized, and less than ~ 100 for oxygen to be an important contribution to the low energy opacity. For comparison, consider the Broad Line Region clouds, which lie outside the nucleus and have a typical density of $\sim 10^{10}\mathrm{cm}^{-3}$. If they were inside the nucleus, ξ would be $\sim 10^5$ and iron would be completely ionized. On the other hand, if the density were $\sim 10^{15}\mathrm{cm}^{-3}$, iron would be on the average unionized.

Can such dense gas exist in the central engine region of a Seyfert 1 galaxy? Guilbert and Rees (1988) demonstrated by a simple argument that such cool, extremely dense material necessary for iron emission might well exist in the central region of an AGN. This is because very dense material can easily cool by bremsstrahlung emission. In particular, if the accretion flow adopts a two phase configuration, and if the confining pressure is large enough to make the clouds dense enough, this process may be possible. Such a large confining pressure may be available from a magnetic field whose energy density is in equipartition with the gravitational potential energy of the infalling material (Rees 1987).

If cold material does exist in the central region, then iron emission features at ~ 6.5 keV are expected to be important spectral components because of several reasons. First, iron is relatively abundant, being 4.5×10^4 less abundant than hydrogen (Morrison and McCammon 1983). More importantly, the fluorescence yield for iron is relatively large. The K-shell electrons of lowly ionized iron can easily absorb an X-ray photon of energy equal to and somewhat greater than 7.1 keV. Because of their relative localization around the nucleus, the cross section of absorption is relatively large. This K-shell vacancy is readily filled by a L-shell or M-shell electron creating a fluorescence photon. If the electron comes from the L shell, then a K_α photon is born, with an energy of ~ 6.4 keV for iron less ionized than XVII. If the electron comes from the M shell, the result is a K_β photon with an energy of $\sim$ 7.1 keV. The radiation probability ratio of K_α/K_β is 0.135 (Weast 1975). As the ionization state of the iron becomes greater than XVII, the energy of the fluorescence photon also increases, becoming 6.7 keV for hydrogen-like iron (Makishima 1986). However, these photons do not always escape the atom. They may instead be absorbed by the atom causing the emission of an Auger electron. The fraction that does escape is known as the fluorescence yield, and iron has the highest fluorescence yield, being 0.34 (Bambynek 1972). Note that this is the fluorescence yield for neutral iron. If the iron is highly ionized, the fluorescence yield increases. For Fe XXIV, the yield is 0.75, for Fe XXV, the yield is 0.7, and for Fe XXVI, the yield is 0.5 (Krolik and Kallman 1987). Third, the iron emission line has energy of 6.4–6.7 keV and the iron edge has energy 7.1–9 keV, depending on the ionization state of the material (Makishima 1986). These features falls in the medium X-ray band where no other strong lines are expected. In contrast, emission lines due to lighter elements such as sulfur, oxygen, and neon, as well as the iron L emission line fall in the soft X-ray band; for example, the iron L line occurs at about 0.7 keV, the oxygen K_α line occurs at 0.52 keV, the neon K_α line occurs at 0.85 keV and the sulfur K_α line occurs at 2.3 keV. Therefore, because of its isolation, the iron line is more likely to be found by the spectral fitting of data from detectors with relatively low energy resolution.

If such cold material is available in the central region of the AGN, what would be the equivalent width of the iron line that might be expected to be measured? Recall that the line equivalent width is defined to be the width of the continuum flux band having the same flux as the line. If the emission arises from the fluorescence from material in the line of sight, the equivalent width will be quite small. For example for a column number density of 10^{22} cm^{-2}, and cosmic abundances, the equivalent width is only about 10 eV (Makishima 1986). On the other hand, if the material is illuminated by the source and not in our line of sight, it can have a thicker column density than if it were in our line of sight. For example, a possible geometry is a flat thin accretion disk, which may be like a wall behind the source, being illuminated by the source. Then the solid angle being illuminated is 2π steradians, but the column density may be much larger, and therefore, the expected equivalent width is much larger. Monte-Carlo simulations indicate that the equivalent width in this situation might be as large as 200 eV, for a flat spectrum with a photon index of 1.4 when the disk system is viewed face on, falling to 0 when the disk is viewed nearly edge on (George and Fabian 1990). Note that the equivalent width has been found to be inversely correlated with the index, as expected (Awaki 1991). The equivalent width of the iron line can also be augmented if the continuum emission to our line of sight is somehow blocked, and we see preferentially the iron emission region (Makishima 1986). Such a situation might be the case in Seyfert 2 galaxies (Awaki 1991). In this case the equivalent width may be more than 1000 eV (Koyama 1989; Awaki 1991). However, very large equivalent widths from Seyfert 1 nuclei may be difficult to explain.

In some cases, the absorption edge due to iron can be measured. This can give some indication of the position of the iron emitting material, since material out of our line of sight with a given column density will show a much less deep edge than material with the same column in the line of sight. It can also indicate the relative abundance of iron in the central region. It is certainly possible to imagine that near the center of such an energetic object as an AGN, iron abundances may be enriched over the cosmic abundance value and in some cases, evidence for such a situation have been found (e.g. Holt et al. 1980). However, overabundance is generally an unattractive explanation, and such apparent overabundances can be explained by geometry or ionization. For example, in some cases the iron edge energy may be measured. If the iron absorption edge has an energy much higher that the neutral edge energy, the contribution of a substantially ionized column is indicated.

The observations of the iron line around 7 keV are now many. Iron emission features have long been known to be present in the spectra of two bright active galaxies, Cen A (Mushotzky et al. 1978; Inoue 1985) and NGC 4151 (e.g. Warwick et al. 1989). Subsequently, the presence of these features has been discovered in the spectra of a Seyfert 1 nucleus, MCG–6–30–15, from a long observation by EXOSAT (Nandra et al. 1989). Iron features were also found in the spectrum of NGC 5506 from the long EXOSAT observation. This result will be described in Chapter 4. Recently, with the larger detector area on-board *Ginga*, iron emission lines were found to be common in Seyfert 1 nuclei (Awaki 1991; Nandra 1991). In the survey by Awaki (1991) sample of 22 Seyfert 1 galaxies were considered. Evidence for an iron emission line was found in all spectra. These features indicate the presence of neutral or partially ionized material being illuminated by the central continuum source. The equivalent widths measured ranged from 100 to 250 eV, with an average of 160 eV and a standard deviation of 60 eV. The study by Nandra (1991) of a sample of 29 spectra from 20 Seyferts found 26 line detections. In this sample the line energy was consistent with 6.4 keV. The average equivalent width found was 140 eV, with a standard deviation of 80 eV (Pounds, Nandra and Stewart 1991).

Note that in general a narrow Gaussian line ($\sigma = 0.05\,\mathrm{keV}$) provides usually an adequate fit to the *Ginga* spectra from Seyfert galaxies. This implies that, unlike the optical lines from the Broad Line Region, the material may not be in rapid motion around the central black hole. Note that, however, the LAC on-board *Ginga* has the poor energy resolution characteristic of proportional counter detectors, and a small amount of broadening may not be detected. The width of the line has been constrained in only one case. This exception is NGC 4151, an exceptionally nearby Seyfert 1, in which the intrinsic width of the iron K_α line was found to be $\sim 38,000\,\mathrm{km\,s^{-1}}$ FWHM, implying that the cold matter lies within 1 light day from the source (Yaqoob and Warwick 1991). Another exception is NGC 3227, a Seyfert 1 galaxy, from which an asymmetrical line was discovered (Pounds et al. 1989). This was subsequently modeled and interpreted to have been emitted from a rotating thin accretion disk, and subsequently to have been broadened due to gravitational redshift and Doppler shift (George, Nandra and Fabian 1990).

In one case, the iron emission line flux has been found to be variable. In NGC 6814, a 1989 *Ginga* observation found the line flux to vary in phase with the continuum flux, with the lag being less than 300 seconds (Kunieda et al. 1990). This observation places severe constraints on the position of the emitting gas, as discussed previously.

Hard X-ray Hump

The Large Area proportional Counter array on-board *Ginga* was the first X-ray detector to have both a large enough area and a large enough optical depth so that the spectra above 10 keV for Seyferts could be measured with fairly good resolution. The *Ginga* spectra from several Seyfert 1 nuclei seem to flatten at energies above ~ 10 keV. Detailed studies from several Seyfert 1 nuclei have found this result; included are MCG–6–30–15 (Nandra, Pounds and Stewart 1990; Matsuoka et al. 1990), NGC 4051 (Matsuoka et al. 1990; Kunieda et al. 1991); NGC

5548 (Nandra et al. 1991), NGC 7469 and IC4329A (Piro, Yamauchi and Matsuoka 1990). Such a tail also was evident in the average of 12 *Ginga* spectra from Seyfert 1 nuclei (Pounds et al. 1990). In fact, a study by Nandra (1991) of 29 *Ginga* observations from 20 Seyferts finds the average of the 2–10 keV energy index to be 0.722, while the average of the 10–18 keV index is 0.37, and a statistical test finds the two index distributions to be different at greater than 99% confidence level (Pounds et al. 1991).

Theoretically, there are at least two explanations for the physical origin of the hard tail. These are the partial covering origin, and the reflection origin.

In the partial covering origin, a fraction of the primary X-rays is assumed to be occulted by a screen of thicker material. This screen can be in the form of clouds which cover the source (Poisson clouds), or in the form of a fraction of the source covered. Thus it is the sum of the two emissions which reach the observer. This model was proposed early to explain some aspects from the soft X-ray spectrum of NGC 4151 (Holt et al. 1980). In this case, the column density of the covered fraction is relatively small, typically $\sim 10^{22}\mathrm{cm}^{-2}$. When this model is used to explain the hard tail above 10 keV, a denser column is needed. Figure 2 illustrates the partial covering model. The incident spectrum with energy index of 0.7 is shown by the dashed line. The spectrum from the covered component is shown by the dotted line. The column density of the covering cloud is $3 \times 10^{23}\mathrm{cm}^{-2}$. The solid line gives the sum of the two components, where the normalization is such that 1/2 of the source would be covered. The spectral break is seen to be at around 9 or 10 keV, for this choice of covering column density and relative normalization.

Another possible origin of the hard tail emerges if the thick material illuminated by X-rays is behind the source instead of in front of it. That is, if very

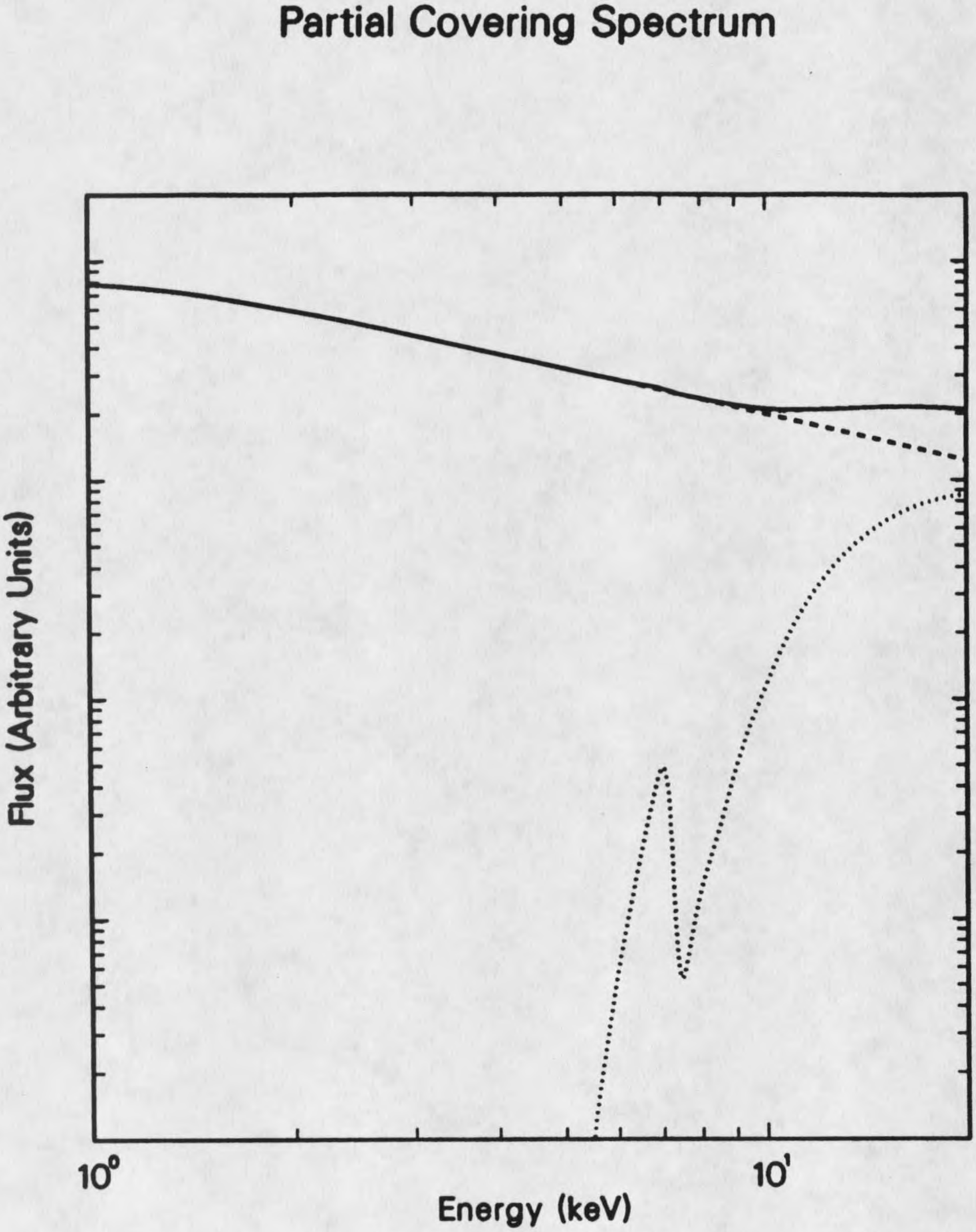

Figure 2. Partial covering spectrum. Here the incident spectrum with energy index of 0.7 is shown by the dashed line, the absorbed ($3 \times 10^{23}\mathrm{cm}^{-2}$) spectrum is shown by the dotted line, and the total is shown by the solid line.

thick material subtends a large solid angle to the primary X-ray source, and if this material can be viewed by the observer, it is expected that some X-rays will be scattered back toward the observer. This effect is due to the energy dependence of the absorption cross section. The absorption cross section decreases with energy, so X-rays which have energies above $\sim$ 5 keV are not so easily absorbed. However, the Thompson scattering cross section which is independent of energy is still appropriate up until about 15 keV, because the scattering is still approximately elastic. At higher energies, the scattering becomes inelastic, and also the scattering cross section becomes smaller, because the Klein-Nishina cross section is appropriate. Therefore, the reflection spectrum rises at low energies, peaks at around 30 keV, and falls off at high energies (Lightman and White 1988). The total spectrum appropriate in this case is illustrated in Figure 3. The incident X-ray spectrum of energy index 0.7 is shown by the dashed line. The reflection spectrum is shown by the dotted line. This was calculated using Lightman and White (1988) Equation 11, and is only appropriate for the elastic regime, less than $\sim$ 15 keV. The degradation of higher energy photons by inelastic scattering into this energy band is not taken into account. The total spectrum is given by the solid line. The normalization between components is such that 1/2 of the flux is emitted toward the observer, while 1/2 is emitted toward an infinite reflecting wall.

The shape of the reflection spectrum is somewhat different than that of the partial covering spectrum shown in Figure 2. Specifically, the flattening due to the reflection spectrum is more gradual and affects lower energies, compared with the partial covering spectrum which has a break. However, note that the energy resolution of the LAC on-board *Ginga* is not good enough in general to distinguish between these two. Note also, the partial covering spectrum assumes transmission

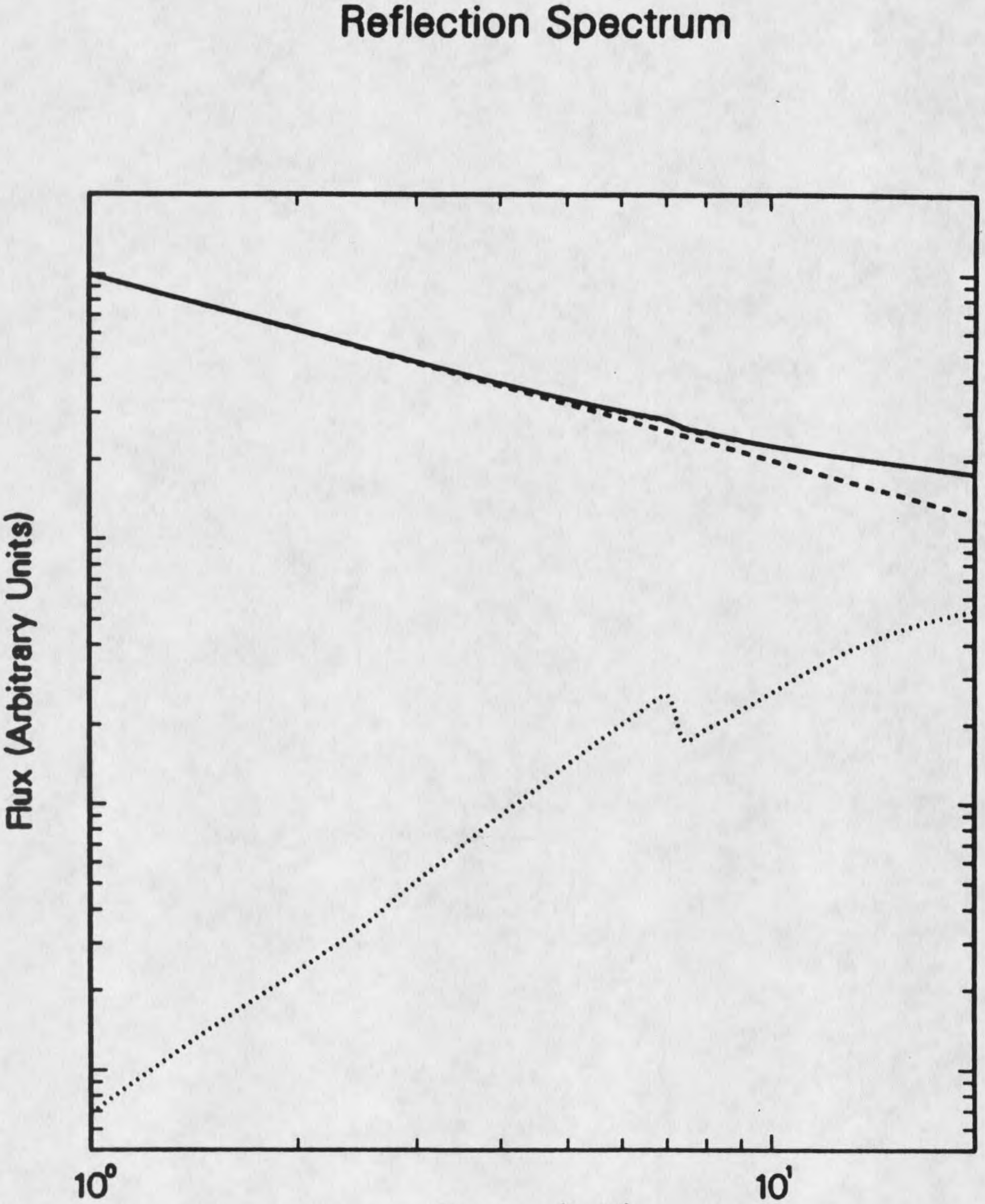

Figure 3. Reflection spectrum. Here the dashed line shows the incident spectrum of energy index 0.7, the dotted line is the reflected spectrum, and the solid line is the total.

through only one column density, corresponding to a cloud with hard edges. In reality, it may be that the column at the edges of such a cloud would decrease only slowly to 0, and the blend of spectra would soften the spectral break. This possibility is discussed further in Chapter 8.

The possibility that the reflection spectra are common from Seyfert 1 nuclei has far reaching implications. The first implication is for the theory of pair models. As discussed in the section on power law spectra earlier in this chapter, a problem with pair models is that they generally produce too many γ-ray photons to be consistent with the γ-ray background if the the X-ray energy index is required to be 0.7. With the addition of a reflection spectrum, the intrinsic index is not required to be so flat; power law spectra with energy indices of ~ 0.9 added to a reflection spectrum would give a 2–10 keV slope of 0.7 (Zdziarski et al. 1990)

The reflection spectrum also affects the soft excess component. Recall that, from the EXOSAT spectral survey, one half of all of the relatively unabsorbed sources showed evidence for a soft excess component. Some of these were based on separate variability of the soft and medium energy light curves. Reflection spectra do not affect this determination. However, others were found on the basis of spectral fitting; that is, a separate, steeper spectral component was required to adequately fit the lowest energies. If the intrinsic energy index of the medium energy power law is ~ 0.9, then because of modification due to the addition of the reflection component, the necessity of an additional spectral component is in question. A steeper intrinsic index may not make a soft excess component necessary. At least, however, even though it may be found that the soft excess component is still necessary, the energy in this component will be reduced. This will affect models of the soft excess, since they will not be required to explain the production of such a large amount of energy. In fact, some old accretion disk models which have been rejected should be re-examined, since they may not have the same super-Eddington problems which they had previously.

CHAPTER 3

THE EUROPEAN X-RAY OBSERVATORY SATELLITE

The EXOSAT Mission

General

The European X-ray Observatory Satellite (EXOSAT) was operational from May 1983 and was operated successfully until April 1986. The payload consisted of three instruments: a large area proportional counter array system known as the Medium Energy (ME) Experiment, two imaging telescopes known as the Low Energy (LE) Experment, and a gas scintillation proportional counter known as the GSPC. Because of the relative weakness of AGN, only the ME and LE experiments are relevant to this discussion; the GSPC could only be used for strong targets.

With this payload, the mission objectives were several, including precise location of sources and mapping of diffuse sources, but the most relevant objective for this discussion was the broad band spectroscopy of sources. The observation energy band for AGN was about 0.1–10 keV.

EXOSAT was placed in a rather unusual orbit. The orbit was highly eccentric with apogee of 2×10^5 km and perigee of 500 km. This resulted in a period of 90 hours. During 80 hours per period the satellite was above the Earth's radiation belts, and so was operational. The primary purpose of this eccentric orbit was to use lunar occultation to precisely locate sources, but the advantage for weak sources such as AGN is that a source could be observed continuously for up to

80 hours, with no earth occultations of the source. Another advantage was that the inclination of the satellite was such that it was continuously in sight of the ground station, so no on-board data storage was necessary. A major disadvantage is that it was subject to a high and unpredictably variable particle background, approximately 10 times larger than that experienced in a low earth orbit. Another obvious disadvantage is the wear and tear experienced while the satellite passed through its perigee.

The satellite was powered by a solar array. The attitude control and pointing was performed using a propane gas thruster system. Less than 90 minutes were required between observations for attitude slew. The attitude measurement system consisted of sun sensors, gyros and two star trackers, and could be determined to better than $10''$.

During EXOSAT's lifetime, 1780 sources were successfully observed. These data are available to the public as automated data products on the EXOSAT Data Base. Information about the EXOSAT Data Base may be obtained from the EXOSAT Observatory, ESTEC.

The ME Experiment

The Medium Energy experiment consisted of a system of proportional counters. An effective area of 2,000 cm^2 was the design goal; however, only 1,800 cm^2 were realized (Turner and Smith 1981). The proportional counters were designed as two chambers, the front one being filled with a mixture of argon and CO^2 while the back one was filled with a mixture of xenon and CO^2. The front window was of beryllium, the thickness of which limited the lowest energy of X-ray that could be measured. The effective energy range for the ME experiment was 1.5 keV to 50 keV; however, for AGN which typically have a steep spectrum and also low flux, the upper limit was about 10 keV. This is because generally the data from the xenon layer, having a small signal to noise ratio, were not used in AGN studies. In this discussion, the data from the xenon layer was only used once.

A proportional counter is a gas filled detector with an anode and a cathode. As the X-ray enters the detector, through photo-electric absorption, it liberates electrons from atoms in the fill gas. By momentum conservation, the momentum of the electron is approximately equal to the photon energy minus the energy of photo-ionization. This electron is accelerated by the applied electric field as it continues through the fill gas, creating by collision a number of ion pairs. Electrons from these ion pairs are also accelerated, liberating more electrons, until the bunch of electrons are detected at the cathode as a charge pulse. The voltage drop is maintained so that the final charge collected is proportional to the original number of ion pairs.

The energy resolution of the detector is an important descriptive measurement of the detector. It defines the response of the detector to a mono-energetic incident pulse. When a mono-energetic signal is applied to the detector, the measured pulse height spectrum, or flux in each energy bin measured, is spread out to a Gaussian function from the incident delta function. The resolution R is defined to be the full width at half maximum (FWHM) of the measured pulse divided by the energy of the incident radiation. For the EXOSAT ME detector, the energy resolution was approximately 20% at 6.4 keV. This means that the probability a given incident photon of energy E will be measured outside the region $E - RE \rightarrow E + RE$ is about 24%.

The limiting, statistical resolution of a proportional counter is always proportional to $1/E^{\frac{1}{2}}$, where E is the incident photon energy. This is because the uncertainty in the number of original ion pairs created is equal to the square root of that number, because the creation of each ion pair is considered to be a Poisson process. Then, because of proportionality, the charge measured also has an uncertainty proportional to the square root of the charge. The original number of charges produced is proportional to the energy of the photon. Therefore, the uncertainty in the measured charge divided by the measured charge is proportional to $1/E^{\frac{1}{2}}$. This uncertainty is the same as the resolution. The proportionality constant depends on the fill gas used and the counter design.

This gives the statistical limit. Another major contribution to the energy resolution is the background radiation. For EXOSAT, at 6.4 keV, the typical count rate of the background in one detector half (4 detectors) is 6 counts s^{-1} in the energy band from 2–6 keV while the source count rate for a typical Seyfert 1 galaxy in the same energy band is 0.5–10 counts $\mathrm{s}^{-1}\mathrm{half}^{-1}$. Because of the additivity of the uncertainties, the uncertainty in the source count rate is much larger than the ideal Poissonian uncertainty.

Because of the high particle background experienced in the eccentric orbit and the weakness of AGN, background rejection and subtraction methods are important. Good background rejection was attained by having several layers of anode and cathode wires. Then anticoincidence logic could be used to discriminate between photon detection and events due to particle interaction. To prevent source confusion, and contamination of weak X-ray sources like AGN by strong sources such as X-ray binaries, the ME was equipped with a collimator reducing the field of view to $45'$ FWHM. This collimator was made by fusing very thin pieces of drawn lead glass together. However, the collimator reduced the transmission rate of X-rays, and so the effective area was modified to 1800 cm^2 from the original 2000 cm^2.

The LE Experiment

The main purpose of these two imaging telescopes was to map extended sources (Taylor et al. 1981; de Korte et al. 1981). However, they could also be used to obtain flux measurements of soft X-rays with low energy resolution. Unfortunately one of the telescopes failed early in the mission.

The two telescopes had a focal length of about 1 meter, and the total collecting area for each telescope was about 90 cm^2. Each telescope consisted of two nested mirrors with grazing incidence optics. Each telescope had two detectors that could be alternately moved into the focal point: a position sensitive proportional counter (PSD) and a channel multiplier array (CMA). Also a series of filters were available for each detector, and for bright sources, a transmission grating could also be placed in the beam.

For weak sources such as AGN, the observing configuration was usually with the CMA at the focal point. To absorb excess UV emission, the CMA had to be operated with a filter. Three filters were available, which each allowed transmission of different energy bands. In this way, low energy flux measurements could be made with poor energy resolution.

In this study, the LE data was used only once, in the study of NGC 5506. The 3000 Å LEXAN filter was used, which allowed through a band of soft X-rays from 0.04 to 1 keV peaking at a wavelength of $\sim$ 100 Å.

Data Analysis and Spectral Fitting

Background Subtraction

The ME Experiment. The X-ray background for the ME consisted of the cosmic X-ray background, particle events, and internal background of the satellite. The ME detector was built of eight proportional counters, with four in each of two halves. For the observation of weak sources the standard mode of operation was to point one half at the source while the other half was aligned toward some near sky source-free background. This method was particularly valuable for rejecting parts of the data which showed flares in both halves, identifying noisy, contaminated data. Examination of the light curves for the on-source and off-source data for flares was usually done. Because the halves had different responses, the off-source data could not be subtracted directly from the on-source data. Instead, two standard methods were used for background subtraction. The method used mostly for short observations was known as the 'slew' method. In this case, the source had been only observed by one half and so the background data was taken from the same half during the time of slewing from target to target before and after the observation, when the field of view was source free. However, the preferred method was known as the 'nod' method. Nod background subtraction was used for longer observations in which the halves were switched, or nodded, so that each was on the source for some time during the observation. Then, the background data could be used from the same detectors which had observed the source, and both types of data would be obtained in the pointed mode. Also, it was found that, of the four detectors in each half, the two closest to the body of the satellite were subject to more internal background than the two farther from the satellite. Therefore, in the case of very weak sources, sometimes the data from only the outer two detectors of each half were used for spectral analysis.

The LE Experiment. The LE flux rate was found from the LE image. Two boxes were used, centered on the source, one of $100'' \times 100''$ and another of $300'' \times 300''$ in area. The background spectrum is estimated from the region between the two boxes. The source rate is then found by subtracting the background from the flux in the smaller box.

In the study of NGC 5506, the LE flux point was used. However, the background subtraction had already been done by I. McHardy.

Spectral Fitting

Once a satisfactory background subtracted spectrum was obtained, spectral fitting was carried out. For the ME data, usually energy channels 6–40 were chosen for spectral fitting, corresponding to the energy band from 2 to 10 keV. X-ray detection is a Poisson process. In the case when many photons are received, the Poisson distribution converges to the Gaussian distribution. However, when weak sources such as AGN are observed, this limit is not appropriate. Therefore, the source spectrum cannot be deconvolved directly from the measured spectrum. Thus spectral fitting proceeded iteratively. A model spectrum was chosen, convolved through the detector response matrix, and then the result was compared with the measured spectrum. The goodness-of-fit of the model with this set of parameters was evaluated using the χ^2 statistic (Bevington 1969). Subsequently, the model parameters were varied, until the χ^2 was minimized. In the case that the LE detector points were used, a detector response matrix for the LE was also made, and the data from the two instruments were fit simultaneously.

The best fit which resulted from the iteration process was evaluated by examining the final χ^2_R , defined to be χ^2 divided by the number of degrees of freedom. Because of the statistical nature of X-ray detection, a good model fit is indicated by a χ^2_R nearly equal to 1. The proximity to 1 necessary to indicate a good fit depends on the number of degrees of freedom. For example, a reduced χ^2 of 1.34 for 30 degrees of freedom indicates that the probability of obtaining such a large value of χ^2 for a correct fitting function is less than 10%, while the χ^2_R must be 1.49 for 15 degrees of freedom for the same confidence level (Bevington 1969). In general, a χ^2_R of very much greater than one indicates that the model was inappropriate, and a χ^2_R of very much less than one indicates that the model was perhaps too complicated, and the measured spectrum was over-fit. If over-fit, there is not enough information in the data to constrain additional parameters.

The calculated χ^2 is a mixture of two things. It is of course a measure of how well the model spectrum fits the measured spectrum, but it also measures the deviation of the measured spectrum from the parent spectrum. Therefore, if very few X-ray photons are received, then the statistical noise in the data dominates, and the parameters cannot be determined. In order to separate the statistical noise from a poor fit, the F statistic maybe used (Bevington 1969). The F statistic can be used to evaluate the improvement of a fit due to the addition of any number of parameters; however, it is particularly useful in the case that only one additional parameter is added to the model. The F for the validity of adding an nth parameter compared with $n-1$ parameters is defined to be

$$F_\chi = \frac{\chi^2(n-1) - \chi^2(n)}{\chi^2(n)/(N-n)} \tag{3.1}$$

where N is the number of points, and n is the number of parameters. Values and confidence levels are tabulated; for example, see Bevington 1969.

CHAPTER 4

IRON EMISSION AND ABSORPTION FEATURES IN EXOSAT X-RAY SPECTRA

The Long Observation of NGC 5506

Towards the end of the EXOSAT mission several AGN were observed continuously for an entire orbit ($\sim$ three days). Although the primary purpose of these extended observations was to investigate variability, a by-product was X-ray spectra with better statistics. Because X-ray detection is a Poisson process, the uncertainty in a flux point is proportional to $\sqrt{N}$, where N is the number of photons observed. Therefore, a longer observation, by virtue of the large number of photons gathered, provides a less noisy spectrum, and finer spectral features such as emission lines can be measured if present.

Such a situation was the case in the observation of MCG–6–30–15, analyzed by Nandra et al. (1989). Fixing the emission line energy at 6.4 keV, he found evidence for a line with equivalent width of 150^{+90}_{-110} eV, with high statistical confidence. There was also evidence of additional absorption by iron. This was the first such discovery of iron features in an ordinary Seyfert 1 galaxy. NGC 5506, also a Seyfert 1 galaxy with similar flux level, was observed for three days directly after the observation of MCG–6–30–15. This observation was analyzed by Leighly with the intention of measuring the iron line emission and iron absorption, if present.

Since the flux and observation times were similar to the previous successful study of MCG–6–30–15, our hopes for success seem justified.

Results

Data Reduction. The Seyfert galaxy NGC 5506 was observed continuously from the 24th through the 27th of January, 1986. Our data analysis was carried out at the University of Leicester, Leicester, U.K. during the first two weeks of September, 1988, and is reported in Pounds et al. 1989. This data was previously analyzed by I. McHardy and B. Czerny for its timing properties, and that analysis is reported in McHardy and Czerny 1987.

The standard nod method of background subtraction was used, as described in Chapter 3. It was found that the background subtraction was not completely satisfactory for all four detectors used per half detector array, so the spectrum was accumulated using the data from only the corner detectors. However, this spectrum was not completely satisfactory, because when the data from each half were fit separately, the spectral fitting results were not consistent. Specifically, the spectral fitting of the data from the corner detectors of half 2, or detectors 5 and 8, resulted in an anomalously large power law spectral index of 2.13. This observation was taken late in the life of EXOSAT, and it may be that some gain changes had occurred in the detectors due to loss of fill gas and this problem was not correctly compensated for in the response matrix. In the final spectrum, therefore, only the data from the half one corner detectors (detectors 1 and 4) were used.

The LE data used for spectral fitting was already available, having been reduced by I. McHardy, and consisting of data using the 3000 Å LEXAN filter with the CMA detector at the focal point of the telescope. This filter admits a band of soft X-rays peaking at the wavelength of ~ 100Å.

Spectral Fitting. A satisfactory spectrum having been obtained, the spectral fitting was carried out using PHA channels 6–40, corresponding to energies 2–10 keV. The spectral fitting results are listed in Table 1. First, a simple power law plus absorption fit was tried, of the following form:

$$F(E) = N\,E^{-\alpha}\,e^{-\sigma(E)N_H}. \tag{4.1}$$

Here N is the fit normalization in units of cm^{-2}s^{-1}keV^{-1} and N_H is column density of the neutral material, while $\sigma(E)$ is the cross section for absorption, taken from Morrison and McCammon 1983. In the table, the photon index Γ is quoted. The photon index is the energy index α plus 1.

This fit was unsatisfactory, as the reduced χ^2 was 3.26 for 33 degrees of freedom. The best fit and the χ^2 residuals are shown in Figure 4. The photon index of the fit was 1.68 ± 0.06, where the uncertainty quoted is the 90% level, for a fit with all parameters of interest. The photon index found by McHardy and Czerny (1987) was larger, being 1.84 ± 0.04. However, the best fit value for the large absorption column agreed with the previous analysis. Therefore, the difference in index is significant. One explanation for the discrepancy in spectral index is that they may have used the data from both detectors. However, the details of their data reduction are not given in the publication.

Examination of the residuals shows that much of the contribution to the χ^2 was from an excess at about 6–7 keV. Therefore, the next spectral fitting tried was the absorbed power law with the addition of a Gaussian emission line, as follows:

$$F(E) = N\,E^{-\alpha}\,[1 + Line(e, \Delta E, Z)]\;e^{-\sigma(E)N_H} \tag{4.2}$$

Table 1. Spectral fitting results from the EXOSAT long observation of NGC 5506.

Normalization (10^{-2}cm^{-2}s^{-1}keV^{-1})	Photon Index	N_H (10^{21}cm^{-2})	Iron Line Flux (10^{-4}cm^{-2}s^{-1})	Equivalent Width (eV)	N_{Fe} ($10^{16.52}$cm^{-2})	χ^2_R /d.o.f.
$2.78^{+0.31}_{-0.27}$	1.68 ± 0.06	27.9 ± 2.3	–	–	–	3.26/33
$3.12^{+0.57}_{-0.33}$	$1.76^{+0.10}_{-0.07}$	$29.3^{+3.4}_{-2.3}$	$1.94^{+0.11}_{-0.08}$	160^{+90}_{-70}	–	2.25/32
$2.65^{+0.75}_{-0.57}$	$1.65^{+0.16}_{-0.15}$	$26.7^{+4.5}_{-4.2}$	1.43 ± 0.12	120^{+100}_{-90}	$140 < 290$	2.05/31

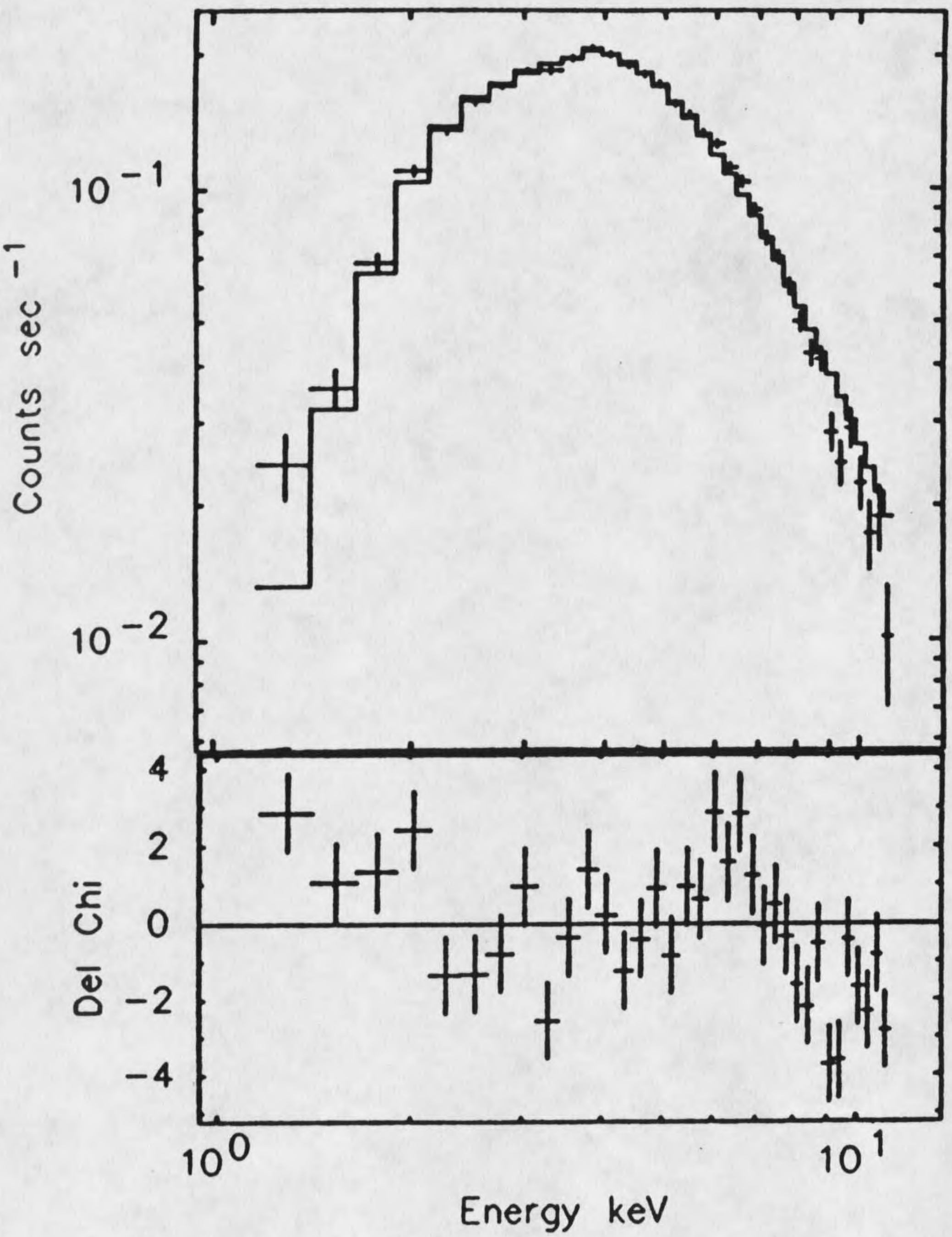

Figure 4. Power law fitting to NGC 5506 data. Fit residuals are shown below in units of χ^2.

where

$$Line(E, \Delta E, Z) = \frac{F_L}{\sqrt{2\pi}\Delta E} \exp \frac{\left(E - \frac{E_L}{1+Z}\right)^2}{(\Delta E)^2}. \qquad (4.3)$$

Here ΔE is the width of the line, and Z is the cosmological redshift. The line energy was fixed at 6.4 keV, corresponding to iron with an ionization state of less than about XVII. The width of the line was also fixed at 0.05 keV, appropriate for a line unaffected by broadening, and appropriate for the resolution of the detector. This fit resulted in a significant reduction in χ^2, finding a reduced χ^2 of 2.25 for 32 degrees of freedom. Using the F test described in Chapter 3 the improvement to the fit was found to be significant at $> 99.9\%$ confidence level. The equivalent width of the line was moderate, being 160^{+90}_{-70} eV.

The fit was still unacceptable, due to the large χ^2_R so a fit including also additional column of iron absorption was tried, as follows:

$$F(E) = N\, E^{-\alpha}[1 + Line(e, \Delta E, Z)]e^{-[\sigma(E)N_H + \sigma_{Fe}(E, E_E, Z)N_{Fe}]} \qquad (4.4)$$

where

$$\sigma_{Fe}(E, E_E, Z) = \sigma_{Fe}\left(E, \frac{E_E}{1+Z}\right). \qquad (4.5)$$

The energy of the additional absorption edge was fixed at 7.1 keV, corresponding to absorption by neutral iron atoms. (Makishima 1986). The fit and the χ^2 residuals are shown in Figure 5 and the fit parameters are listed in Table 1. The reduced χ^2 for this fit was found to be 2.05, and calculation of the F statistic showed this reduction to be significant at the $90\% \rightarrow 95\%$ level. Notice however the lower limit of the additional column is 0, at the 90% level, so the value of the additional absorption column is not well determined. The units of the iron column are given in $10^{16.52}\mathrm{cm}^{-2}$. This means that for a hydrogen column of $10^{21}\mathrm{cm}^{-2}$, the iron would have cosmic abundance if the iron column were equal to $1 \times 10^{16.52}\mathrm{cm}^{-2}$.

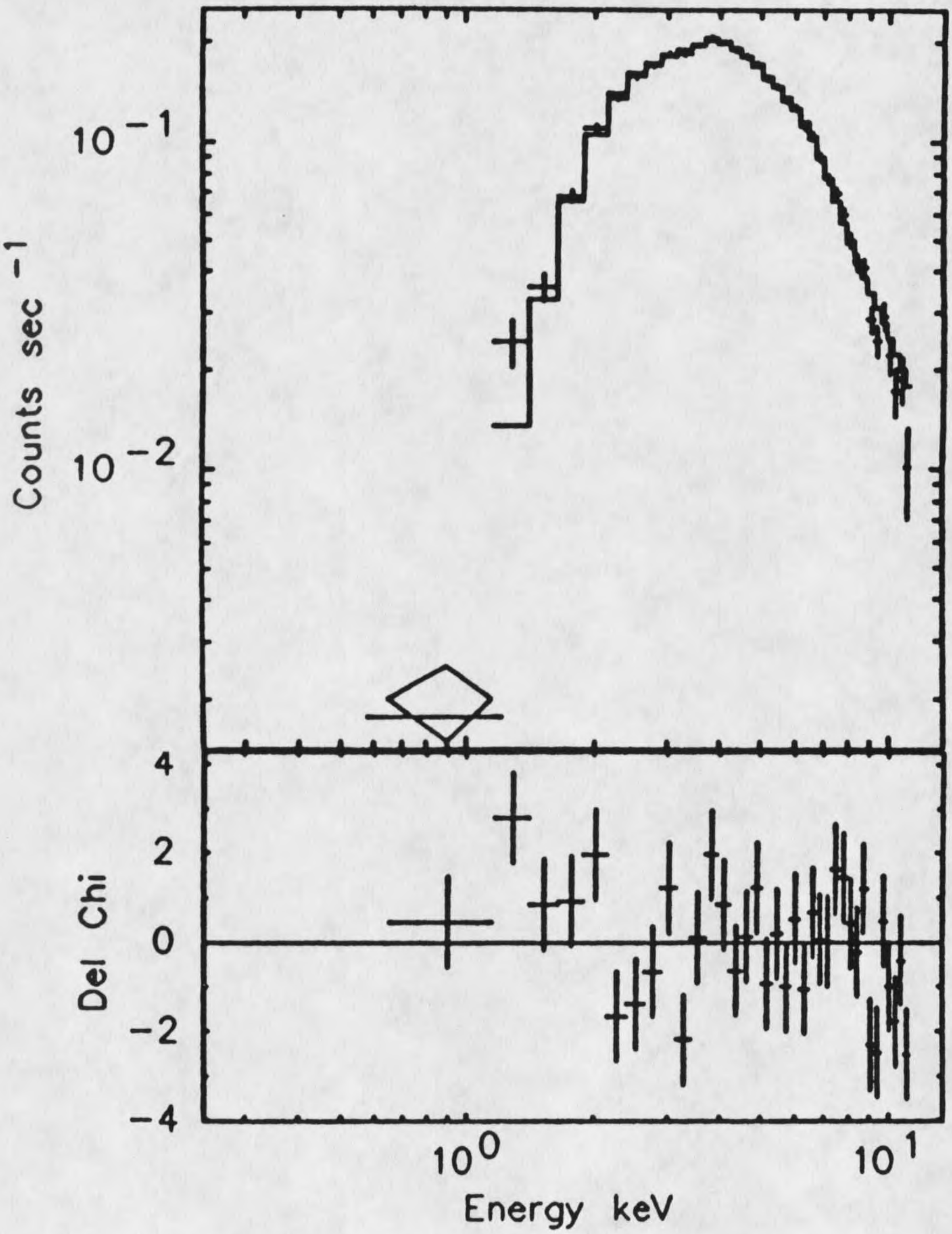

Figure 5. Power law plus line fitting to NGC 5506 data. Fit residuals are shown below in units of χ^2.

Therefore, since the N_H column is $\sim 30 \times 10^{21}\mathrm{cm}^{-2}$, and the iron column best fit is $140 \times 10^{16.52}\mathrm{cm}^{-2}$, then iron is found to be about 4 times overabundant.

The equivalent width of the iron line was reduced to 120^{+100}_{-90} eV. The reduction of the line equivalent width is easy to understand. If an additional cold column is present, creating an absorption edge at 7.1 keV, and the data is fit with a model including only the line and not an additional edge, the spectral fitting program will tend to fall into the edge, and find a χ^2 minimum which measures s a larger line. Because they are coupled, a larger spectral index will be measured, as is indeed the case in this instance (1.68 for simple power law, and 1.76 for power law plus line).

This final fit is still not particularly satisfactory, since the reduced χ^2 is 2.05. However, examination of the residuals shown in Figure 5 show that much of the contribution to the χ^2 is due to the residuals in the low energy. In the higher energy region, from 5 to 8 keV, the residuals are quite flat, indicating that at least the iron features are well fit.

Discussion

Simultaneous to my analysis of the EXOSAT data of NGC 5506, the analysis of a *Ginga* observation of NGC 5506 was performed by G. Stewart. The results of this analysis are also reported in Pounds et al. 1989. The results of the two analyses were nearly consistent. The photon index found from the *Ginga* data was somewhat larger, being 1.76. A similar low energy column, iron column, and line equivalent width were found. Another interesting difference was the energy of the iron edge. Because of the better resolution and greater area of the *Ginga* detector, the iron line energy and iron edge energy could be allowed to remain free during spectral fitting. The best fit iron line energy was 6.34 keV, consistent with the assumption of cold iron emission used in the analysis of the EXOSAT data. However, the edge energy was $8.3^{+0.8}_{-0.3}$ keV. This is inconsistent with the assumption of a cold iron absorption edge that was used in the EXOSAT analysis. However, there may not have been a discrepancy, because warm edge models were not tried in the EXOSAT spectral fitting. In fact, the residuals shown in Figure 4 from the power law fit show a flux deficit in the 8–10 keV region. Therefore, it may be that a warm edge would have provided a better fit.

The presence of an extra column of cold iron can have several explanations. First, it is not unreasonable to expect a significant enrichment of heavy elements in the center of an AGN compared with the cosmic abundance. Presumably the accreted material to the center of the AGN has come from the surrounding galaxy, and has undergone its share of being part of the birth and death of stars. This may be the best explanation if we knew for sure that the iron was required to be neutral. However, there is another more attractive explanation, suggested by the edge energy found in the spectral fitting of the *Ginga* data. An iron edge at this energy indicates that the column producing it is ionized to the $\sim$ XXI ionization state (Makishima 1986). This state is dominant at ionization parameter $\xi > 100$. At this ionization, oxygen can be expected to be completely stripped of its electrons (Kallman and McCray 1982), and thus the material may be quite transparent to low energy X-rays. Therefore, the presence of an additional, partially ionized column would not be measured by the curvature at low energies by which the spectral fit finds the value of the N_H.

Assuming this to be the case in the EXOSAT data, even though a warm edge fit was not tried, what would be the effect on the equivalent width of the line measured? The iron line due to the cold column of N_H ($\sim 3 \times 10^{22} \mathrm{cm}^{-2}$) would be only about 40 eV. However, the ionized column will also produce iron line emission, with energy close to 6.4 keV if the material has an ionization state less than XXVI (Makishima 1986). An upper limit of the equivalent width of the iron line produced by an ionized column $\sim$ 4 times the cold column is then 160 eV, which is nearly the best fit value of 120 eV.

The EXOSAT Spectral Survey Sources

A major EXOSAT program was designed to obtain X-ray spectra of a large sample of hard X-ray selected AGN, and was continued throughout the lifetime of EXOSAT (Turner and Pounds 1989). The results of the analysis of these spectra were very important because of the model constraints imposed by careful examination of the soft X-ray continuum, as discussed in Chapter 2.

Because simple power law fits were generally fairly good in most cases above $\sim$ 2 keV, these X-ray spectra were not systematically examined by Turner and Pounds (1989) for the presence of iron features. Most of the observations were fairly short, ($\sim$ 20000 seconds), so because of the poor energy resolution of the detector and the high rate of X-ray background, it was not thought that these data could tightly constrain the size of the equivalent width of the iron line in AGN data. However, some of the observations were longer, up to nearly 52000 seconds in the case of NGC 1068. Additionally, some of the sources exhibited quite high flux levels. For example, from 3C273, 5.23 counts $s^{-1}half^{-1}$ were measured by the ME experiment (Turner and Pounds 1989). Also, in some cases, examination of the power-law fit residuals, or difference between the data and the best fit model, revealed an excess of flux in the region of $\sim$ 6.5 keV. Therefore, it was thought that some useful upper limits might be found, and even some detections. The likelihood of a detection depended on the length of the observation, the strength of the source, and the strength of the emission line.

Data Reduction and Analysis

The EXOSAT spectral survey examined 48 galaxies (Turner and Pounds 1989). Of these, acceptable spectra were found for only 42, due to the faintness and problems with background subtraction in the other six. I considered only 40, because NGC 4151 and MR 2251 are bright sources and are therefore well studied, and the results are reported elsewhere (Yaqoob, Warwick and Pounds 1989; Pan, Stewart and Pounds 1988). For some of the sources, multiple observations were available. The total number of spectra fit was 47. The observing log for these 40 sources is given in Table 2.

Because the iron emission line and absorption edge fall near the middle to high energies (6–9 keV) of the ME bandpass (2–10 keV), only the ME data were considered for spectral fitting. Background subtracted pulse height (PHA) spectra were available for 33 of the forty sources, the background subtraction having previously been performed by T.J. Turner. Background subtracted PHA spectra were not available for the remaining seven sources: NGC 7314, ESO 103–G35, NGC 4051, NGC 2992, MCG–6–30–15, NGC 5506, and III Zw 2. Of these, the data from five were reduced using the nod background subtraction method, while the data from two (NGC 4051 and NGC 7314) were reduced using the slew method of background subtraction. For ESO 103–G35, a heavily absorbed source, the xenon layer data was used as well as the argon, and the resulting pulse height spectrum was fit to nearly 20 keV.

Next spectral fitting was performed. The ME data was first fit with a simple power law plus absorption model as given by Equation 4.1. The absorption cross section was taken from Morrison and McCammon 1983. In Table 3 the χ^2 and number of degrees of freedom for this fit are listed. A star (*) marks those with an unacceptable fit at the 90% confidence level.

Table 2. Observation log of the EXOSAT spectral survey sources.

Source name	Position (1950) R.A.(h,m,s)	Position (1950) Dec.(°,′,″)	Type*	Redshift	Date	Exposure† (seconds)	ME Flux (10^{-11} erg s^{-1}) (2–10 keV)
Mkn 335	00 03 45.2	+19 55 28.6	S1	0.0258	85/199	23300	1.35
					85/334	28910	1.64
					85/358	23080	1.60
III ZW 2	00 07 56.0	+10 41 48	S1/QSO	0.090	85/354	24318	3.29
Mkn 1152	01 11 22.0	−15 06 39	S1	0.0527	84/203	36210	7.81
NGC 526a	01 21 37.3	−35 19 32	S1/NELG	0.191	83/249	22510	2.56
					84/357	18590	0.90
Fairall 9	01 21 51.2	−59 03 58.2	S1	0.0461	83/249	19309	1.45
Mkn 590	02 12 00.0	−00 59 58	S1	0.0263	84/003	13910	2.71
Mkn 1040	02 25 17.4	+31 05 22	S1	0.0165	84/259	17400	2.02
3A0234 − 526	02 36 40.9	−52 24 30	S1		83/249	13380	2.03
NGC 1068	02 40 7.08	−00 13 31.5	S2	0.036	85/008	51960	0.56
0241 + 622	02 41 00.7	+62 15 28	S1	0.044	83/245	18910	3.76
3C111	04 15 00.6	+37 54 20.0	S1	0.049	84/027	11000	1.79
3C120	04 30 31.2	+05 14 59.8	S1	0.0330	84/277	21910	4.56
Akn120	05 13 37.9	−00 12 15.3	S1	0.0325	85/024	23910	3.62
NGC 2110	05 49 46.4	−07 28 06	NELG	0.0071	83/251	12980	4.24

Table 2 continued.

Source name	Position (1950)		Type*	Redshift	Date	Exposure† (seconds)	ME Flux (10^{-11} erg s^{-1})
	R.A.(h,m,s)	Dec.(°,′,″)					(2–10 keV)
MCG 8–11–11	05 51 10.0	+46 25 51	S1	0.0205	84/306	14100	5.26
3A0557	05 56 21.0	−38 20 15	S1	0.0344	86/021	31720	1.44
Mkn 79	07 38 47.3	+49 55 40.9	S1	0.0219	84/090	16820	2.60
NGC 2992	09 43 18.0	−14 05 42	NELG	0.0079	84/337	14330	5.03
MCG 5–23–16	09 45 28.4	−30 42 57	NELG	0.0442	83/347	16410	6.64
NGC 3227	10 20 46.8	+20 07 06	S1.2	0.0037	85/131	21810	0.76
					85/329	24930	2.85
					85/342	21810	5.48
					85/349	26520	3.09
					85/361	22860	3.34
NGC 3783	11 36 33.0	−37 27 40.9	S1	0.0096	85/138	21350	4.76
NGC 4051	12 00 36.4	+44 48 34.7	S1	0.0023	84/099	31000	1.97
3C273	12 26 33.3	+02 19 43.7	QSO	0.1580	85/138	22460	8.27
NGC 4593	12 37 04.0	−05 04 01	S1	0.0089	84/154	21400	3.44
MCG–6–30–15	13 33 01.9	−34 02 27	S1	0.0570	84/202	26460	3.74
IC4329A	13 46 27.9	−30 03 40.6	S1	0.0138	84/201	20680	7.29
NGC 5506	14 10 39.1	−02 58 26.3	S1	0.0060	85/041	22000	8.57

Table 2 continued.

Source name	Position (1950)		Type*	Redshift	Date	Exposure† (seconds)	ME Flux (10^{-11} erg s^{-1}) (2–10 keV)
	R.A.(h,m,s)	Dec.(°,′,″)					
NGC 5548	14 15 43.5	+25 22 01	S1	0.0169	84/193	28840	3.72
Mkn 290	15 34 44.8	+58 04 00.5	S1	0.0308	86/056	28790	1.02
ESO103–G35	18 33 22.0	−64 28 18	S1.9	0.013	85/124	22500	4.95
ESO141–G55	19 16 57.0	−58 45 52	S1	0.0368	83/306	16860	2.87
NGC 6814	19 39 55.8	−10 26 35.4	S1.2	0.0054	83/307	24780	2.92
Mkn 509	20 41 26.3	−10 54 18.2	S1	0.0355	83/307	17050	4.81
NGC 7172	21 58 56.0	−32 07 54	NELG	0.0054	85/301	18900	3.28
NGC 7213	22 06 06.8	−47 24 39	L1.8	0.0058	83/310	14830	4.87
3C445	22 21 14.7	−02 21 26.8	S1.5	0.0562	84/159	25860	1.23
NGC 7314	22 33 01.0	−26 18 37	NELG	0.0056	84/315	21000	3.69
NGC 7469	23 00 44.1	+08 36 25	S1	0.0161	84/332	25820	3.24
MCG–2–58–22	23 02 07.2	−08 57 19.4	S1	0.0480	84/321	13380	6.34
NGC 7582	23 15 36.4	−42 38 42	S1.9	0.0051	84/161	14390	1.69

* Type of AGN. S=Seyfert, L=LINER. See Chapter 1 for definitions.

†Exposure times taken from Turner and Pounds 1989, except for NGC 5506.

Table 3. Iron line spectral fitting results from the EXOSAT spectral survey sources.

Source name	Power law χ^2/d.o.f.	Line fit results: Status	Energy (keV)	Equivalent Width (eV)	χ^2/d.o.f.	*Ginga* † Equivalent Width (eV)	Axial ‡ Ratio
Mkn 335						155 ± 70	0.8
(85/199)	20.3/22	Rejected	6.7	< 560	20.3/21		
(85/334)	18.0/32	Rejected	6.7	< 910	17.9/31		
(85/358)	28.1/28	Accepted	6.7	330 < 1000	27.2/27		
III ZW 2	23.6/28	Rejected	6.4	< 200	23.8/27		0.66
Mkn 1152	28.2/22	Rejected	6.7	< 930	28.1/21		0.18
NGC 526a						240 ± 60	0.67
(83/249)*	44.4/27	Accepted	6.4	120 < 530	43.1/26		
(84/357)	26.4/22	Rejected	6.7	< 2400	26.3/21		
Fairall 9	17.4/29	Accepted	6.7	300 < 1300	16.8/28		0.8
Mkn 590	23.9/24	Accepted	6.4	560 < 1530	21.3/23		0.79
Mkn 1040	35.4/32	95% < 97.5%	6.4	470 < 1020	30.7/31		0.21
3A0234 − 526	33.7/32	Rejected	6.7	< 670	33.7/31		
NGC 1068*	19.5/12	95% < 97.5%	6.7	1700 ± 1600	12.5/11	1300 ± 100	0.88
0241 + 622 (1)	31.0/33	Accepted	6.4	15 < 360	31.1/31		0.70

Table 3 continued.

Source name	Power law χ^2/d.o.f.	Line fit results				*Ginga* † Equivalent Width (eV)	Axial ‡ Ratio
		Status	Energy (keV)	Equivalent Width (eV)	χ^2/d.o.f.		
3C111	7.3/10	Rejected	6.4	< 1150	7.3/9		
3C120	29.3/32	Accepted	6.7	$30 < 310$	29.1/31		0.6
Akn120	26.1/32	Rejected	6.7	< 340	26.0/31	100 ± 50	0.67
NGC 2110	32.0/29	Accepted	6.4	$110 < 430$	30.8/28		0.85
MCG 8–11–11	39.7/33	95% < 97.5%	6.7	$390 < 770$	33.5/32		0.47
3A0557	21.8/22	Accepted	6.4	$230 < 820$	20.9/21		0.32
Mkn 79*	45.8/29	Accepted	6.4	$240 < 680$	44.1/28		0.69
NGC 2992*	46.2/29	95% < 97.5%	6.4	330^{+390}_{-310}	39.8/28		0.21
MCG 5–23–16*	46.0/28	Accepted	6.7	$140 < 360$	43.3/27		0.23
NGC 3227						190 ± 50	0.45
(85/131)*	22.3/9	No fit					
(85/329)	22.9/32	99.9%	6.7	650^{+590}_{-570}	14.7/31		
(85/342)	32.8/27	Accepted	6.7	$190 < 510$	30.5/26		
(85/349)*	46.3/32	95% < 97.5%	6.4	$430 < 870$	40.7/31		
(85/361)	30.5/32	Rejected	6.7	< 270	30.5/31		

Table 3 continued.

Source name	Power law χ^2/d.o.f.	Line fit results				Ginga † Equivalent Width (eV)	Axial ‡ Ratio
		Status	Energy (keV)	Equivalent Width (eV)	χ^2/d.o.f.		
NGC 3783*	34.8/22	Rejected	6.4	< 300	34.8/21		0.80
NGC 4051	21.2/27	97.5% < 99%	6.4	$580 < 1300$	16.7/26	230 ± 30	0.68
3C273	32.0/29	Accepted	6.7	$40 < 140$	31.0/28	~ 50	
NGC 4593*	40.1/30	Accepted	6.4	$170 < 490$	38.1/29	170 ± 30	0.78
MCG–6–30–15*	41.4/29	99.5% < 99.9%	6.4	320^{+290}_{-220}	29.2/28	130 ± 20	0.5
IC4329A	41.5/32	99.5% < 99.9%	6.4	150^{+140}_{-120}	31.9/31	70 ± 15	0.16
NGC 5506*	44.0/32	99.5% < 99.9%	6.4	260^{+230}_{-170}	31.4/31	150^{+40}_{-50}	0.17
NGC 5548	30.0/32	Accepted	6.4	$140 < 380$	27.7/31	110 ± 20	0.83
Mkn 290	25.7/27	Accepted	6.4	$660 < 1800$	23.8/26		0.86
ESO103 – G35	26.6/30	Accepted	6.4	$100 < 520$	26.6/29	210 ± 50	0.2
ESO141 – G55	21.4/28	Accepted	6.7	$400 < 1220$	19.2/27		0.65
NGC 6814	34.4/32	Accepted	6.7	$90 < 610$	34.2/31	240 ± 20	0.71
Mkn 509*	39.5/29	99% < 99.5%	6.4	380^{+320}_{-310}	30.2/28	80 ± 40	0.85
NGC 7172	19.5/32	Accepted	6.4	$80 < 460$	19.1/31		0.44

Table 3 continued.

Source name	Power law χ^2/d.o.f.	Line fit results				*Ginga* † Equivalent Width (eV)	Axial ‡ Ratio
		Status	Energy (keV)	Equivalent Width (eV)	χ^2/d.o.f.		
NGC 7213	34.9/33	Accepted	6.4	$60 < 310$	33.6/32		0.9
3C445	29.8/27	Rejected	6.7	< 440	29.7/26	260 ± 60	
NGC 7314	23.5/29	Rejected	6.4	< 280	23.5/28	100 ± 30	0.5
NGC 7469	38.7/32	$97.5\% < 99\%$	6.4	280^{+280}_{-270}	32.2/32	80 ± 40	0.58
MCG–2–58–22	34.7/32	Accepted	6.4	$60 < 250$	34.2/31	180 ± 80	0.67
NGC 7582*(f)	42.5/28	$\sim 90\%$	6.4	$620 < 1150$	38.3/27		0.42

(*) These power law fits were unacceptable at the 90% confidence level.

† The *Ginga* equivalent widths were taken predominately from Awaki (1991). Exceptions are for NGC 5506 taken from Pounds et al. 1989, and 3C 273 taken from Turner et al. 1989.

‡ The axial ratios were mainly taken from de Zotti and Gaskell 1985.

(1) Here the χ^2 for the simple power law plus absorption model for only ME data was unavailable, so the χ^2 for the ME+LE from Turner and Pounds 1989 is given.

(f) Here it was necessary to fix the power law photon index to 1.7 in order to obtain a fit.

In order to investigate the presence and strength of a possible line, the ME data were fit with a power law plus cold hydrogen absorption model with a Gaussian line included, as given in Equation 4.2. Note that the model including the Gaussian line has three more free parameters than the simple power law model: the intensity, the width, and the line energy. Because it was known that the quality of the data was such that so many parameters could not be constrained, the line energy and the width were fixed during spectral fitting. The width chosen was 0.05 keV, appropriate for a narrow line. The data was fit with two line energies: 6.4 keV, appropriate for emission due to cold iron fluorescence, and 6.7 keV, appropriate for fluorescence or recombination of partially ionized iron (Makishima 1986; see also Chapter 2). Because of the poor energy resolution and the width chosen for the line, most of the line photons could be gathered by one of these. The results of these spectral fittings is given in Table 3. In this table, the line fit parameters and the resulting fit χ^2 are quoted, but for only one of either the 6.4 keV fit or the 6.7 keV fit. The line energy quoted provided the better fit, in most cases; however, in some cases, the 6.7 keV fit is quoted because the fit results to the 6.4 keV fit are unavailable. In many cases, except for some of the detections, the fit parameters for the 6.7 keV line were nearly identical to those obtained with the 6.4 keV line. This result is consistent with the poor energy resolution of the detector.

Another set of spectral fittings were done in order to test for the presence of an additional absorption edge in the data. To do this, the data were fit with a power law model plus additional absorption, as follows:

$$F(E) = N\,E^{-\alpha}e^{-[\sigma(E)N_H+\sigma_{Fe}(E,E_E,Z)N_{Fe}]} \qquad (4.6)$$

where the form of the absorption column is given in Equation 4.5.

Note that two parameters are free in the edge fitting. Because of the reasons outlined above, the edge energies were fixed, and only the edge depth, implying extra absorption, was measured. The absorption edge energies chosen were 7.1 keV, corresponding to absorption by neutral iron, and 8.3 keV, corresponding to well ionized, He-like iron (Makishima 1986). The results of these spectral fits are given in Table 4. In this table, the results from two sets of fits are given: those with the energy of the iron edge fixed at 7.1 keV, referred to as the cold edge fit, and those with the energy of the iron edge fixed at 8.3 keV, referred to as the warm edge fit.

Results

Iron Line Fitting. The spectral fitting results to the line fits are given in Table 3. In the first column, the name of the source is listed. In the second column the χ^2 and number of degrees of freedom for the simple power law fit are given. These are given primarily for use in the calculation of the F statistic (Equation 3.1) to evaluate the improvement in the fit when the line is included. Next to some of the names of the sources is a (*). In these cases, the simple power law plus absorption model was not acceptable at the 90% confidence level, as evaluated by the χ^2 goodness of fit criterion. In columns 3–6 the results to the line fitting are given. In column 3 the status of the line fit is listed. There are three possible designations in the status column. If the fit has been 'rejected', then this means that spectral fitting found the best fit value of the line flux to be zero, and there is no change in the χ^2 due to the inclusion of the line in the model. 'Accepted' means that some non-zero best fit value for the line flux was found; in this case, however, the resulting reduction in χ^2 is minimal. The third designation gives a range of

Table 4. Iron absorption edge spectral fitting results from the EXOSAT spectral survey sources.

Source name	Power law χ^2/d.o.f.	Channels Fit	Cold edge fit results			Warm edge fit results		
			Status	Column†	χ^2/d.o.f.	Status	Column†	χ^2/d.o.f.
Mkn 335								
(85/199)	20.3/22	6–32	Accepted	$35 < 120$	20.1/21	No Fit		
(85/334)	18.0/32	6–40	Rejected	< 150	18.0/31	No Fit		
(85/358)	28.1/28	6–36	Rejected	< 120	28.1/27	No Fit		
III ZW 2	23.6/28	7–38	Accepted	$80 < 180$	23.5/27	No Fit		
Mkn 1152	28.2/22	6–30	Accepted	$70 < 300$	27.8/21	No Fit		
NGC 526a								
(83/249)*	44.4/27	6–35	Accepted	$200 < 330$	41.5/26	No Fit		
(84/357)	26.4/22	6–30	Accepted	$340 < 930$	25.7/26	No Fit		
Fairall 9	17.4/29	5–36	Rejected	< 130	17.4/28	No Fit		
Mkn 590	23.9/24	6–32	Rejected	< 110	23.9/23	No Fit		
Mkn 1040	35.4/32	6–40	Rejected	< 60	35.3/31	Rejected	< 900	35.3/31
3A0234 − 526	33.7/32	6–40	Rejected	< 110	33.7/31	Rejected	< 1600	33.7/31
NGC 1068*	19.5/12	6–34	Rejected	< 100	19.5/11	No Fit		
0241 + 622 (1)	31.0/33	6–40	Accepted	$70 < 150$	30.7/31	Rejected	< 1000	31.1/31

Table 4 continued.

Source name	Power law χ^2/d.o.f.	Channels Fit	Cold edge fit results			Warm edge fit results		
			Status	Column†	χ^2/d.o.f.	Status	Column†	χ^2/d.o.f.
3C111	7.3/10	8–32	Rejected	< 250	7.3/9	No fit		
3C120	29.3/32	6–40	Accepted	$20 < 70$	29.1/31	$97.5\% < 99\%$	$700 < 2300$	24.1/31
Akn120	26.1/32	6–40	Accepted	$20 < 80$	25.7/31	No Fit		
NGC 2110	32.0/29	6–37	Rejected	$110 < 430$	32.0/28	No Fit		
MCG 8–11–11	39.7/33	5–45	Rejected	< 30	39.7/32	Accepted	$140 < 1400$	39.6/32
3A0557	21.8/22	6–30	Rejected	< 100	21.8/21	No Fit		
Mkn 79*	45.8/29	6–37	Rejected	< 60	45.9/28	No Fit		
NGC 2992*	46.2/29	6–37	Accepted	$50 < 140$	45.9/28	No Fit		
MCG 5–23–16*	46.0/28	6–36	Accepted	$30 < 120$	45.9/27	Accepted	$500 < 2000$	43.7/26
NGC 3227								
(85/131)*	22.3/9	7–30	No fit					
(85/329)	22.9/32	6–40	Rejected	< 360	22.8/31	Accepted	$300 < 2400$	22.1/31
(85/342)	32.8/27	6–35	Rejected	< 30	32.8/26	Accepted	$300 < 2400$	32.2/26
(85/349)*	46.3/32	6–40	Accepted	$60 < 150$	45.6/31	Accepted	$1000 < 7000$	43.7/31
(85/361)	30.5/32	6–40	Accepted	$190 < 310$	29.6/31	Rejected	< 900	30.5/31

Table 4 continued.

Source name	Power law χ^2/d.o.f.	Channels Fit	Cold edge fit results			Warm edge fit results		
			Status	Column†	χ^2/d.o.f.	Status	Column†	χ^2/d.o.f.
NGC 3783*	34.8/22	6–30	Rejected	< 80	34.8/21	No fit		
NGC 4051	21.2/27	6–35	Rejected	< 80	21.2/26	No fit		
3C273	32.0/29	9–40	Rejected	< 50	31.9/28	Rejected	< 240	31.9/28
NGC 4593*	40.1/30	6–38	Rejected	< 80	40.1/29	Accepted	$400 < 1600$	39.3/29
MCG–6–30–15*	41.4/29	7–38	Accepted	$40 < 110$	40.4/28	99.5% < 99.9%	1050^{+1800}_{-800}	30.6/28
IC4329A	41.5/32	6–40	Accepted	$40 < 620$	41.3/31	Accepted	$160 < 450$	39.8/31
NGC 5506*	44.0/32	6–40	90% < 95%	$260 < 330$	39.9/31	97.5% < 99%	600^{+700}_{-590}	37.2/41
NGC 5548	30.0/32	6–40	Rejected	< 50	30.0/31	Accepted	$200 < 1000$	28.9/31
Mkn 290	25.7/27	6–40	Rejected	< 190	25.7/26	No fit		
ESO103 – G35	26.6/30	6–47	$\sim 99.5\%$	1040^{+1290}_{-1010}	20.2/29	No fit		
ESO141 – G55	21.4/28	6–36	Rejected	< 100	21.4/27	Rejected	< 1900	21.4/27
NGC 6814	34.4/32	6–40	Rejected	< 170	34.4/31	No fit		
Mkn 509*	39.5/29	6–37	Rejected	< 60	39.5/28	No fit		
NGC 7172	19.5/32	6–40	No fit			No fit		
NGC 7213	34.9/33	5–40	Accepted	$10 < 60$	34.8/32	90% < 95%	$700 < 2400$	31.0/32

Table 4 continued.

Source name	Power law χ^2/d.o.f.	Channels Fit	Cold edge fit results			Warm edge fit results		
			Status	Column†	χ^2/d.o.f.	Status	Column†	χ^2/d.o.f.
3C445	29.8/27	6–35	Accepted	$310 < 880$	29.5/26	Accepted	$400 < 4000$	28.9/26
NGC 7314	23.5/29	6–37	Accepted	$20 < 180$	23.5/28	No fit		
NGC 7469	38.7/32	6–40	Rejected	< 30	38.7/32	Rejected	< 350	37.7/32
MCG–2–58–22	34.7/32	6–40	Rejected	< 30	34.7/31	Rejected	< 430	34.7/31
NGC 7582*(f)	42.5/28	6–35	Rejected	< 1400	42.5/27	No fit		

(*) These power law fits were unacceptable at the 90% confidence level.

† The iron column is listed in units of $10^{16.52}\mathrm{cm}^{-2}$, which corresponds to cosmic abundance if $N_H = 10^{21}\mathrm{cm}^{-2}$.

(1) Here the χ^2 for the simple power law plus absorption model for only ME data was unavailable, so the χ^2 for the ME+LE from Turner and Pounds 1989 is quoted.

(f) Here it was necessary to fix the power law photon index to 1.7 in order to obtain a fit.

percentages. This means that inclusion of the iron emission line in the model has resulted in a dramatic decrease in χ^2, so much so that the F statistic finds the change significant at $\geq$ 90% confidence. This group is composed of the detections. Of the detections there are two kinds. There are those for which the power law model was not acceptable at the 90% confidence level, which are marked by a star (*) by the source name. For these the improvement in χ^2_R is because of a model improvement; i.e., the line is indeed necessary for an acceptable fit. On the other hand, there are those for whom the power law model was acceptable at the 90% confidence level, and yet the F statistic indicates a significant improvement. For these, since the power law fit is acceptable, statistical noise dominates. Therefore we cannot know that a line is absolutely necessary in the model from this data in these cases. The final status designation was 'No Fit'. In this case, fit results were not available.

The fourth column of the table shows the energy of the line which was fit. Two line energies were possible, 6.4 keV and 6.7 keV. As mentioned before, in most cases, the results from the line energy which provided the better fit are quoted. In some cases, the results from the 6.7 keV fitting are quoted, because the results from the 6.4 keV line fitting were not available. In many cases there was very little difference in the fit parameters for either line energy, especially for non-detections, because of the noisiness of the data, and also the width of the line. In the fifth column the line equivalent width or upper limit is listed. The uncertainties quoted are the 90% confidence level for one degree of freedom (Lampton, Margon and Bower 1976). In the sixth column, the resulting line fit χ^2 and degrees of freedom are quoted. In the seventh column, the equivalent width of the line as measured by *Ginga* is given for comparison, when available. Most of these were taken from Awaki 1991. Finally, in the eighth column, the axial ratio, b/a, of the host galaxy is quoted. Most of these were taken from deZotti and Gaskell 1985.

Forty seven spectra from 40 sources were fit. Of these, 13 were not fit well enough by the simple power law plus absorption model at the 90% confidence level. Seven of these 13 spectra showed a significant improvement in χ^2 as measured by the F statistic when a line was added to the model. These were NGC 1068, NGC 2992, one observation of NGC 3227, MCG–6–30–15, NGC 5506, Mkn 509, and NGC 7582. The χ^2 of the other six was not reduced significantly by the addition of the line, indicating that the large χ^2_R was due to excess residuals in some other region in the spectrum; for example, soft excess components were implied in NGC 526A and NGC 4593 (Turner and Pounds 1989). Six other spectra were adequately fit by the power law plus absorption model, but showed a significant improvement in χ^2 when a line was added to the model. These were Mkn 1040, MCG–8–11–11, another observation of NGC 3227, NGC 4051, IC4329A, and NGC 7469. Of these twelve sources in which lines were detected, the presence of lines has subsequently been verified in 8 of them from *Ginga* data. As an example, Figure 6 shows the simple power law fit plus residuals for NGC 3227, while Figure 7 shows the power law plus line fit and residuals for the same source.

The equivalent width of the lines were not well determined. It is not surprising that in the case of all non-detections, the lower limit was consistent with 0 at the 90% confidence level. Of the detections, only 8 of the 13 find the lower limit larger than 0 at the 90% confidence level. All of the line equivalent widths or upper limits as measured from the EXOSAT data are consistent with those measured by the *Ginga* data. However, in two cases, the results are suggestively larger than those measured from the *Ginga* data. In the case of MCG–6–30–15, the line equivalent width measured from the EXOSAT data was 320^{+290}_{-220} eV, while the equivalent

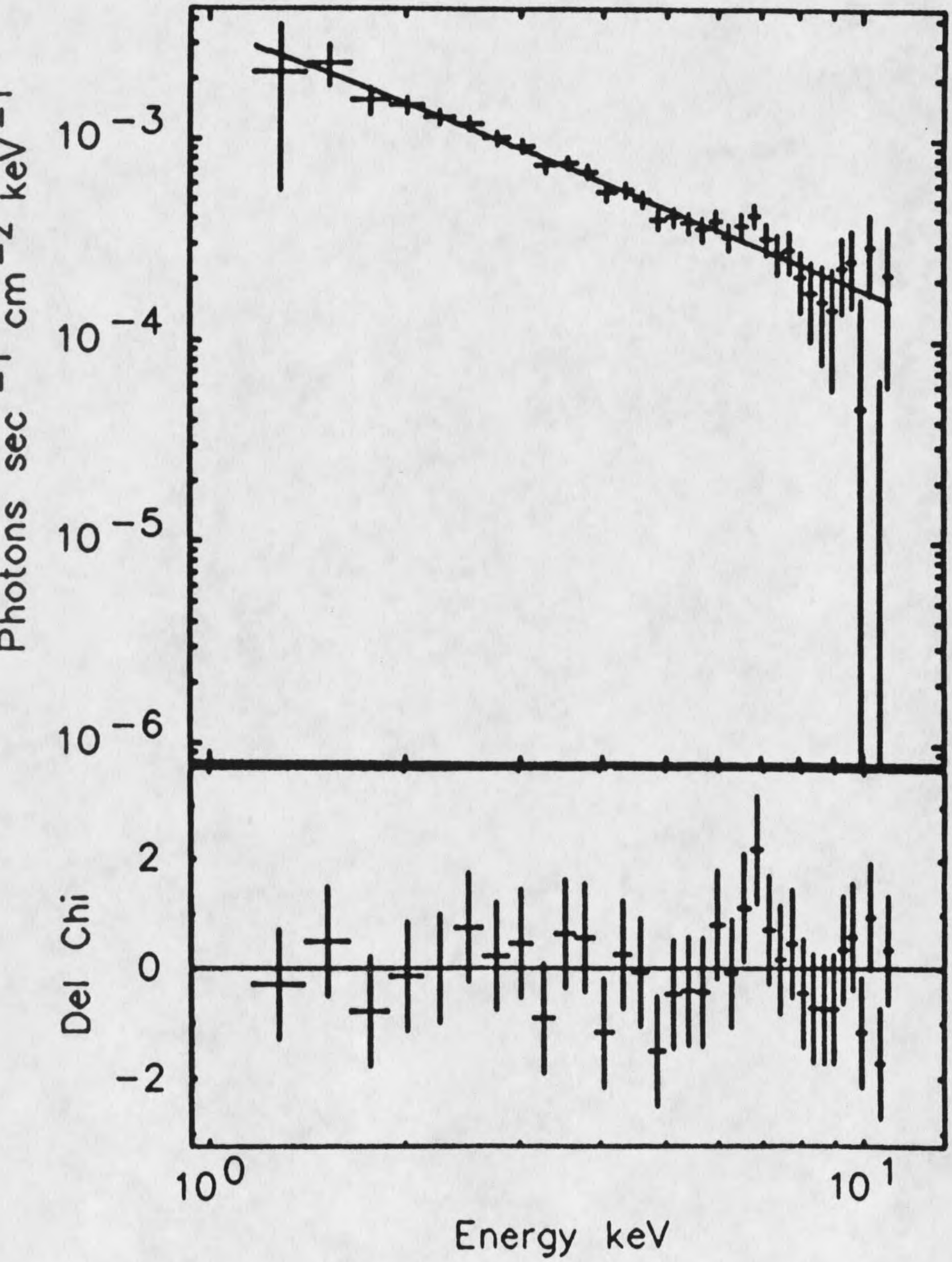

Figure 6. Power law fit plus residuals from NGC 3227.

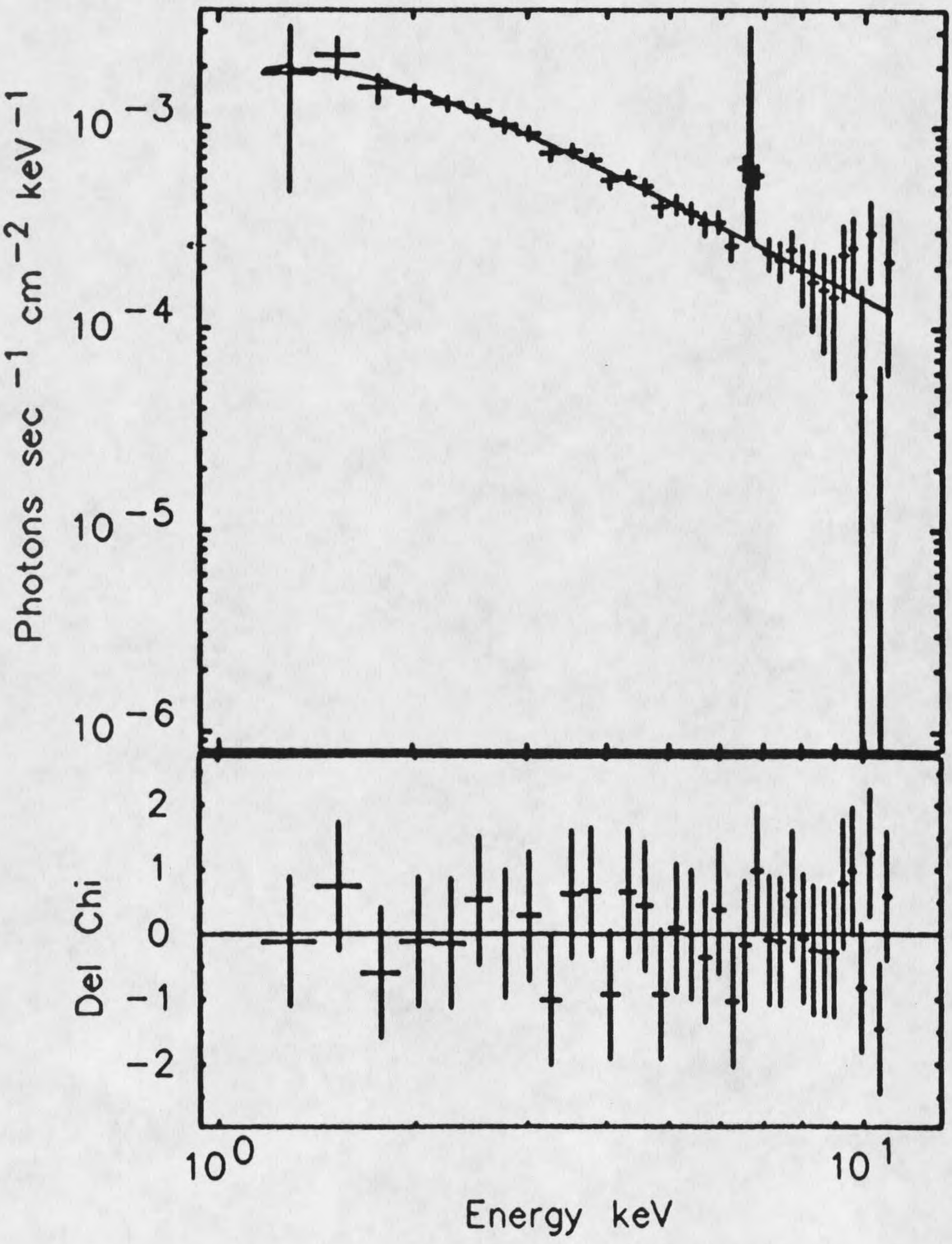

Figure 7. Power law plus an iron emission line fit plus residuals from NGC 3227.

width measured from the *Ginga* data was found to be 130 ± 20 eV. Likewise, for NGC 5506, the line equivalent width measured from the EXOSAT data was 260^{+230}_{-170} eV, while the equivalent width measured from the *Ginga* data was found to be 150^{+40}_{-50} eV. Although the values are consistent, the EXOSAT results are larger than they should be. The reason for this will be discussed in the section on combined spectral fitting.

Iron Absorption Edge Fitting. The results of the edge fitting are given in Table 4. As in Table 3, the source name is again listed in column 1 while the χ^2 and degrees of freedom for the simple power law fit are listed in column 2. In column 4, the numbers of the energy channels which were the lower and upper limits for the spectral fitting are given. For most spectra, the channels fit are usually 6–40 corresponding to 2 to 10 keV. However, for some spectra, particularly those from weak sources and those in which the background subtraction is not particularly good, the size of the energy band which is used for spectral fitting is reduced. Usually, this is accomplished by reducing the upper limit where the signal to noise ratio may be quite low. The upper limit of the energy band fit is of crucial importance when trying to fit an absorption edge to the data, since the edge energies of 7.1 keV and 8.3 keV are so near the upper cutoff, that in some cases only a few points are being fit above the edge. Clearly, statistical fluctuations due to unavoidable systematic errors in the background subtraction can greatly affect the outcome.

In the next two major columns are the fit results from the cold absorption edge model (7.1 keV) and from the warm absorption edge model (8.3 keV). Under each column heading are three subcolumns. The first subcolumn is the status of the fit result. These evaluations are the same as in Table 3, for the iron line fits. However, for the warm edge, the 'No Fit' category includes one more possibility.

In some cases no upper limit was obtained or the upper limit was essentially infinite. Usually this occurred if the spectral fitting upper limit was chosen at a lower energy, like channel 30, corresponding to $\sim$ 7.5 keV. There were 25 spectra with the 'No Fit' designation. The upper limit was less than or equal to $\sim$ 9 keV for 11 of those with the 'No Fit' designation. No fit was also obtained if the source was weak. The average source flux for the remaining 'No Fit' listings was $3.15 \times 10^{-11} \mathrm{ergs\,s^{-1}}$ while the average source flux for those with some fit recorded was $4.24 \times 10^{-11} \mathrm{ergs\,s^{-1}}$. The standard deviations of these show that the fluxes do not differ significantly; however, the result is suggestive. There is also dependence on the length of observation, and the number of detectors used. The second subcolumn lists the column of iron measured, times $10^{16.52}$. A value of $1 \times 10^{16.52} \mathrm{cm^{-2}}$ represents a cosmic abundance of iron if the hydrogen absorption column is $1 \times 10^{21} \mathrm{cm^{-2}}$. Finally, the third subcolumn lists the χ^2 and degrees of freedom for the edge fit.

For a cold edge, there were two detections. An edge at 7.1 keV was detected in NGC 5506, and also in ESO 103–G35. As shown in the preceding section, the long observation of NGC 5506 showed evidence for additional absorption in this Seyfert galaxy. The value of the iron absorption column measured is consistent with that measured previously. For ESO 103–G35, the detection can be considered to be reliable. This is because of several reasons. First, in this spectrum, data from the xenon layer was used as well as data from the argon layer. The xenon layer shows a larger detection efficiency for high energy photons, although for most AGN it is not usually used because of the small signal to noise ratio. However, in this case it was used, and therefore spectral fitting was carried out to $\sim$ 20 keV. Then, in this case, the edge energy is not near the highest energy considered in the spectral fitting, so more than just a few data points are being fit above the edge energy. Another reason is because the source is so heavily absorbed. The column density was found to be $N_H = 210^{+90}_{-70} \times 10^{21}\mathrm{cm}^{-2}$ for a simple power law fit; also see Turner and Pounds 1989 and Warwick, Pounds and Turner 1988. The best fit column for the additional iron absorption was $1040^{+1290}_{-1010} \times 10^{16.52}\mathrm{cm}^{-2}$. Therefore, the overabundance of iron necessary to explain this is only a factor of 5. Note also, however, the 90% confidence limit nearly includes 0. Also, it is interesting that EXOSAT data from ESO 103–G35 found a cold absorption edge, because a *Ginga* observation found the energy of the edge to be significantly above that of cold iron (Warwick et al. 1991). Figure 8 shows the power law fit including iron absorption fit for ESO 103–G35, as well as the fit residuals.

For the warm edge fits, there were four detections at the 90% confidence level. These were 3C 120, MCG–6–30–15, NGC 5506, and NGC 7213. Of these four, the detection of a warm edge in MCG–6–30–15 is not surprising, since a cold edge was detected in the long EXOSAT observation (Nandra et al. 1989), while an edge with shifted energy was detected in a previous *Ginga* observation (Nandra, Pounds, and Stewart 1990). The detection in NGC 5506 was also not surprising, because as discussed in the previous section, the *Ginga* observation found a warm edge. However, the detections in the other two sources have not been confirmed by *Ginga* observations. Note that evidence for extra iron absorption has been detected from *Ginga* data (Awaki 1991). *Ginga* can detect $N_{Fe} > 10^{17.5}\,\mathrm{Fe\,atoms\,cm^{-2}}$. In half of the 22 Seyfert 1 nuclei, considered in the *Ginga* sample, evidence for extra iron absorption at 7.1 keV is found. Other detections in the EXOSAT spectral survey sources may be due to systematic errors in the background subtraction. In general, it may be considered that it is not very easy to detect absorption edges in this data, because of the low signal to noise ratio and because of the relatively low upper limit on the band pass.

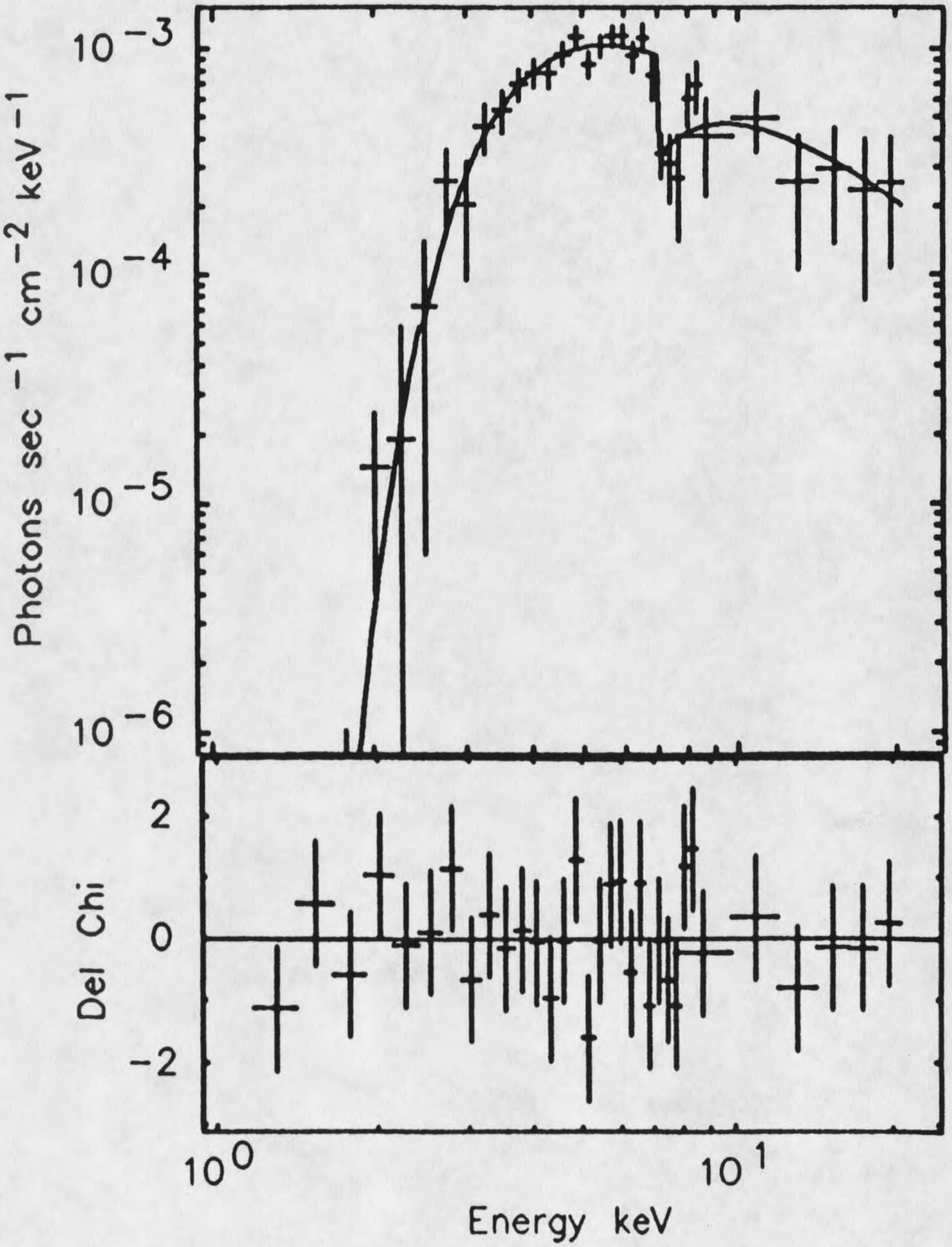

Figure 8. Power law plus absorption fit for ESO 103–G35. The iron edge energy was fixed at 7.1 keV, and the fit residuals are show below.

Combined Fitting. The previous two sections discussed the spectral fitting to the power law model including the line and the edge separately. From these spectral fittings, two of the observations indicated evidence for both a line and an edge separately at greater than 90% confidence level. These were the observations of MCG–6–30–15 and NGC 5506. Since both showed evidence for the necessity of a line and an edge separately, it is useful to fit these spectra with a model including both a line and an edge. Therefore, the combined line and edge fit for these two were made, and the results are listed in Table 5. The best fits resulted with a neutral iron line at 6.4 keV, and a warm iron edge, at 8.3 keV. The addition of an edge in the combined fit resulted in a reduced line equivalent width. This is expected; the low energy resolution of EXOSAT is such that the line and the edge fitting should be coupled. In both sources, the best fit parameter value for the line equivalent width was reduced, from 320 eV to 240 eV, in the case of MCG–6–30–15, and from 260 eV to 240 eV in the case of NGC 5506. The best fit parameter values for the line equivalent width and the edge column are consistent with the previous values measured from the EXOSAT long observations, and also from *Ginga* results. The best fit iron absorption columns are large, pointing to a large overabundance of iron; however, note that the 90% confidence uncertainties are consistent with 0. Finally, the best fits plus residuals for NGC 5506 are shown in Figure 9, while the best fits plus residuals for MGC–6–30–15 are shown in Figure 10.

Statistical Analysis. In this survey sample 13 spectra from 12 sources revealed evidence for line emission. From most of the other 34 spectra from 28 sources, line emission upper limits were found. Using the detections and the upper limits,

Table 5. Iron line and edge spectral fitting results from the EXOSAT spectral survey sources. Iron line energy fixed at 6.4 keV and iron edge energy fixed at 8.3 keV.

Source name	Photon Index	N_H (10^{21}cm^{-2})	Line Flux (10^{-4}ph cm^{-2}s^{-1})	Equivalent Width (eV)	N_{Fe} ($10^{16.52}$cm^{-2})	χ^2_R/d.o.f.
MCG–6–30–15	$1.76^{+0.36}_{-0.54}$	$4.2 < 12.2$	$1.04 < 2.27$	$240 < 780$	$650 < 2400$	0.95/27
NGC 5506	$1.99^{+0.30}_{-0.10}$	$30.6^{+8.7}_{-17.2}$	$2.45 < 4.92$	$240 < 720$	$230 < 1050$	1.01/30

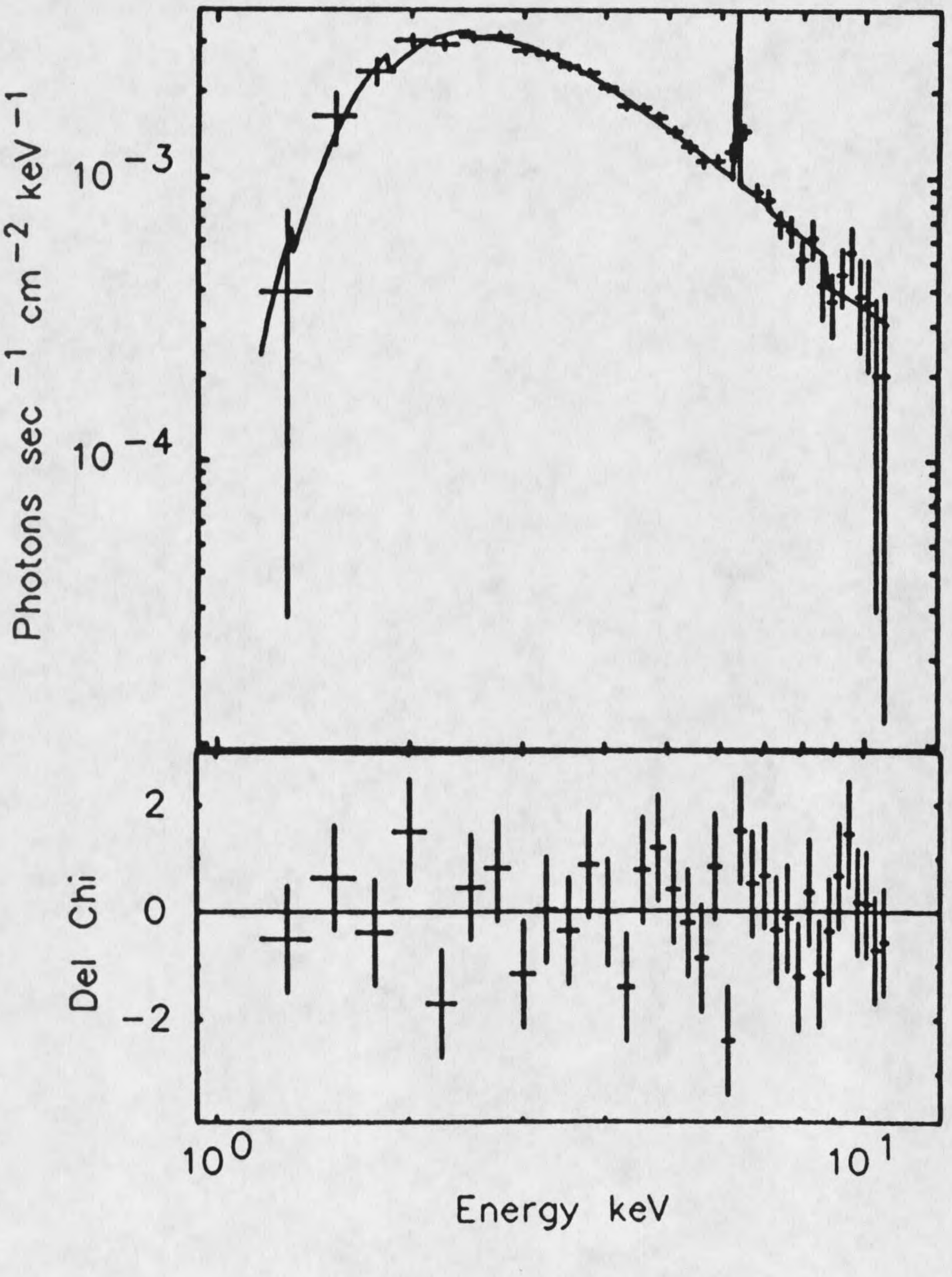

Figure 9. Line and edge fit for NGC 5506. The line energy was fixed at 6.4 keV, while the edge energy was fixed at 8.3 keV. Fit residuals are shown below the fit.

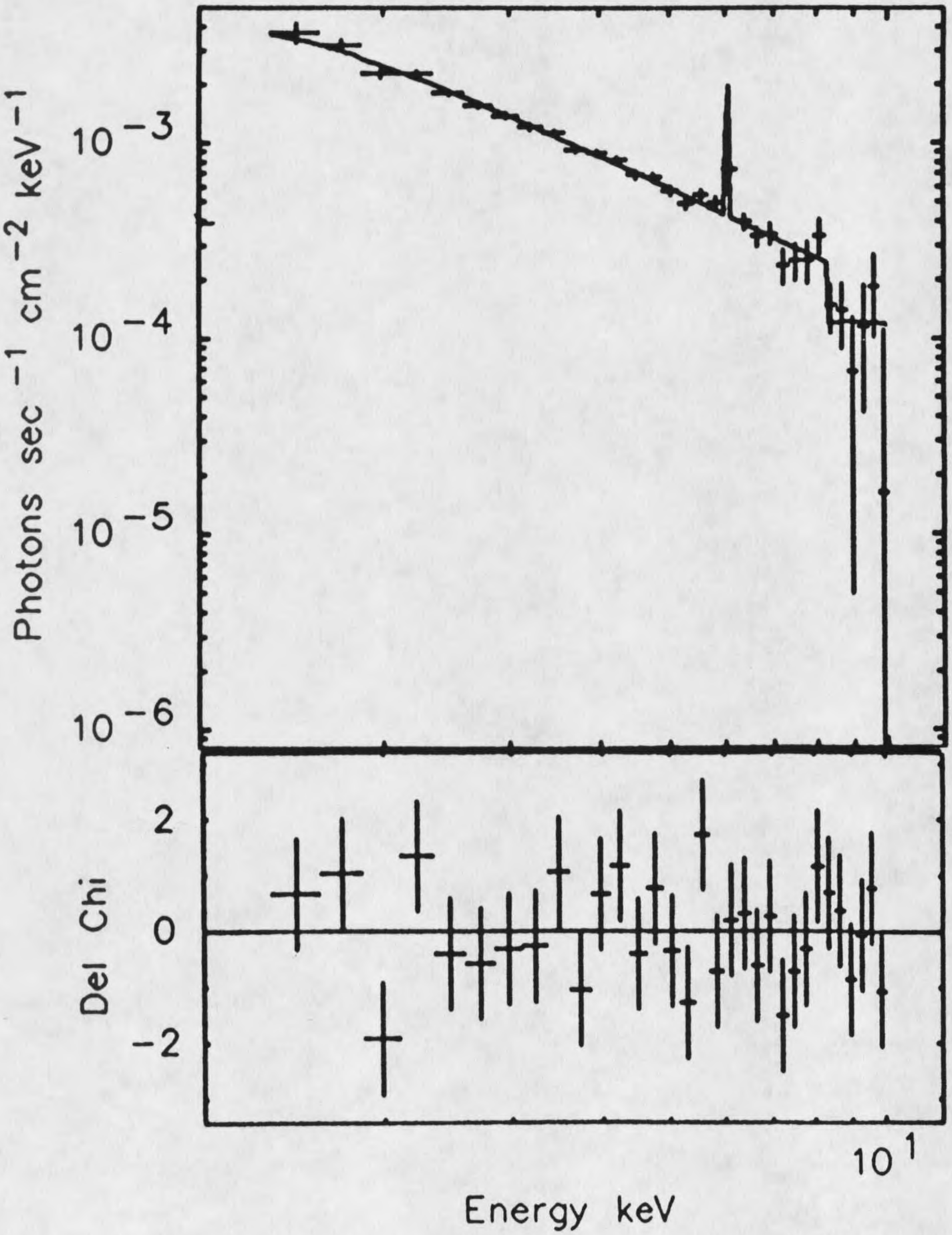

Figure 10. Line and edge fit for MCG–6–10–15. The line energy was fixed at 6.4 keV, while the edge energy was fixed at 8.3 keV. Fit residuals are shown below the fit.

statistical tests may be used to investigate the relationship between the line flux and the equivalent width and other parameters.

Special statistical techniques exist to find means and correlations from data which consist of detections and upper limits (Avni et al. 1980; Schmitt 1985; Feigelson and Nelson 1985; Isobe, Feigelson and Nelson 1986). These methods are modifications of methods described in the branch of statistics called survival analysis. These methods were usually implemented to take lower limits into account, because they were invented for disciplines such as biology, where a test animal might die before the test is completed. These methods are the correct way to examine the statistics of the data from the EXOSAT sample. However, this technique has been applied only to calculate the mean of the sample. The programs to calculate the correlations have not yet been written. So in most of this analysis, the detections and upper limits are considered to be independent populations.

If the detections are used as the sample, the results of correlation must be interpreted carefully. This is because the uncertainties are so large, that the equivalent widths of the sample of detections can be shown not to vary significantly (χ^2_R against constant hypothesis of 0.74 for 11 degrees of freedom). Therefore, no correlation can be considered significant, since the slope of the straight line fit to equivalent width and any other parameter cannot be significantly different from 0. There is some uncertainty in this calculation, because of several reasons. First, the uncertainties found in spectral fitting are 90% confidence levels. Here to reduce them to 1σ, they were divided by 1.65. This is not really correct, because it assumes a Gaussian distribution of uncertainty, and this assumption may not be completely justified. Parameter uncertainties are usually over-estimated by spectral fitting programs, because they estimate the uncertainty by extrapolation of a parabola defined by a few points near the best fit point. However, usually the χ^2 increases faster than a parabola. Second, the uncertainties were calculated assuming one interesting parameter. This is also not necessarily justified, because the coupling between line flux and other parameters besides the line energy and the line width is not strong. Certainly line flux is coupled to the photon index, but not necessarily coupled so strongly to the low energy absorption. So in general, the line uncertainties are over-estimated.

H. Awaki, in his thesis, considered the *Ginga* spectra from 22 Seyfert 1 galaxies. He detected significant line emission in all of them at the 1σ confidence level. The mean of the equivalent widths that he measured was 160 eV with the standard deviation of 60 eV. In the EXOSAT sample of detections, NGC 1068 is neglected because it is a Seyfert 2 galaxy, and Seyfert 2 galaxies are expected to have much larger equivalent widths than Seyfert 1 galaxies (see Awaki 1991). For the EXOSAT sample, considering only the detections, the log of the average line equivalent width is 2.64 and the standard deviation is 0.25, corresponding to a 1σ range of $240 < 430 < 770$ eV. These figures are not completely representative of the data, however. Only thirteen lines were detected, but upper limits from 34 other spectra were available. It is more representative to use statistical methods to find the mean and standard deviation which take the upper limits into account. Such a method is described in Avni et al. 1980. Using this method to take the upper limits for the non-detections into account, the average of the log of the line equivalent width is found to be 2.50 with standard deviation 0.21. Then the 1σ range of equivalent widths is $200 < 320 < 500$ eV. There is an overlap of 20 eV between this result and that of Awaki (1991).

Awaki also finds that the line equivalent width for Seyfert 1 galaxies is correlated with the X-ray continuum emission for the *Ginga* sample. For the EXOSAT sample, it was found that the log of the equivalent width for the sample of the thirteen detections was inversely correlated with the log of the X-ray continuum emission. Here, the linear correlation coefficient was $r = -0.77$ for 11 degrees of freedom. This corresponds to a probability of greater than 97.5% that the sample was drawn from a correlated parent population. NGC 1068, being a Seyfert type 2 galaxy, is expected to have a large equivalent width and a low luminosity. Since this point could heavily weight the distribution, it was neglected, and the correlation again calculated. Strong evidence for inverse correlation was again found, with $r = -0.68/10 d.o.f.$ and $P > 90\%$. The upper limits for the log of the line equivalent widths for the non-detections were found to be uncorrelated with the luminosity ($r = -0.15/25 d.o.f.$ and $P > 50\%$). This non-correlation is not surprising, because a selection effect is also folded into the data. More luminous sources can be seen from farther away; however, they may not be observable at a sufficient flux level to find a line. But if the flux is large enough, the upper limit might be quite small, decorrelating the data.

Awaki also finds a correlation at the 98% confidence level that the equivalent width is correlated with the photon index. This result is expected if the line is due to fluorescence, because of the relative larger number of hard X-ray photons above the iron K edge which may be absorbed for a lower photon index. Such a test has not been performed with the EXOSAT sample.

If the iron line emission is due to fluorescence from material arranged in a thin accretion disk, one might expect a larger equivalent width to be found from those galaxies in which the disk is oriented face-on towards us. With this idea in mind, statistical tests were applied to check if there is any correlation. From the *Ginga* data (Awaki 1991), for the 15 of the Seyfert 1 galaxies for which the axial ratios were available, the correlation was significant at the 90% level. With the Seyfert 2 NGC 1068 removed from the sample, the correlation was significant at the

95% level. A similar correlation between the EXOSAT detection data equivalent widths and axial ratios find a significant correlation. However, note that the active nucleus and host galaxy need not be coupled by angular momentum. A classic example is the Seyfert 2 galaxy, NGC 1068, whose host galaxy is nearly face-on, having an axial ratio of 0.88, but for which the most successful model requires the active nucleus to be edge-on (e.g. Antonucci and Miller 1985). It is interesting to note that significant line detections were found more often from sources with host galaxies more nearly edge-on than face-on. This may be a selection effect, as face-on galaxies are more common and thus represent the lower source fluxes of our sample. However, the line upper limits for sources with host galaxies more nearly face-on are in general larger than the sources with host galaxies more nearly edge-on.

Approximately half of the spectral survey sample indicated substantial intrinsic column in the source galaxy (Turner and Pounds 1989). Only four of the 12 sources with significant lines have substantial intrinsic column. These were NGC 2992, MCG–6–30–15, NGC 5506, and NGC 7582. Fits for three of these, excepting NGC 7582, were improved by the addition of a warm absorption edge. There is a suggestion of a positive correlation between line equivalent width and absorption column ($r = 0.77$/4d.o.f. and P=0.30).

Excess soft X-ray emission was established in eight of the spectral survey sources and implied in another seven (Turner and Pounds, 1989). A significant line was found in three of these: NGC 4051, MCG–6–30–15, and NGC 7469.

Discussion

Perhaps the most significant result of this investigation is the presence of detectable lines at the 90% confidence level in $\sim$ 1/3 of the sample. Because of the poor energy resolution of EXOSAT and the small detector area, the line equivalent widths were not well determined. The measured equivalent widths are comparable in size with the upper limits, but are smaller for the most part. This fact indicates that lines might be present in many of these sources, although not detectable with EXOSAT in such short observations. A calculation shows that the detection limit for the equivalent width is expected to be inversely proportional to the square root of the length of the observation times the square root of the continuum flux in the line band. Subsequently, of course, analysis of *Ginga* data have confirmed the presence of lines in Seyfert 1 spectra (Awaki 1991).

The suggestion that the line equivalent width is inversely correlated with the source luminosity seems to indicate that there is more material around low luminosity sources to fluoresce. This may be because cold or partially ionized material cannot survive around powerful sources. This result is supported by the suggestion of a correlation between the line equivalent width and the intrinsic column, since it is known that intrinsic columns are associated with low luminosity objects (e.g. Turner and Pounds 1989).

Perhaps a more significant correlation with soft emission is expected, since an iron emission line and thermal emission might be expected to originate in the same place. However, disk lines are expected to be $< 200\,\mathrm{eV}$ (George and Fabian 1991) and such small lines would not easily be observed by EXOSAT in these short observation.

The iron line features can help determine the geometry of the emission region and can help determine the structures responsible for the emission or reprocessing. The comparison of axial ratio with line equivalent width lends some support to current theories of line emission from thin accretion disk. George and Fabian (1991) have done extensive Monte-Carlo simulations in order to estimate the equivalent width of the line as a function of inclination angle from a thin accretion disk. They find that the equivalent width of the line drops dramatically with inclination angle. This is because fluorescence photons trying to escape the disk with a large inclination angle see a larger optical depth than those emerging normal to the disk plane and so are more likely to be re-absorbed.

Features due to the emission and absorption of iron atoms in a low state of ionization seem to be a common phenomenon. This fact has a strong impact on models of AGN, since such models must provide such neutral material to fluoresce. There is some latitude, however, since in most AGN line variability is not observed. Therefore, the line emission site need not be in the central engine. On the other hand, with current detectors, line variability is difficult to detect. Only from bright Seyfert 1s with lines having a large equivalent width has line flux variability been confirmed (Kunieda et al. 1990).

CHAPTER 5

VARIABILITY OF X-RAYS FROM SEYFERT NUCLEI

The nature of the variability of X-ray emission from Seyfert nuclei can be divided into two related parts: the total flux or temporal variability and the spectral variability. Evidence for both types of variability was found in all three of our *Ginga* observations. The results from the detailed spectral and temporal analysis of these observations will be given in Chapters 7 and 8. The purpose of this chapter is to give a non-comprehensive review of the current status of theories and observations of the temporal and spectral variability of X-rays from Seyfert nuclei, from the observer's point of view. This review will serve as a framework against which the results of the subsequent chapters will be analyzed. As will be seen, much more information about the nature and environment of the central engine can be obtained by examining in detail the variability, compared with just evaluating the time averaged spectra.

Intensity Variability of X-Rays

Observations

The intensity variability of X-rays from AGN has been observed to have many different time scales, depending on the source. Early studies using Ariel V found variability on the time scale of a year or less in about half the AGN studied (Marshall, Warwick and Pounds 1981). A subsequent study using the *HEAO 1 A–2* experiment found that rapid variability (time scales of minutes to hours) was rare in a sample of 54 observations from 38 AGN which were mostly Seyfert 1's (Tennant and Mushotzky 1983). However, using EXOSAT and *Ginga*, rapid variability has been found from some low luminosity Seyfert 1 nuclei. Continuous, remarkably fast variability, with time scales of minutes to hours, has been observed consistently from MCG–6–30–15 (Pounds, Turner and Warwick 1986; Matsuoka et al. 1990; Nandra, Pounds and Stewart 1990), NGC 4051 (Marshall, Holt and Mushotzky 1983; Lawrence et al. 1985, 1987; Matsuoka, et al. 1990; Kunieda et al. 1991), Mkn 335 (Turner and Pounds 1988), NGC 6814 (Tennant et al. 1981; Mittaz and Branduardi-Raymont 1989; Done et al. 1990) and NGC 5506 (McHardy and Czerny 1987). Rapid variability has also been observed intermittently from NGC 4593 (Barr et al. 1986). Longer time scale variability has been observed from NGC 4151 (Yaqoob and Warwick 1991, and references therein). In addition, some objects have been observed to flare at one time or another. Examples are NGC 7469 (Marshall, Warwick and Pounds, 1981), and NGC 7314 (Turner 1987). Rapid variability from quasars seems to be much rarer. Of 51 quasars observed with the *Einstein Observatory* only four were found to vary on a time scale of 1 day (Zamorani et al. 1984).

In general, it appears that low luminosity Seyfert galaxies are observed to vary more rapidly than high luminosity quasars. In order to investigate this point, Barr and Mushotzky (1986) looked for and found a correlation between the luminosity of the source and the variability doubling time scale. They found that low luminosity Seyfert galaxies were observed to vary by a factor of 2 on a time scale as small as 100 seconds, while high luminosity quasars were observed to vary on a time scale of one year. A study of only low luminosity Seyferts verifies this relationship; however, instead of using the doubling time scale to measure the variability, the normalized amplitude of the power at a given frequency was used (McHardy 1989).

The most intriguing type of variability is the continuous rapid variability expressed by some of the low luminosity Seyferts. This variability usually lacks characteristic time scales, but rather is characterized by a power spectrum that can be described by a power law function of frequency with a range of negative power law slopes (McHardy 1989).

The slope that is exhibited by the power spectrum has a physical interpretation (Press 1978). White noise is described by a power spectrum with a slope of zero. This describes entirely uncorrelated variability. White noise has the property that the power is convergent at low frequencies but divergent at high frequencies. Thus the time series is infinitely choppy, and successive points are always nearly the maximum distance from each other. In contrast, random walk processes are described by power spectra with the slope of -2 and are, by definition, the frequency integral of white noise. This type of noise is convergent at high frequencies, but divergent at low frequencies. This is because points can be quite far from each other at long time scales, while quite close to each other at short time scales. An intermediate case is that of flicker noise which has a power spectral slope of -1. Flicker noise is also called $1/f$ noise. This type of noise is divergent at both low and high frequencies.

Physically speaking, the variability power must converge. Therefore, if the variability of a Seyfert galaxy is of the power law type, it must have spectral breaks such that the slope is zero at low frequencies (no net variability at very long time scales) and slope is -2 at high frequencies (no net variability at very short time scales). However, what has been generally observed is that many variable low luminosity Seyfert 1s display variability with power law slopes of around -1 over the several decades of frequency which can be conveniently measured, and the turn-overs to the low frequency and high frequency ends have not been clearly identified. However, some spectral breaks have been found for some. For example, NGC 4593 was observed to have a power spectral slope of -2 (Barr et al. 1986) and clear high and low frequency turnovers have been identified for NGC 5506 (McHardy, 1989). Two problems with finding the break frequencies are clear. Low frequency observations are hampered by the small number of X-ray missions available for flux measurements over the years. Also detectors able to observe AGN in X-rays have been available for only a relatively short time. High frequency observations are limited by Poisson noise. However, $1/f$ variability has been observed in some Galactic black hole candidates, and spectral breaks have been identified. For example the black hole candidate Cygnus X-1 is found to exhibit such $1/f$ variability, with the $1/f$ region found for frequencies above $\sim 0.04 - 0.06$ Hz and the power spectrum flattens below (Nolan et al. 1981). Here the convergent region, and the break frequencies have been clearly identified.

Note that most AGN have not been found to have any characteristic time scales which can be interpreted as a physical characteristic of the system. Only one low luminosity Seyfert has clearly been found to exhibit a characteristic time scale; this is NGC 6814, and the properties of this source will be discussed in Chapter 8.

Models

One model which has been explored to explain the $1/f$ variability of the low luminosity Seyferts is discussed by Lehto (1989). His model is based on the fact that similar $1/f$ noise is found in a variety of physical systems, including electronic systems. In electronics systems a shot noise model is often used. Lehto's model uses shots with a variety of decay times. When shot noise of only one decay time is used, the region of the power spectrum with slope -1 spans in effect less than one decade of frequency. Therefore, a variety of decay times are used. Adjusting the parameters can produce slopes of $\sim 1/f$ over a range of frequency. Physically, the range of shot decay times might be due to shocks or other non-thermal phenomena in a variety of densities (McHardy 1989).

Another new explanation of $1/f$ noise has just been proposed by Bak, Tang and Wiesenfeld (1987, 1988). The idea here is roughly that some dynamical systems will evolve into a critical state, and $1/f$ noise will be generated, as the system, under perturbations, goes back to the critical state. The example used is of a pile of sand. Starting with no sand, if sand is added, it will pile up until the slope reaches a critical value. If more sand is added, excess sand will slide off so that the critical slope is maintained. The amount of sand which slides off will exhibit $1/f$ noise (Bak, Tang and Wiesenfeld 1988). As far as I know, this model has not yet been applied in detail to astronomical $1/f$ noise.

Several other models have recently been described. A 'reservoir' model has been proposed by Begelman and De Kool (1991). In this model the variability is produced by a sum of pulses, with a correlation assumed between the pulse height and the mean rate of pulses. In this reservoir process, a large flare would drain the system of a large amount of energy, and so a long time would be required for the energy reservoir to store up enough energy for another flare. Another model uses hot spots in an accretion disk, with some apparently augmented by the Doppler beaming effect (Zhang 1991).

This short review shows that many of these models can explain $1/f$ variability quite well. Begelman and De Kool (1991) point out that one of the problems is that too many models are successful, and the reason is partially because the power spectrum is a relatively crude measure of the characteristics of the light curve (Press 1978).

Spectral Variability

The spectra of Seyfert galaxies can vary in many ways. Conceivably all of the spectral components discussed in Chapter 2 could vary independently of one another, under special circumstances. This may be because some physical process may vary the magnitude of one of the components. Then, when observed with instruments of poor energy resolution, many types of spectral variability could masquerade as simple variability of the spectral index. Therefore, the most closely studied type of spectral variability is that of apparent spectral index change. Since the one other characteristic which is easily measured is the flux of the source, the most common type of investigation has focused on the correlation between flux and spectral index. Such a correlation has been found. Most often the spectral index is correlated with the flux; i.e. the spectrum of the source is observed to soften as the source brightens. In addition, other types of variability have been observed. For example, changes in the low energy absorption column have been seen. The remainder of this chapter will explore the types of variability which have been observed, and will give some explanations which have been proposed. The focus will be on those types of spectral variability which can appear to be intrinsic spectral index variability, and on analysis methods which can be used to diagnose the origin of the spectral variability. This is necessary for the understanding of the results of the analysis of the two observations of NGC 6814; here rapid spectral variability was observed. We propose a specific model to explain the observations; however, since it is a new variation of the partial covering model, other models must be ruled out.

Absorption Column Variability

Variability of Cold Column. In at least a few objects the measured low energy absorption column has been observed to change from observation to observation. For example, the measured line of sight column in ESO 103–G35 was observed to show a factor of 2 decrease in a period of 90 days (Warwick, Pounds and Turner 1988). This decrease was interpreted as being due to the motion out of the field of view of broad line clouds assumed responsible for the large column measured in this source. EXOSAT data from NGC 3227 was also found to exhibit variable column from observation to observation (Turner and Pounds 1989). In addition, one of 5 observations of NGC 6814 showed a marked increase in the absorption column (a factor of 20), while the source flux decreased by 30%. Mittaz and Branduardi–Raymont (1989) claim that this may be due to broad line cloud absorption also.

Most of the observations for which column variability has been verified have been from EXOSAT. This is because EXOSAT had such a large band pass, particularly in the low energies where absorption column is measured, that both the absorption column and spectral index could both be measured fairly accurately. However, a re-analysis of SSS and MPC data by Turner et al. (1990) find also column density variability in several other objects. For example, 3C120 and 3C111 showed index and column variability.

Absorption column changes may be confused with spectral index changes, because the energy index is usually tightly coupled to the measured absorption column. χ^2 contours plotting energy index and N_H usually are an ellipse with the long axis along the direction of increasing column and index. Only by plotting these contours for each observation can pure column or index variability be identified, if the fits use only one parameter of interest (Lampton, Margon, and Bower 1976).

Warm Absorber. This model for spectral variability was first introduced by Halpern (1984). In this case, an enormous change in the absorption was measured between two observations of the QSO MR2251-178. Data from the Monitor Proportional Counter on-board *Einstein*, sensitive in the energy range from 1.2 to 20 keV, as well as data from the simultaneous observation using the High Resolution Imager, sensitive in the range from 0.1 to 3 keV, were available. The MPC fit showed the remarkable change in absorption, while the flux level from the HRI showed no significant change. The warm observer model was proposed to explain this observation. Central to this model is the fact that not all energies of X-rays are equally absorbed. Above 0.53 keV, oxygen is the major absorber, while below, helium dominates. If the absorbing column is partially ionized, so that helium is completely stripped, the absorbing column will be transparent below 0.7 keV. However, oxygen need not be completely stripped, and so the absorbing column may be optically thick at 1 keV. Therefore, a partially ionized column can explain a spectrum with substantial low energy absorption and a very low energy excess emission. Also, the absorption of other elements will be changed, causing the spectrum to in general soften in the presence of the warm absorber (Krolik and Kallman 1984). Such an absorber is called 'warm' by Halpern, because the temperature of the absorbing material is only about 10^5 K, as the ionization is assumed to be caused by photoionization, and not thermal ionization.

What will be the identifying variability characteristics of this situation? As the luminosity changes, the ionization state of the absorption column will change. Therefore, the apparent N_H column measured will be inversely correlated with the luminosity of the source. Another diagnostic is the time scale of variability for the column. The variability time scale depends only on the ionization and recombination rates, which typically depend on the density. If the material is not very dense, the recombination will be slow, and fast variability cannot be explained. Assuming the temperature of the gas is smaller than 10^4K, the density must be $> 10^8 \mathrm{cm}^{-3}$ for the time scale for recombination to be less than 10^4 seconds.

This model can explain flux correlated spectral variability. If the spectra are fit to a simple power law model, the power law index will decrease as the source brightens. This is because the excess emission below 1 keV, as well as the reduction in opacity above the oxygen edge, causes the power law index to be pulled up. However, for the warm absorber as described by Halpern (1984), where the degree of ionization is relatively small, the spectral index change above about 3.5 keV would be very slight.

Since Halpern used this model in the spectral fitting of the QSO MR2251–178, it has been used again to describe other data from MR2251–178 (Pan, Stewart and Pounds 1990) and also at times to explain data from other objects. For example, in EXOSAT observations of NGC 4151, the low energy flux was found to remain constant while the medium energy varied by a factor of 10. The hardness ratio was found to vary with the luminosity also, showing the spectrum to soften as the source brightens. Detailed analysis showed that this data could be fit by a constant spectral index when a partially ionized screen having a variable ionization parameter was included (Yaqoob, Warwick and Pounds 1989).

A larger change in ionization parameter will cause changes in spectral index for a larger range of energies; however, other spectral features will be observed, because a highly ionized absorber will leave characteristic features on the X-ray spectrum. First, the iron line flux will be enhanced over the flux expected from the measured cold absorption screen. The iron absorption edge will also be enhanced. This is because the N_H column measured does not reflect the presence of the warm absorber, and the warm absorber is assumed not to be ionized to such a degree that iron would be completely stripped. However, if the ionization parameter is large, the energy of the iron absorption edge will increase. For very high ionizations, the energy of the iron line from the warm absorber will increase also (Makishima 1986). The change in the absorption edge energy is potentially one of the most valuable diagnostics to interpret the presence of the warm absorber, for high energy resolution instruments.

An example of the use of this model with a more highly ionized absorber was an analysis of a *Ginga* observation of MCG–6–30–15 by Nandra, Pounds and Stewart (1990). They found spectral variability below $\sim$ 5 keV only, and they found that the spectral index for a simple power law fit was correlated with the flux. Also, they found that the best fit value of the absorption edge energy was 7.8 keV, although the confidence level for this result did not reject the 7.1 keV edge energy. Thus they interpreted this spectral variability to be due to a partially ionized screen, which modified the spectrum below 5 keV. They interpreted the shifted edge energy to be due to the sum of an edge at a higher energy from the ionized screen and the edge due to the cold screen which determined the column density.

These two examples point out the important restriction of the warm absorber model where the absorption screen lies between the observer and the source of the X-ray flux. It can only be used to explain spectral variability of the low energy region of the spectrum. For the medium energy region to be modified the ionization would have to be very high, and the deep absorption edge at a much higher energy would be measured. Again, fast spectral variability could not be explained.

Another application of the warm absorber that has not been investigated thoroughly yet is reflection from a partially ionized region. This would remove part of the iron edge energy constraint, because the edge seen by reflection is smaller than the edge seen through the material in the line of sight (Mushotzky 1984).

Variability in Relative Normalization of Separate Spectral Components

The soft excess and hard tail are two spectral components which were discussed in Chapter 2. In some situations, the relative normalization of these components with respect to the medium energy power law can vary. This can cause apparent softening of the spectrum as the source brightens.

This explanation of spectral variability has been used on at least two occasions. First, the EXOSAT long observation of Mkn 335 (Turner and Pounds 1988) found rapid variability with a 1–2 hour time scale in the medium energy X-rays, while the LE data varied with a much longer time scale, $\sim$ 10 hours. There were suggestions that the ME lagged the LE, and that the LE increased more. The best fits were determined to be two power laws of constant index, with the normalizations of both allowed to vary. Physically this could arise if the ME power law emission is due to Comptonization of the soft, possibly thermal LE flux. Then the ME would be expected to lag the LE. Therefore, the brightening of the source would be accompanied by a softening of the spectrum, due to the lag of the ME, and also the larger magnitude increase of the LE. Note that, like the warm absorber model, variability in the normalization of the soft excess component compared with the medium energy power law only affects the low energy part of the spectrum. Therefore this type of variability can be distinguished by making power law fits to spectra excluding the soft region. The spectral index of the medium to hard energy spectrum should not change, unless the soft component is described by an additional power law with a mild slope. Then this component may be a significant addition to the medium energy X-rays.

In another case of the analysis of five *Ginga* observations of NGC 5548, the best five fits involved a power law plus a hard tail due to reflection (Nandra et al. 1991). The conclusion was that the apparent spectral variability of the spectral index from a simple power law fit could be accounted for by variability in the relative normalization of the power law component and the reflected component. So the intrinsic power law was found to have constant spectral index, and the apparent flux correlated intrinsic index variability became a less likely explanation. The normalization of the reflected continuum was consistent with a constant. Physically this is reasonable if the time scale for changes in the normalization of the reflected continuum is longer than the time scale for changes in the normalization for the primary power law emission. This could be because variability of the primary power law is washed out by light travel effects in the reflected continuum. In this way apparent spectral index correlations would be observed, because flux increases of the primary power law, dominating the medium energies of the spectrum, would not be matched by changes in the hard reflected continuum.

If the reflection component is from cold unionized material, it will dominate the hard X-ray region above 10 keV. This situation was shown in Figure 3. Therefore a diagnostic analysis plan for this situation would be to measure the spectral index in the hard X-ray region, and the medium X-ray region separately. If the index in the hard region does not change, but the index in the medium region does change, this model is supported. This is because since the reflection component dominates the spectrum above 10 keV, the measured spectral index in this region will be the slope of the reflection spectrum. However, as can be seen in

Figure 3, the reflection spectrum will modify the slope in the 2–10 keV region, so the spectral index of this region will show flux correlated variability. Note, however, variability of the spectral index in the region above 10 keV does not rule out a reflection model, if the intrinsic power law index is variable. In this case, a diagnostic would be the expected lag of the hard flux from the reflection region over the medium flux, mostly from the primary power law flux, if this could be measured and if the variability were not washed out by light travel effects.

One other set of parameters have not been mentioned, however. These are the disk (reflector) inclination angle, and the solid angle by which the disk subtends the source. It can be seen that these are coupled, since a disk at a highly inclined angle will produce less reflected flux, and if a larger solid angle subtends the source, more reflected flux will result. Finally, the role of reflection from a partially ionized region has not been explored. In this case at least one more parameter would be necessary, to describe the ionization state.

Spectral Variability Due to Compton Effects

As mentioned in Chapter 2, one likely candidate for the production of the power law X-ray emission is inverse Comptonization of soft photons by a relativistic plasma. For thermal models, the distinguishing characteristic of inverse Comptonization is the lag of the medium energy over the soft. For example, if there is a rise in the soft photon output, there will be a lag between such an increase and the increase in the flux in the medium energy band. This is because the harder photons require more scatterings, since each scattering boosts the energy by only a given amount each time. In this way a flux correlated spectral variability would also be seen; as a source becomes brighter, the low energy flux would increase faster, showing a spectral softening.

A thermal Compton model was used by Lawrence et al. (1985) to explain the flux correlated spectral variability found in a long EXOSAT observation of NGC 4051. For this to be appropriate a large population of very hot electrons is necessary. Such a population is present in the 'two temperature torus' model (Shapiro, Lightman and Eardley 1976). The other component is a soft seed photon source, which could be thermal. Two mechanisms are possible to describe the variability: the electron temperature may vary, or the number of seed photons may vary. If the temperature varies, the photon index would be anti-correlated with the flux, so this mechanism can be rejected. However, the mechanism in which the soft seed photon flux varies was found to be a possible explanation, if the predicted lag were smeared enough to be unrecognizable.

A modification of the thermal Compton model to include the effects of pairs was proposed to explain the flux correlated spectral variability (White, Fabian, and Mushotzky 1984). Their idea is that if the switch between the high and low state occurs at about 1% Eddington luminosity, this would also be the luminosity at which an optically thick electron positron plasma will form. The abundance of pairs formed will cool the plasma, creating a softer spectrum. The main problem with this idea as applied to AGN is that the initial, intrinsic spectrum must be quite hard, and such a spectrum will produce too many γ-ray photons, as discussed in Chapter 2.

A slightly different model was used to explain the flux correlated spectral variability of NGC 4151 (Yaqoob and Warwick 1991). This study involved a series of *Ginga* observations, and the relatively high energy resolution of this instrument gave spectra which seemed to require an intrinsic index variability. A non-thermal Comptonization model was used to explain the change in index. Again these authors found that pairs were important in the high state, but do not exist in the low state.

Other thermal models have also been found which predict spectral index – flux correlations. A model recently proposed by Dermer (1989) uses a two temperature ion supported torus. The spectral index flux correlation is due to changes in the ion temperature, with the scattering optical depth remaining constant. Again this model predicts the hard X-rays to lag the soft X-rays.

For thermal Compton models, one diagnostic test is the time variation. In thermal Compton models which produce spectral softening when the flux increases, because the harder photons lag the soft photons, the increases and decreases in flux will be characterized by lags of the medium energy over the soft energy. With the relatively high time resolution of *Ginga* (16 seconds for AGN), strict constraints on the lag times can be gained. Qualitatively, if the lag is found to be very short, but not zero, the source is required to be very compact, and such compactness would require the source to be radiating at very near the Eddington limit. A further constraint is that only the lag of hard photons over soft photons should be seen; these models do not predict the lag of soft photons over hard.

For non-thermal models, the situation is more complicated. Part of the complication arises because of the many parameters available for variation in non-thermal models; however the variation of some parameters do not produce variability. Three parameters are usually varied in non-thermal pair models (Ghisellini 1991). These are the energy (compactness) in the soft photons, the energy in the energetic electrons, and the maximum relativistic γ of the electrons. Variation of the energy in the soft photons does not in general change the high energy spectrum. Varying the compactness of the high energy electrons, l_h, has a larger effect. For low l_h, pairs are not important and the radiation spectrum follows the injected electron spectrum. For high l_h, pairs are saturated and a constant index is found $0.8 < \alpha < 1.0$. Dramatic changes are found around $l_h = 10$. This variability has been studied by Done and Fabian (1989). Finally if the maximum energy of the electrons is less than the pair production threshold, few pairs will be produced even though the compactness may be quite large. Then if the maximum energy rises above the threshold, copious pairs will be produced, and the spectrum will soften dramatically (Ghisellini 1991).

Understanding this, what are the diagnostics for the non-thermal pair models? First, the lags as outlined above are not a diagnostic for non-thermal models because geometric effects can produce the lag of the hard over the soft as well as the soft over the hard (Done and Fabian 1989). Apparently, spectral changes can happen quite quickly (Fabian et al. 1986). However, it seems for most models which have been investigated in detail, the change in spectral index is usually fairly moderate (< 0.3) while the change in flux is quite large (an order of magnitude) (Done and Fabian 1989; Yaqoob and Warwick 1991). This may be simply because the models were intended to explain observations which exhibited such behavior. However, perhaps the most restrictive diagnostic is that models in which pair modification of the spectrum is important on a short time scale require optically thick pair plasmas. Such plasmas will affect the variability, in general, by damping out the fastest variability (Done and Fabian 1989). Therefore, the doubling time scale for variations may be many times (3–10, Done and Fabian 1989) the light crossing time scale. For some of the most rapidly variable sources, this will cause the inferred black hole mass to be very small, and the source to be radiating at much more than the Eddington limit.

Spectral Variation by Partial Covering

A final method has been used in some cases to explain the flux correlated spectral variability observed from some Seyfert nuclei. This method employs absorption of a variable fraction of the intrinsic flux by clouds or some kind of absorbing screen. The spectra produced by partial covering is discussed in Chapter 2 and an example of such spectra is shown in Figure 2. If the fraction of the intrinsic flux absorbed is changing, then a flux correlated spectral variability can result. Apparent spectral variability is found when this bumpy spectrum is fit to a single power law model. If the fraction covered is temporarily low, and the flux modulation of the source originates from the absorption of only a small part of the intrinsic flux, the source spectrum will appear soft and bright. Then as the covered fraction increases, the total flux decreases and the absorbed component appears as a hump in the higher energies. When fit with a simple power law model, the source spectrum will appear hard.

Note that this model can explain variability between any two regions of the spectrum. Unlike the warm absorber model and variable normalization of the soft excess model, which applied only to the low energies, and the variable normalization of the hard tail, which mostly applied to hard energies (at least for cold reflection), the break in energy can occur anywhere in the partial covering model.

This model has been applied in many different instances. As mentioned in Chapter 2, the Poisson cloud model was proposed by Holt to explain the low energy variability of NGC 4151 (Holt et al. 1980).

This model was applied to the *Ginga* observations of the Seyfert 1 galaxies MCG–6–30–15 and NGC 4051 by Matsuoka et al. (1990). In this analysis, they found that to explain the spectral variability of these sources, an intrinsic change in spectral index and also partial absorption and scattering by a thick absorber of

$N_H > 10^{24}\,\mathrm{cm}^{-2}$ were required. This data was also analyzed by Nandra, Pounds and Stewart (1990), who found that a model consisting of a warm absorber and hard reflection tail superimposed on a primary power law of constant spectral index provided a better description. The fact that the same data can have equally valid descriptions points out one problem with the partial covering model. If the absorber is very thick, on the order of $N_H \approx 10^{23-24}\mathrm{cm}^{-2}$, the partial covering model cannot be easily distinguished from the reflection model by just examining the spectrum, because of the limited energy range and poor resolution of current detectors.

However, the details of the variability can convincingly distinguish the partial covering spectrum from the reflection spectrum. The partial covering model was applied to a *Ginga* observation of NGC 4051, by Kunieda et al. (1991). Here the spectral fits also could not distinguish between the reflection and partial covering models. However, careful examination of the light curves showed regions where the soft flux appeared to flare, while the hard flux remained constant. This behavior was interpreted as the uncovering of the source during the flare. Other regions showed that the soft flux and the hard flux varied together, indicating intrinsic flux changes. Such variability would be difficult to explain using only the reflection model for the hard tail. However, to explain the strength of the iron line, assumed to originate from fluorescence in a cold disk, a reflection component was also deemed necessary.

Such variability can provide a diagnostic for this model. Also, in the case of clouds with hard edges, which are well described by a single thicker column, spectral fitting ought to find that the partial covering models is statistically preferred. However, a difficulty emerges, if the cloud does not have a hard edge, and is better described by a range of column densities. Such a situation will be described in Chapter 8.

CHAPTER 6

THE *GINGA* X-RAY SATELLITE

General

Astro-C is the third Japanese X-ray satellite, following Hakucho and Tenma (Makino and the Astro-C team, 1987). It was launched on February 5, 1987 from the Kagoshima Space Center (KSC) by a M-3SII-3 rocket. It was renamed *Ginga*, which means galaxy in Japanese. *Ginga* is small, weighing 420 kg, with the main rectangular body being 1m $\times$ 1m $\times$ 1.5m. There are also 4 solar paddles, each 1.7m long and 0.7m wide. These can generate a maximum power of 500 watts. A schematic view of *Ginga* is given in Figure 11. The z–axis is defined to be the axis of rotational symmetry of the satellite.

Unlike EXOSAT, it was launched into a low earth orbit, with a perigee of 505.5 km, apogee of 673.5 km, inclination of 31.1°, and orbital period of 96.5 minutes. This period means that the satellite makes 15 orbits per day. During five of these, it is in contact with the ground station at KSC, at which time it dumps its memory from the 40 – Mbit bubble memory data recorder, and receives new observing instructions.

The attitude of *Ginga* is controlled by a momentum wheel and 3 magnetic torquers. There are three attitude modes available: maneuvering of the z–axis (maximum rate $5^\circ\,\mathrm{hour}^{-1}$), slewing about the z–axis (maximum rate $14^\circ\,\mathrm{min}^{-1}$), and pointing (stability $0.1^\circ\,\mathrm{day}^{-1}$; however, see Chapter 7). The attitude was

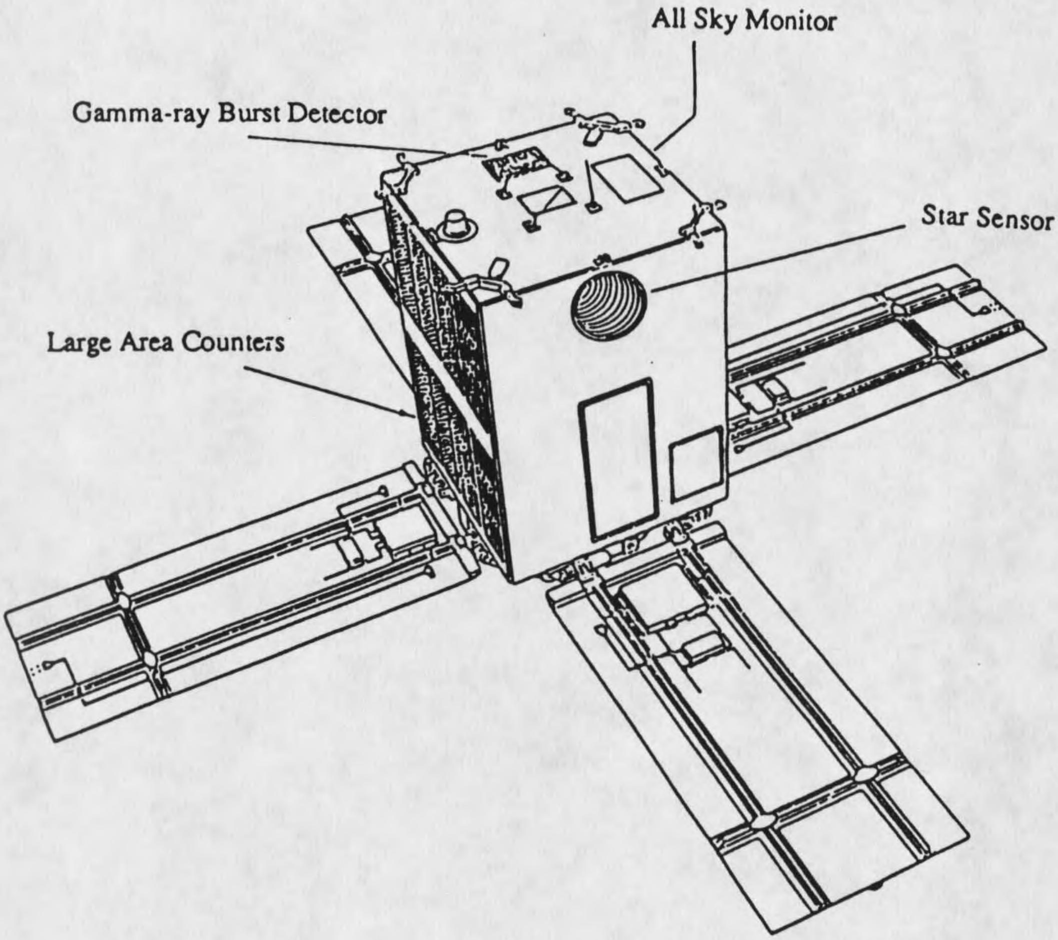

Figure 11. Schematic view of the *Ginga* satellite. The three main instruments, the Large Area Counter (LAC), All Sky Monitor (ASM), and Gamma-ray Burst Detector (GBD) as well as one of the two STar Trackers (STT) are shown. Taken with permission from Makino et al. 1987.

measured by geomagnetic aspectmeters, sun sensors, gyroscopes, and also by two star trackers with CCD detectors which can measure to position of a star of greater than 6th magnitude to an accuracy of $0.5'$.

There are three instruments on-board *Ginga:* the Large Area (proportional) Counter (LAC), the All Sky X-ray Monitors (ASM), and the Gamma-ray Burst Detectors (GBD). Only the LAC was used for this study, so only it will be described (see next section).

As the LAC was the main instrument on-board *Ginga*, the principle objectives of the mission were to study the time variability of a wide variety of Galactic and extra-Galactic X-ray sources and to make spectral surveys in the medium energy band of faint sources. The pointing direction between the LAC field of view and the sun is constrained to be between 50° and 130° by power requirements, and pointing direction between the LAC and the sun must be $> 90°$ by solar contamination requirements.

Contact with *Ginga* was lost October 30, 1991. The reason for its demise was that the orbit was decaying due to increased solar activity. In December 1990, despite the loss of two of the eight proportional counters and the loss of one star tracker, *Ginga* was still functional and very much involved in doing good science. An added benefit of its long life is that during the last period, many simultaneous observations with the ROSAT satellite, which observes a much softer energy band, were being performed.

The Large Area Counter

Design Characteristics. The LAC was built as a collaboration between the Institute of Space and Astronautical Science, Japan, and the University of Leicester and Rutherford-Appleton Laboratory, U.K. (Turner et al. 1989). It consists of eight proportional counters with a total effective area of $4000\,\mathrm{cm}^2$. The counters are filled with a mixture of 75% argon, 20% xenon, and 5% CO^2. The entrance window was made of a 62μm thick beryllium layer. As with EXOSAT, the thickness of this layer determines the lowest photon energy which can be measured. The counters are arranged in two layers. The TOP layer is sensitive to X-rays in the energy range of 1.5–37 keV, while the MID layer, being twice as thick as the TOP layer, can detect X-rays in the range $\sim$ 5–37 keV. The detection efficiency as a function of energy is shown in Figure 12 for the total and for the TOP and MID layers separately. This illustration shows that the MID layer is designed to detect more energetic photons, and the detection efficiency for the MID layer is larger than that for the TOP layer for energies greater than $\sim$ 12 keV. Because of the collimator provided, the counter field of view is approximately elliptical, with dimensions $1.1^\circ \times 2.0^\circ$, and the long axis is in line with the satellite z-axis.

The energy range from 0 to 37 keV is divided into 64 energy channels, and the upper 32 are combined into pairs. The data compression mode chosen depends on the type of source observed, but in general for weak sources like AGN, the MPC–1 mode is chosen. In this mode, the data are stored separately for the TOP and MID layers and for each of the eight detectors, resulting in 16 spectra. This mode provides the greatest spectral resolution. The low bit rate (16 s) is generally chosen for the storage of the data with the MPC–1 mode. This is because faint objects are usually observed during the non-contact (remote) orbits, and if a high bit rate were chosen, the memory would be filled long before the contact orbits. The low bit rate provides rather poor time resolution, although adequate for faint sources. In contrast, the PC-L mode with High time resolution has a bit rate of 0.98 ms. No energy information is retained, because this mode by-passes the analog to digital converter in order to provide the best time resolution. This mode is generally used for bright variable Galactic sources observed during contact orbits.

Calibration. Part of the calibration of the LAC was carried out on the ground, but the LAC was also calibrated in orbit during the performance verification (PV) phase, by measuring the well known spectrum of the Crab Nebula. Most of the calibration measurements agreed with that expected from the design; however, there was one discrepancy. The low energy absorption cut-off of the Crab Nebula

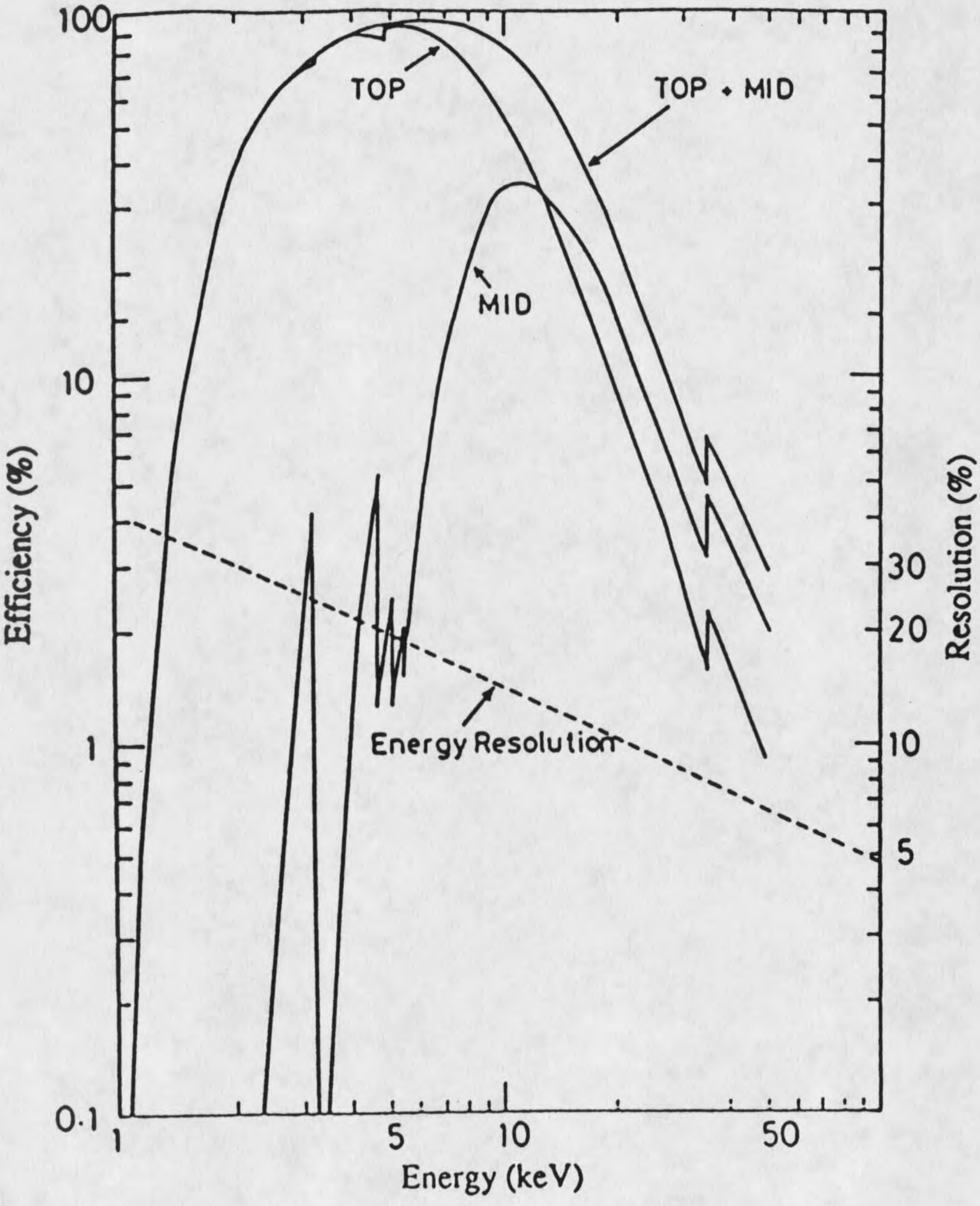

Figure 12. The efficiency of detection as a function of energy of the LAC. The TOP, the MID and the sum are shown separately. The dashed line shows the measured energy resolution. Taken with permission from Makino et al. 1987.

was found to be larger than found from previous measurements. This fact was subsequently taken into account by assuming a thicker beryllium window in the response matrix.

Another important aspect of the response was the effect of satellite aspect with respect to the source. Recall that the field of view of the LAC is $\sim 1^\circ \times 2^\circ$. If the source is off-center in the direction of the slew (X–Y) plane, there can be soft X-ray reflection from the collimator. This can amount to a few percent in the spectrum below 6 keV. It is estimated that no bright source should be within 3° of the target in the slew plane in order to totally avoid this effect. Also, spectral fitting programs available can correct for the deviation in aspect for sources less than 0.5° from the center of the field of view in the slew plane direction. For greater angles, the spectral fitting correction was not reliable.

X-Ray Background. Unlike EXOSAT, *Ginga* provides no simultaneous background monitor. Also, because of the large detector area, for faint sources systematic background errors dominate the uncertainty. Therefore, the background must be carefully studied and modeled so that reliable background subtraction can be made. The background contribution to the signal over the whole energy range may be 70 counts s^{-1}, while the source contribution may be 5–30 counts s^{-1}, for AGN.

There are two sources of background (Hayashida et al. 1989). When the LAC is pointed at the dark earth there is a residual count rate of ~ 50 counts s^{-1}. This is known as the internal background and the magnitude may vary by a factor of 2 in one day. Note that, as in EXOSAT, sophisticated anti-coincidence background rejection techniques are used; otherwise, the internal background would be ~ 20 times higher.

There are three sources to the internal background: cosmic rays, geomagnetically trapped particles, and radioactivation of the satellite.

The cosmic rays create background by Compton interactions of gamma rays which they produce in the material of the satellite. The density of cosmic rays depends on the magnitude of the local magnetic field, because a cosmic ray requires more energy to penetrate a larger magnetic field. The energy necessary, called the cut-off rigidity (COR), is one of several housekeeping parameters which are monitored, and only data with COR greater than 9 GeV/c are selected.

The earth's magnetic field also traps particles. These may have energies from several hundred keV to several hundred MeV. The high energy particles act like cosmic rays, while the low energy particles cause flares. Restrictive data selection can partially remove the effects of these contributions to the background. *Ginga* passes through the South Atlantic Anomaly (SAA) during several of its orbits per day. The SAA is a region of high particle background because in that region the geomagnetic field is weak. Therefore, the radiation belt is hanging down. For weak sources the data obtained near SAA passage are not selected.

During the SAA passage the high voltage on the proportional counters is turned off, but the effect of the SAA passage is felt even after the satellite emerges. This is because the high energy protons in the SAA cause radioactive isotopes to be created in the material of the space craft. It has not been possible to identify the isotopes involved (Hayashida et al. 1989). These decay after SAA emergence, and can cause spurious signals due to Compton interaction of the nuclear gamma rays. This is known as the radioactivation component of the internal background. The half lives of the isotopes have been found to be 5 minutes, 41 minutes and 8 hours. The most persistent and annoying contributions to the spectra are variable spectral features at about 3 and 5 keV due to the decay. The contribution of these components to the internal background depends on the altitude of the satellite during its SAA passage, and also the amount of time it spends in the SAA. The magnitude of the contributions varies with a 37 day period, due to the small eccentricity of the orbit.

There is also a contribution to the background by the diffuse X-ray background. This adds about 18 counts s^{-1}. The diffuse X-ray background is constant in time, but varies by location. In order to shield the detector from the diffuse X-ray background not in the LAC field of view, the satellite was covered with a layer of 0.2 mm thick tin.

Data Analysis

General

The data analysis of the *Ginga* observations by Leighly was carried out at Nagoya University and also at Montana State University. The background subtraction was done at Nagoya University. The spectral fitting was necessarily done at Nagoya University, due to the size of the detector response matrix (700×700). However, much of the timing analysis was completed at Montana State University.

Data Selection and Background Subtraction

As stated earlier, the main contribution to the uncertainty for faint sources are the systematic background subtraction errors. Therefore, the data selection and background subtraction are performed very carefully.

First of all, faint sources are observed only in remote orbits, when the ascending node is between 180° and 320°. During these orbits the satellite does not pass through the SAA. Next the data from these orbits are chosen by examining the values of several housekeeping parameters. As explained earlier, data are only accepted when the cut-off rigidity is greater than 9 GeV/c. The data are also chosen so that the earth elevation angle, or the angle between the LAC and the bright limb of the earth, is larger than 6°. This is because otherwise reflected solar X-rays could enter the LAC. Finally, the value of the another parameter called the Surplus over Upper Discriminator (SUD) is examined. The SUD counting rate is a housekeeping parameter recording the count rate of X-ray-like events whose energy exceeds an upper discriminator. The upper discriminator was chosen to be 24 keV. However, the LAC detection efficiency for real events is not 0 at 24 keV, so some source counts are contained in the SUD. Therefore a variation of the SUD, called the SSUD, is calculated, which is the SUD with the LAC counts above 24 keV subtracted. Therefore, the SSUD monitors the rate of events with energy above 37 keV. These can not be genuine X-rays originating from the target, because the detection efficiency at those energies is essentially 0. Therefore, the SSUD monitors the number of internal background events. If this value is high, the data are rejected, because they could be contaminated by flares. The SSUD is a particularly useful parameter because it scales linearly with the internal background level from 1–18 keV (Awaki 1991).

After having employed this strict data selection, the background is subtracted. In the analysis of the faint sources, the best way to model the background is a hotly debated issue, and subsequently, several ways to model it have been devised. However, only the methods will be discussed here which were subsequently used in the analysis presented. However, note that there were some problems in the background subtraction for one object, discussed in Chapter 7.

For many observations, the background is measured by monitoring a field of blank sky for one day adjacent to the observation. Through this the internal and diffuse background spectra are recorded. For those observations for which a background observation is available, a simple SSUD scaled background subtraction is usually used. In this method, the background observation is sorted by SSUD level and several background spectra are made. These are then subtracted from the source spectra which have the same SSUD levels. Since SSUD is linearly related to the internal background level, and because the internal background decreases because of radioactive decay after SAA passage, this method provides some time dependence. The major problem with this method is that the number of background spectra that can be made is small; one needs at least 300 seconds of background data to produce an acceptable spectrum. Therefore, the rapidly varying spectral features at 3 and 5 keV can not always be adequately subtracted. For further discussion of this aspect, see Chapter 7. This method of background subtraction was used for the observation of NGC 7469 (discussed in Chapter 7) and the second observation of NGC 6814 (discussed in Chapter 8).

For the first observation of NGC 6814, no adjacent background was available, so another background subtraction method was used. This method is known as the Nagoya method of background subtraction, and was developed by H. Awaki at Nagoya University (Awaki 1991).

The Nagoya method of background subtraction estimates the internal and cosmic diffuse components separately. The internal background spectrum was estimated by examining large amounts of data obtained while the satellite was pointed at the dark earth. Because of the extremely time dependent contribution to the internal background from SAA passage, three internal background spectra were compiled, grouped according to the ascending node of the satellite. Then careful correlations were made to find housekeeping parameters which would help describe the background state. One such parameter, SSUD, was found to be well correlated with the internal background, as described before. Several others were found, but the other one most useful for faint sources observed in the MPC–1 mode was the LMID. The LMID is the count rate in the MID layer of the LAC in the energy range 1.11–4.50 keV. In this energy range, the MID layer detection efficiency is less than 5% (see Figure 12), and for faint sources, the LMID count rate is below the source confusion limit. Therefore, LMID counts are due to background. Then the internal background was modeled by:

$$IBG = A + B \times SSUD + C \times LMID. \tag{6.1}$$

Next, the cosmic diffuse X-ray background spectrum was found by examining 50 high Galactic blank sky fields. The internal background was subtracted from each and the mean spectrum was determined. To use these spectra for subtraction, if adjacent background observation is available, the average cosmic diffuse X-ray background was scaled to that of the adjacent field. If no such observation was available, as was the case for the April observation of NGC 6814, then the mean spectrum was subtracted.

Spectral Fitting

The spectral fitting was in general carried out as with the EXOSAT spectra, as described in Chapter 3. One difference is that the energy range in general extended to ~ 20 keV, and in general the absorption columns were more poorly determined, due to the limited low energy extent of the *Ginga* band pass. When the power law with line and absorption model was fit (Equation 4.1), only the TOP layer data were used, because the signal to noise ratio in the 2–10 keV range, where these parameters are primarily determined, is larger for just the top layer, compared with the TOP + MID data. For more complicated models involving the 10–20 keV range (see Chapter 2), the TOP + MID data were used. This is because the detection efficiency of the TOP layer is equal to that of the MID layer at ~ 12 keV.

Time Series Analysis

In contrast with the spectral analysis, the timing analysis was carried out on the sum of the data from the TOP and MID layers. The timing analysis for NGC 7469 was carried out completely at Montana State University, and all of the programs were written by K. Leighly. These programs were very simple, including linear fits and similar simple programs. For the NGC 6814 timing analysis, some of the timing analysis was carried out at Nagoya University, and it was continued at Montana State University. Much of the software for this was written by C. Done, and modified by K. Leighly as necessary.

Because of the low earth orbit of *Ginga,* the data typically have many gaps, at least one per orbit, and the data stream is typically shorter than the gaps. Because of this, standard methods of timing analysis, including autocorrelation and power spectral analysis, cannot be used on *Ginga* data. New methods have recently been developed, and because they are somewhat different from standard methods, a short review is provided here.

Standard time series analysis for continuous functions is based on the calculation of the autocorrelation function (and related cross correlation function) and the power spectral density (Press et al. 1986). The correlation of two functions is defined to be

$$Corr(g,h) \equiv \int_{-\infty}^{\infty} g(\tau + t)h(\tau)d\tau \qquad (6.2)$$

(Equation 12.0.10, Press et al. 1968), where g and h are continuous time series. As stated, this function finds the cross correlation of the functions g and h. If g equals h, then the autocorrelation is found. The resulting dependence is on t, and thus t is the lag. If there is a periodic component in the data, then when t equals the period, the value of the autocorrelation will be large. An analogous situation is true for the cross correlation function. The autocorrelation and cross correlation are the major types of analysis performed in the time domain.

An analogous test for periodicity may be made in the frequency domain. In this case, a convenient function to calculate is the power spectral density, defined to be

$$P_h(f) \equiv |H(f)|^2 + |H(-f)|^2 \qquad 0 \leq f < \infty \tag{6.3}$$

(Equation 12.0.14 from Press et al. 1986), where $H(f)$ is the Fourier transform of $h(t)$. As is true for the autocorrelation, if there is a periodic component of frequency f in the function, then the value of the power spectrum will be large at that frequency. If the total power is defined by

$$\text{Total Power} \equiv \int_{-\infty}^{\infty} |h(t)|^2 dt = \int_{-\infty}^{\infty} |H(f)|^2 df \tag{6.4}$$

(Equation 12.0.13 from Press et al. 1986), then the power and the autocorrelation form a Fourier transform pair.

In general, time series data are not continuous. There is always a characteristic sampling time. Therefore, the functions defined above cannot be used as they are. Discrete forms must be used. For the correlation functions the discrete form is:

$$CCF(t) = \frac{E\{[a(t) - \bar{a}][b(t) - \bar{b}]\}}{\sigma_a \sigma_b} \tag{6.5}$$

(Equation 2, Edelson and Krolik 1988) where $E\{f\}$ is the expectation value, a and b are the evenly sampled time series, $\bar{a}$ and $\bar{b}$ are the means, and σ_a and σ_b are the standard deviations.

However, this form cannot be used either, because in astronomical data often the sampling times are not evenly spaced. This is known as *data windowing.* For *Ginga*, breaks in the time series result from Earth occultations of the source and from the data selection criteria. For the analysis in the time domain, there have been several different solutions to the problem of uneven spacing proposed. One has been to interpolate between the points that are available (e.g., Gaskell and Sparke 1986). This approach would not work at all with *Ginga* data, if the source is rapidly variable, because the gaps between the data are so long. Another technique, which was used here, was developed by Edelson and Krolik 1988. Their method involves calculating first the unbinned discrete correlation:

$$UDCF_{ij} = \frac{(a_i - \bar{a})(b_i - \bar{b})}{\sqrt{(\sigma_a^2 - e_a^2)(\sigma_b^2 - e_b^2)}} \tag{6.6}$$

(Equation 3 from Edelson and Krolik 1988) where a_i and b_j are the data pairs. The standard deviation of the data ,σ, is modified by the subtraction of the average measurement error associated with the data, e. This is required to maintain the normalization of the correlation function. From the unbinned correlations, the discrete correlation function is made. This is defined to be

$$DCF(\tau) = \frac{1}{M}\sum UDCF_{ij} \tag{6.7}$$

(Equation 4 from Edelson and Krolik 1988) where the sum is performed for all M pairs for which $\tau - \Delta\tau/2 \leq \Delta t_{ij} \leq \tau + \Delta\tau/2$. The uncertainty on the discrete correlation function is defined by

$$\sigma_{DCF}(\tau) = \frac{1}{M-1}\{\sum [UDCF_{ij} - DCF(\tau)]^2\}^{1/2} \tag{6.8}$$

(Equation 5 from Edelson and Krolik 1988) where the sum is over appropriate pairs as in Equation 6.7. This equation is what would be expected if the points were uncorrelated. However, for AGN, because the variability is usually characterized by $1/f$ noise, the points are correlated, but the length of the correlation is unknown. Therefore, the error bars calculated using Equation 6.8 are in general too small, and the error is underestimated.

In the frequency domain, if the data are evenly sampled, the discrete Fourier transform must be used, defined as follows

$$H_n \equiv \sum_{k=0}^{N-1} h_k e^{2\pi i k n/N} \tag{6.9}$$

(Equation 12.1.7 from Press et al. 1986), and the discrete power spectral density calculated from this is called the periodogram. The periodogram is subject to several uncertainties, including what is known as *aliasing.* Aliasing is a result of having a finite length data stream, and results in power from high frequencies be moved to low frequencies. For unevenly sampled data, the periodogram is calculated by a somewhat different equation, as follows (Press and Teukolsky 1988).

$$P_N(\omega) \equiv \frac{1}{2\sigma^2}\left(\frac{[\sum_j (h_j - \bar{h})\cos\omega(t_j - \tau)]^2}{\sum_j \cos^2\omega(t_j - \tau)} + \frac{[\sum_j (h_j - \bar{h})\sin\omega(t_j - \tau)]^2}{\sum_j \sin^2\omega(t_j - \tau)}\right) \tag{6.10}$$

where τ is defined by

$$\tan(2\omega\tau) = \frac{\sum_j \sin 2\omega\tau_j}{\sum_j \cos 2\omega\tau_j} \tag{6.11}$$

(Equations 4 and 5 from Press and Teukolsky 1988). The reason this is chosen is because, for evenly sampled data, the statistical distribution of the periodogram turns out to be exponential, assuming that the signal is Gaussian. This formula retains this property with unevenly sampled data, and this result is shown in Scargle 1982. Scargle (1982) also explains that the effect of aliasing is reduced by uneven sampling, but Press and Teukolsky (1988) point out that when large gaps in the data occur, such as is experienced in *Ginga* data, much of the power will show up at low frequencies. Note that the errors in the periodogram are calculated by propagation of errors through the formula, and are underestimated in the same way that the correlation errors are.

The autocorrelation function and periodogram calculated by these methods show many spurious peaks due to the window, and due to aliasing, in the case of the periodogram. It is perhaps impossible, *a priori*, to evaluate which ones are real and which are a result of the data sampling. Therefore, to address this issue, the standard method employed (Edelson and Krolik 1988; Done et al. 1990) is to make simulated data, run it through the programs, and compare the results with the results from the actual data. Because the most frequently observed type of AGN variability is red noise, the simulated data are made to have a $1/f$ power distribution. So far this is only used to qualitatively compare with the observed results; however, it is necessary to expand this treatment to estimate a probability of accidental occurrence (Mittaz and Branduardi-Raymont 1989). This is a difficult task if data windowing is a factor.

CHAPTER 7

THE *GINGA* OBSERVATION OF NGC 7469

Simultaneous Observations of Seyfert Galaxies

The problem of temporal and spectral variability of X-rays is important in constraining models of AGN. To this end, S. Tsuruta has developed a campaign to observe carefully selected Seyfert 1 galaxies in several wave bands simultaneously. Already this campaign has produced one very important result from the simultaneous observation of NGC 4051 (Done et al. 1990b). In this observation it was found that the X-ray flux varied by a factor of 2 with a time scale of tens of minutes, while the optical continuum flux varied less than 1%. This is an important result because it implies that the same electron population cannot be producing both bands of emission, and further, the optical must be produced from a region 6–10 times larger than that producing the X-rays.

Two other Seyfert 1 galaxies were observed by *Ginga* in this simultaneous observation effort. They were NGC 7469, and NGC 6814. The author's contribution was to perform the X-ray data analysis of the single observation of NGC 7469, and two observations of NGC 6814. This chapter discusses results from the *Ginga* observation of NGC 7469, while the results from the *Ginga* observations of NGC 6814 are discussed in Chapter 8.

Results From Previous Observations

NGC 7469 is a moderate luminosity Seyfert 1 galaxy. The 2–10 keV luminosity is $2.8 \times 10^{43}\,\mathrm{erg\,s^{-1}}$. Broadened optical nuclear emission lines were reported by Seyfert (1943). X-ray emission was identified from this source using UHURU (Forman et al. 1981). Previous observations of this source have found rapid, large amplitude flux variability. An early X-ray observation by Ariel V reported by Marshall, Warwick and Pounds (1981) found a remarkable flare lasting about 2 days, in which the flux increased by a factor of six. Subsequent observations also showed evidence for substantial variability. Barr (1986) reported the results of four EXOSAT observations within a period of 10 days. Both the LE and the ME flux rates varied significantly within the 10 day period. Rapid variability was also found during one of the observations, in which the ME flux decreased by a factor of 2 in 5–6 hours. There was also evidence for day to day variation of the spectral index for the ME data only.

The spectra of NGC 7469 have shown evidence of interesting components, as described in Chapter 2. Specifically, a soft excess component, line emission and a hard tail have been found.

The EXOSAT data analyzed by Barr (1986) revealed that spectral fitting to the ME plus LE data found a column density below that of the Galaxy in the direction of NGC 7469, implying a soft excess spectral component. Spectral fitting from the Imaging Proportional Counter (IPC) on-board *Einstein* found a soft spectrum, with an energy index of 1.85 in the 0.2–4.0 keV region (Kruper, Urry and Canizares 1990). The soft excess component was also found in the IPC + Monitor Proportional Counter (MPC) fits by Urry et al. (1989). The suggestion of the soft excess was found in the Solid State Spectrometer (0.4–4.5 keV) data when considered alone (Petre et al. 1984). Subsequent fits to the SSS + MPC data, performed by Turner et al. (1991), including better modeling for the ice on the SSS, show a soft excess component necessary, although the form of the soft excess cannot be identified.

NGC 7469 was also observed with *Ginga* in July 1988 (Piro, Yamauchi and Matsuoka 1990). The source was found to be in a bright state; the 2–10 keV flux was $4.0 \times 10^{-11}\,\mathrm{ergs\,cm^{-2}s^{-1}}$. The simple power law plus absorption fit could not describe the time averaged spectrum ($\chi^2_R = 8.3$). Residuals were found, including excesses at the iron emission line, at low energies, and at high energies. The best fit found was either a partial covering or a reflection model, plus an iron emission line. The fitting could not distinguish between the partial covering and the reflection model; however, the presence of a hard energy tail was undeniable. The iron line equivalent width was moderately large, being $150 \pm 35\,\mathrm{eV}$, and there was marginal evidence for broadening, although a narrow line could not be rejected. Evidence for an iron line was found in the EXOSAT Spectral Survey sample, at the 97.5% confidence level (see Chapter 4).

Because of the previous history of medium to rapid time scale variability and the presence of interesting spectral components, this object was chosen as an interesting candidate for the simultaneous observation campaign. We had every reason to expect that temporal and possibly spectral variability might be observed. Therefore, this source was observed November 22–24, 1989, as part of Tsuruta's simultaneous campaign.

Results

The *Ginga* Observation

NGC 7469 was observed by *Ginga* for two days, November 23–24 1989, and the data from the remote orbits from two days were available for analysis. A background observation was made on November 22, 1989. The details of the observation and data selection are given in Table 6.

During this observation, the satellite was plagued with pointing problems. Apparently one of the stabilizing gyros failed during the observation before this one. Although later the aspect of the satellite could be more or less controlled, even though the drift rate can be up to $2^{\circ}\,\mathrm{hr}^{-1}$, at the time of this observation the method of correction had not yet been devised. In the third column of the table the transmission coefficient for each continuous data group is listed. In general, the satellite would start out each day with the transmission coefficient fairly high, and the aspect would subsequently deteriorate.

Because of the smaller signal-to-noise ratio of regions where the transmission coefficient was low, the resulting amount of useful data is not large. This fact is reflected by the effective time, which is the real time multipled by the average transmission coefficient. The total effective time for the two days of observation was 11264 seconds. All of these data were used for the time series analysis. However, only data with transmission coefficient larger than 0.6 were used for final spectral fitting, and the total effective time for this subgroup is 7374 seconds.

The background subtraction method used was the SSUD sorted method, discussed in Chapter 6.

The flux of the source was low. Before aspect correction the source count rate was about 5 $\mathrm{count\,s^{-1}}$. This is about 0.5 mCrab, and the *Ginga* 3σ source confusion

Table 6. Observing log from the *Ginga* observation of NGC 7469. Data selection criteria were SSUD < 6500, COR < 9 and the earth elevation angle (EELV) > 6. Included in this table are the subframes therefore chosen using these data selection criteria. Also shown are the corresponding satellite ascending nodes, and for the source observation, the transmission coefficient of the data.

Subframes	Ascending Node	Transmission Coefficient
Background. Resulted in 7575 seconds (live time):		
139 – 146 (1,2)	307 – 304	
149 – 154 (1,2)	302 – 300	
176 – 186 (1,2)	287 – 282	
195 – 198 (1,2)	277 – 275	
221 – 228 (1,2)	263 – 259	
241 – 243 (1,2)	252 – 251	
266 – 273 (1)	238 – 235	
286 – 288	227 – 226	
311 – 319	214 – 209	
Source observation, first day. Resulted in 5455 seconds (effective time):		
68 – 71	320 – 319	0.78
97 – 107 (*)	304 – 299	0.75
111 – 113 (*)	297 – 296	
156 – 162 (*)	282 – 279	0.72
175 – 178 (*)	272 – 270	
200 – 208 (*)	257 – 254	0.66
220 – 223 (*)	247 – 246	
246 – 253	233 – 229	0.58
266	222	0.52
308 – 317	209 – 204	0.50
349 – 357	184 – 180	0.43
Source observation, second day. Resulted in 5809 seconds (effective time):		
118 – 125	320 – 319	0.77
127 – 136	319 – 314	
162 – 172 (*)	300 – 294	0.72
176 – 181 (*)	292 – 289	
202 – 210 (*)	278 – 274	0.64
222 – 226 (*)	267 – 265	
247 – 255	253 – 249	0.56
268 – 270	242 – 241	
338 – 346	229 – 224	0.46
358 – 361	218 – 216	0.42
383 – 391	204 – 200	0.38
404 – 406	192 – 191	0.34

(1,2) Background data which should be used for (1) first day or (2) second day background subtraction.

(*) Preferred data selection.

limit is 0.2 mCrab (Hayashida 1989). This fact made the results very sensitive to the systematic errors in the background subtraction. The final background subtraction was not completely satisfactory; this point will be discussed further later in this chapter.

Time Series Analysis

Much of the time series analysis was performed in Montana, because of a problem with the analysis software in Nagoya. Partially because of the pointing problem, there was also some uncertainty in the attitude determination for part of the observation. Therefore a systematic error of 0.037 in the transmission coefficient was included in the early part of the first day. Since the transmission coefficient was fairly large for those data affected (0.78–0.75), the correction made only a small decrease in signal to noise. For the 1.2–20.9 keV flux, the decrease was less than $\sim$ 10% for data not binned in time. Subsequently, the timing analysis was continued in Montana, using the background subtracted time series data brought from Japan..

The aspect corrected light curves in the energy range of 1.2–20.9 keV for the two days of observation are shown in Figure 13. The data are shown for the two days separately. There is a $\sim$ 13 hour gap between the data from the first day and the second day. During this time the contact orbits and the SAA passage occur, as discussed in Chapter 6. Although the detector was pointed at the source during this time, high and variable background prevents these data from being used. Note also that the data are not continuous. This is due to the data selection as described in Chapter 6. The gaps are due to Earth occultation of the source, contamination by the bright limb of the Earth, or high SSUD levels. Therefore, each group of data corresponds roughly to one satellite orbit. Note that the error

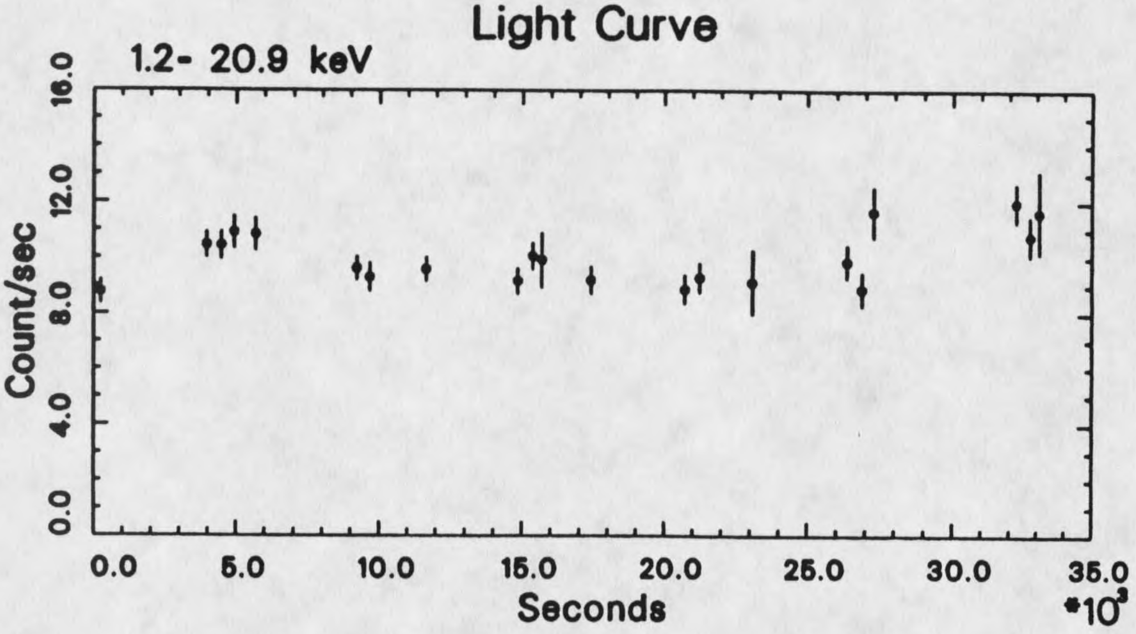

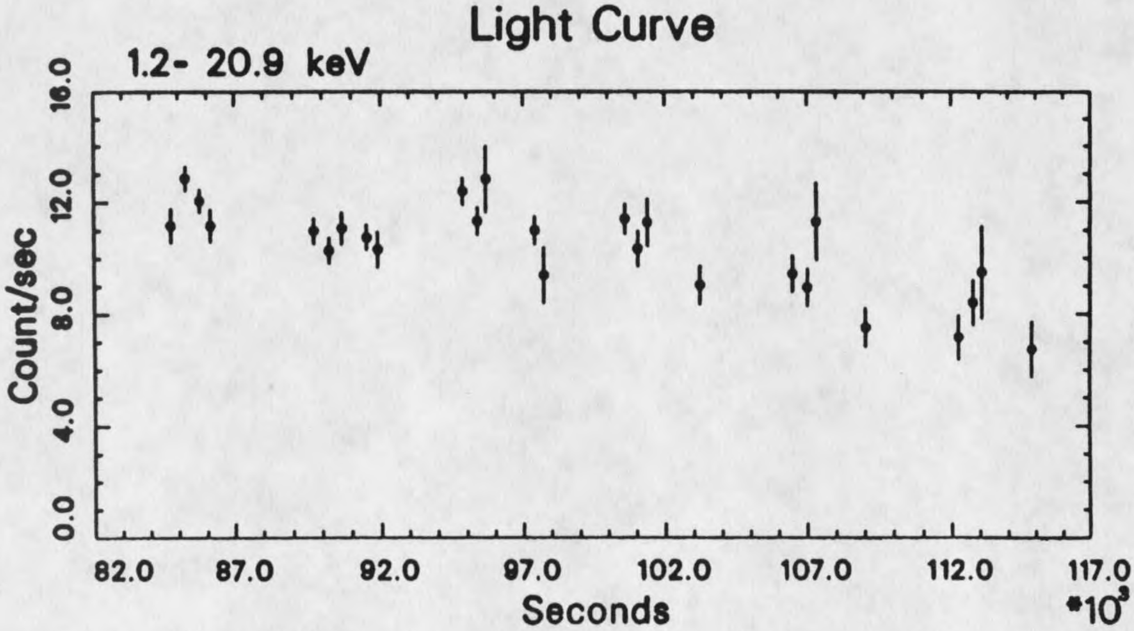

Figure 13. Light curve for NGC 7469 in the energy range 1.2–20.9 keV. The data from the two days of observation are shown separately. The bin size is 512 seconds.

bars are not all of the same length. This is because of the binning. Recall the intrinsic time binning for the MPC–1 mode of operation is 16 seconds. However, it is desirable to combine the data into large time bins to obtain a larger signal to noise ratio, and to examine long term variability. The bin length chosen here was 512 seconds. However, in some cases, 512 seconds of continuous data were not available from each orbit, or there were gaps in the orbit due to high background. In these cases, smaller amounts of data were combined for one data point, resulting in a larger error bar.

This shows the root of the problem in the software at Nagoya. The binning program was written, for some reason, so that if the bin size was so large that there were not enough continuous points to combine, instead of combining the smaller number of points with a larger error bar, the program would repeat the last point. This treatment is adequate if the variability time scale is on the order of a few times the sampling time scale. However, NGC 7469 is known to be variable on a longer time scale than one orbit, so a different treatment was necessary. Note that the problem with the software did not apply when data were binned at the sampling time scale. Therefore, this was done, and the data were taken to Montana, and a program was written to bin the data correctly.

Another influence to the error bar is the transmission coefficient. Toward the end of each day, note that the error bars become in general larger. This is due to the fact that these data were characterized by low transmission coefficients, and since this is the aspect corrected light curve, the error bars are correspondingly larger.

Figure 13 shows that the source was mildly but significantly variable during these two days of observation. The source flux was variable during the first day; the χ^2 against the constant hypothesis was 34 for 10 d.o.f. It was also variable during the second day ($\chi^2 = 99.8$ for 11 d.o.f.), but it also exhibited a trend, decreasing by about one third, during the last ~ 5.5 hours of observation.

An important characteristic of variable data is the smallest time in which a significant change occurs, where a significant change is defined as being a 3σ change in flux. For *Ginga* data, this time scale is hard to estimate, if it is larger than one satellite orbit. Then, if the flux varies significantly between orbits, the upper limit to the time of significant change is the satellite period. This is the case with NGC 7469, so the shortest significant change is about 100 minutes. For this observation there were four instances in which the flux was observed to vary significantly between orbits.

As stated earlier, there was a trend in the flux of the second day observation. The decrease began at $\sim 95,000$ seconds and continued until the end of the observation at $\sim 115,000$ seconds. Figure 14 shows the light curve for the second day with the superimposed straight line fit. Extrapolating the straight line fit indicates a halving time scale of 25,000 seconds. The decrease is fairly linear; the linear correlation coefficient is $r = -0.94$. The probability of such correlation by chance is less than 0.5%. The non-parametric Spearman rank correlation coefficient also shows a high degree of correlation, being $R_S = -0.86$. The straight line fit is fairly good having a χ^2_R of 1.43 for 7 d.o.f. This is significant at the 90% confidence level. Also, the slope was found to be $-2.38 \pm 0.28 \times 10^{-5} \mathrm{counts\,s^{-2}}$. The determined 1σ error is nearly 9 times smaller than the best fit value. This is another indication of the significance of this linear trend.

To investigate the possibility of spectral change during the observation, first the data were plotted in three different energy bands: the soft band from 1.2 to 3.5 keV, the medium band from 3.5 to 8.7 keV, and the hard band 8.7 to 20.9

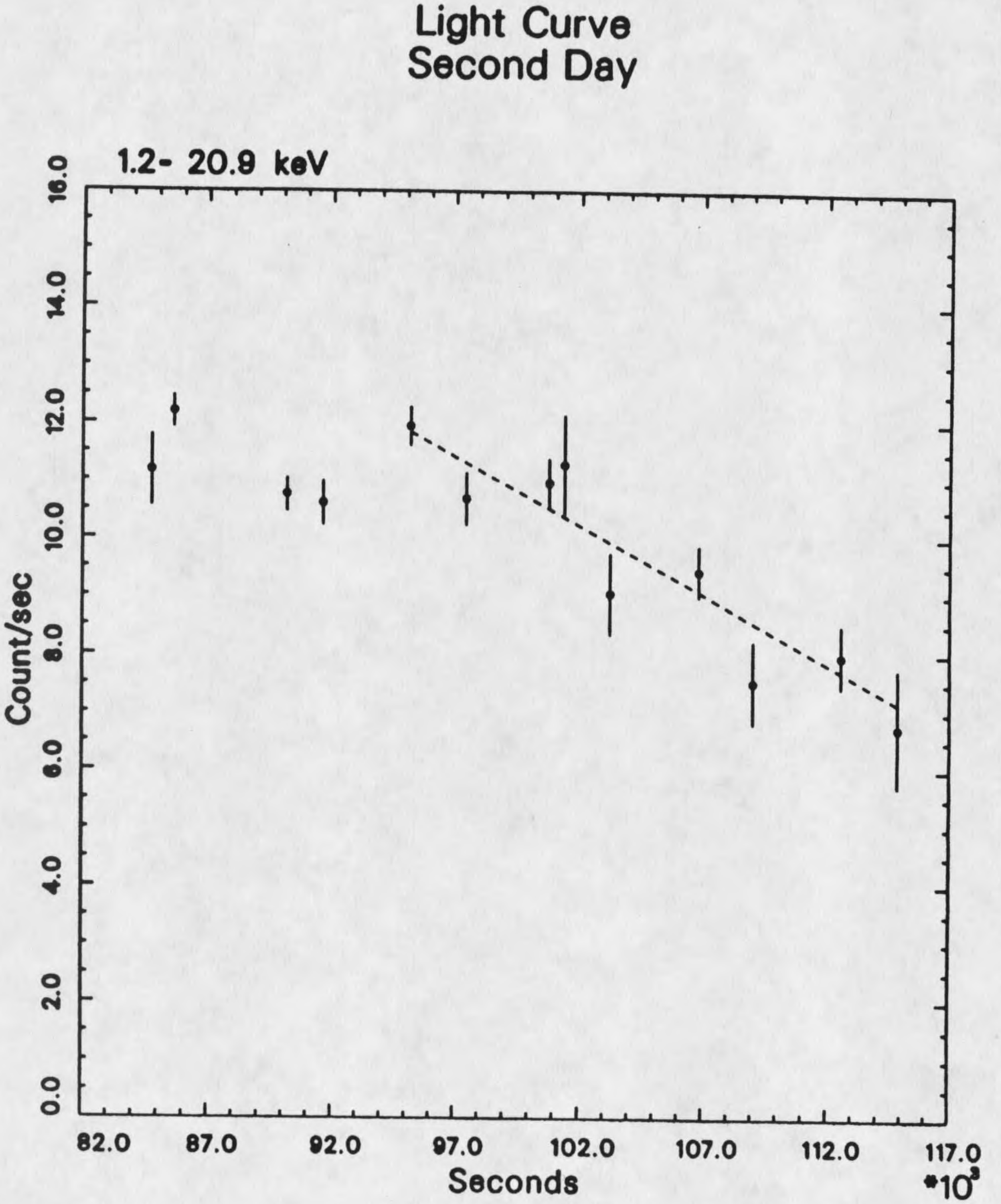

Figure 14. Trend in total flux for NGC 7469. Shown is the light curve for the second day. The dashed line shows the best fit straight line for the last 9 points, comprising the approximate linear decrease. The time bin is the maximum possible, so that each group of continuous data points is binned together.

keV. These energy ranges were chosen because separate variability in these separate bands would indicate variability in different spectral components: variation in soft band could indicate changes in the soft excess or absorption column, while variation in 8.7–20.9 keV band could indicate changes in the hard tail component. Figure 15 shows these light curves for the first day of the observation, while Figure 16 shows these light curves for the second day of the observation. As expected each energy band varies significantly separately at the 90% confidence level. For the first day, the soft band shows a steady increase. A linear fit to this trend is acceptable with the slope different from 0 by 4σ. However, the medium and hard light curves do not show trends. The slope for the medium energy light curve is not different from 0, although the linear fit is poor, and the best linear fit for the hard light curve shows a negative slope. Much of the contribution to this negative slope is due to the second and third points in this light curve. With these points removed, the light curve is consistent with constant flux. Thus, the general increase in the soft data, while the medium and hard do not exhibit such a trend, seems to be an indication of spectral variability. There seems to be a softening of the spectra during the first day of observation.

For the second day, significant decreases are found, especially for the last nine points. For the soft and medium light curves, the linear fits for the last nine points show slopes significantly different from 0 by 5σ and nearly 7σ, respectively. For the hard flux, the slope was different from 0 by only 2σ, for the last 9 points. All of the linear fits were good. This indicates that there may or may not be evidence for spectral variability.

In order to investigate the question of spectral variability further, flux ratios were made. The softness ratio, defined to be 1.2–3.5 keV/3.5–20.9 keV, and the hardness ratio, defined to be 8.7–20.9 keV/1.2–8.7 keV, are useful. This is because

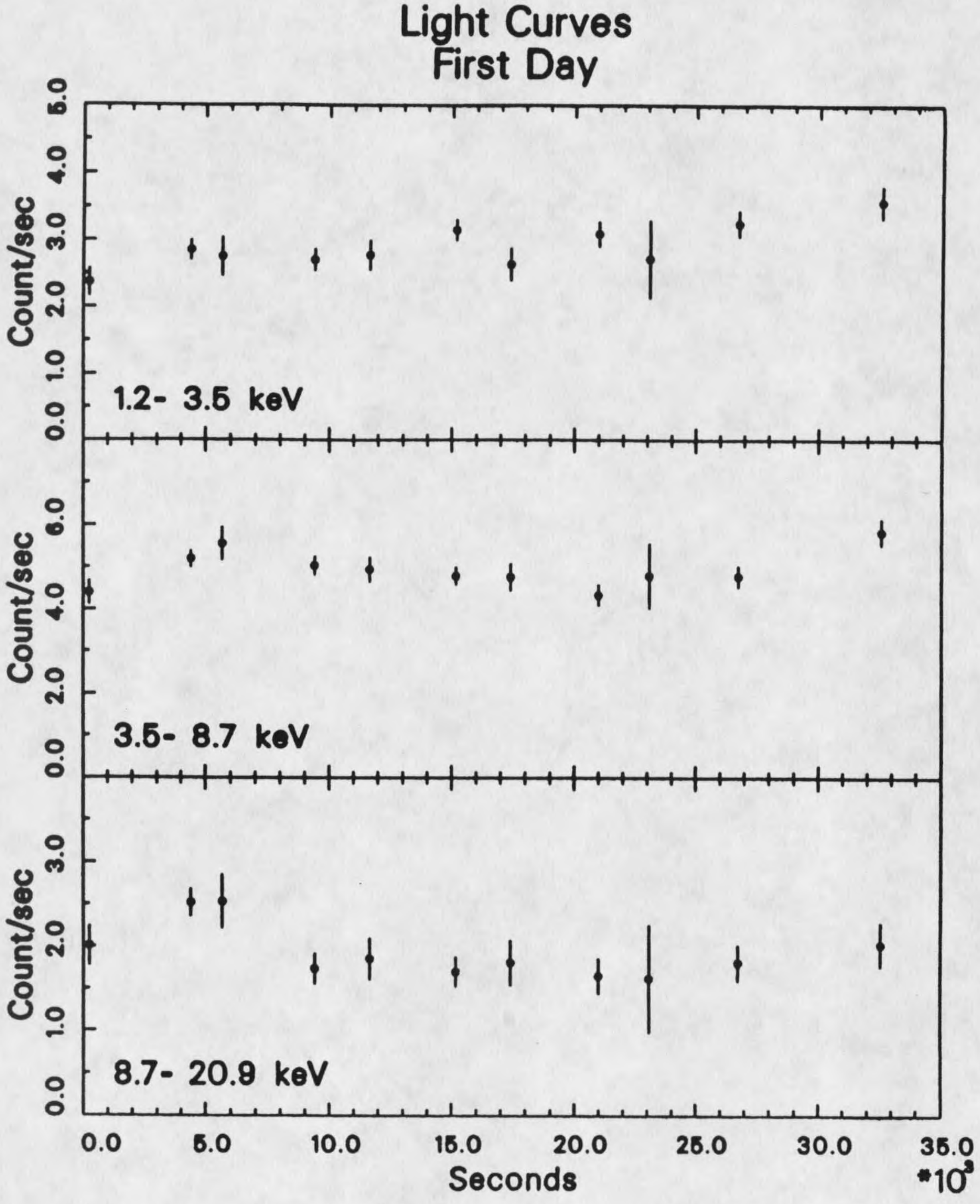

Figure 15. Soft, medium and hard light curves for the first day of observation. The bin size is the maximum.

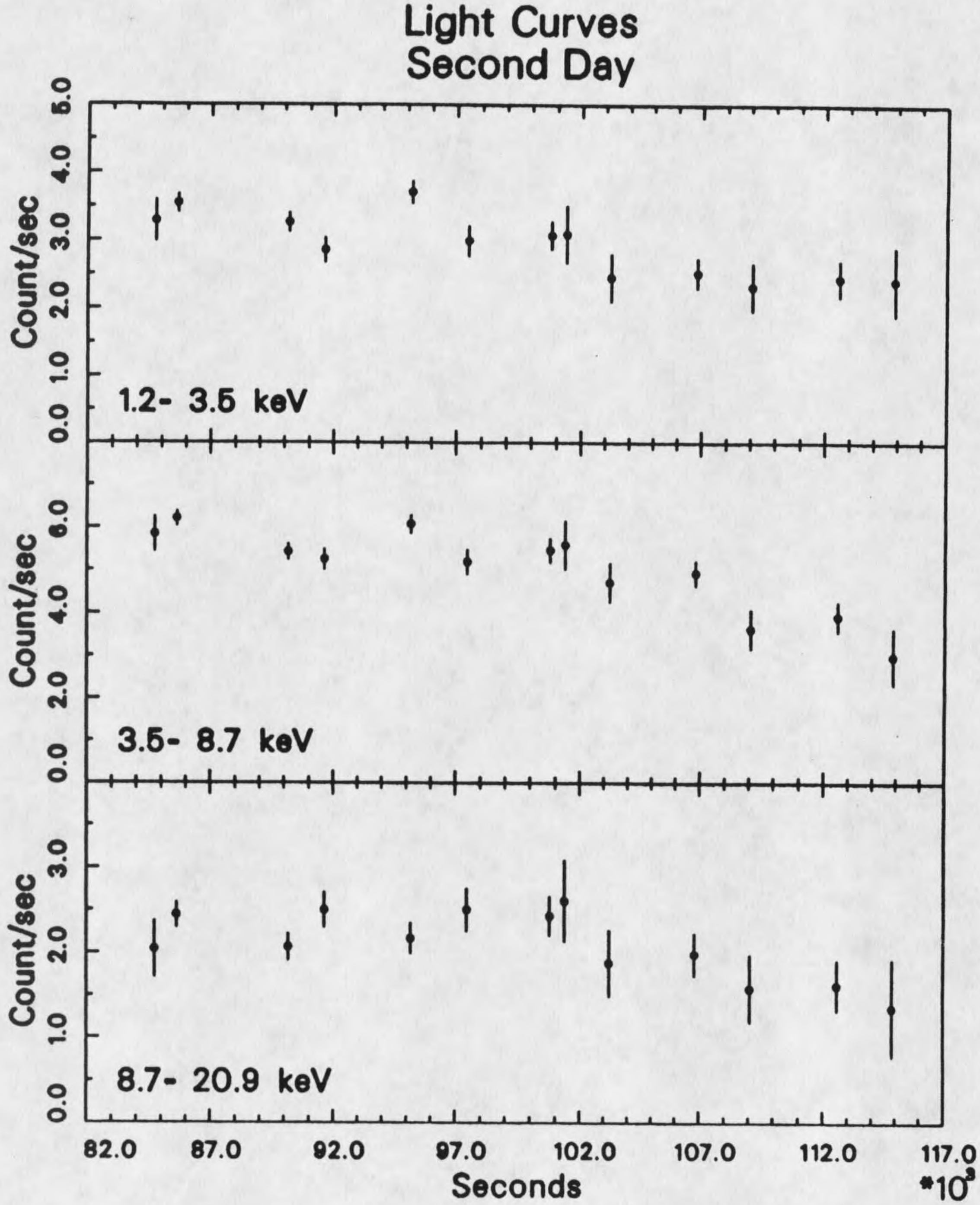

Figure 16. Soft, medium and hard light curves for the second day of observation. The bin size is the maximum.

the variation of the softness ratio can imply variation of the soft excess component or the absorption column with respect to the power law index, while the hardness ratio can find the variation of the hard tail with respect to the power law. Figure 17 shows the softness and hardness ratio light curves for the first day, and Figure 18 shows the corresponding light curves for the second day. The softness for the first day varies significantly; the χ^2 against a constant hypothesis was 24.5 for 10 d.o.f. The hardness for the first day varies marginally ($\chi^2 = 17.9$ for 10 d.o.f.) For the second day, even though the flux decreased significantly, no significant variation in either softness or hardness ratio was found. The variation in softness during the first day can be described by a trend. Figure 17 shows superimposed on the the softness ratio light curve the best fit straight line. The straight line fit is good ($\chi^2 = 9.25$ for 11 d.o.f.), and the slope is different than 0 by 3.9σ. The hardness for the first day can also be described by a trend with 3σ significance; however, this actually appears more like a step function. If the first three points are removed, then the remaining 8 points are consistent with a constant ratio. The softness and hardness ratios therefore seem to indicate that spectral variability is present during the first day, but not during the second day.

The apparent trend describing the spectral variability during the first day is that of a softening of the spectrum. At least part of this softening is due to the increase found in the soft light curve. However, recall from Chapter 6 that if the transmission coefficient is not one, and if the movement of the satellite is in the slew plane, there can be contamination by soft X-ray reflecting from the collimator. Table 6 shows that the transmission coefficient drops during the first day of observation. Although we cannot be sure that the motion is in the slew plane, it is important to estimate the contribution of reflected soft X-rays. First, the field was checked for other X-ray sources which could be contaminating the

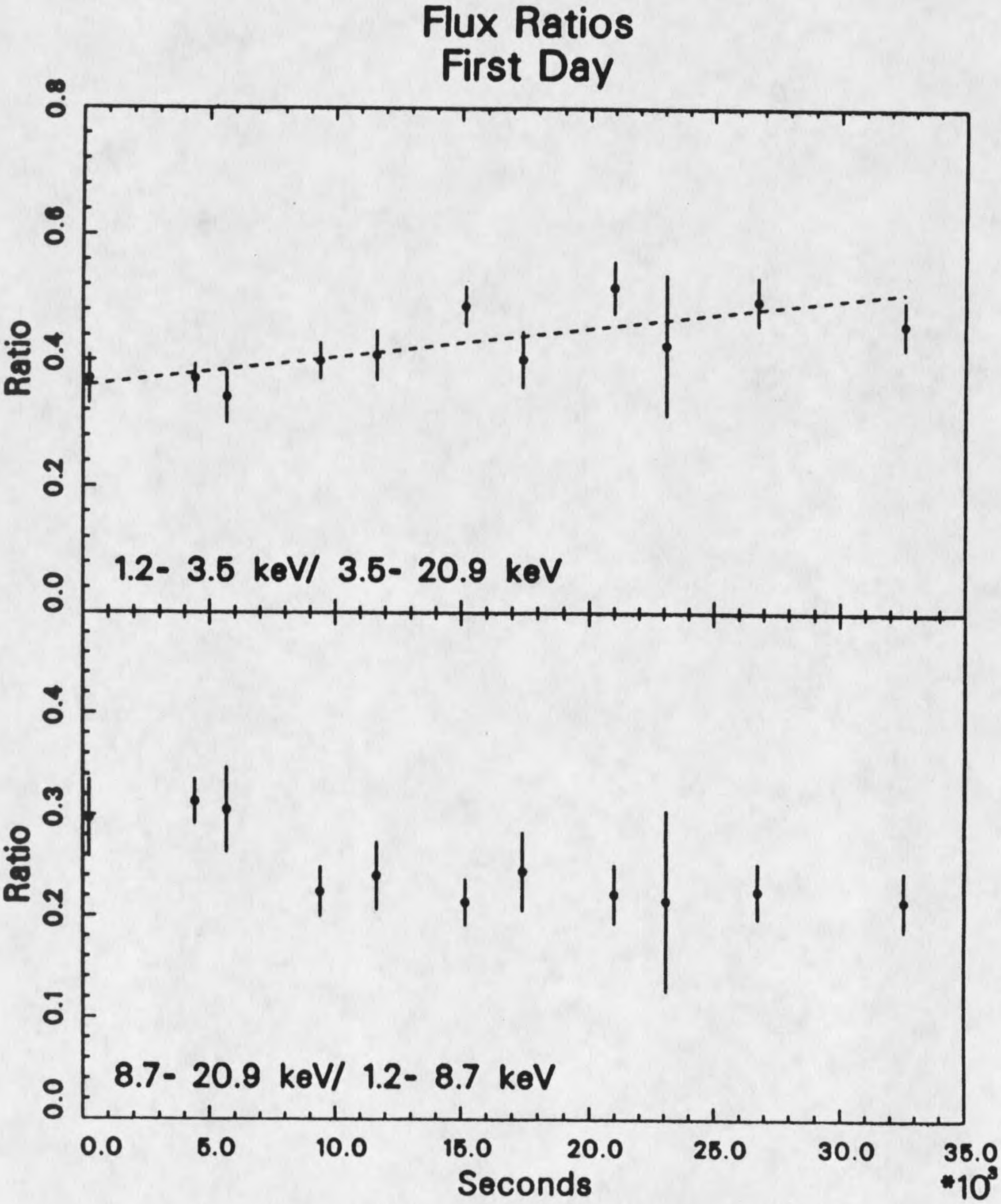

Figure 17. Softness and hardness ratios for the first day of observation. The bin size is the maximum.

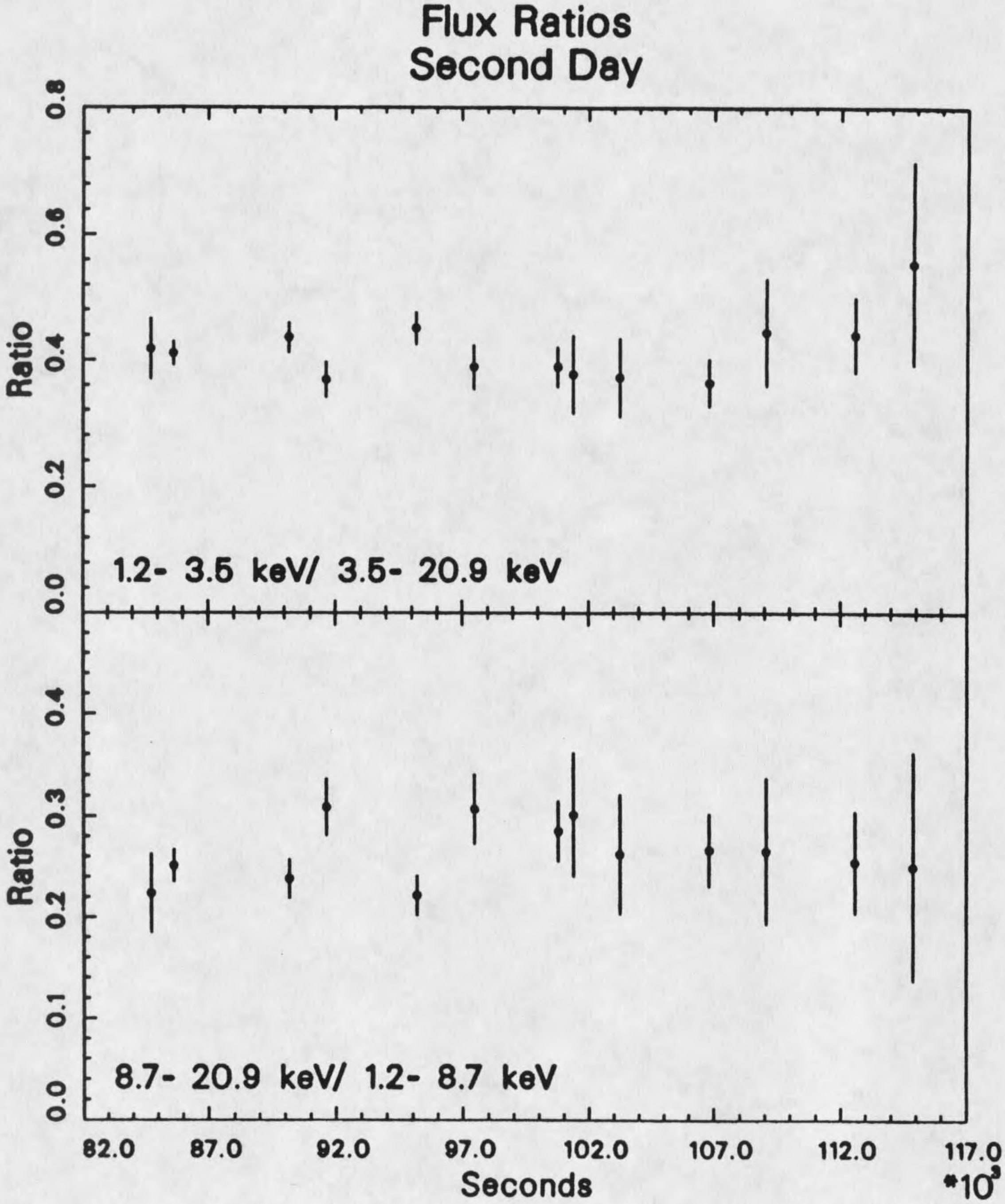

Figure 18. Softness and hardness ratios for the second day of observation. The bin size is the maximum.

soft flux. However, in the IPC Pointing Catalog, NGC 7469 was the brightest object in a cone with apex angle of 4°, sufficient to remove the possible effect of other contaminating sources (Hayashida et al. 1989).

Next the effect of self-reflection into the collimator was examined. To check this effect, the contribution due to reflection was estimated and subtracted from the soft X-ray flux, and the line fit for the softness ratio was again calculated. The amount of reflected soft X-rays was estimated to be 0.04 (4%) times the soft X-ray flux times (1 − trans.coef.) (Turner et al. 1989). Since the magnitude of the uncertainties is largely determined by the magnitude of the background, the size of these was left unchanged. This reduction in the soft X-ray flux caused the significance of the line fit to change from 3.9σ, before reflection was taken into account, to 3.7σ, after reflection was taken into account. Therefore, the trend in softness observed is still significant.

The second day showed no variation or trend in either softness or hardness, even when the estimated contribution from reflection to soft flux was taken into account.

As will be discussed in the next section, the background spectrum was observed to soften with time. This could also be a source of systematic error in the softness ratio. In order to estimate this effect, two spectra were made and compared. The first spectrum consisted of the data with transmission coefficient greater than 0.6 which had had the background spectrum from the first half of the background observation subtracted from it. The second spectrum consisted of the same data but with the background spectrum from the second half of the background observation subtracted from it. This approach was necessarily crude because only the plotted spectra were available for examination. For the first two energy channels, corresponding to PHA channels 2–5, the spectra were consistent.

Therefore the effect using the average background on the softness ratio is probably negligible, or at least could not be estimated using this crude method.

Therefore the significant results of the timing analysis were that the source was found to be variable, with the decreasing trend being observed during the second part of the observation. Evidence for spectral variability was found, as a trend in softness ratio during the first part of the observation.

Spectral Analysis

The spectral fitting was necessarily performed in Nagoya, and proceeded as follows. The spectra were fit from PHA channels 2 to 28, corresponding to energy 1.11 – $\sim$ 20 keV.

To examine the possibility of change of spectral index with respect to time, the data were split into 15 spectra along the light curve. Table 7 summarizes the spectral fitting results. Only results from simple power law plus absorption fits (Equation 4.1) are given; this model was adequate at the 90% confidence level for all but 3 fits. An emission line, with line energy fixed at 6.4 keV was statistically not necessary, as determined by the F statistic (Equation 3.1) except in three cases marked by an (*). Two of these spectra were also not fit adequately the 90% confidence level. The number of degrees of freedom for each fit is different because of different energy binning. In general, all data were fit in the same energy band.

As mentioned in Chapter 6, the lowest absorption column which can be measured using *Ginga* is $10^{21}\mathrm{cm}^{-2}$. However, the Galactic column in the direction of NGC 7469 is 5×10^{20} cm^{-2} (Barr 1986). Therefore during spectral fitting, the column density was fixed at the Galactic value, if the fitting routine found a value lower than $10^{21}\mathrm{cm}^{-2}$. However, when the absorption column was not fixed at the Galactic value, the spectral fit value found was consistent with the Galactic value,

Table 7. Orbit spectral fitting results for NGC 7469. The model used was only a simple power law (Equation 4.1), as a line was in general not required.

Subframes	Time (s)	Photon† Index	Flux‡ (1.2–9.3 keV)	χ^2_R/d.o.f
First Day:				
68–71	403	1.43 ± 0.09	6.45 ± 0.30	1.17/17
97–103	627	1.38 ± 0.12	7.59 ± 0.27	0.99/18
104–107, 111–113	582	1.49 ± 0.21	7.92 ± 0.28	1.01/17
156–162, 175–178*	996	1.48 ± 0.17	7.42 ± 0.21	1.57/17
200–208, 220–223	1066	1.56 ± 0.19	7.60 ± 0.22	0.90/17
246–253, 266	643	1.82 ± 0.14	7.49 ± 0.29	1.46/18
308–317	637	1.62 ± 0.13	8.40 ± 0.31	1.25/17
349–357	489	1.74 ± 0.09	9.55 ± 0.39	1.07/15
Second Day:				
118–125, 127–136	1139	1.49 ± 0.08	8.65 ± 0.21	1.17/15
162–170	761	1.48 ± 0.06	8.18 ± 0.25	1.53/16
171–172, 176–181	680	1.51 ± 0.20	7.85 ± 0.26	0.77/17
202–210, 222–226*	1117	1.59 ± 0.09	8.68 ± 0.22	1.63/18
247–255, 268–270	822	1.50 ± 0.07	7.55 ± 0.23	1.18/17
338–346, 358–361*	733	1.47 ± 0.15	6.94 ± 0.31	1.06/16
383–391, 404–406	554	1.60 ± 0.04	5.90 ± 0.38	0.73/15

† Error in Photon Index are 90% confidence.

‡ Error in Flux are one standard deviation.

* The addition of an emission line with energy 6.4 keV improves this fit significantly (> 90% confidence, using the F statistic).

in all cases. Although, because of the low detection efficiency at low energies, *Ginga* cannot distinguish the presence of a soft excess component, unless it is very strong, the fact that the data were adequately fit from 1.11 keV shows that there is no evidence for the soft excess previously found in this object (e.g., Barr 1987).

A significant variation was found in the photon index during the first day (χ^2 against constant hypothesis being 33 for 7 d.o.f.). This variation took the form of a trend, the slope of the best fit straight line being $1.06 \pm 0.21 \times 10^{-6}\,\mathrm{s}^{-1}$. However, when only data were considered for which the transmission coefficient was greater than 0.6, the data were consistent with a constant photon index ($\chi^2 = 1.2/4$ d.o.f.). For the second day, the photon index again varied significantly ($\chi^2 = 12.4/6$ d.o.f.), but no significant (greater than 3σ) trend was observed, and again for data with transmission coefficient greater than 0.6, the photon indices were consistent with a constant ($\chi^2 = 3.0$ for 3 d.o.f.). This trend in spectral index may or may not be real, because a significant correlation between photon index and transmission coefficient was also found ($r = -0.67$, significant at the 90% level). Recall from Chapter 6 that in general, the spectral fitting program available at Nagoya can account for the soft photon reflection from the collimator wall when the transmission coefficient is greater than 0.5. Here, the last two spectra from the first day have transmission coefficient smaller than 0.5. Therefore the spectral fitting results for these cannot be considered reliable. Although this correlation might be accidental, until the correction for reflection of soft X-rays is verified, the conservative view was taken, and only the data with transmission coefficient greater than 0.6 were used for subsequent spectral fitting.

Ignoring the possible spectral index trend, the data were split into four parts along the light curve, of approximately equal integrated time (2609, 2846, 2581, and 3228 seconds) and fit. The photon indices were consistent with a constant (1.44 ± 0.04, 1.66 ± 0.04, 1.50 ± 0.04, 1.55 ± 0.05, with average 1.54 ± 0.08).

Next in the spectral analysis the total spectrum from all data with transmission coefficients greater than 0.6 was accumulated and fit. This spectrum was called FINAL6T. This combination of these data into one spectrum is justified because the photon indices for this group of data are consistent with a constant ($\chi^2 = 7.21/8$ d.o.f.). The 2–10 keV flux for this spectrum was 7.95 ± 0.11 counts/sec. Assuming $H_0 = 50\,\mathrm{km\,s^{-1}Mpc^{-1}}$ and 1 Ginga count= $2.0 \times 10^{-12}\,\mathrm{erg\,cm^{-2}}$, the luminosity from 2–10 keV was $1.77 \pm 0.03 \times 10^{43}\,\mathrm{erg\,s^{-1}}$.

The spectral fitting results for the final combined spectra are given in Table 8. The best fit for a simple power law plus fixed absorption column and residuals is shown in Figure 19. Note that here the raw data and best fit model are shown. This is in contrast with the EXOSAT spectral fits shown in Chapter 4, which show the model deconvolved from the detector response. The simple power law fit is not satisfactory, having a reduced χ^2 of 1.64 for 17 d.o.f. The residuals show an excess at around 7 keV, attributable to an iron line, with some hint of a tail toward the high energies. A large contribution to the χ^2 is from a point at ~ 4 keV.

The residual at ~ 7 keV prompted the addition of a narrow Gaussian emission line to the power law fit, shown in Figure 20. This provided a reduction in the reduced χ^2 to 1.31 for 15 d.o.f., and the reduction is found to be significant, using the F test (Equation 3.1), at greater than 99% confidence. Note that the power law fit shown in Figure 19 found the residual at nearly 7 keV, but the spectral fit found the line energy consistent with 6.4 keV. The χ^2 plot as a function of line energy was examined and was found to be nearly symmetric, so the line energy is consistent with the emission being from neutral or lowly ionized iron. The line equivalent width was found to be 250 ± 140 eV, which is fairly large, but consistent with the average equivalent width for a Seyfert 1 (Awaki 1991). Examination of the low energy residuals shows no evidence for the tail of the soft excess previously observed in this object (e.g., Barr 1986). However, because *Ginga* has limited response in soft X-rays, the existence of a soft excess component can neither be

Table 8. Spectral fitting results for the final combined spectra. In all cases, the N_H column was fixed at the Galactic value of $5 \times 10^{20}\mathrm{cm}^{-2}$.

Spectrum*	Model	Photon Index	Line Energy (keV)	Equivalent Width(eV)	χ^2_R/d.o.f
FINAL6T	Power law	1.49 ± 0.05	–	–	1.64/17
	Power law plus line	1.53 ± 0.06	6.41 ± 0.26	250 ± 140	1.31/15
FNLP6T	Power law	1.54 ± 0.06	–	–	0.91/17
	Power law plus line	1.57 ± 0.06	6.4(f)	210 ± 160	0.69/16
FNLQ6T	Power law	1.36 ± 0.09	–	–	2.17/17
	Power law plus line	Rejected Model			

* FINAL6T = Data with T > 0.6– all background data.
FNLP6T = Data with T > 0.6– first half of background data.
FNLQ6T = Data with T > 0.6– second half of background data.

(f) Line energy fixed at value given.

confirmed nor ruled out. Examination of the high energy residuals showed some (weak) indication of a hard tail.

The spectral fit including the Gaussian emission line was still not completely satisfactory having a reduced χ^2 of 1.31 for 15 d.o.f. This reduced χ^2 shows that there is a 25% probability that such a large χ^2 could have been obtained from the correct fitting function. The major contribution to the χ^2 is the residual at ~ 4 keV. This provides a contribution to the χ^2 of ~ 5 and to the reduced χ^2 of ~ 0.35. Neglecting this point causes a reduction of the reduced χ^2_R to $\sim 1.04/14$ d.o.f., a good fit.

What might be the cause of this anomalous point? The cause of this was traced to the background spectrum used. Even though the SSUD sorted back-

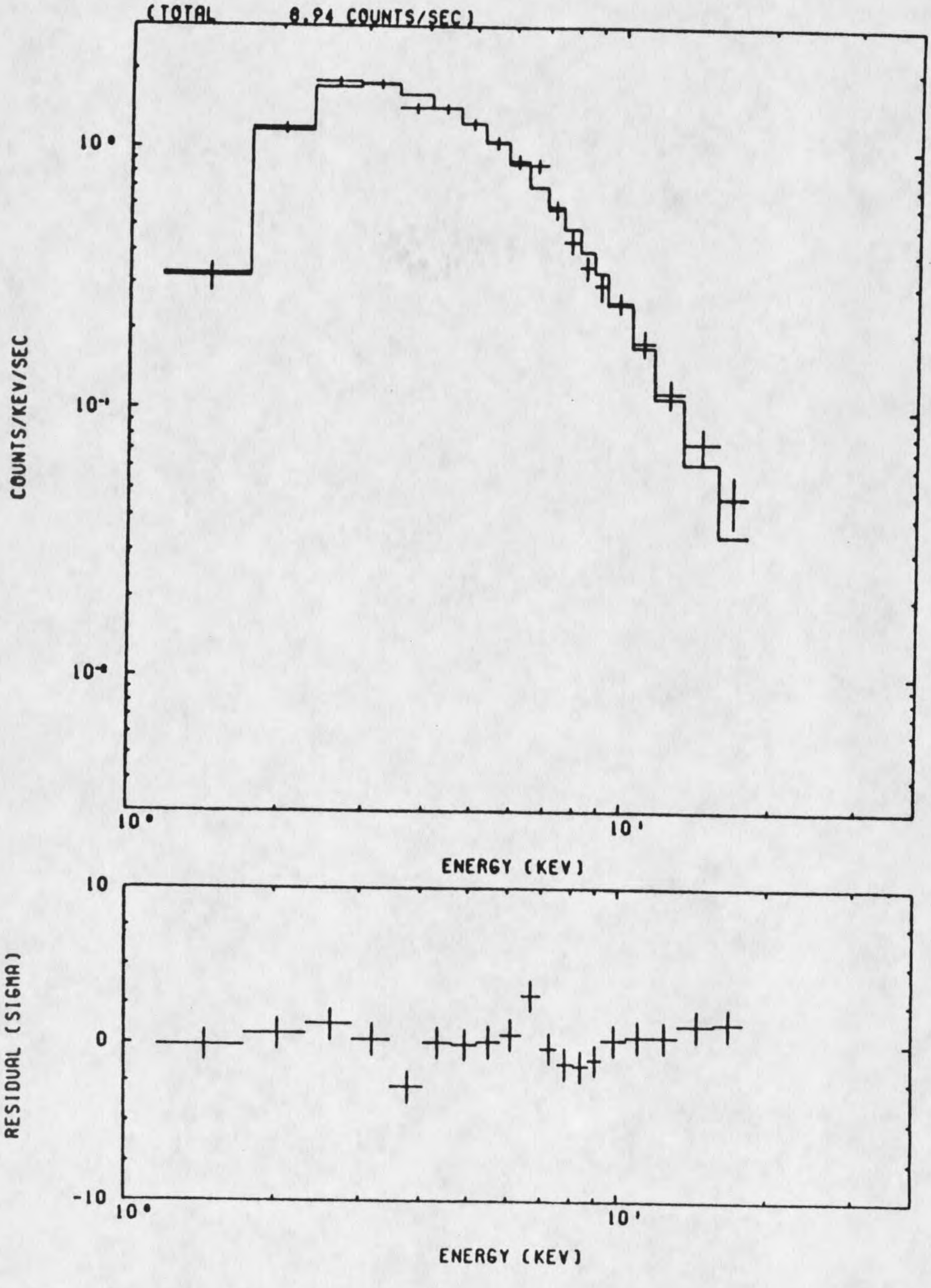

Figure 19. Power law fit to FINAL6T. Included are all data having a transmission coefficient larger than 0.6. Fit residuals are shown at the bottom of the plot, while best fit parameters may be found in Table 8.

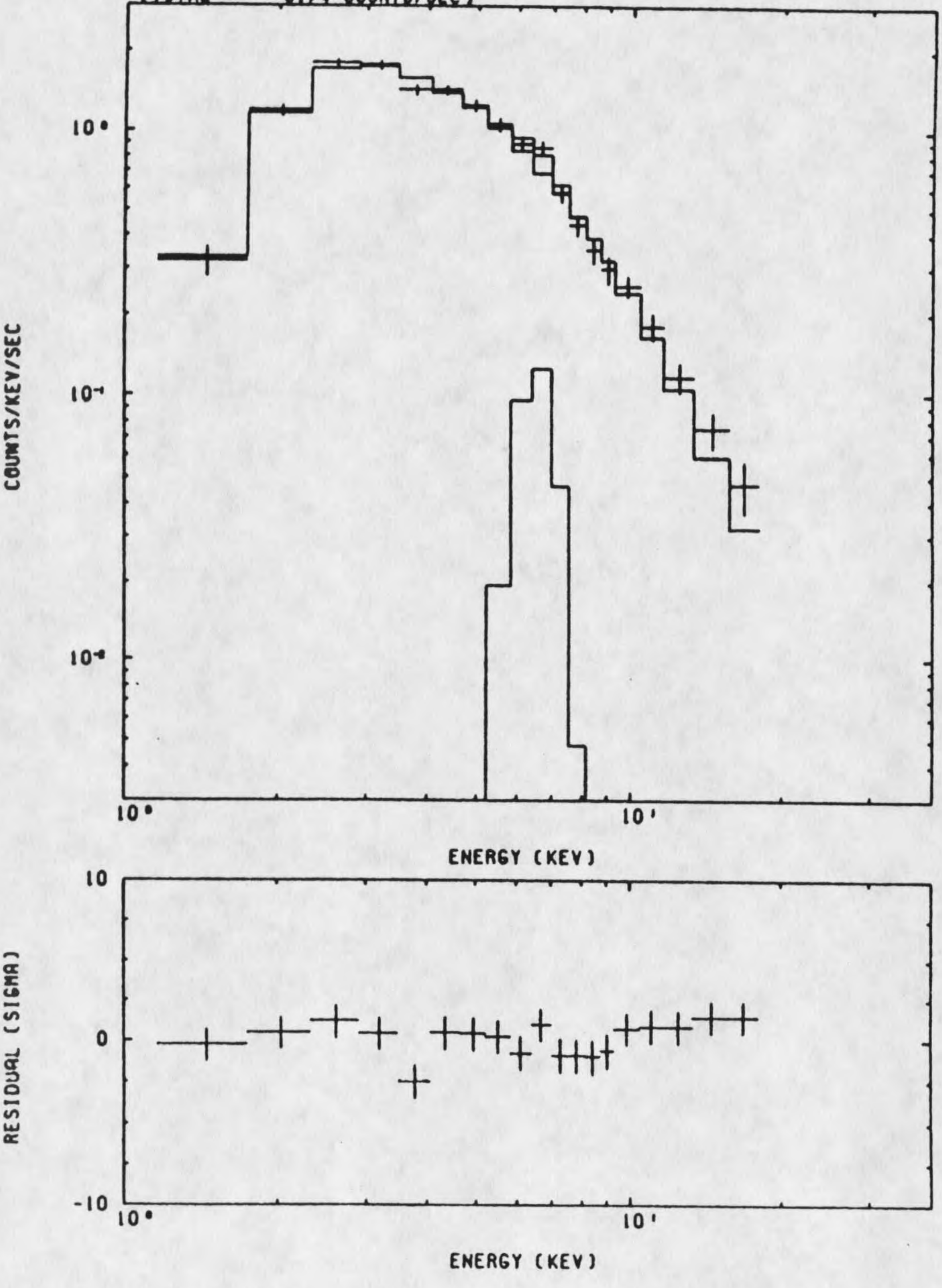

Figure 20. Power law plus line fit to FINAL6T. Included are all data having a transmission coefficient larger than 0.6. Fit residuals are shown at the bottom of the plot, while best fit parameters may be found in Table 8.

ground subtraction method is designed to account for some time dependent spectral changes in the background spectrum, it can not, in general, adequately model the line emission at 3 and 5 keV from the radioactive origin to the internal X-ray background, discussed in Chapter 6. If the background spectrum is examined as a function of time during the observation, it is observed to decrease and soften due to the decay of the radioactive elements in the body of the satellite.

To examine this point further, two background spectra were made. One was selected from data having ascending node of the satellite in the range from 259–307, called the first half background, and the other was selected from data having ascending node in the range from 209–252, called the second half background. These were both subtracted, by the same method as before, from the data with transmission coefficient greater than 0.6. The resulting aspect corrected spectrum which had the first half background subtracted was called FNLP6T, and this spectrum is shown in Figure 21. The corresponding spectrum which had the second half background subtracted was called FNLQ6T, and this spectrum is shown in Figure 22. The 4 keV residual is clearly seen in FNLQ6T, while not evident in FNLP6T. Results of spectral fitting for these two spectra are given in Table 8. It is important to notice that, for the simple power law fits, the spectral indices are *not* consistent with each other, although they are consistent with the simple power law photon index for the data with all the background subtracted (FINAL6T), as expected. These spectra are fit also with power law plus line models; the results are that, for FNLP6T, the line energy was required to be fixed, while for FNLQ6T, the fit would not admit a line. Note that this is probably not because there is really no line emission. Rather, since the amount of data used to find each background spectrum is reduced, the uncertainties in the background spectrum are enhanced, and so the source spectrum uncertainties are also enhanced when

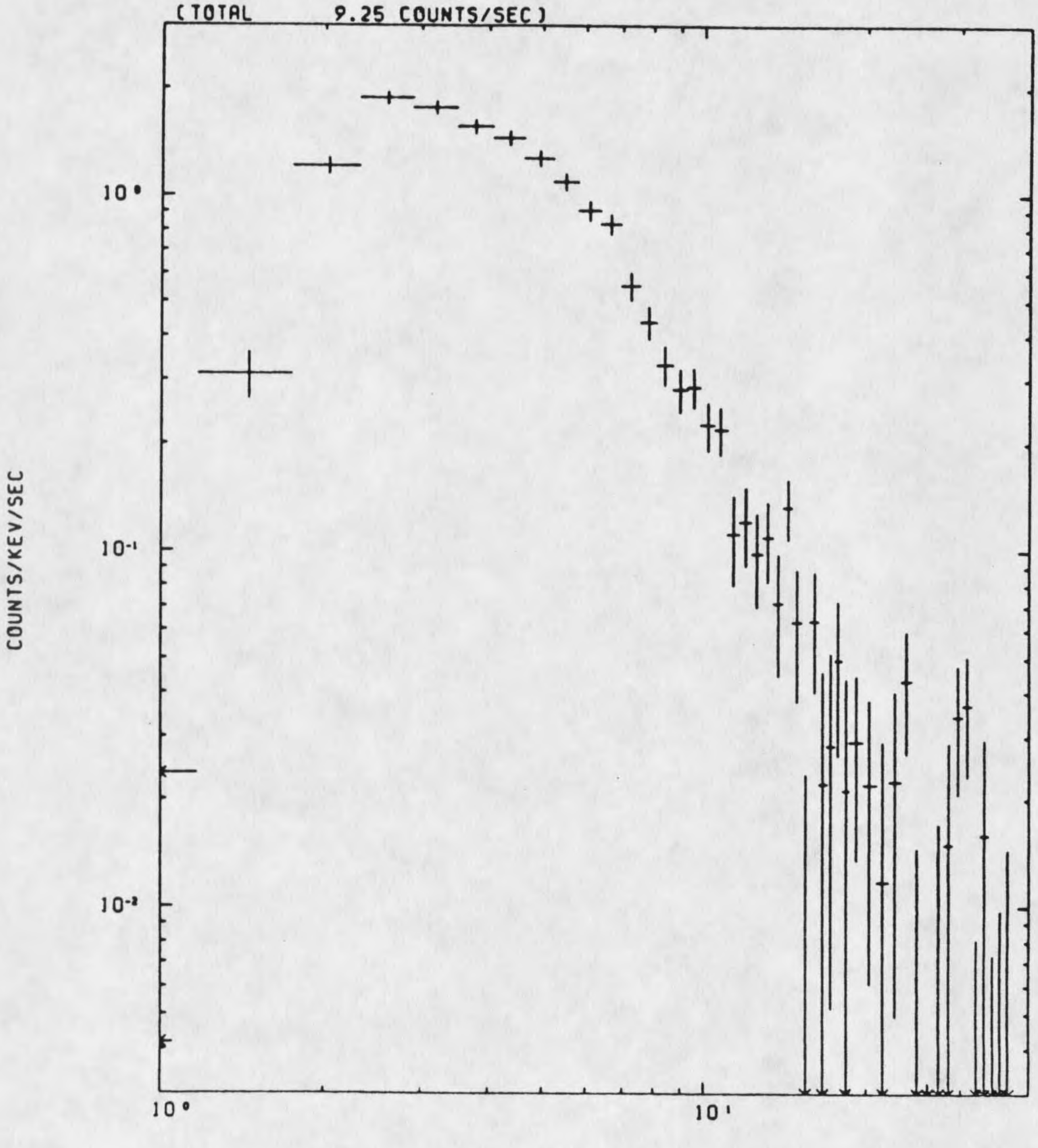

Figure 21. Spectrum FNLP6T. This spectrum consists of data having transmission coefficient larger than 0.6, and having the first half background spectrum subtracted.

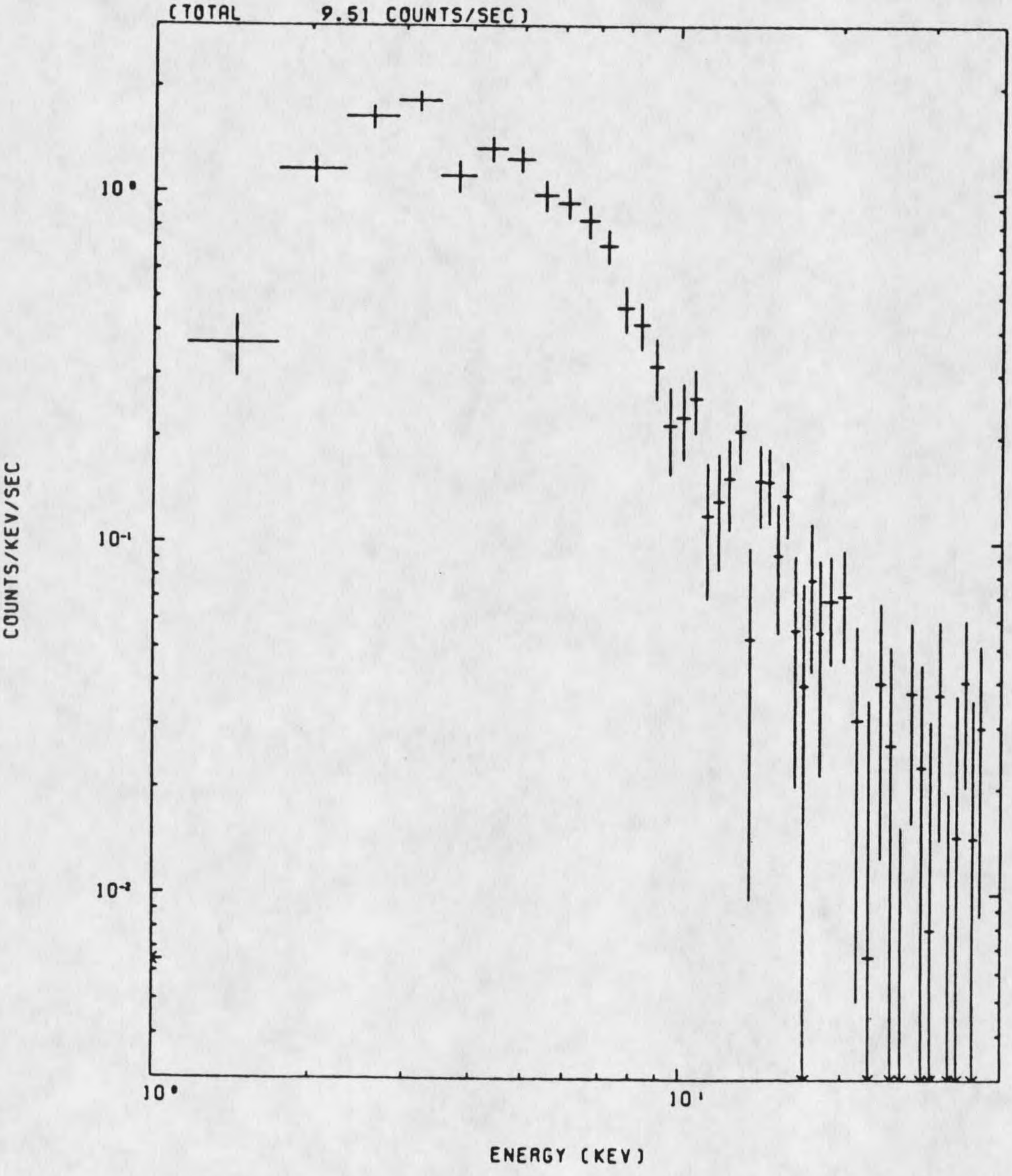

Figure 22. Spectrum FNLQ6T. This spectrum consists of data having transmission coefficient larger than 0.6, and having the second half background spectrum subtracted.

background subtraction takes place. These larger uncertainties lead to a spectrum which requires fewer parameters for an adequate fit. The discrepancy between these spectra shows that the 4 keV residual is due to time dependence of the background spectrum. What is the cause of this difference? The reason is that there is a subtlety in the SSUD background subtraction method for faint sources.

It is known that the internal background varies as a function of ascending node of the satellite, because the ascending node is an indication of how long it has been since the satellite left the SAA. After emergence from the SAA, the internal background decreases due to the decay of radioactive isotopes activated by passage through the SAA. This effect is partially compensated for by using the SSUD sorted background subtraction method, which attempts to model the background as a function of time, as discussed in Chapter 6, because the SSUD scales linearly with the internal background level. This method is generally very successful for modeling the magnitude of the background, but for very faint sources, the shape of the background may not be adequately modeled. One solution to this problem which will be discussed next is to use the same range of ascending node for the background spectrum as for the source spectra.

As can be seen in the Table 6 the ascending node (AN) of the background observation starts at AN $= 307$ and then decreases. However, the source data start at AN $= 320$. Thus there are source data present in the time averaged spectrum which do not have corresponding background data for an appropriate background subtraction. This statement can be quantified by considering the mean SSUD and standard deviation (σ) for the background spectrum used and comparing with the mean SSUD of the source for each day. These numbers are given in the first three lines in Table 9. For the first day, the background is probably fairly accurately modeled. However, the larger $1\,\sigma$ uncertainty in SSUD for the second day means that there are data in the second day which do not have corresponding background data for an appropriate background subtraction.

Table 9. Mean SSUD count rates in source and background data. The uncertainties are 1σ.

Data	SSUD
All Data:	
Background	4727 ± 99
First day	4727 ± 106
Second day	4765 ± 146
Data with $T > 0.6$:	
First day	4763 ± 103
Second day	4822 ± 100
New data selection and $T > 0.6$:	
Background for first day	4745 ± 104
First day	4764 ± 103
Background for second day	4768 ± 102
Second day	4788 ± 98

The situation is worse if only data with transmission coefficients greater than 0.6 are considered. The average SSUD rates for these data are shown in lines 4 and 5 of Table 9. Again the background subtraction for the first day is probably adequate, but the difference in average SSUD for the background and the second day again indicates that some of the source data does not have corresponding background data for appropriate subtraction. Examination of the separate spectra for each day supports this idea; the 4 keV residual is much larger in the second day spectrum.

Therefore, the better background subtraction would be obtained by using only data for which there is background available (i.e., the same range of ascending node), for each day. These data are marked in Table 6. Those background data with a '1' should be used with the first day's background; similarly, those marked with a '2' should be used with the second day's background. The data marked with an (*) are those for which background is available, and the transmission coefficient is larger than 0.6. Comparison of the SSUD levels for these data shows that in this case, the SSUD levels are consistent between the source data and the corresponding background for each day, as listed in the last four lines of Table 9. After subtracting each background spectrum from each day's data, the resulting spectra could be added together for time-averaged spectral fitting. The above selection of background and source data assures that background will be subtracted from data which have approximately the same radiation state. The biggest problem with this method is that since the amount of background data available for the spectrum is reduced, the uncertainty in the background spectrum is enhanced, and consequently, the uncertainty in the source spectra is also enhanced.

Another, probably better way to take care of this problem, which was not available at the time of this analysis, is to use the Nagoya method of background subtraction described in Chapter 6. Recall in this method the internal and diffuse background are subtracted separately. The time dependence of the shape of the background spectrum is taken into account by forming three different internal spectra. This would be a better method because no data need be rejected, provided that the transmission coefficient is larger than 0.6, and also because so much data are available that the uncertainties are small in the background spectrum, so the background subtraction does not add more uncertainty than necessary to the source spectrum. This method was designed for weak sources; it was used successfully in Awaki et al. 1990 and Awaki et al. 1991.

Discussion

During this observation NGC 7469 was at a low flux level. This fact, combined with the problems with the satellite pointing resulting in periods of low transmission, made the flux level for this observation near the source confusion limit for *Ginga*. Also, due to the low flux level, there were problems with the background subtraction. However, despite these problems, some significant results were obtained, and although by themselves they cannot strongly constrain models from this source, comparison with previous results supports some speculation about the nature of the differences.

Low Activity

Noteworthy in this observation is the relatively low flux state of NGC 7469, finding the source to be less active than during other observations. The 2–10 keV observed luminosity was only $1.8 \times 10^{43}\,\mathrm{ergs\,s^{-1}}$. In comparison, when observed by *Ariel V*, the 2–10 keV luminosity was $5.4 \times 10^{43}\,\mathrm{erg\,s^{-1}}$ (Marshall, Warwick and Pounds 1981). When measured by the SSS+MPC on-board *Einstein*, the 2–10 keV luminosity in three observations was found to be $4.0 - 5.3 \times 10^{43}\,\mathrm{erg\,s^{-1}}$ (Turner et al. 1991). The *HEAO1 A2* experiment found the 2–10 keV luminosity to be $6.3 \times 10^{43}\,\mathrm{ergs\,s^{-1}}$ (Mushotzky 1984). Compare this with the average of four EXOSAT observations reported by Barr (1986), in which 2–10 luminosity was found to be $2.8 \times 10^{43}\,\mathrm{ergs\,s^{-1}}$. Turner and Pounds (1989) report another EXOSAT observation having the 2–10 keV luminosity of $6.17 \times 10^{43}\,\mathrm{ergs\,s^{-1}}$ at the nucleus. Also, another earlier Ginga observation indicated a higher degree of activity, having a 2–10 keV luminosity of $4.5 \times 10^{43} \mathrm{erg\,s^{-1}}$ (Piro, Yamauchi and Matsuoka 1990). These figures reveal that the present observation found NGC 7469 the least active that it has been measured, and also it appears that the luminosity is variable over the 16 year period represented.

Flux Variability

Significant variability was found during this observation of NGC 7469. During the first day, significant variability was observed, although it could not be described by a trend. During the second day of observation, a clear decrease was observed with a halving time scale of 25,000 seconds, or $\sim$ 7 hours.

Rapid variability measurements have not been in general available for AGN until recently, due to small detector size. However, some measurements of rapid variability have previously been made from this source. Marshall, Warwick and Pounds (1981) report an Ariel V observation in which a flare was observed, with the flux increasing by a factor of 6 on a time scale of 2 days, and subsequently decreasing on a slightly longer time scale. Barr (1986) observed that the hard X-rays decreased in only one of four EXOSAT observations, while there was no significant change in the soft X-rays (LE instrument). He found the halving time scale was 5–6 hours, comparable to the halving time scale of this *Ginga* observation. Therefore it seems that, although variability on the time scale of hours has been observed on several occasions from this source, it cannot be predicted to vary on such a time scale during any given observation.

Flat Spectral Index

The spectral analysis from this *Ginga* observation, for the combined data with transmission coefficient greater than 0.6, revealed a relatively flat spectral index

(1.53 ± 0.06). It is difficult to analyze the significance of the difference. Comparison is difficult because different observers chose a different number of interesting parameters to evaluate their parameter range (Lampton, Margon and Bower 1976) and this is a problem because of the tight coupling between the index and the column density. In this analysis, the uncertainties are evaluated considering only one interesting parameter; this is a valid method in this case because the absorption column was fixed to the Galactic value during spectral fitting. In many other cases, the uncertainties are evaluated considering two interesting parameters. This takes into account the coupling of the index and column density, and is appropriate when the column density is measured by the fit.

Previous observations found the spectral index to be much steeper. Specifically, Barr (1986) found evidence for day to day variations in the spectral index, but the unweighted average was 1.85 ± 0.14 and all four individual photon indices were significantly larger than that found here. Turner and Pounds (1989) found a steep spectral index of $1.78^{+0.09}_{-0.05}$, again inconsistently steeper than the result found here. Petre et al. (1984) report the analysis of three SSS observations of this source, finding indices of $1.7^{+0.24}_{-0.25}$, 1.98 and 1.93 for data in the energy range 0.5–4.5 keV. Only the first of these observations was consistent with the present analysis. The results for two simultaneous MPC observations in the 2–10 keV range are also quoted, being 2.04 and 1.96. Neither of these values are consistent with the spectral index of the *Ginga* observation under investigation. Mushotzky (1983) gives the results from an *HEAO1 A2* observation, finding the index to be $1.78^{+0.25}_{-0.20}$, which is barely consistent with the result found here. Finally, the SSS+MPC analysis found the three indices from the combined simple power law fit to be also significantly larger than that given here (Turner et al. 1991). A fit from the IPC+MPC found the spectral index to be larger as well (Urry et al.

1989). Finally, another previous *Ginga* observation finds the simple power law index to be 1.83 ± 0.01 (Piro, Yamauchi and Matsuoka 1990).

Since this observation shows both a low luminosity and a flat spectral index, the question arises as to whether there is a flux–index correlation during the history of observations of this source. To test this idea, the unweighted linear correlation coefficient as well as the Spearman rank correlation coefficient were calculated using the average value from the SSS+MPC (Turner et al. 1991), the average of four EXOSAT observations (Barr 1986), the *HEAO1 A2* result (Mushotzky 1983), and the previous *Ginga* result (Piro, Yamauchi and Matsuoka 1990) as well as the current result. No significant correlation was found. This result is probably due to the fact that, besides this observation, all the other observations found the photon index to be in a small range between 1.78 and 1.88, over a wide range in luminosity, from 2.8–6.3 $\mathrm{erg\,s^{-1}}$. Therefore, this photon index resulting from this observation indeed seems to be anomalously flat.

Soft Excess

As mentioned in the spectral analysis section, no evidence for a soft excess component was found from this *Ginga* observation. However, it is difficult to conclusively say that there was no soft excess observed. This is because, as mentioned in Chapter 6, the smallest column density which is measurable by the LAC is $10^{21}\mathrm{cm}^{-2}$. However, the Galactic column density in the line of sight to this source is only $5 \times 10^{20}\mathrm{cm}^{-2}$. Previously the presence of the soft excess component has been inferred, from other instruments, when the spectral fitting finds a column less than the Galactic column (Barr 1986; Turner and Pounds 1989). This course of action is thus not open for *Ginga* observations. However, other observations have found the presence of a soft excess significant from the addition of a separate spectral component, adequately modeled as thermal bremsstrahlung (Turner et al. 1991; Urry et al. 1989). If the temperature of this thermal bremsstrahlung component is sufficiently high, some of the low energy residuals for the simple power law fit for *Ginga* data should be affected, so that they would be inconsistent with the power law fit. Such residuals are observed in the previous observation by *Ginga* reported by Piro, Yamauchi and Matsuoka (1990). From this spectrum a low energy excess is seen from 2–3 keV. However, for the *Ginga* observation under investigation here, the low energy residuals lie completely flat to 1.11 keV, as seen in Figure 20. These comments seem to suggest that, at least temporarily, the soft excess has become unobservable in this source.

Much caution must be used, however, in this deduction. Perhaps the strongest caution is the fact that *Ginga* was not built to measure soft excess components. Another caution is the noted problems in background subtraction for this observation, especially in the low energies. It is fairly clear that the trend in the background subtraction would be to increase the low energy flux. This can be understood by calculating the observed MID to TOP layer ratio in the low energies. This should ideally be the same as the energy dependent ratio of the efficiencies for detection for these two layers. The observed excess of MID counts in the low energies indicates under-subtraction of the background in this energy band, since in the low energies, the detection efficiency of the MID layer is nearly 0. Under-subtraction of background implies too many source counts in the spectrum, which would lead to low energy positive residuals for the power law fit. Therefore, this is another support of the absence of the soft excess; however, it is difficult to estimate this contribution.

Short Term Spectral Variability

Marginal evidence for spectral softening during the first day was found from this observation. This was largely due to an increase of soft flux, while the medium to hard flux remained constant. In contrast, during the significant decrease of total flux found during the second day, no spectral variability was found. Although many of the previous observations could not have measured spectral variability within an observation, at least EXOSAT could have found some. However during the decrease observed by EXOSAT, the softness ratio (LE to ME) did not vary significantly (Barr 1986). On the other hand, evidence for day to day variation in the spectral index was found.

It is hard to identify the cause of the spectral softening. Since the flux level in this observation was so low, it is impossible to perform many of the diagnostic procedures described in Chapter 5. It is impossible to rule out a column density change or warm absorber, since the column could not be measured by the instrument. A change in intrinsic spectral index is possible, but perhaps unlikely, since the ratio of the hard flux to the medium flux did not vary significantly. A change in soft excess emission may be the most likely possibility; however, this hypothesis is impossible to confirm since no soft excess component can be measured by spectral fitting.

Model Speculations

It is very difficult to make any type of model constraints on the basis of this observation alone, since it is of such poor quality. However, some ideas may tie together to form a self-consistent model.

The major evidence includes the following: the flux level is exceptionally low, the spectral index is exceptionally flat, there is some evidence of mild spectral softening, and there is no evidence for a soft excess component previously observed in this source. Therefore perhaps a possible model might be one in which the reason that the spectral index is so small is because the soft excess is temporarily quiescent. Since the soft excess has in some previous observations been found to be evident by a deficit in measured column, the implied slope of the soft excess might be not very steep. In this case, the soft excess can affect the flux level in the region of the spectrum with $E > 2$ keV. If the soft excess is indeed missing from this spectrum, such a loss could explain in part the low luminosity.

Physically, what could be the reason for the loss in soft excess? If the soft excess is due to a thermal optically thin gas emitting bremsstrahlung radiation, if the temperature of such radiation dropped, the soft excess component would move to a lower energy. If it is due to thermal accretion disk radiation, a drop in temperature would also result in decreased X-ray emission. If the power law emission is due to Comptonization of the soft component emission, then a drop in input soft photons, with a fixed population of Comptonizing electrons would result in a flatter spectrum. If the soft component is due to a blend of soft X-ray lines, as found occurring in some cases (Turner et al. 1991), a decrease in such line emission can be due to a decrease in ionizing flux.

This model may be self consistent, but we cannot rule out other possibilities from our feeble flux. For example, a suggestion of a hard tail was observed in this spectrum. If important, it could result in spectral flattening. Therefore, it is easy to see that for definite model constraints to be made, more careful data analysis, particularly with respect to the background subtraction, must be performed. In addition, because of the low flux level, an interesting project would be to compare this observation carefully with another observation. Fortunately, such a plan is now possible. We now have permission to re-analyze the previous

Ginga observation. Our main objection with the previous authors' analysis is that they did not examine the variability of this observation. A quick look at this data indicates that during the three days of observation, the source flux decreased by about 1/3, and during one 5 hour section the flux decreased by 25%. The analysis of this observation will occur during November and December of 1991, hopefully. Other interesting points which we will examine are the significantly steeper photon index, and the hard tail component which were found by the previous authors.

One last remark should be made. Recall that this X-ray observation was made under Tsuruta's simultaneous campaign. Significant variability was found in the X-rays. An interesting question is whether any variability was found in the optical observation. However, the weather was uncooperative for exactly simultaneous observation, and thus the optical observation occurred approximately two weeks later, and has yet not been analyzed.

CHAPTER 8

THE *GINGA* OBSERVATIONS OF NGC 6814

Simultaneous Observations of Seyfert Galaxies Continued

As discussed in Chapter 7, a campaign to observe variable Seyfert 1 galaxies in both the X-ray band and the optical band has been organized by Tsuruta. The X-ray analysis of NGC 7469 was discussed in the last chapter, and the X-ray analysis of NGC 6814 will be discussed in this chapter.

Two observations of NGC 6814 were available for analysis. The first observation was performed on April 16–17, 1990 as part of Tsuruta's simultaneous campaign. NGC 6814 was observed again on October 5–7, 1990, during the consortium phase of observation.

Results from Previous Observations

NGC 6814 is a low luminosity ($10^{41-43}\,\mathrm{erg\,s^{-1}}$) Seyfert 1 galaxy. Seyfert (1943) mentions it having nebular type emission lines superimposed on a generally stellar continuum. It was observed by *Ariel V* but short term (0.5–5 day) variability was not found (Marshall, Warwick and Pounds 1981). Rapid variability was found in observation by the *HEAO1 A2* experiment (Tennant et al. 1981). NGC 6814 was found, of a sample of 54 observations from 38 AGN, to be the only one to have significant rapid variability (Tennant and Mushotzky 1981). This source was found to exhibit significant variability during all orbit periods of the observation. Flux variations of a factor of 2.5 in 90 minutes were observed. There was also evidence for significant variations on the order of 100 seconds. However, throughout these large flux variations, no evidence for spectral variability was found. Marginal evidence for lags was found, and the sense of the lag was that the hard flux lagged the soft. However, the lag time was very small, ~ 6 seconds.

This source was subsequently observed five times by the ME and also the LE experiments on-board EXOSAT. Four of the observations were relatively short, being only $\sim 20,000$ seconds, but the last observation was longer, about 1 day. This set of observations yielded some very interesting and unique results, reported by Mittaz and Branduardi-Raymont (1989). They found that the low energy spectrum, as observed with the LE, varied significantly from observation to observation, decreasing by more than an order of magnitude in nine months. However, variability within an observation was not detected. The ME flux (2–10 keV) varied in all observations. There was no correlation between the ME and the LE light curves. There was some evidence for spectral variability, as the ME hardness ratio ($4 - 6\,\mathrm{keV}/2 - 4\,\mathrm{keV}$) varied significantly; however, the hardness ratio was not correlated with the ME flux. Between separate observations, there was evidence for change in absorption column, with one observation showing a large increase in column.

The most interesting result of the EXOSAT analysis, however, came from the power spectral analysis of the long (1 day) observation. Evidence was found for periodic flares, separated by 12,000 seconds. There was also weak evidence for a 3000 second quasi-periodic oscillation in one of the other observations. Note that this observation provided the first clear and convincing evidence of a characteristic time scale found in AGN, and to date, this is the only AGN known to exhibit a characteristic time scale.

The first *Ginga* observation of this source revealed more surprising results. The first report on this observation was by Kunieda et al. (1990). They verified the rapid variability, finding a two-folding time scale of ~ 50 seconds. The magnitude of the overall variability was large, being a factor of five during the observation. They also found that the absorption column observed was larger than that found in four of five of the EXOSAT observations, although the spectral index and flux were essentially the same. However, the most interesting result of this analysis was that the iron line flux varied essentially in phase with the continuum flux. Cross correlation analysis revealed that the lag was less than 256 seconds. The line equivalent width was large, about 300 eV, and nearly constant. There was no evidence for broadening of the line. The fact that the line flux varied in phase with the continuum flux is especially important because it is the first clear evidence that the line is being produced in the central region. Note that the spectral index was consistent with a constant.

Subsequently, the *Ginga* observation was analyzed for the detailed time variability. An early report of this work is given in Done et al. 1990a. She was able to verify the 12,000 second periodicity discovered first in the EXOSAT observation. The nature of the variability was different, though, being smoother with continuous variability; the EXOSAT variability consisted of flares superimposed on a noisy, approximately DC, signal. The cross correlation function was also used in this analysis, and no clear lag was found, although the CCF was asymmetric, in the sense that the hard flux lagged. Even during the 50 second decrease, no lag was observed.

Given the previous fast variability that has been consistently observed from this source, an interesting X-ray observation seemed guaranteed, whether the simultaneous observation was successful or not. Also, because of the apparent difference in the type of variability exhibited on two occasions (the EXOSAT long observation and the *Ginga* observation), it also seemed likely that another *Ginga* observation would not necessarily give identical results to the previous one. Therefore, this source was observed again twice. This chapter discusses the X-ray data analysis of this source, and presents some simple model calculations which successfully describe several aspects of the observations. Finally, implied model constraints are discussed.

Results

The *Ginga* observations

The data from two *Ginga* observations were available for analysis. The first observation was performed April 15–17, 1990, as part of Tsuruta's simultaneous observation campaign. The second observation was performed October 5–7, 1990, as part of the consortium observation phase.

For the April data, there were no adjacent background data available. Therefore, two methods of background subtraction were used. For the spectral analysis, the background was subtracted using the Nagoya method, as described in Chapter 6 (see also Awaki 1991). Gain changes had been experienced by the detectors on the LAC, so it was necessary to adjust the relative gain by hand. The change in gain was determined by fitting the 22.1 keV silver line to a Gaussian function, and finding the measured line energy relative to 22.1 keV. This was done for each detector separately, since the gain change of each detector was different, and the resulting spectra were scaled appropriately. Also for the spectra on the first day, since the transmission was low, the aspect correction had to be put in by hand.

For the time series of the April data, the Nagoya method of background subtraction could not be used, so the SSUD sorted background subtraction method was used, as described in Chapter 6, using background obtained approximately 37 days earlier, on March 9, 1990.

For the October data, there was an adjacent background observation available, so the background subtraction used for both timing and spectral analysis was the SSUD sorted method. The gain of the detectors again had to be adjusted by hand, as in the April observation. Here only 6 of the 8 original detectors were available, detectors 4 and 5 having failed.

There were no obvious problems in the background subtraction for either observation.

Figure 23 shows the total flux light curve (1.11–20.9 keV) for the April observation. Two days of data were available, separated by $\sim 60,000$ seconds. On the first day, only the data from the first orbit had transmission coefficient greater than 0.5, so the remainder of the first day data is not included in the time series analysis and spectral analysis. This fact is illustrated by the large error bars on the four other groups of data for the first day. The second day had good transmission, greater than 90%. The peak flux was about 35 counts per second, while the lowest flux was nearly 0 counts per second.

An interesting component in the light curve are three obvious dips in flux. These dips have similar structure; in all three the flux drops nearly to zero. Appendix 1 contains supplementary light curves for this chapter, including Figure 81 showing the dip from the first day, Figure 82 showing the first dip from the second day, and Figure 83 showing the second dip from the second day. The bin size shown is the intrinsic bin size, 16 seconds. Recall that previous observations of this source have found a periodic component to the variability for this source, with period 12000 seconds. These dips seem to indicate some periodicity. In fact, the second and third dips are separated by almost exactly 12000 seconds. The first

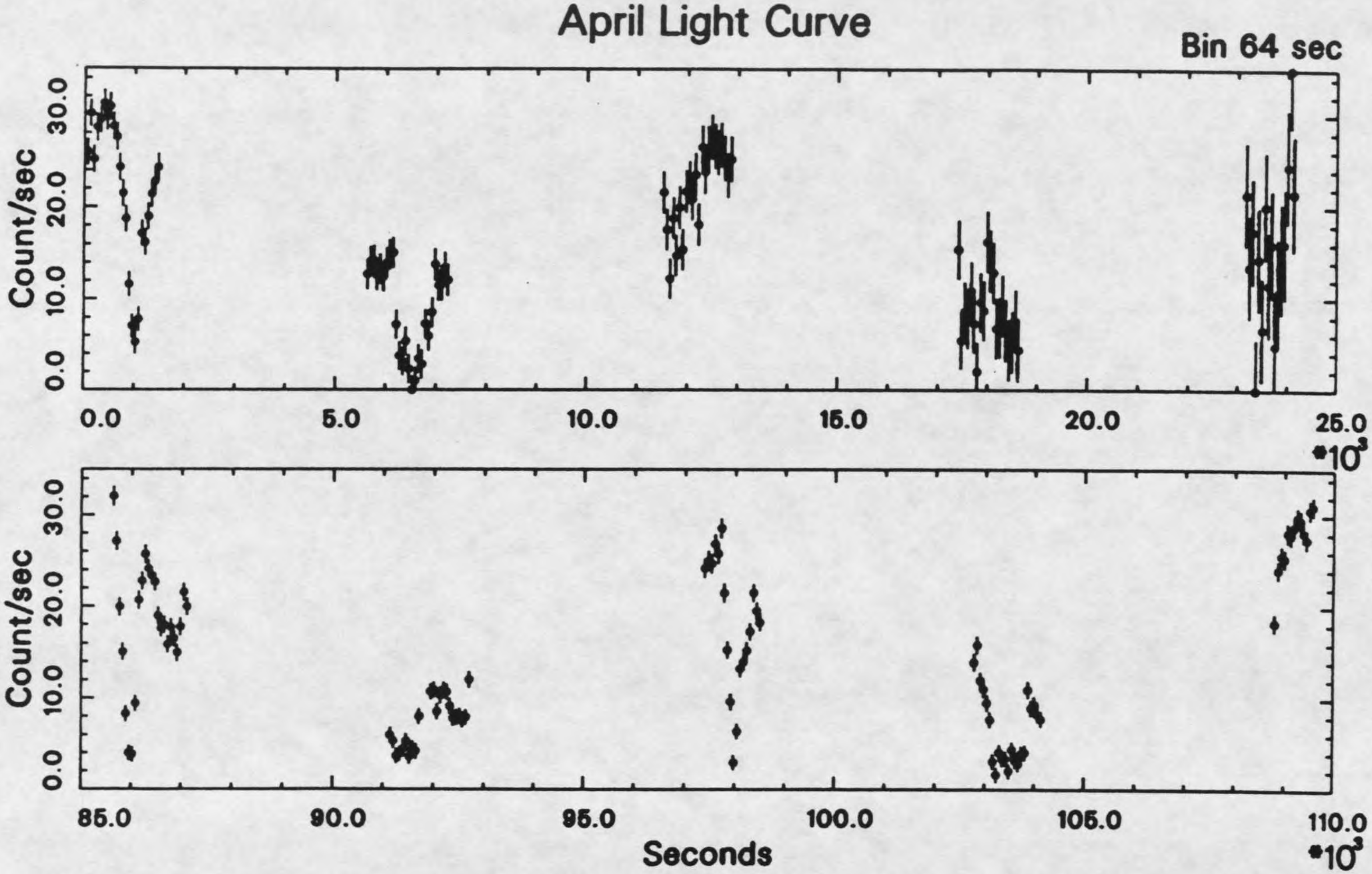

Figure 23. April total light curve. Bin size is 64 seconds.

and second are separated by $\sim$ 85000 seconds, a bit more than $7 \times 12000 = 84000$ seconds.

Figure 24 shows the total flux light curve for the October observation. Here only 30,000 seconds of data were available, with good transmission of greater than 98%. However, even though the observation was shorter, the coverage is better; i.e., the data gaps are shorter. Also, the source flux was larger; the peak flux was nearly 45 counts/second, and considering that two detectors of eight were not operating, the peak flux was nearly doubled when compared with the peak flux of the April observation. The minimum flux was larger too; the total flux dipped to no lower than 7 counts/sec. No periodic dips are observed; indeed, periodicity is not obvious. However, this figure is plotted on axes of length 12000 seconds, and if the first data groups of the the middle and bottom parts of the figure are combined, it can be imagined that they respectively show the increase in flux after a dip, and the decrease in flux before the dip, separated by 12000 seconds.

Looking at the light curves in different energy bands, as well as flux ratios, is an easy way to look for spectral variability. Figures 84, 85 and 86 in Appendix 1 show the light curves for the April observation in several different energy bands. Shown are the light curves in 1.11–3.36 keV, 3.36–5.69 keV, 5.69–8.00 keV, and 8.00–20.9 keV energy bands. Many of the data from the first day are omitted, due to the low transmission coefficient. Figures 25 and 26 show the April light curves in 1.11–5.69 keV and 5.69–20.9 keV energy bands and the hardness ratio. All of the data are included here, and the effect of the low transmission at the end of the first day is illustrated by the very large error bars in the hardness ratio. However, regions can clearly be seen in which the hardness is varying, indicating spectral variability. Especially during the dips of the second day, the hardness can be seen to increase as the flux decreases.

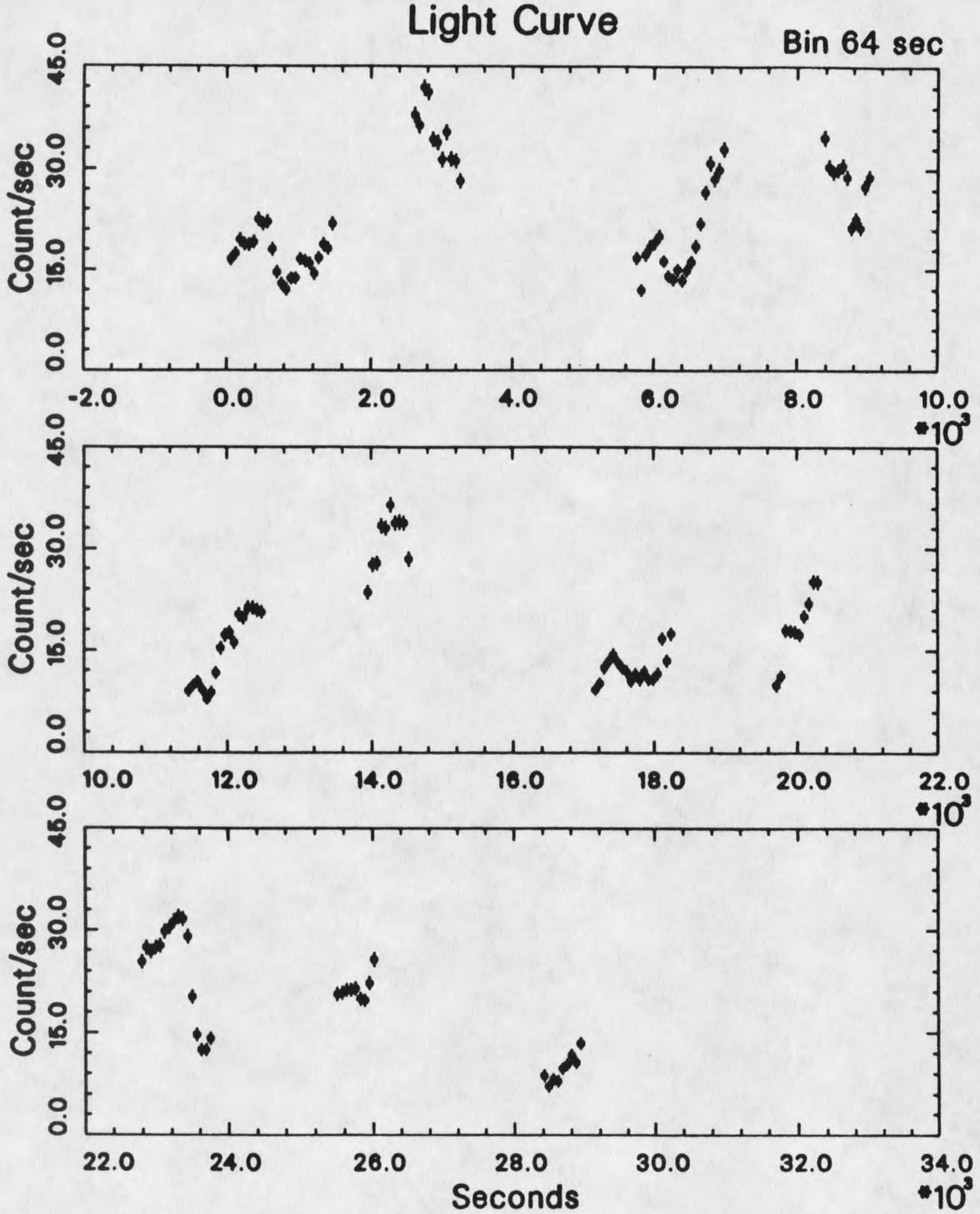

Figure 24. October total light curve.

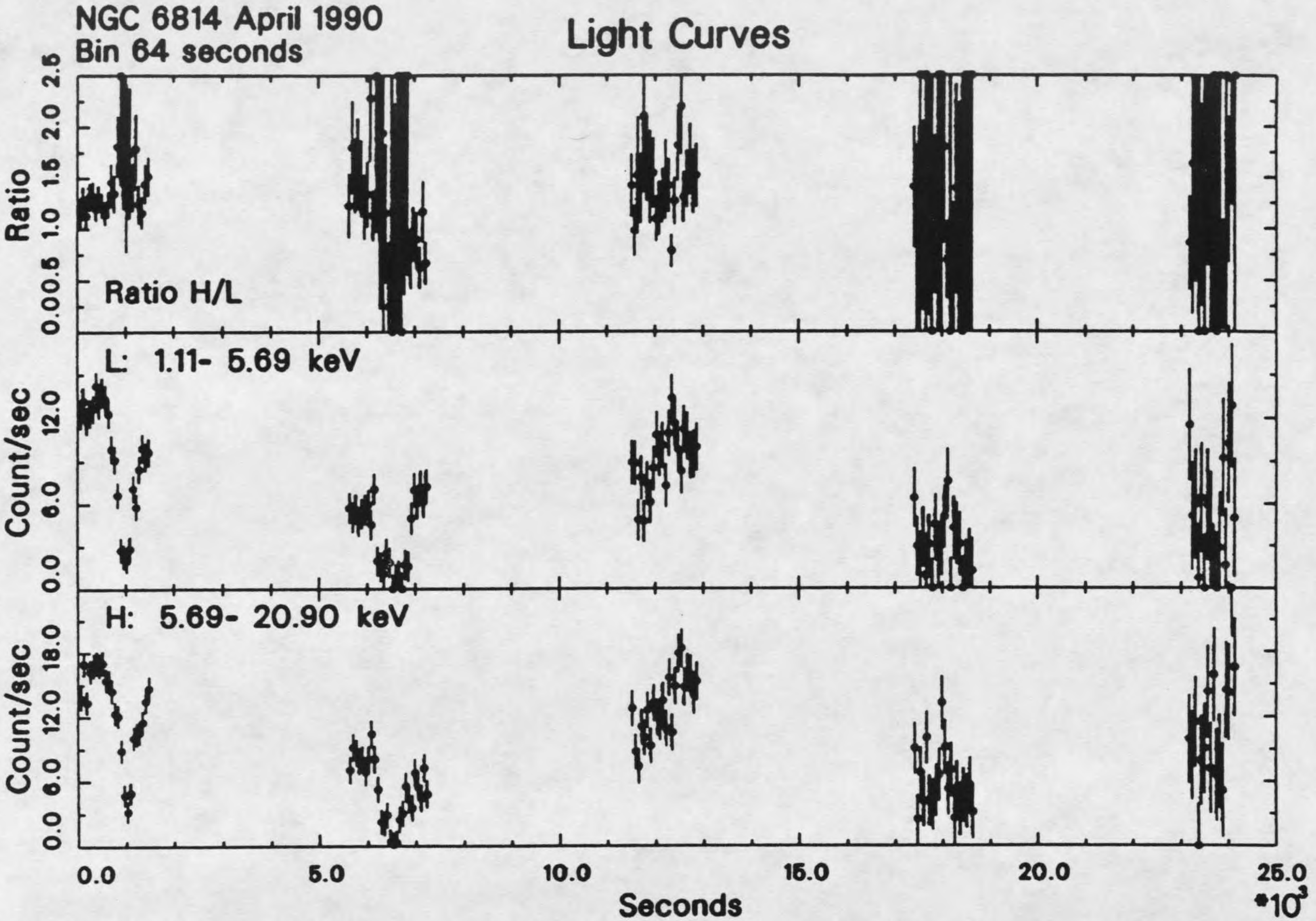

Figure 25. Light curve and hardness ratio for first day of observation for April data. The bin size is 64 seconds.

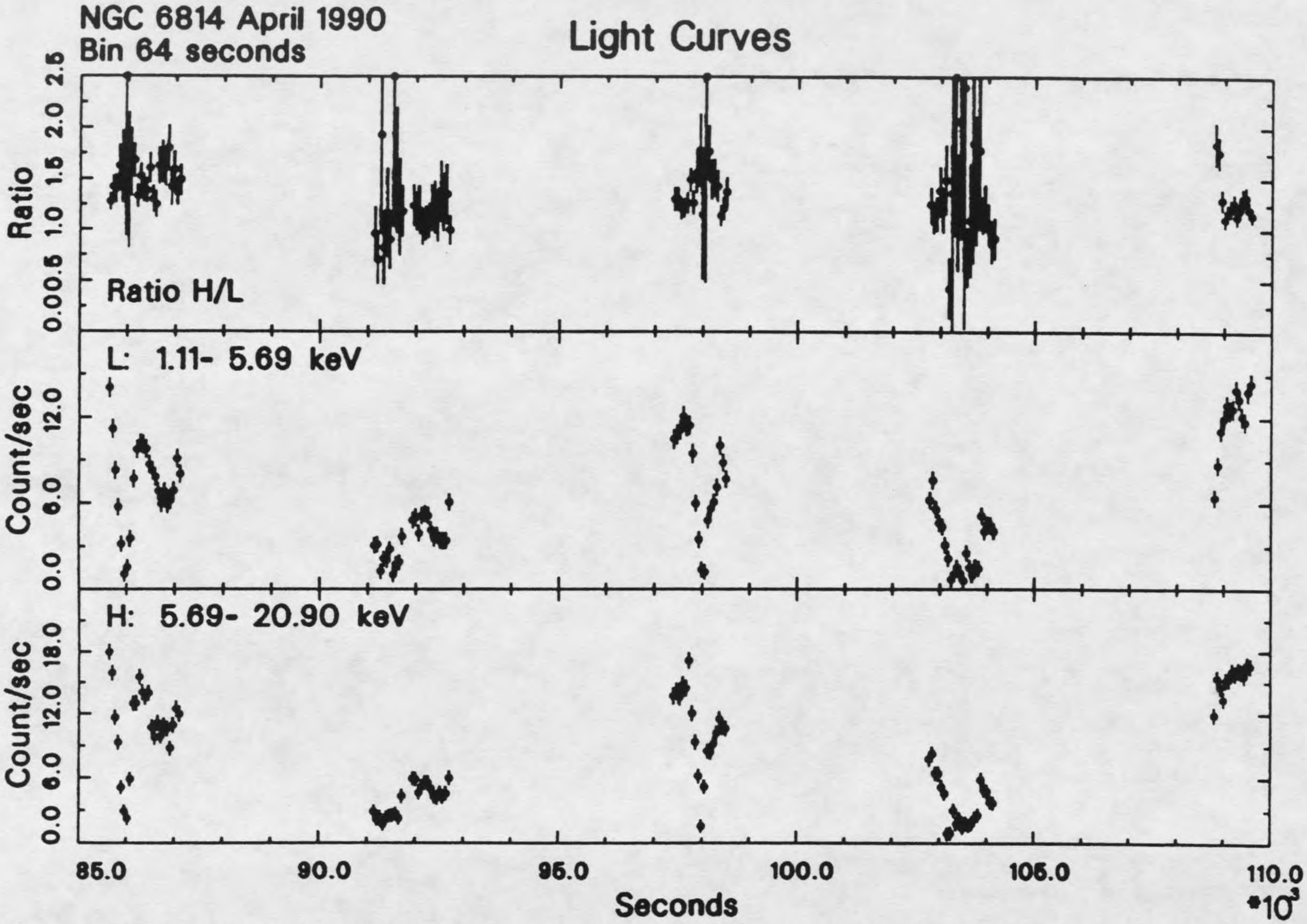

Figure 26. Light curve and hardness ratio for second day of observation for April data. The bin size is 64 seconds.

Figures 87 and 88 of Appendix 1 show the October light curves in four different energy bands, as for the April data. Figure 27 shows the flux ratio; however, this plot shows the softness ratio L/H with the low energy band being 1.11–5.69 keV and the high energy band being 5.69–20.9 keV. Examination of the softness ratio shows clear significant spectral variability during the entire observation.

Periodicity

As discussed earlier in this chapter, one unique property of this source seems to be the presence of a periodic component in the variability (Mittaz and Branduardi-Raymont 1989; Done et al. 1990a). The periodic dips separated by multiples of approximately 12000 seconds seem to support the idea that a periodic component is also present in these data. Therefore, the April and October data were examined for the presence of a periodic component. As discussed in Chapter 6, the gaps in the data make detection of periodic signals difficults. Therefore, the analysis proceeded using the methods outlined in Chapter 6. The correlation was calculated using the method of Edelson and Krolik (1988), and the power series was calculated using the method of Press and Teukolsky (1988); and significant variation for specific cases are explained below. The programs were implemented by Chris Done, and modified as necessary.

First, the time series analysis of the April data was performed. The data used were that from the first and second day, with a transmission coefficient greater than 0.5. The data from periods with a lower transmission coefficient were not used because of two reasons: (1) The large error bars from data with lower transmission coefficient causes decorrelation and an increase in noise, and washes out the variability of the other data because of the increase in the average measurement error, e^2, and (2) this data cannot be used for spectral fitting because of the

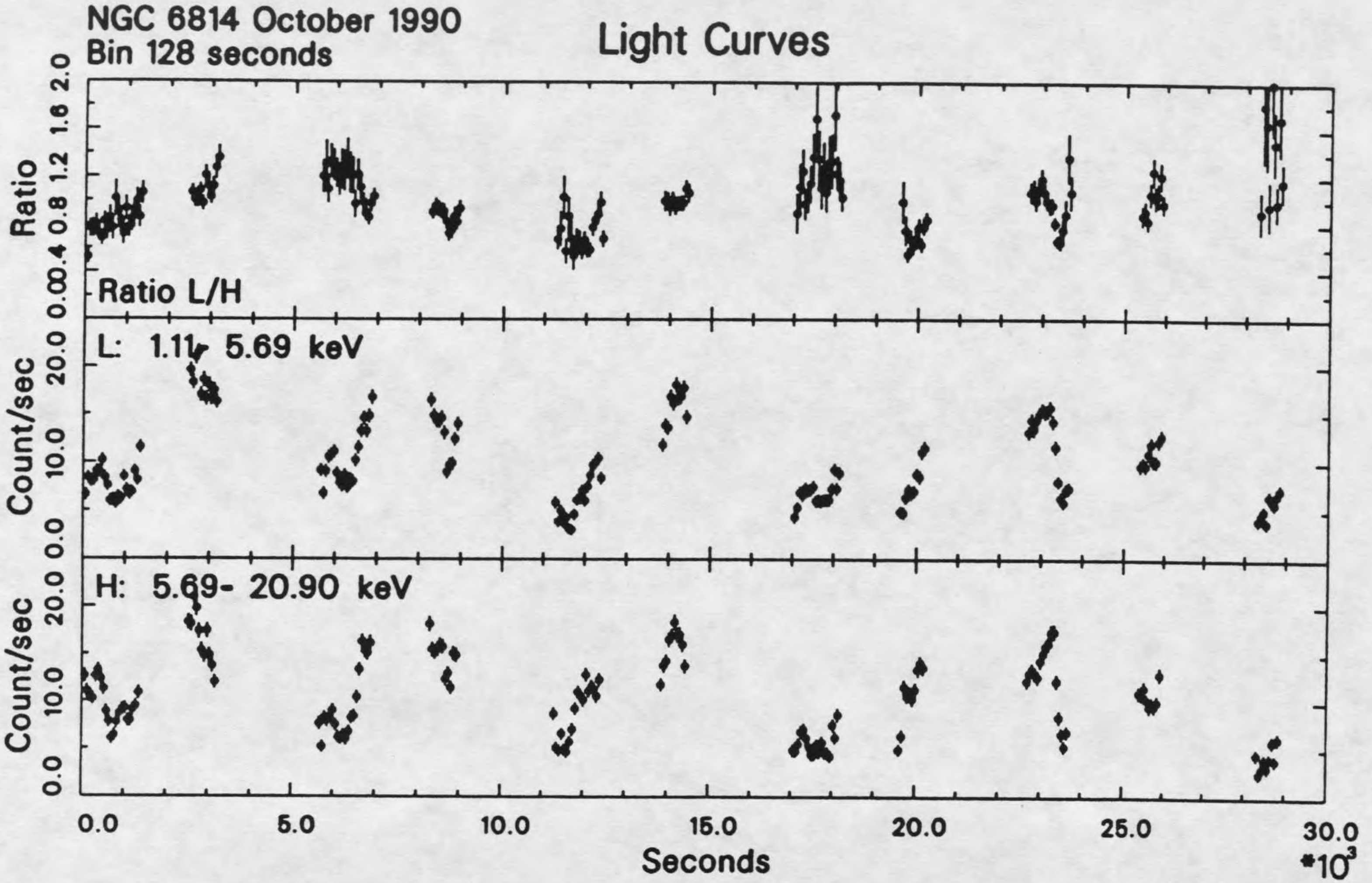

Figure 27. Light curve and softness ratio for October data. The bin size is 64 seconds.

uncertain correction for reflection of soft X-rays from the collimator surface, as discussed in Chapter 6. The autocorrelation function of the data from 1.11–20.9 keV having transmission coefficient greater than 0.5 is shown in the top panel of Figure 28. Much structure is immediately apparent. There are several lags which have zero autocorrelation, because of the sparse sampling of the data.

Because of the many structures apparent, the significance of such structures must be evaluated. In order to evaluate the significance of the structures observed, two methods are available. First, simulated data having the same mean, variance and sampling, but with a power spectrum proportional to $1/f$ were made and the autocorrelation function was calculated. This method is recommended by Edelson and Krolik (1988). This result is shown in the lower panel of Figure 28. Comparison of these two indicate an anticorrelation at $\sim$ 6000 seconds and a peak at 12050 seconds that are not mirrored in the autocorrelation of the simulated data. These are the most significant structures. There is also an anticorrelation at $\sim$ 18000 seconds, but there is confusion here with the edge of the 0 autocorrelation region.

Another, more intuitive, way to evaluate the significance of peaks in the autocorrelation of the real and simulated data is to look at how many UDCFs (see Equation 6.6) are contributing to the discrete ACF sum at each lag. This is shown in Figure 29. It is easy to see that at the lags near the middle of each group the autocorrelation is probably reliable, because so many points (more than 1000) are contributing to the correlation sum. Near the edges of the groups, the number contributing is smaller, so there is probably less significance in these ACF points Careful evaluation of the significance of the peaks is necessary, both because of the data windowing and also because the errors in the ACF are underestimated. The

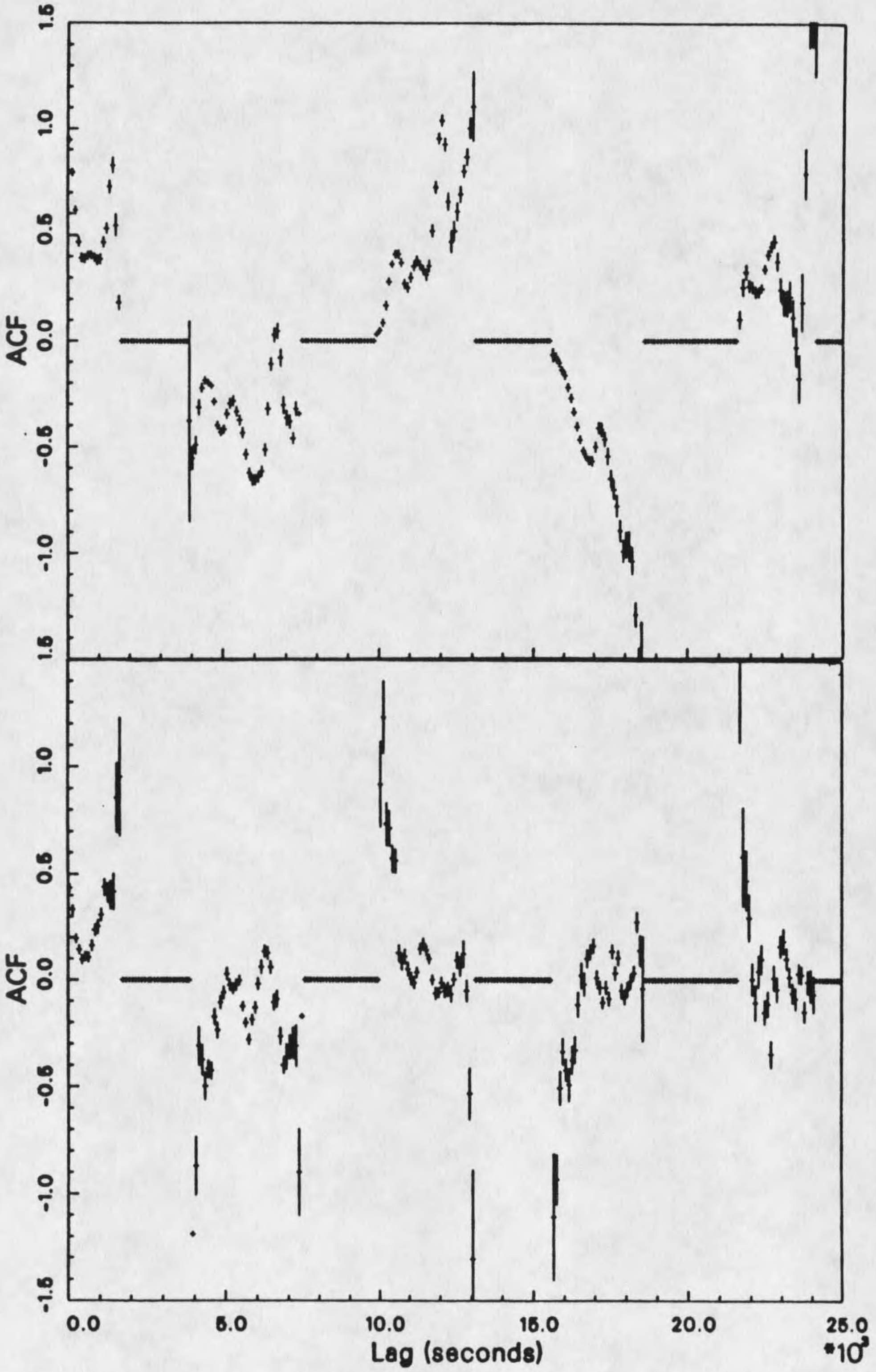

Figure 28. Autocorrelation of April data, in the energy band 1.11–20.9 keV. In the top panel the ACF of the measured data with transmission coefficient greater than 0.5, while in the lower panel the ACF of the $1/f$ simulated data is shown.

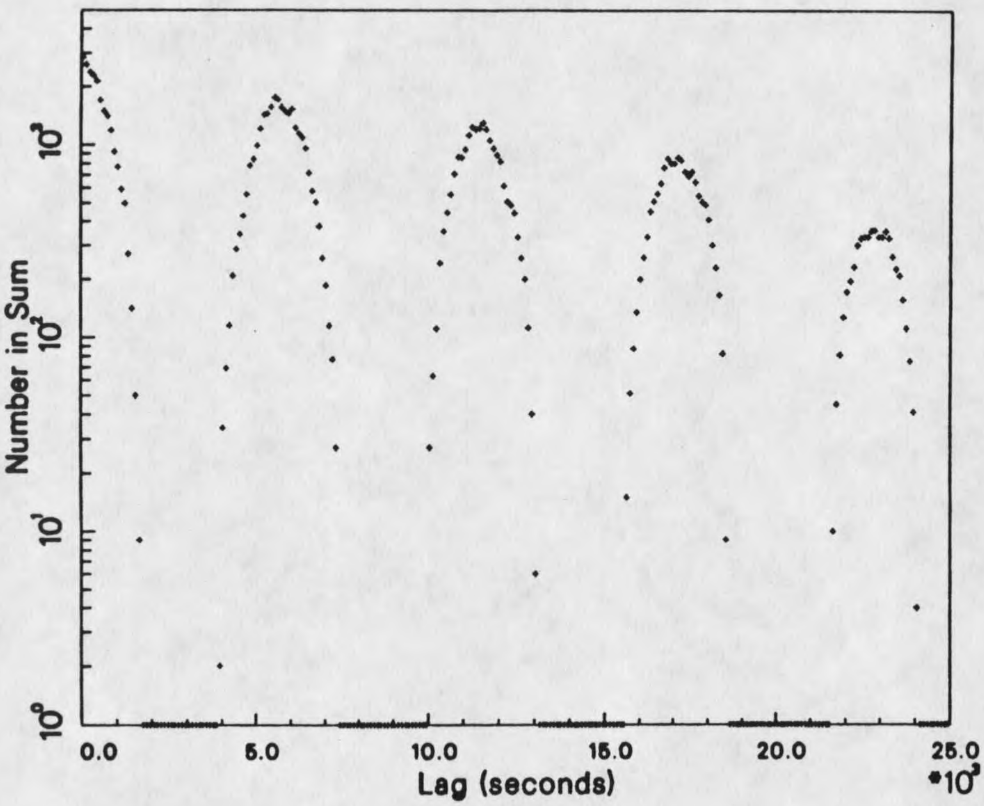

Figure 29. Number of UDCFs contributing to the correlation sum, for the April data.

errors are calculated by assuming that the data are uncorrelated. Since the variability data from this Seyfert are clearly correlated, error underestimation results (see Equation 6.8, and also Edelson and Krolik 1988).

Further confirmation of the 12000 second period can be gained by examining the periodogram, calculated according to Equation 6.10 (Press and Teukolsky 1988). In the top panel of Figure 30 the periodogram for the April data having transmission coefficient greater than 0.5 is shown. The corresponding periodogram of the simulated data is shown in the lower panel of Figure 30. In the real data periodogram, there is a peak at around 8.3×10^{-5}Hz corresponding to a period of ~ 12050 seconds. There is no corresponding peak in the simulated data. The peak

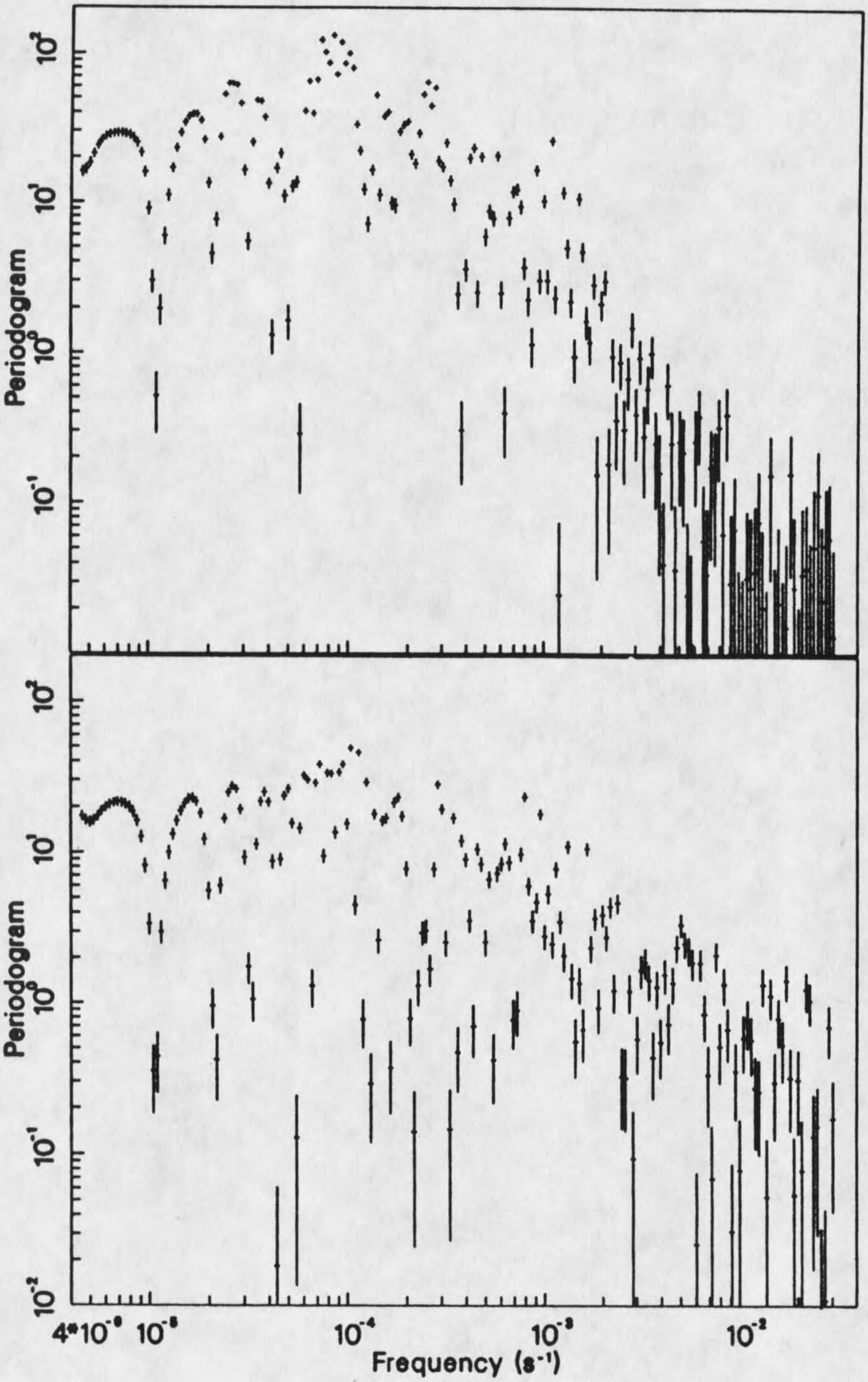

Figure 30. Periodograms for the April data, in the energy band 1.11–20.9 keV. In the top panel the ACF of the measured data with transmission coefficient greater than 0.5, while in the lower panel the ACF of the $1/f$ simulated data is shown.

in the real data is not sharp, but has some spread. This may be due to the fact that the amount of time between dips is not exactly a multiple of 12000 seconds, but is 85000 seconds between the first and the second dip, and 12000 seconds between the second and the third. For perfect 12000 second periodicity, the gap between the first and the second should have been 84000 seconds. The peaks to the left of the 12000 second peak in the periodogram are probably spurious, because they correspond to wavelengths longer than the length of the second day part of the observation, and thus represents the interaction in the algorithm of the small section of data from the beginning of the first day with the second day data. Again, errors here are probably underestimated, since they result from propagation of the measurement errors through the algorithm.

Next the similar time series analysis of the data from the October observation was performed. First the total light curve from 1.11–20.9 keV was considered. The top panel of Figure 31 presents the autocorrelation function of these data, while the lower panel shows the corresponding autocorrelation of the $1/f$ simulated data, having the same mean, variance and sampling as the real data. There are several noticeable structures in the autocorrelation of the real data which do not occur in the simulated data. The most noticeable is a sharp spike at $\sim$ 4300 seconds, which has an autocorrelation of greater than 1.0. Although there is no corresponding peak in the autocorrelation of the simulated data, this peak is spurious. This fact can be understood by examining the plot of the number of UDFC's contributing to the discrete correlation function sum, shown in Figure 32. The spike at 4300 seconds falls in a region where relatively few data contribute to the sum; therefore the large correlation is most likely accidental. The next most noticeable peaks are a minimum at $\sim$ 3400 seconds, a maximum at $\sim$ 6400 seconds, and several maxima at $\sim$ 12000 seconds. The degree of correlation in each of these is not

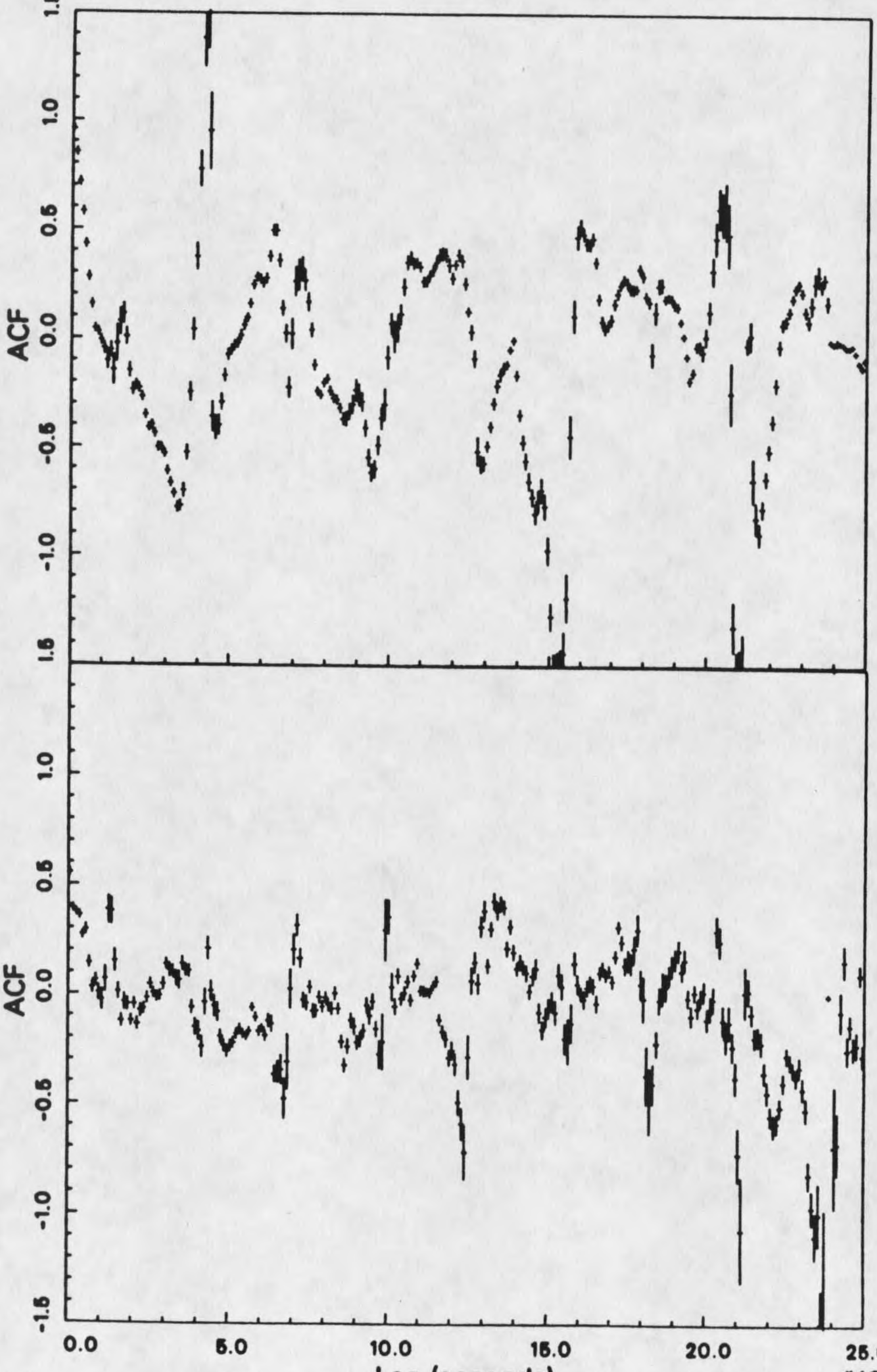

Figure 31. Autocorrelation of October data, in the energy band 1.11–20.9 keV. In the top panel is the ACF of the measured data while in the lower panel is the ACF for the $1/f$ simulated data.

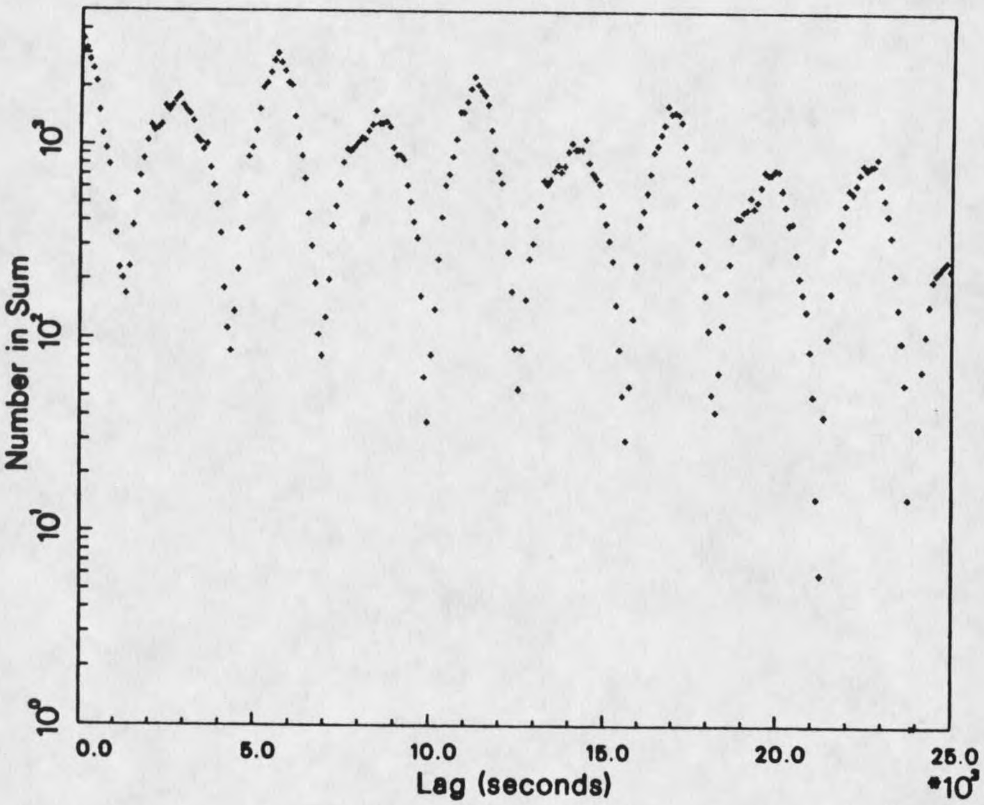

Figure 32. Number of UDCFs contributing to the correlation sum, for the October data.

particularly strong. Also the peaks are affected by the number contributing to the correlation sum. The periodicity of the data is more clearly revealed by the periodogram, given in the top panel of Figure 33. Here there is a clear peak at a frequency corresponding to a period of between $\sim$ 5500 and $\sim$ 6000 seconds. No such strong peak is evident in the periodogram of the simulated data, shown in the lower panel of Figure 33. It is remarkable there is no peak at $\sim$ 12000 seconds corresponding to a frequency of 8.3×10^{-5} Hz. This may be an effect of the relatively short length of the observation, being only 30000 seconds. There is a smaller peak at about $10^{-4}\mathrm{s}^{-1}$, but there is a corresponding peak of slightly

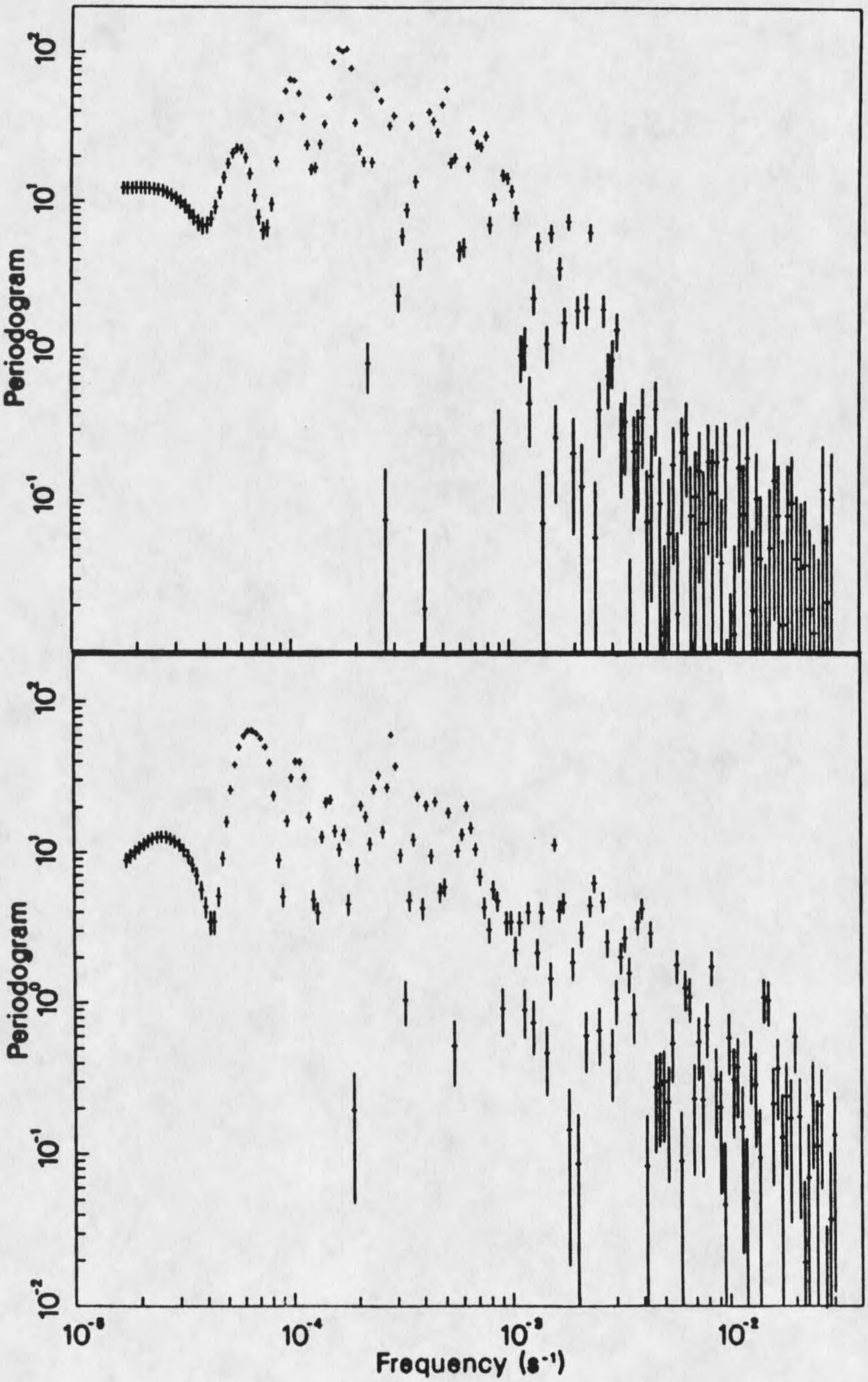

Figure 33. Periodograms for October data, in the energy band 1.11–20.9 keV. In the top panel is the periodogram of the measured data while in the lower panel is the periodogram for the $1/f$ simulated data.

smaller amplitude in the simulated data, indicating that this is probably not a periodicity of the data, but an effect of the sampling.

The periodicity observed in the total light curves of the April and October data is not new. As explained in the previous section, a previous observation of NGC 6814 by *Ginga* revealed the periodic component with a clear 12000 second period (Done et al. 1990a), and the EXOSAT observation also found periodic flares of the same period. The major difference is that the 12000 second periodicity is not so apparent in the October data; the data seem rather to indicate a 6000 second period.

However, it is possible from these data to investigate periodicity of the hardness ratio. Examination of Figures 25, 26, and 27 show that the flux ratios vary during both observations. Although flux ratio variability has been observed previously from this source (Mittaz and Branduardi-Raymont 1989), it has not been confirmed to be periodic. Beyond this, periodic changes in hardness ratio have never been observed before from AGN, and if verified, would lead to important model constraints.

In order to investigate the periodicity of the hardness ratio, one important modification of the basic technique for producing the simulated data was necessary. In the basic technique, the uncertainty of the simulated light curve data is estimated to be a linear function of the source flux count rate. The slope and intercept in this relation are of course found by fitting the uncertainty versus the flux of the real data to a straight line. This approximation is very good in the case that the data were taken during periods of uniform transmission. Clearly as the transmission coefficient increases the magnitude of the uncertainty increases with no accompanying increase in flux, destroying the linear relationship. In the case of the April data, the uncertainties of the first and second days of observation, characterized by different transmission coefficients, were generated separately. A problem occurs also if the data are some function of the count rate, like the hardness ratio; the uncertainties are again not a linear function of flux.

If the data are the hardness ratio, the linear relation is not a good fit. It turns out that much of the reason for the poor fit is that the values of the slope and intercept from the line fit are heavily skewed by outlying points. This results in the simulated data having a larger average measurement error than the real data. This fact is particularly important when the autocorrelation function of the simulated data is calculated (Equations 6.6–6.8; see also Edelson and Krolik 1988), because the discrete correlation function is normalized to take into account the measurement error by dividing by $\sigma^2 - e^2$, instead of just σ^2, where σ^2 is the variance of the data, and e^2 is the average measurement error, as shown in Equation 6.6. Therefore, if the average measurement error is overestimated due to the presence of outliers, the autocorrelation function of the simulated data will be spuriously large, and peaks in the autocorrelation function of the real data will be erroneously considered to be insignificant.

The remedy for the autocorrelation function is easy. The autocorrelation function program was modified so that two files are input, one being the simulated data file, suitably renormalized so that it has the same mean and variance as the real data. The other input file is the real data, from which the average measurement error is calculated. This method completely bypasses the estimation of the simulated uncertainty.

For the periodogram, this problem is not as serious, but neither is the solution so straight-forward. The problem is not as serious because the periodogram is calculated, in essence, by fitting the data to sinusoids, and the measurement errors are not used directly for calculation of the power (Press and Teukolsky 1988; see also Equation 6.10). However, the measurement errors are necessary to calculate the uncertainties in the periodogram values, which are found by propagating the errors through the algorithm. So for this, the linear relation $dy = ay + b$ is used, with caution. The adequacy of the approximation is evaluated using the ratio R where $R = \sigma^2/e^2$. This ratio must have a value greater than 1, or the data does not vary significantly. To use this to evaluate the linear approximation, R was calculated for the real data and for the simulated data and compared. A symptom of outlier influence is a very large R_{sim} compared with R_{real}. In this case it is useful to plot the errors in the real data versus the data, and remove outliers by hand. Because the periodogram is plotted on a log-log scale, a perfect match is not necessary, as the difference in length of the error bars will be small. Performing these modifications to the basic technique made accurate time series analysis for the hardness ratio possible.

For the April data the periodicity in the hardness ratio is apparent because of increase in hardness during each dip seen in Figures 25 and 26. However, it was impossible to use the autocorrelation function or the periodogram to check for periodicity in the hardness ratio. This was because the lower flux level throughout the observation, and particularly during the dips, leads to larger error bars in the ratio, and these make the error bars in the autocorrelation function and the periodogram as large as the calculated values.

However, the situation is somewhat different in the October data. Here the softness ratio changes dramatically throughout the observation, not only at the sudden changes in flux (see Figure 27). Therefore it is possible to analyze the periodicity of the hardness ratio in this data using the autocorrelation function and the periodogram. Several hardness ratios were considered, but the one finally chosen was the ratio H/L where H is from 5.69–20.9 keV and L is 1.11–5.69 keV.

This ratio led to the largest values of the autocorrelation, and thus the largest contrast with the simulated data. The reason that this is true is because the H and L bands chosen for this ratio give nearly the same values of σ^2/e^2.

In the top panel of Figure 34 the autocorrelation of the hardness ratio thus defined is shown. The corresponding autocorrelation function from the $1/f$ simulated data is shown in the lower panel of Figure 34. Immediately apparent is the anticorrelation at $\sim$ 6000 seconds and correlation at $\sim$ 12000 seconds. These are the most strongly correlated and significant peaks in this figure, although there are several peaks with smaller ACF values. No such strong peaks are found in the autocorrelation of the simulated data. Therefore, periodicity of the hardness ratio is found in this source.

The periodogram shown in the top panel of Figure 35 substantiates these results. In contrast to the periodogram from the simulated data, shown in the lower panel of Figure 35, there is a clear peak at 8.6×10^{-5} Hz corresponding to a period of 11600 seconds. This peak is rather broad, so the period indicated is near enough to 12000 seconds. There is no corresponding peak at this frequency in the simulated data. There is a peak in the simulated data at $\sim 6.0 \times 10^{-5}$ Hz corresponding to a period of $\sim$ 17000 seconds. However, it is not quite as large as the peak in the real data, and it is at a substantially different frequency as well, so it is most likely due to the window function. Another support of this result is the fact that the level of the noise can be seen in the periodogram. For frequencies larger than $\sim 2 \times 10^{-3}$ Hz, the periodogram flattens, and the level of the noise is about 0.5. The peak at nearly 12000 seconds has a magnitude more than 100 times the noise level.

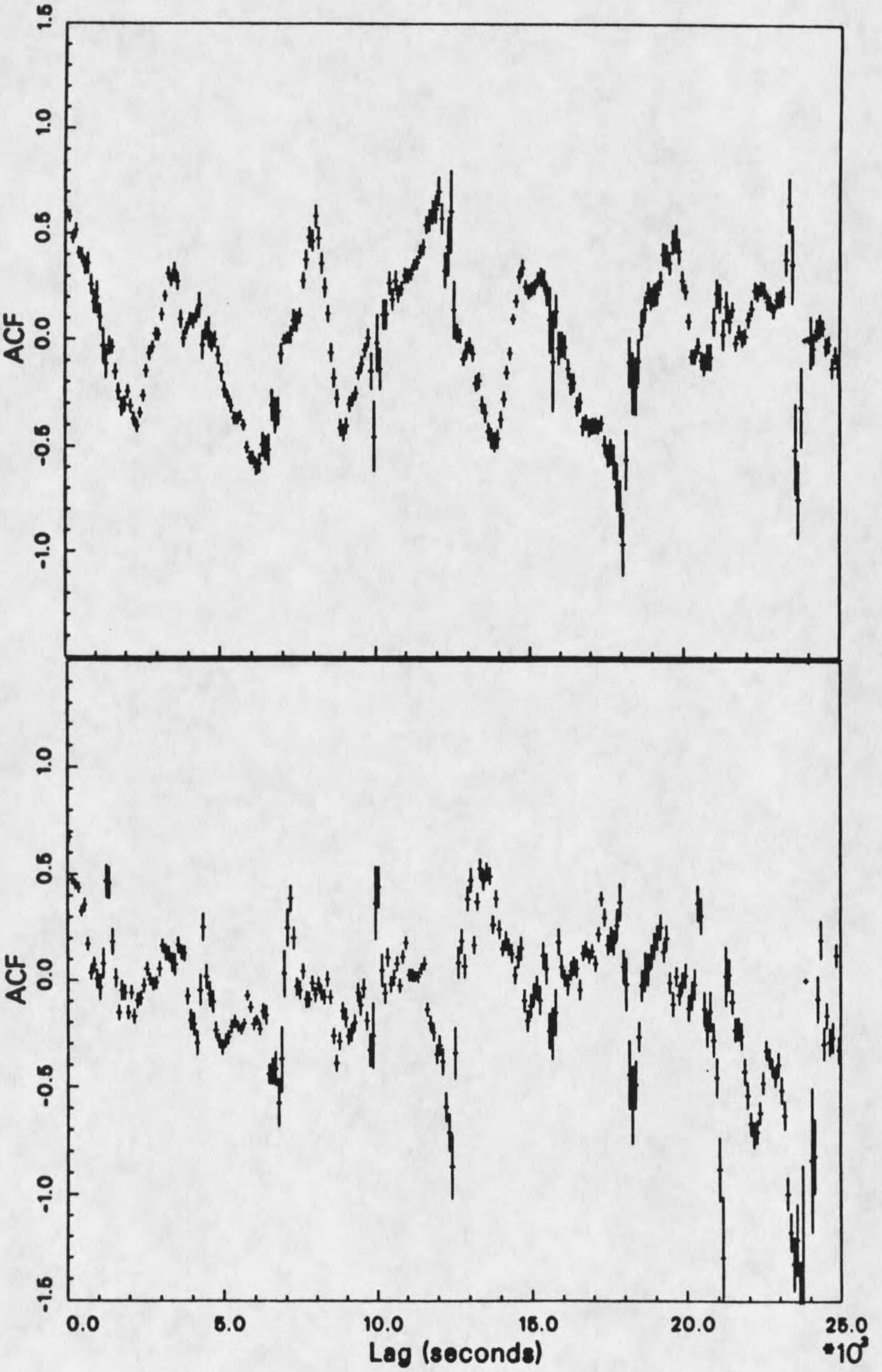

Figure 34. Autocorrelation of October data hardness ratio. The ratio 5.69–20.9 keV/1.11–5.69 keV is shown. In the top panel is the ACF of the measured data while in the lower panel is the ACF for the $1/f$ simulated data.

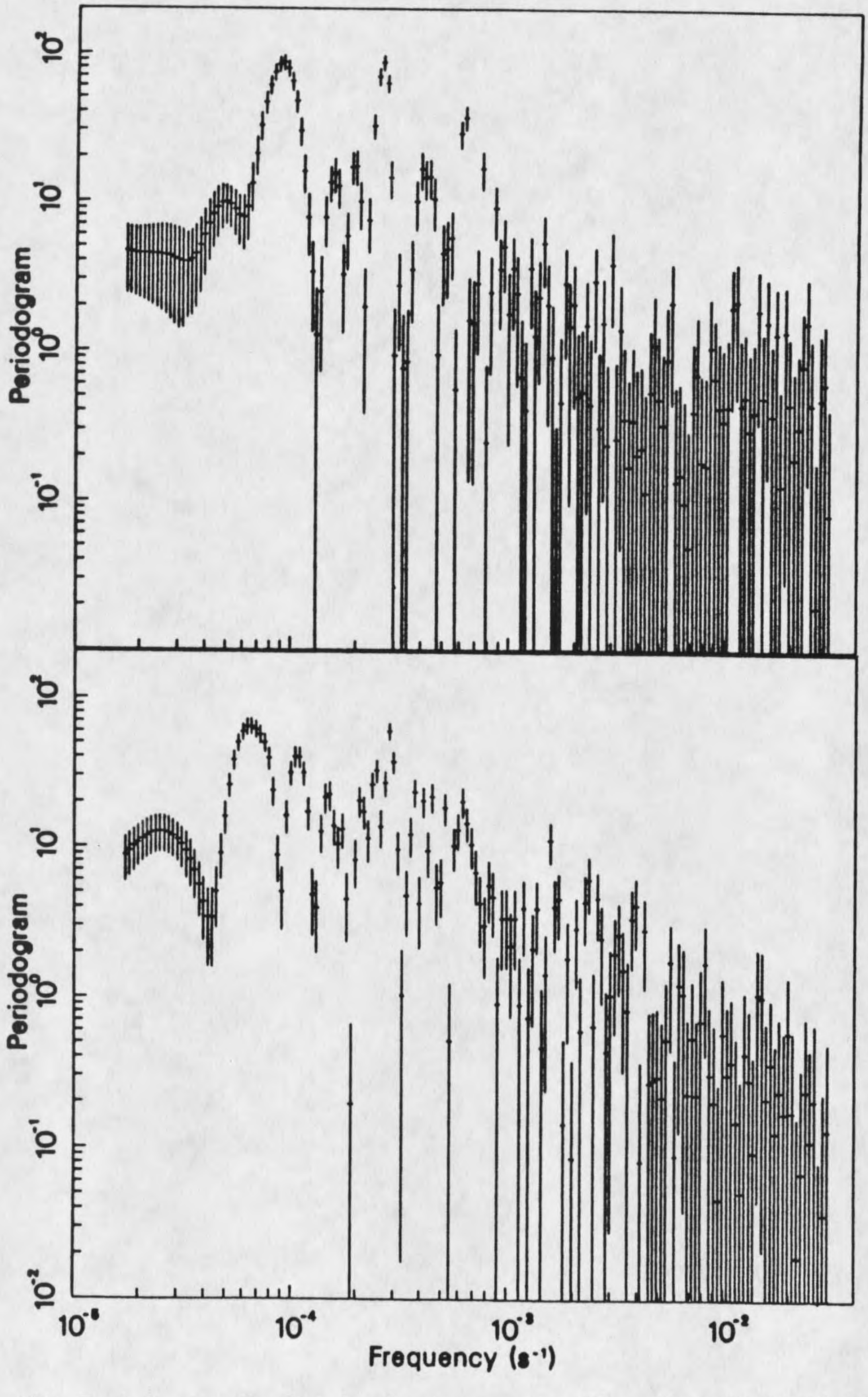

Figure 35. Periodogram for October hardness ratio. The ratio 5.69–20.9 keV/1.11–5.69 keV is shown. In the top panel is the periodogram of the measured data while in the lower panel is the periodogram for the $1/f$ simulated data.

The proper thing to do next is to obtain a probability for occurrence of the periodic component. This type of analysis was done by Mittaz and Branduardi-Raymont (1989), for the long EXOSAT observation of this source. They produced 1000 random sets of data with the same frequency dependent variance as found in the real data. Then by comparing the power in the real data with that in the simulated data, they could estimate the probability of occurrence by chance of such a peak was less than 1 in 1000. This procedure is straight forward in EXOSAT data, because of the even sampling available due to the long period of the satellite orbit. However for *Ginga* data, the windowing function describing the gaps in the data make this procedure less straightforward. This is because the usual procedure in producing simulated data is to make an evenly sampled data stream having the desired power spectrum, and then fold the window function onto it. If this is done with the *Ginga* data, the window function would be then essentially applied twice, once from the power spectrum and second from the data sampling. Since I have not figured out a better way to do this, the probability of detecting such a periodic component by chance has not been estimated. Note that the significance of the peaks cannot be evaluated by the method described by Press and Teukolsky (1988), because that method assumes the background variability is white. Here, the background variability is assumed to be $1/f$, appropriate for AGN.

Prompted by the periodicity that is found, the folded light curves for the April and October data were made, shown in Figures 36 and 37 respectively. Only the data from the second day were used for the April folded light curve, since the amount of time between the first dip and the second dip is not exactly a multiple of 12000 seconds. In Figure 38, the folded light curve for the hardness ratio is also shown. The folding period for the total flux light curves was chosen to be

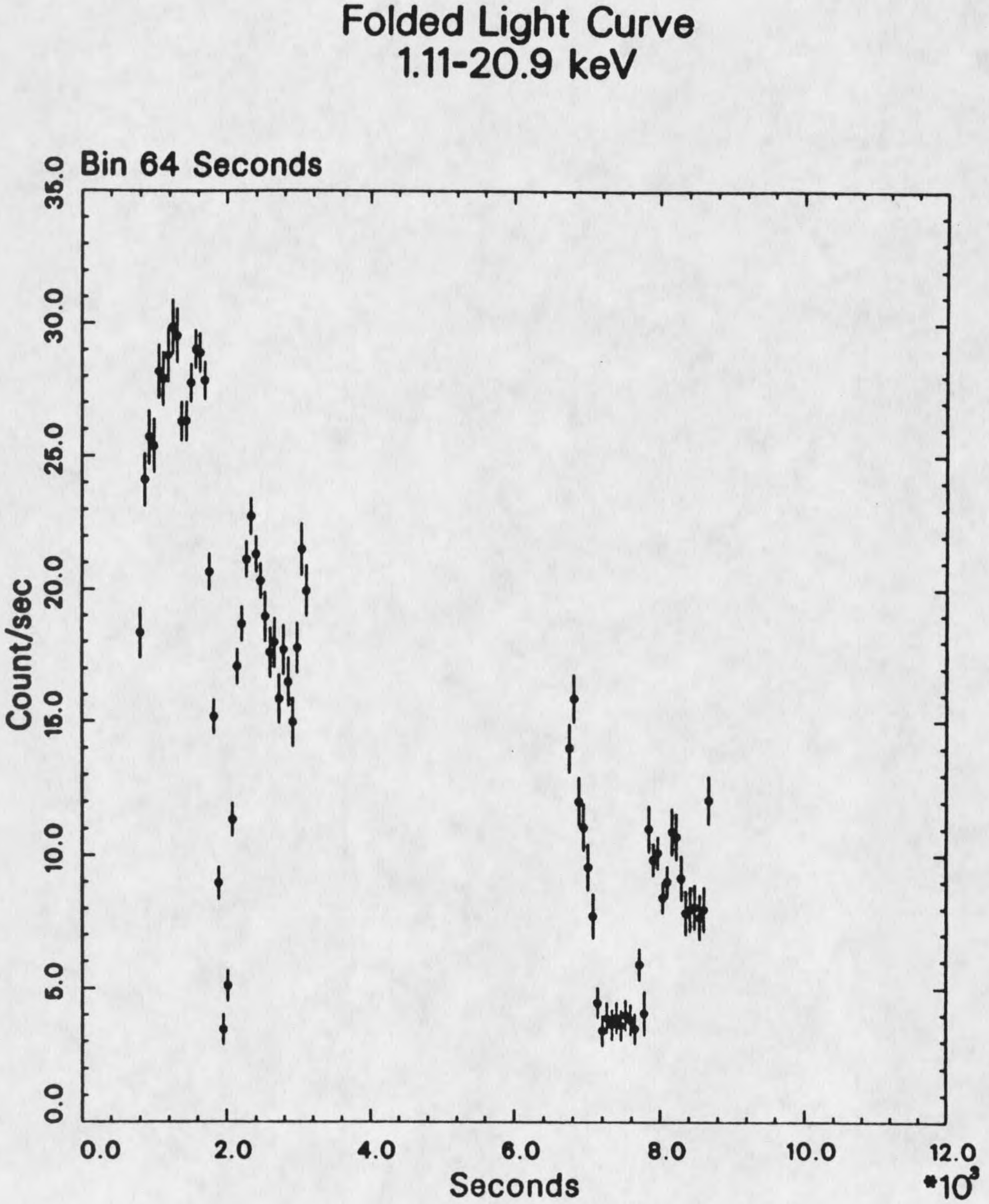

Figure 36. Folded light curve for the April data. Only the data from the second day of observation are shown. The bin size is 64 seconds.

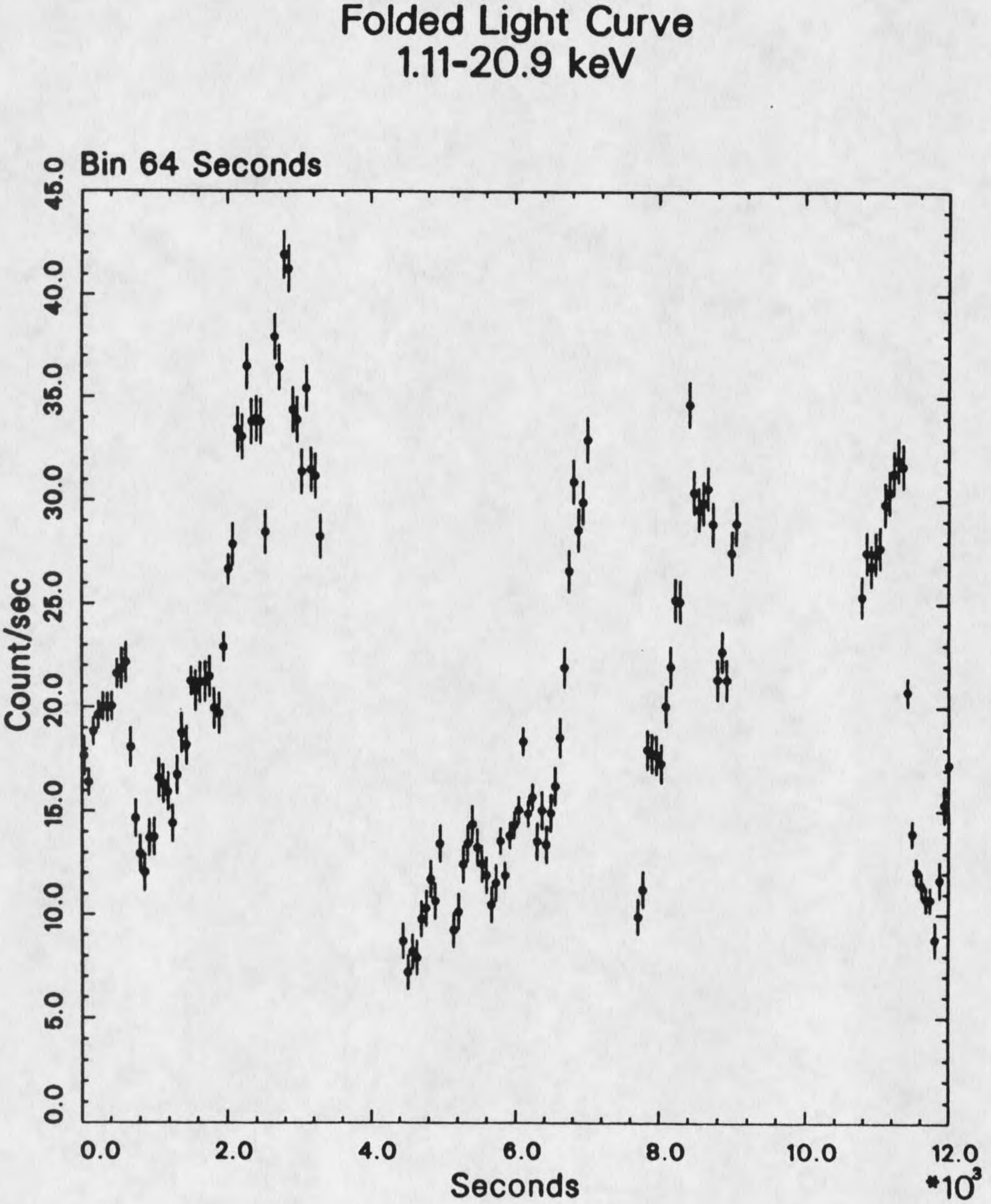

Figure 37. Folded light curve for the October data. The bin size is 64 seconds.

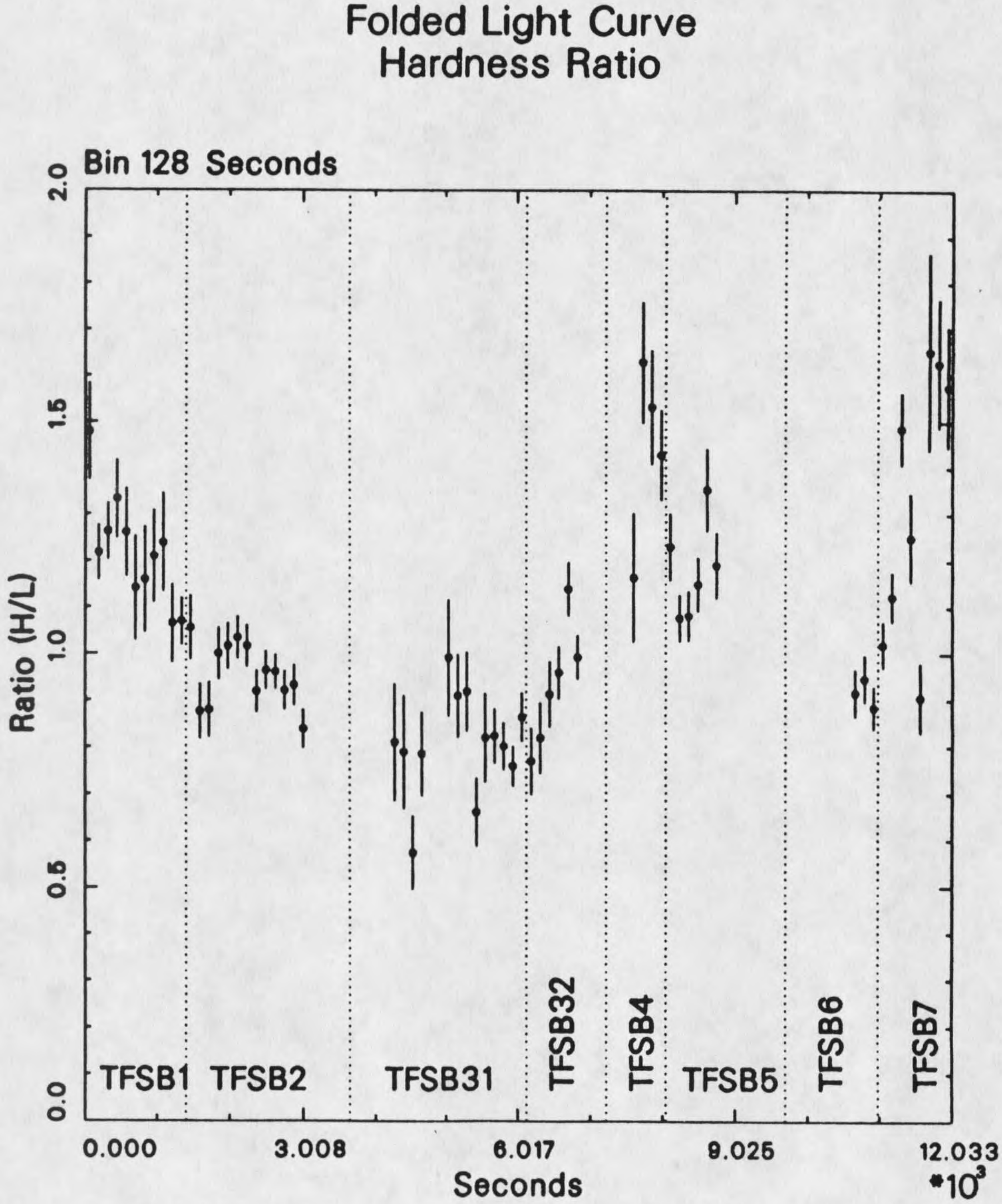

Figure 38. Folded light curve for the October data hardness ratio. The hard band used was 5.69–20.9 keV, while the soft band used was 1.11–5.69 keV. The bin size is 128 seconds. Also shown are the divisions used to accumulate spectra along the folded light curve, along with the names of the spectra.

12000 seconds, while the folding period for the hardness ratio was chosen to be 12032 seconds. The reason that 12032 seconds is used for the hardness ratio is that spectra were accumulated along the folded light curve as shown, and 12032 is the nearest multiple of 128 seconds to 12000 seconds, 128 seconds being the intrinsic spectra bin size. The divisions used to accumulate spectra on the folded light curve are also shown in Figure 38. These spectra were accumulated and fit to characterize the whole observation and will be discussed in the next section.

The character of the variability shown in the folded light curves of the total flux is clearly not sinusoidal. The dips characterize the April light curve, while the October light curve shows regions of flares and dips. A 12000 second periodicity is not very apparent in the October light curve, and the multiple flares suggest a 6000 second periodicity. On the other hand, the 12000 second periodicity is apparent in the folded light curve of the hardness ratio. Comparing the folded light curve for the total flux in the October data with the folded light curve of the hardness ratio shows that clearly the hardness is not correlated with the flux throughout the entire observation. There are some regions where a correlation seems apparent, and others where the data looks nearly anticorrelated.

The time series analysis of both of the observations find significant evidence for the 12000 second periodicity, although the evidence that the period for the October observation is 12000 seconds is not as strong. In addition, the hardness ratio from the October data was also found to exhibit 12000 second periodicity.

Spectral Analysis – Entire Observation

Previously, the iron emission line flux from this source has been observed to vary in phase with the continuum flux (Kunieda et al. 1990). Also, the variation in the hardness ratio demonstrated in the previous section should be an indication of photon index variability. To more closely examine these two issues, the spectra were accumulated for each observation and fit.

In general, the spectral fitting was carried out from energy channel 5 to energy channel 33 (3.36–20.9 keV) with only the top layer being fit. The first five energy channels were not used to avoid contamination by the soft excess component, which is strong in this source. Only the top layer was fit because the fitting function used was a power law plus line and absorption. All components of this model can be determined by the spectrum below 10 keV; the spectrum above 10 keV serves to further constrain the power law index. Also, the top layer data have higher signal to noise ratio, and so can better constrain parameter values.

Because of the rapid variability observed, spectra were accumulated in the smallest amounts possible to fit a power law plus line model (see Equation 4.2). The smallest amount was found to be 256 seconds, so spectra were formed by combining 2 subframes of data, each 128 seconds long. Because there were two subframes accumulated for each spectrum, non-mutually exclusive spectra could also be formed. For example, instead of combining subframes 1–4 into two spectra (1–2 and 3–4), three spectra could be formed (1–2, 2–3, and 3–4). Since they are not mutually exclusive, they cannot all be used for statistical analysis, but serve rather to provide more data in parameter light curves.

These spectra were first fit with a power law plus absorption model (Equation 4.1), followed by the simple power law with the addition of a narrow line at 6.4 keV (Equation 4.2). Rejection of this model was implied if the 90% error for the line flux was greater than the line flux measurement. Finally, the spectra were fit with a line model having the line energy as a free parameter. In some cases, the absorption column measured by the fit was found to be less than $10^{21}\mathrm{cm}^{-2}$. This is the lower limit of column density which *Ginga* can measure, so in these cases the column was fixed at the Galactic value of $10^{21.2}$cm^{-2} (Turner and Pounds 1989).

First the parameters were examined to see if they vary significantly by using the constant hypothesis test on mutually exclusive data. The test used did not take into account the upper limits of some of the parameters, particularly the line flux and equivalent width. In these cases, these points were excluded. There are more correct methods available, in which the upper limits are taken into account, as discussed in Chapter 4 (Avni et al. 1980; Schmitt 1985; Feigelson and Nelson 1985; Isobe, Feigelson and Nelson 1986). For the April data, three parameters varied significantly at the 90% confidence level: the total flux, the photon index and the line flux. The remaining three parameters, N_H, equivalent width and line energy, did not vary significantly. For the October data, the situation was similar, except the line flux did not vary significantly at the 90% confidence level. For 36 degrees of freedom, the χ^2_R for 90% is 1.31, while the measured χ^2_R was only 1.25. However, as noted before, the upper limits were not taken into account. For the October data, there were four points for which only upper limits were available. In Figures 98, 90 and 91 of Appendix 1, the parameter light curves for the 2–10 keV continuum flux, photon index, line flux and equivalent width from the April observation are shown, while the corresponding parameter light curves for the October data are shown in Figures 92, 93 and 94 of Appendix 1. Note that results from all spectral fits are shown, so the results are not mutually exclusive.

In the April data, the correlation of the line flux with the continuum flux is easy to see, especially during the dips. The photon index was also found to be variable, but the correlation with flux is less apparent. In particular, during the second dip at $\sim 86,000$ seconds, shown in Figure 86 of Appendix 1, the photon index reaches its minimum well after the flux minimum.

For the October data the photon index is found to vary. The line flux varies but not statistically significantly over the whole observation. These two parameters seem to be correlated with the flux, but in a local manner. That is, in each orbit of data, the light curves have roughly the same shape. However, the flux and photon index vary on a much larger scale from orbit to orbit, and so in some cases the flux appears anticorrelated with the photon index. Also, like the hardness ratio, the photon index for the October data varies smoothly, and the periodicity of variation appears to be 12000 seconds. Because of this, the folded light curve for the photon index is shown in Figure 39. It can be seen that the variation has a broad, almost sinusoidal shape.

The next question to be answered is whether any of these variable fit parameters are correlated with one another. Especially important is the question of the continuum flux–line flux correlation. Recall that a strong correlation was found by Kunieda et al. 1990. Figure 40 shows the correlation plot of the line flux versus the 2–10 keV continuum flux for the April data. Note that here of course mutually exclusive data are used. Some correlation is evident. The linear correlation coefficient was found to be $r = 0.73$ for 28 points. This implies that the parent population is at least as correlated as 0.5. Note that again the data with upper limits are not taken into account, although there is a correct way to do this (Avni et al. 1980; Schmitt 1985; Feigelson and Nelson 1985; Isobe, Feigelson and Nelson 1986). Fitting this correlation to a straight line, it is found that the intercept is consistent with 0. That is, zero 2–10 keV flux implies zero line flux. The slope of the fit was $2.8 \pm 0.6 \times 10^{-2}$, indicating that the slope is different from 0 by more than 4σ. The line fit is quite good, having a χ^2 of 38.6 for 46 degrees of freedom.

The correlation plot of the line flux versus the 2–10 keV continuum flux for the October data is shown in Figure 41. Again some degree of correlation seems

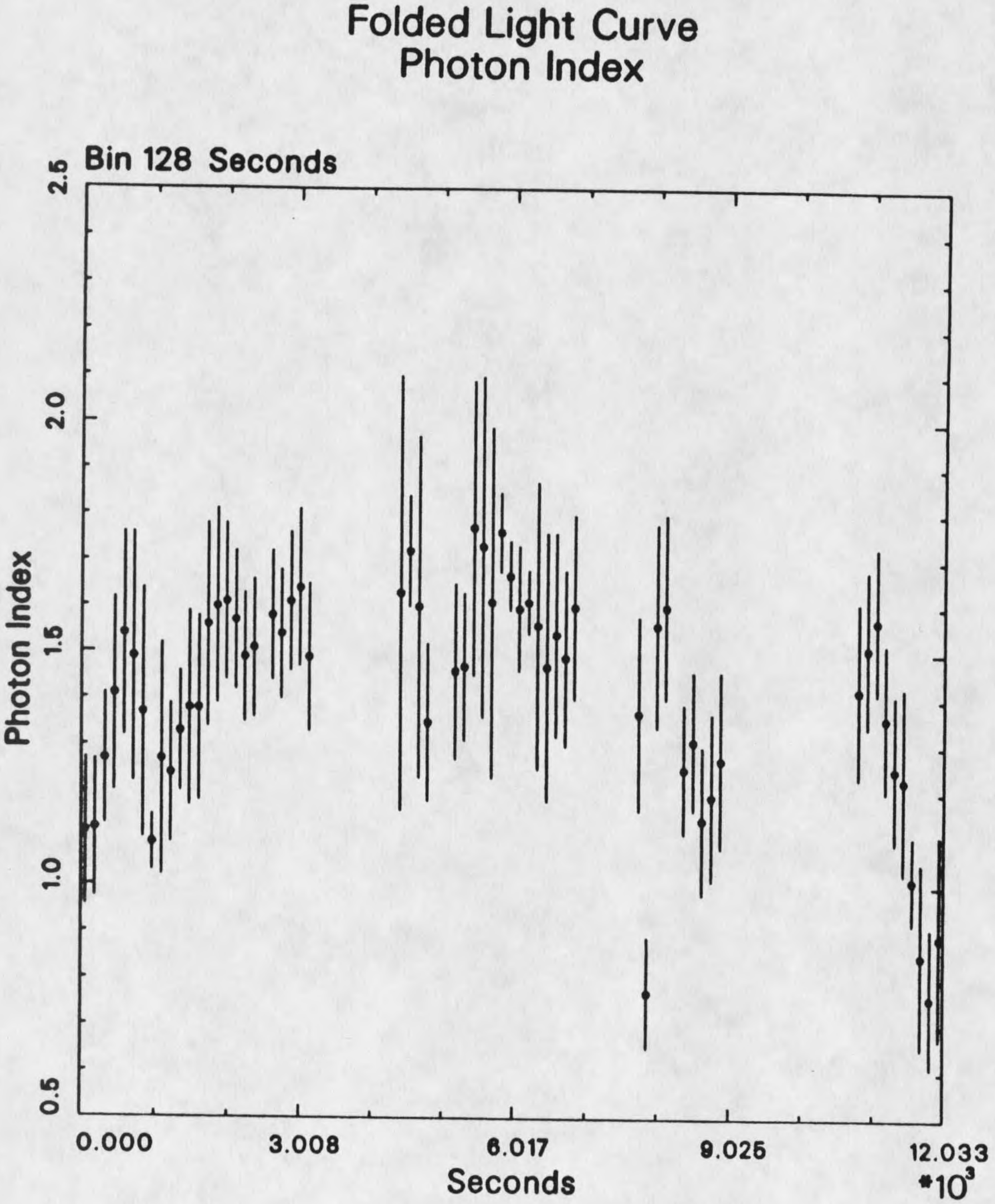

Figure 39. Folded light curve of the photon index, for the October observation.

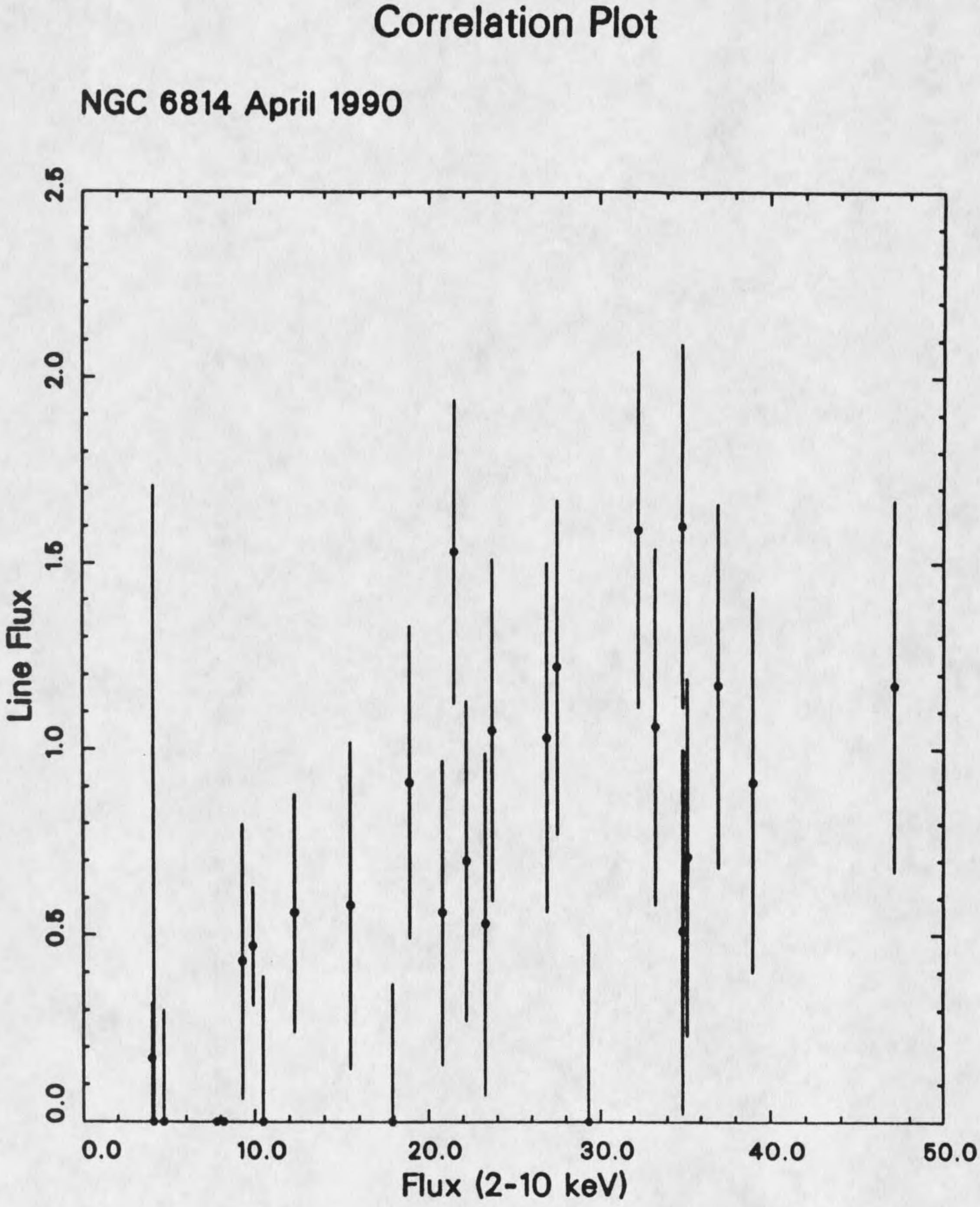

Figure 40. Line flux versus continuum flux correlation plot of April data. Uncertainties are 90% for one parameter of interest.

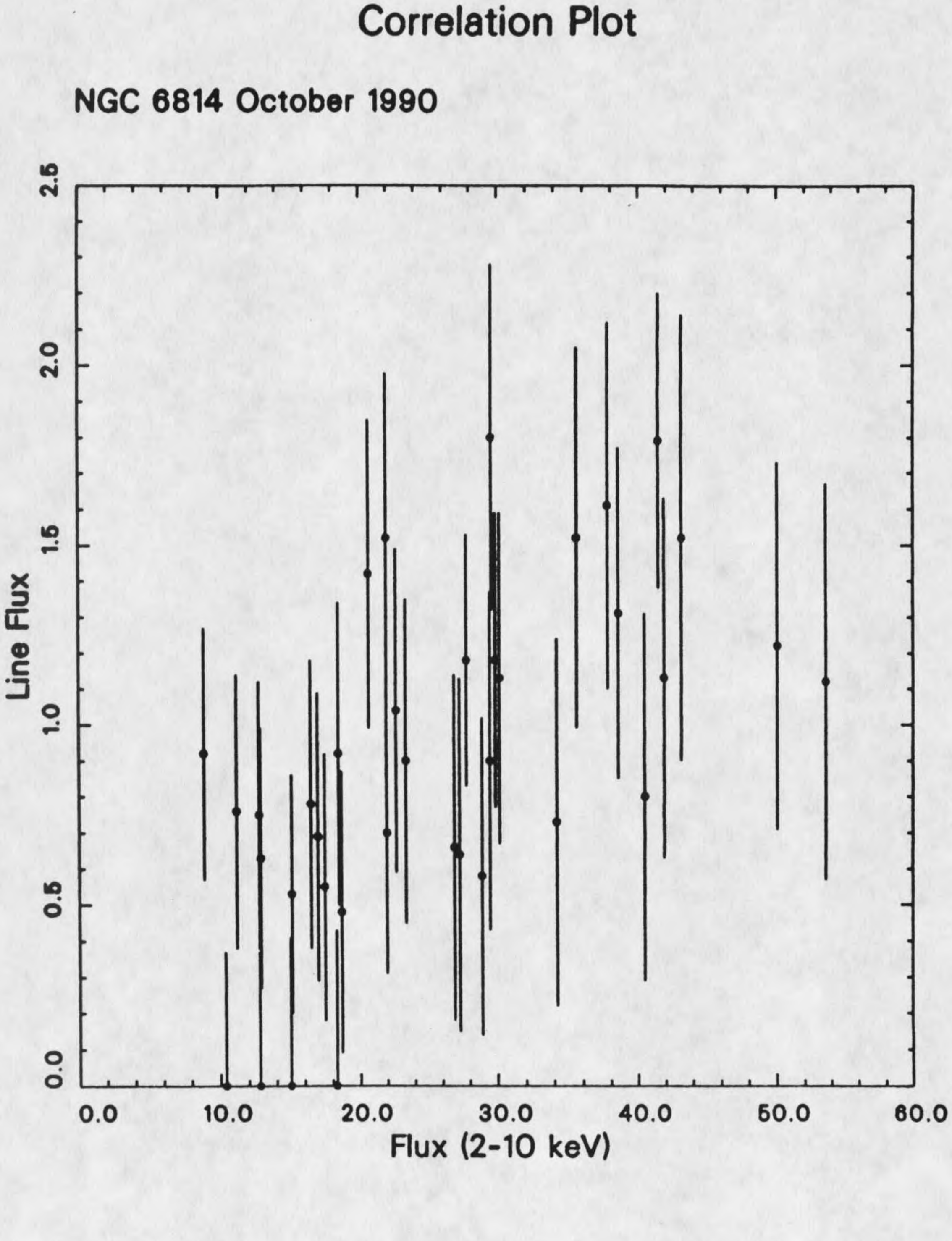

Figure 41. Line flux versus continuum flux correlation plot of October data. Uncertainties are 90% for one parameter of interest.

evident. The linear correlation coefficient was $r = 0.62$ for 37 points, implying a parent population correlation of at least 0.4. The intercept of the straight line fit in this case was found to be 0.21 ± 0.17 where the uncertainty is 1σ. This is not consistent with a 0 intercept; however, the 0 intercept is not rejected either. The slope of the line fit was $2.7 \pm 0.6 \times 10^{-2}$, nearly the same as for the April data. Again the line fit is not inappropriate; the χ^2 was 27.9 for 35 d.o.f. It may be that the continuum flux–line flux correlation still holds but the significance of the correlation appears to be weaker. Also recall that the line flux is not significantly variable at the 90% confidence level; but also recall that the points with upper limits only available has not been taken into account. Another influence is that the line fluxes were found from spectral fitting with the line energy left free. If the line energy had been fixed, because of the coupling of the line flux and line energy, the line flux would have been better determined. This may result in statistical variability being observed.

As discussed in Chapter 5, it has been found that a continuum flux–photon index correlation has been observed in other AGN. Because of the significant variability of the photon index in both observations, this correlation was also examined. The correlation plot of photon index versus 2–10 keV continuum flux for the April data is shown in Figure 42. Some degree of correlation is present. However, the linear correlation coefficient is not large, being only $r = 0.14$. Also the line fit is not good, having a χ^2 of 47 for 26 d.o.f. So the presence of a flux–index correlation cannot be readily verified by these data.

The flux–index correlation for the October data is more interesting. This is shown in Figure 43. Because a linear correlation is not apparent, all fit points are included, including the non-mutually exclusive data. For high flux, the photon index is nearly ~ 1.6 consistently. However, for low flux, there is a spread of

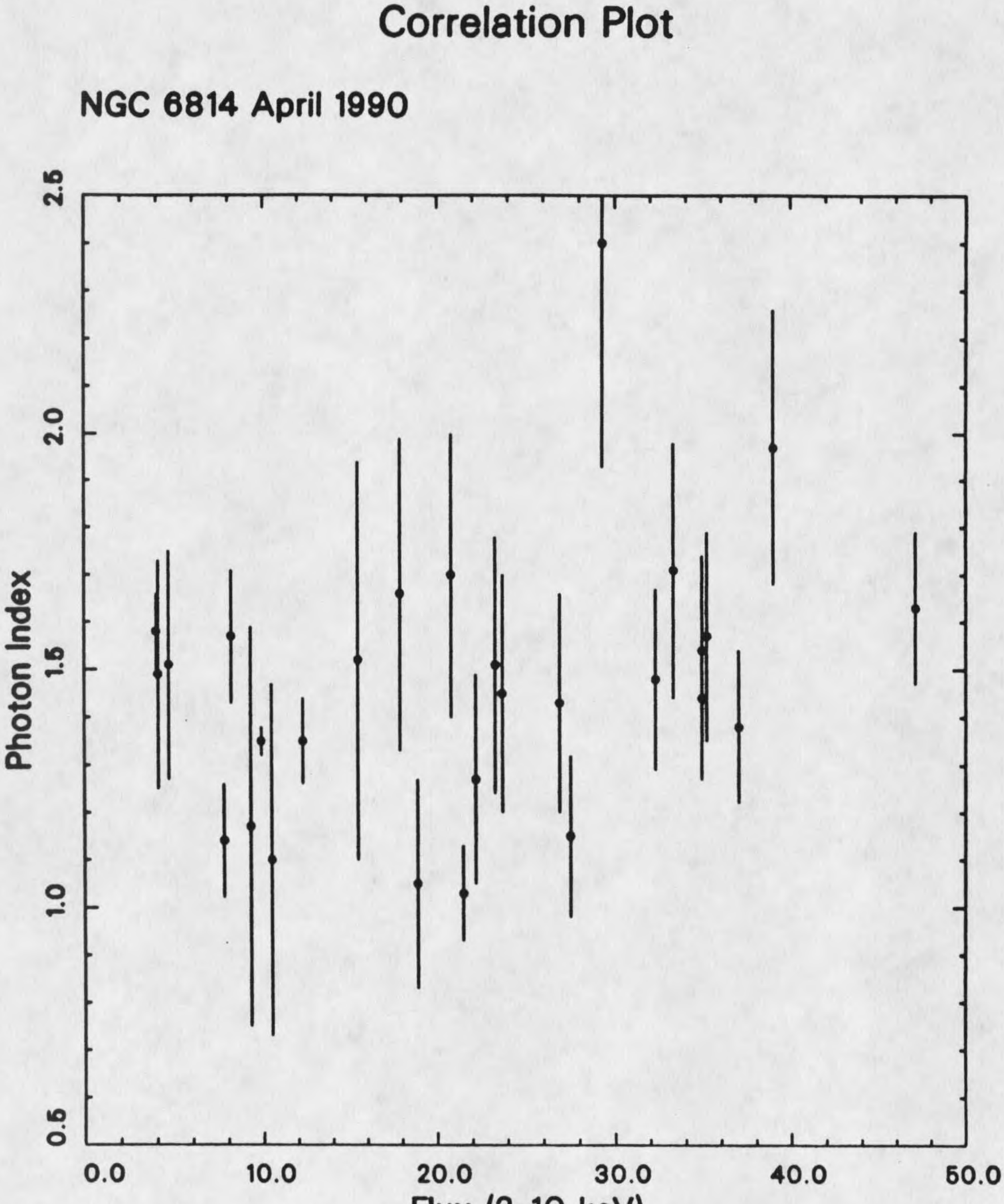

Figure 42. Photon index versus continuum flux correlation plot of April data. Uncertainties are 90% for one parameter of interest.

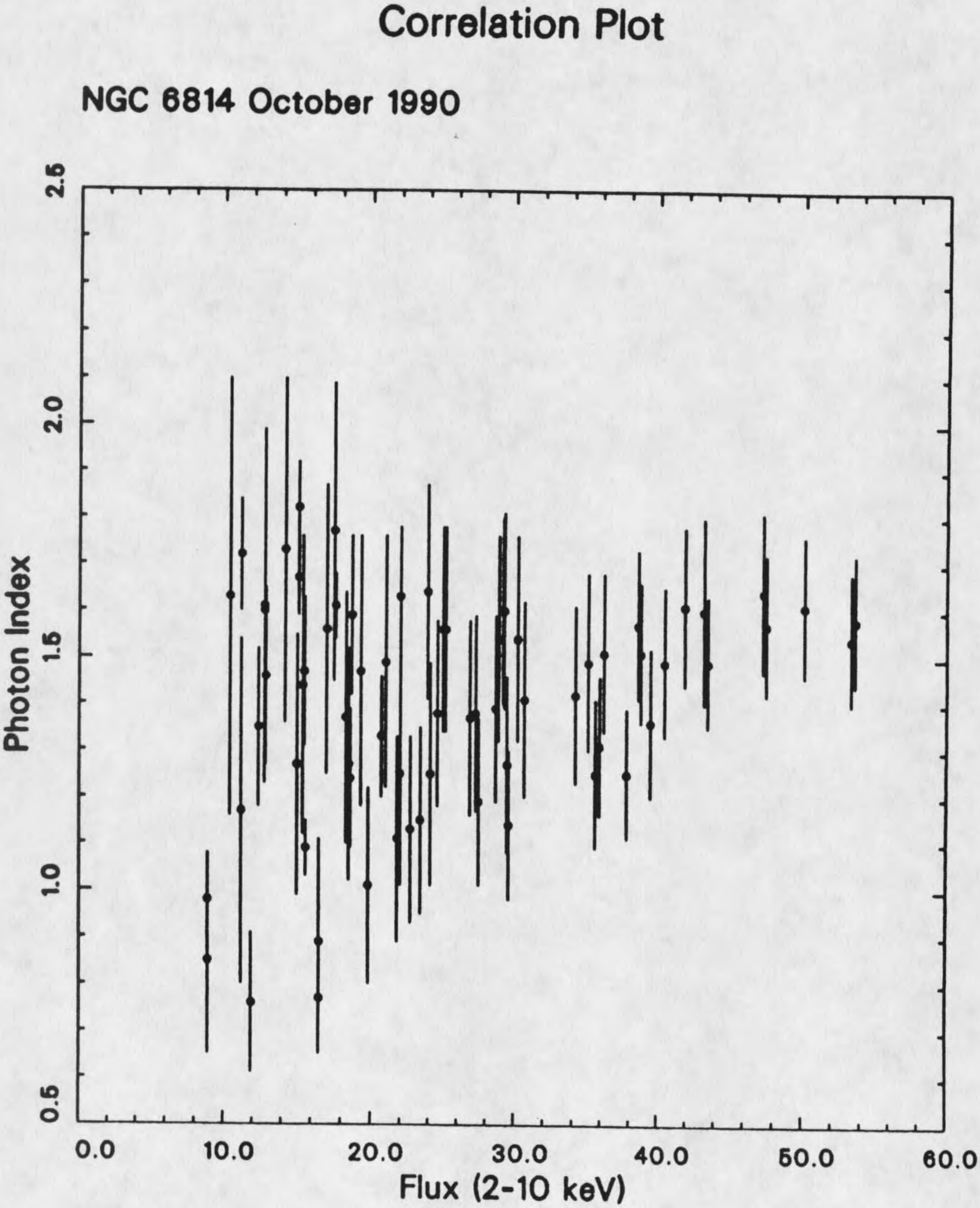

Figure 43. Photon index versus continuum flux correlation plot of October data. Uncertainties are 90% for one parameter of interest. Note that here non-mutually exclusive data are shown.

indices. There is a suggestion of two branches for the low flux region; a lower diagonal branch where the flux and index appear to be correlated, and a higher, nearly horizontal branch where the flux and index might be slightly anticorrelated. This behavior is expected, since the hardness shows 12000 second periodicity, while the flux shows apparent periodicity of $\sim$ 6000 seconds.

Because the evidence for the 12000 second periodicity in the hardness ratio and related photon index is so strong, spectral analysis was performed along the folded light curve. Eight spectra were used, accumulating the data shown in Figure 38 on the folded light curve. The spectral fitting results are listed in Table 10, and the regions of the folded light curve included in the spectra listed in Table 10 are marked on the figure. The fit parameters are marked with an (*) if the parameter value found is significantly different than the one preceding at greater than the 1σ confidence level, and with (**) if the confidence level lower boundary is 90%. χ^2 contours were also found for the column versus the index for all of these eight spectral fits. Because column and index are sometimes quite highly correlated, examination of the χ^2 contours is necessary to verify an index change. The χ^2 square contours showing N_H column versus index for these spectra are shown in Figure 44. Examination of the χ^2 contours finds that significant variation in the index and/or absorption column occurred from spectrum to spectrum.

In general, it was found that for each of these folded spectra, except for the first and the last, the photon index and absorption combination vary significantly at at least the 90% confidence level from one to the next. Also in some cases, the line energy and/or the line flux differ significantly. Note that the line energy and line flux are also coupled, so to look for significant variation in these parameters, the χ^2 contour plotting these parameters should be examined. However also note

Table 10. The results of spectral fitting to the folded October data. All errors are 90% confidence.

Spectrum	Time (sec)	Photon Index	$\log(N_H)$ (cm^{-2})	Line Energy (keV)	Line Flux (count s^{-1})	Equivalent Width (eV)	Flux† (count s^{-1})	χ^2_R /d.o.f.
TFSB1	1964	1.28 ± 0.09	22.51 ± 0.14	6.48 ± 0.10	0.96 ± 0.17	500 ± 90	23.0	0.79/24
TFSB2	1742	**1.52 ± 0.08	**22.43 ± 0.11	*6.68 ± 0.10	1.19 ± 0.20	410 ± 60	39.9	0.93/24
TFSB31	2186	1.53 ± 0.08	*21.34 ± 1.23	*6.35 ± 0.16	*0.49 ± 0.13	440 ± 110	14.6	0.70/24
TFSB32	697	1.54 ± 0.14	**22.46 ± 0.20	6.32 ± 0.20	0.81 ± 0.28	370 ± 120	28.2	0.74/24
TFSB4	602	**1.22 ± 0.16	22.63 ± 0.20	6.28 ± 0.21	0.99 ± 0.31	470 ± 140	23.5	0.84/24
TFSB5	760	1.21 ± 0.10	**22.24 ± 0.25	6.47 ± 0.12	1.41 ± 0.28	510 ± 100	32.2	0.92/24
TFSB6	380	**1.51 ± 0.15	22.42 ± 0.23	6.72 ± 0.75	*0.52 ± 0.38	190 ± 130	36.4	0.91/24
TFSB7	1140	**1.09 ± 0.11	22.20 ± 0.33	6.46 ± 0.12	1.04 ± 0.21	600 ± 120	19.4	0.73/24

†Continuum flux is from 2–10 keV, intrinsic.

* This fit parameter differs from the previous one at greater than the 1σ confidence level.

** This fit parameter differs from the previous one at greater than the 90% confidence level.

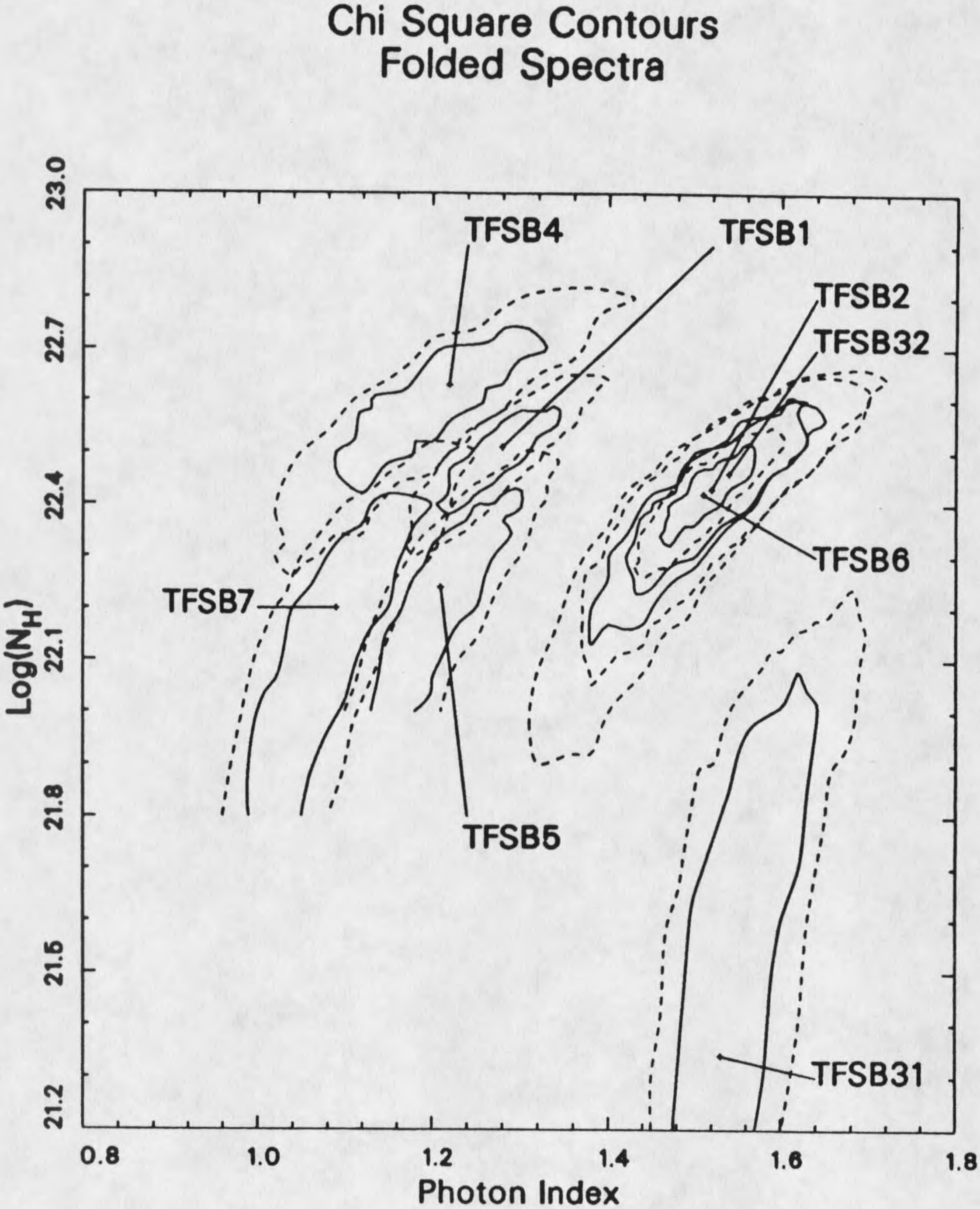

Figure 44. χ^2 contours of folded spectra from the October observation. The $log(N_H)$ is plotted against the photon index. The solid lines give the 1σ contours, while the dashed lines show the 90% contours.

that because of the poor energy resolution of *Ginga*, line energy variability would be very difficult to verify.

Fastest Variability

As described in Chapter 5, NGC 6814 has long been known to be the AGN with the fastest time scale of variability. Finally, using high time resolution *Ginga* data, the nature of this fast variability may be understood. Therefore, it is important to closely examine those parts of our observations which show the largest flux changes in the shortest time. Spectral variability during flux changes can be important to constraining models, as discussed in Chapter 5. Also, lags between different energy bands can be important in constraining models.

The regions of fastest variability for the April data are the three dips, starting at 0, $\sim 85,000$, and $\sim 97,000$ seconds shown in Figure 23 (see also Figures 81, 82 and 83 in Appendix 1). Changes in the hardness ratio are also observed during these dips, as shown in Figures 25 and 26. The data from these three sections of the April observation are referred to as the 'dip' data. For the October data, the fastest decrease occurs at about 23,500 seconds shown in Figure 24. These are referred to as the 'ingress' data, for reasons which will become apparent in the section discussing the model calculations. There are no corresponding fast increases, but an increase at about 12,000 seconds is approximately 12,000 seconds previous to the decrease. These are referred to as the 'egress' data. Both of these sections show the fastest variation in the softness ratio, as shown in Figure 27. They are also interesting because, the beginning of the egress data is about 12400 seconds from the end of the ingress data, and if the ~ 12000 second periodicity is assumed, then the combination of these two regions may represent a dip similar to those discovered the April data.

Correlation plot analysis. Much information about the nature of the variability can be gained by examining the correlation plots. These plot the flux in one energy band against the flux in another energy band. If there is no spectral variability during flux changes, the correlation plot is characterized by a single linear trend intercepting 0. However, if there are spectral changes or lags or leads in the data, the correlation plot may have one or more branches, and the main branch may not intercept 0.

The correlation plots for the April dip data are shown in Figures 45 and 46. In Figure 45, the flux from the medium (3.36–5.69 keV) energy band is plotted on the horizontal axis, while the flux from the soft (1.11–3.36 keV) energy band is plotted on the vertical axis. In this figure, the data marked with a square, a circle and a triangle are from the first, second and third dips respectively. A non-correlation is apparent because the 1.11–3.36 keV data drops to zero faster than the 3.36–5.69 keV data. Since there are 3 or 4 points from each dip in the very low flux section, it is clear that the 1.11–3.36 keV flux is in its lowest state for 3 or 4 times longer than the 3.36–5.96 keV flux. Finally, note that the part of the correlation plot with higher flux has a fan shape. Careful examination shows that the second and third dip points are nearly linear for this section, but the first dip has a larger spread with a lower 1.11–3.36 keV flux for the same 3.36–5.69 keV flux. Caution must be used when interpreting this plot, because though the 1.11–3.36 keV band is useful for examining changes in flux due to changes in moderate column absorption, this band can also be contaminated by the soft excess component.

In Figure 46, the correlation plot between the hard (8.00–20.9 keV) energy band and the medium (3.36–5.69 keV) energy band is shown for the April dip data. Again, the square, circle, and the triangle denote the first, second and third dips respectively. The bend in the correlation plot at the low flux levels shows lack

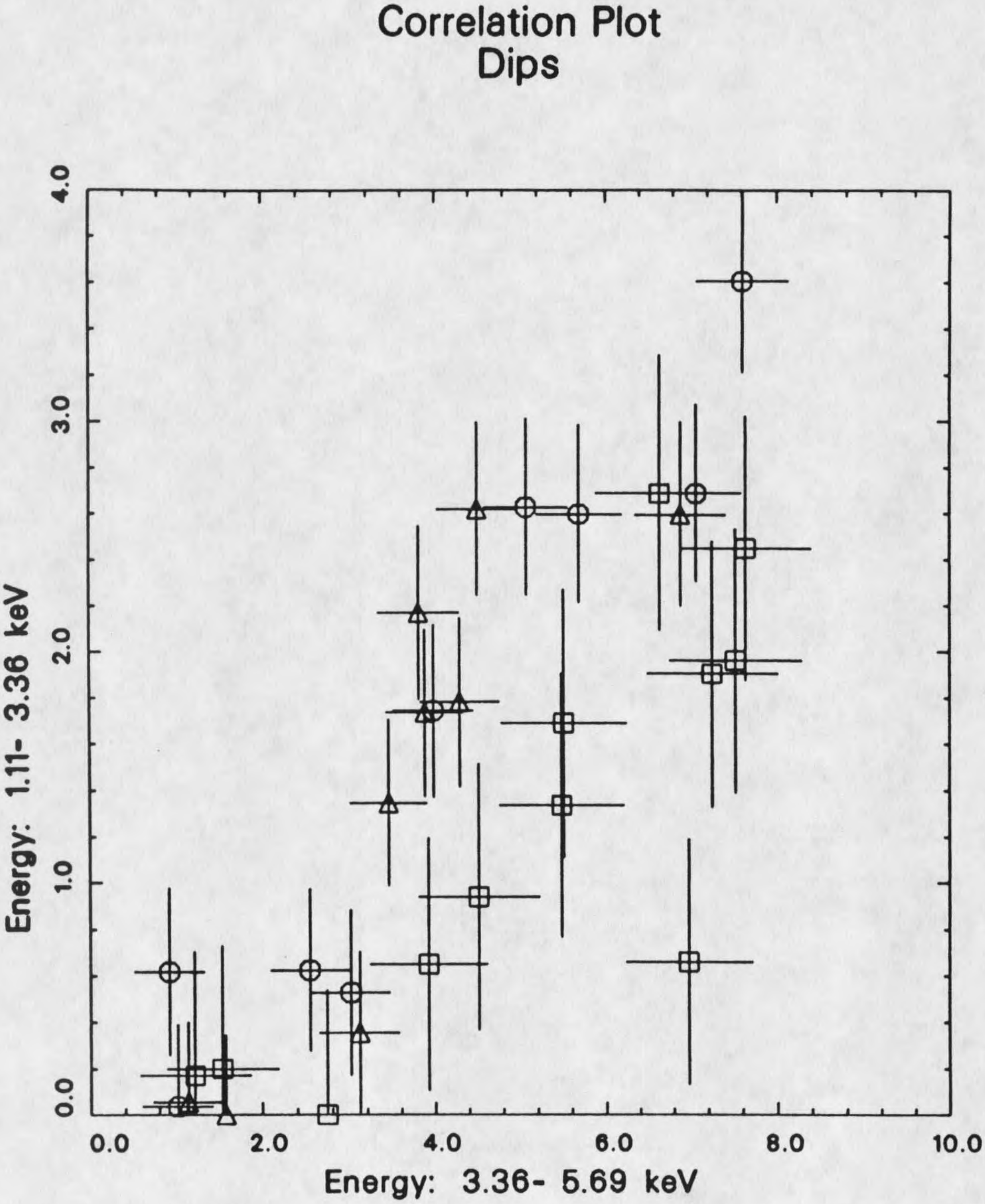

Figure 45. Soft versus medium energy flux correlation plot for April data, around dips. This shows the correlation between the soft band (1.11–3.36 keV) and the medium band (3.36–5.69 keV). The square, circle and triangle show the data from the first, second and third dips, respectively. Bin size is 64 seconds.

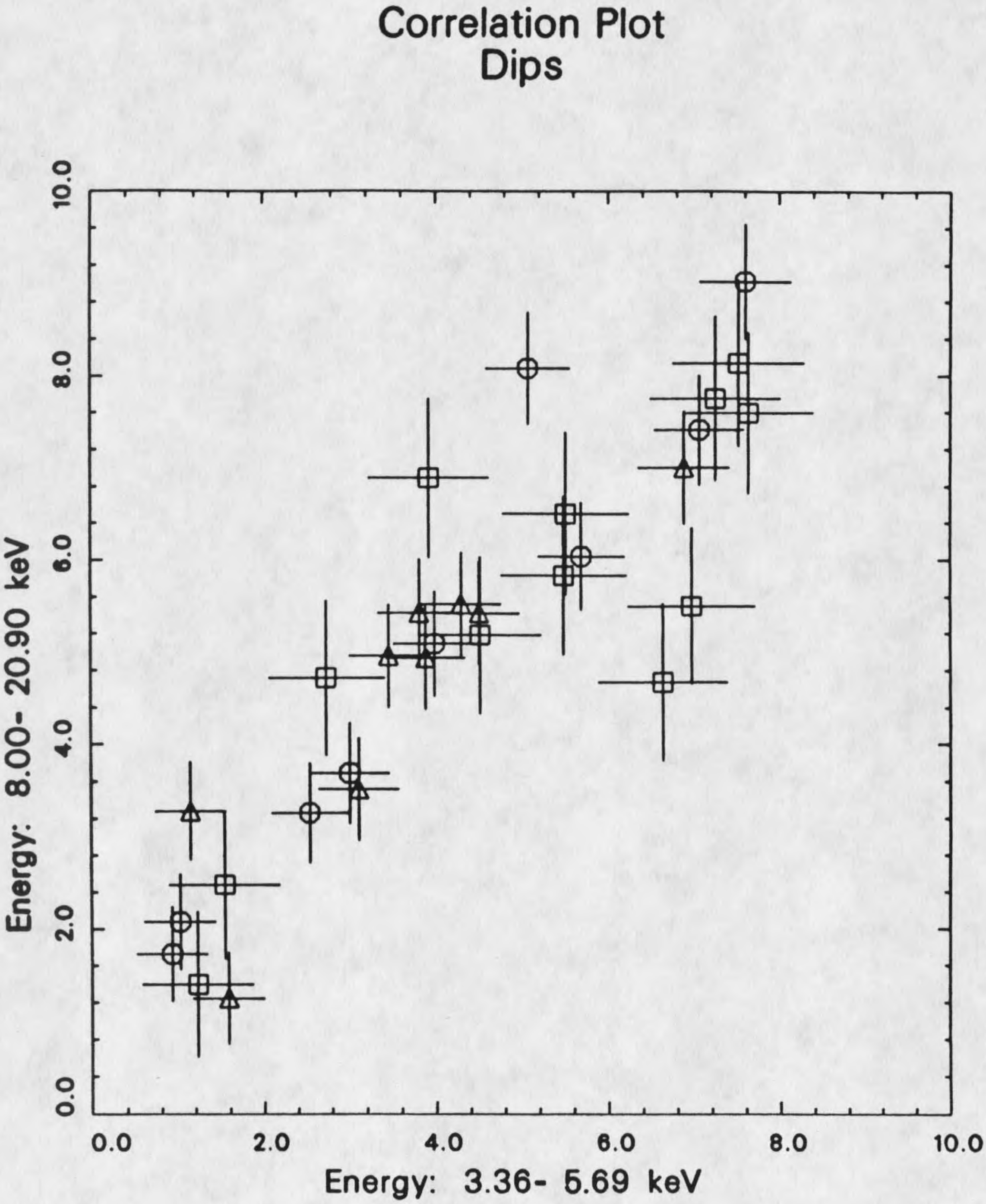

Figure 46. Hard versus medium energy flux correlation plot for April data, around dips. This shows the correlation between the hard band (8.00–20.9 keV) and the medium band (3.36–5.69 keV). The square, circle and triangle show the data from the first, second and third dips, respectively. Bin size is 64 seconds.

of correlation. The lack of correlation is not so clear, but is still evident. However, there are only about 2 points from each dip in each section, indicating that the 3.36–5.69 keV flux is in its lowest level only about twice as long as the 8.00–20.9 keV flux.

Because of the larger signal to noise ratio, the October data yielded more revealing correlation plots than the April dip data. In Figures 47 and 48 are shown the correlation plots for the ingress data. Figure 47 shows the hard versus the medium data. There is seen in the lower flux region of the graph a horizontal branch and a vertical branch. First, during the higher flux level horizontal branch, the hard flux is nearly constant while the 3.36–5.69 keV flux is decreasing. Then, during the vertical branch, the hard flux decreases while the softer flux is nearly constant. The increase of the hard flux at high flux levels occurs because of a hardening of the spectrum before the dip. This observation not only indicates the presence of a spectral change during the ingress, but also indicates a lag of the hard flux over the softer flux. The number of points in the horizontal branch gives an indication of the magnitude of the lag. At least 4 points are readily apparent so the lag is about 120 seconds. This observation is quantified in the following section discussing the cross correlation analysis. Figure 48 plots the medium flux (3.36–5.69 keV) versus the soft flux (1.11–3.36 keV). Here again it can be seen that the drop is very sharp, because the points cluster in two sections. A large lag in flux is therefore not apparent.

The correlation plots for the egress data are shown in Figures 49 and 50. Figure 49 shows the hard flux versus the medium flux. This plot has a different shape than that of the ingress plots, indicating that the lag or spectral change has a somewhat different character. In particular, except for a few very low flux points, this curve can mostly be described by diagonal branch and a relatively high

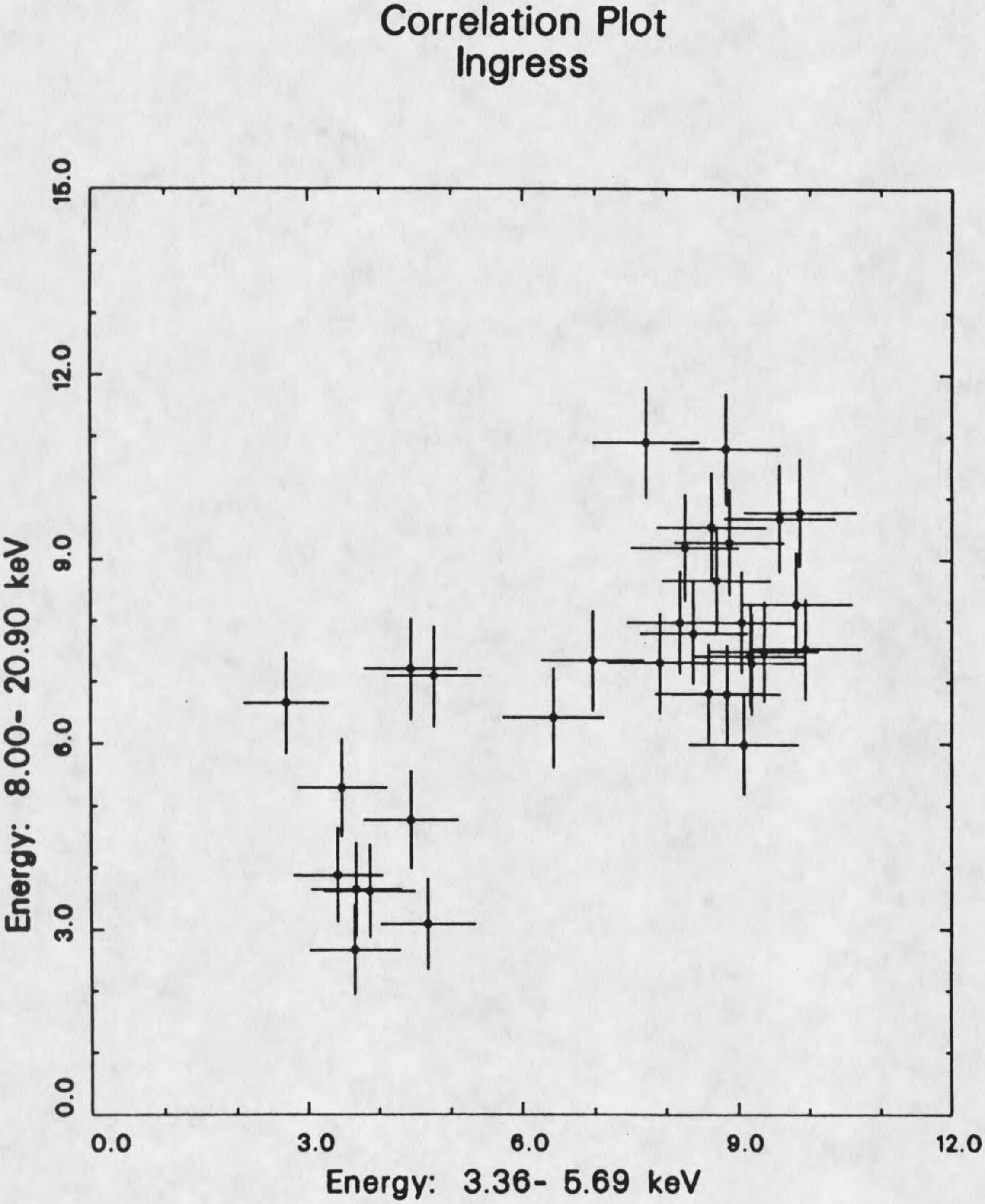

Figure 47. Hard versus medium energy flux correlation plot for the ingress section of the October data. This shows the correlation between the hard band (8.00–20.9 keV) and the medium band (3.36–5.69 keV). Bin size is 32 seconds.

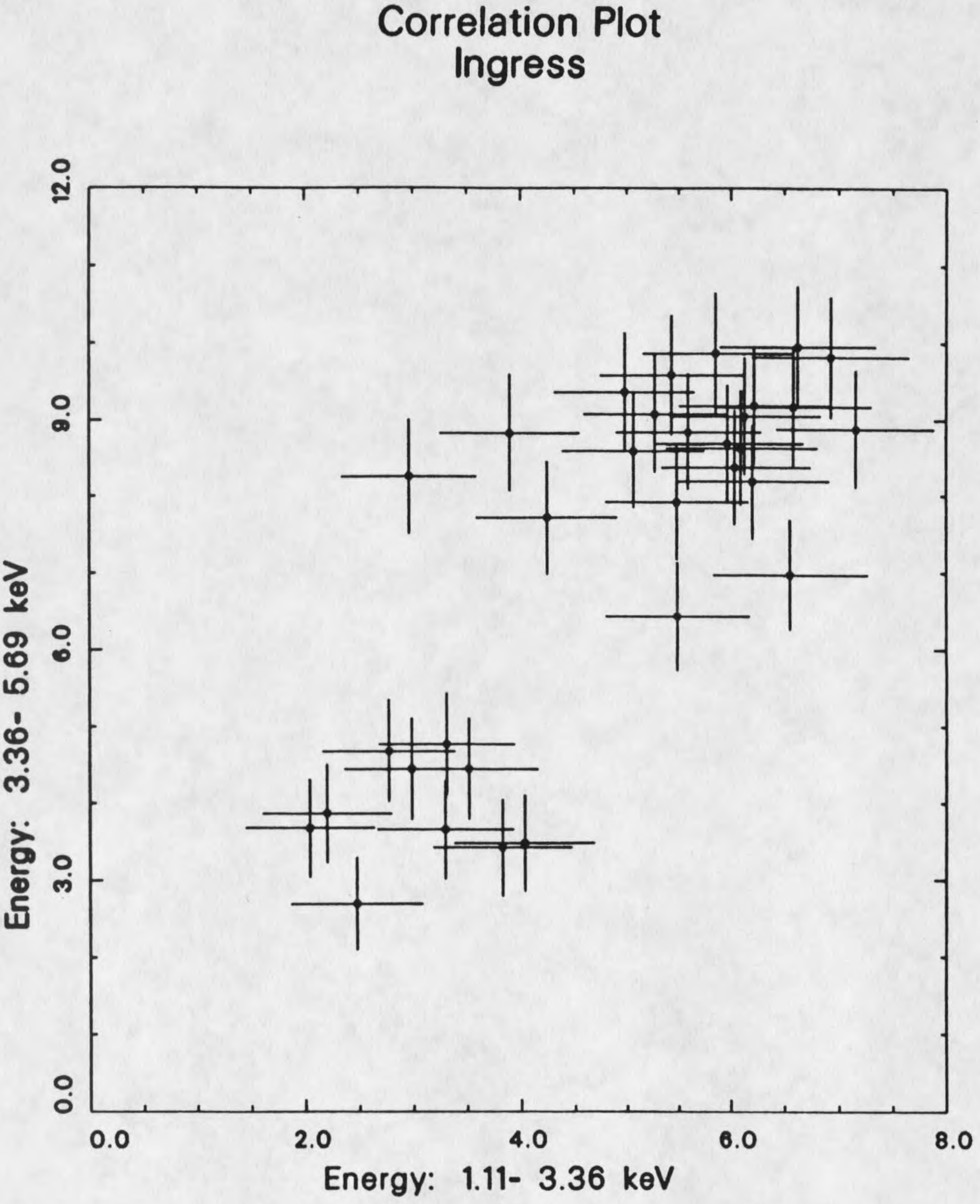

Figure 48. Medium versus soft energy flux correlation plot for the ingress section of the October data. This shows the correlation between the medium band (3.36–5.69 keV) and the soft band (1.11–3.36 keV). Bin size is 32 seconds.

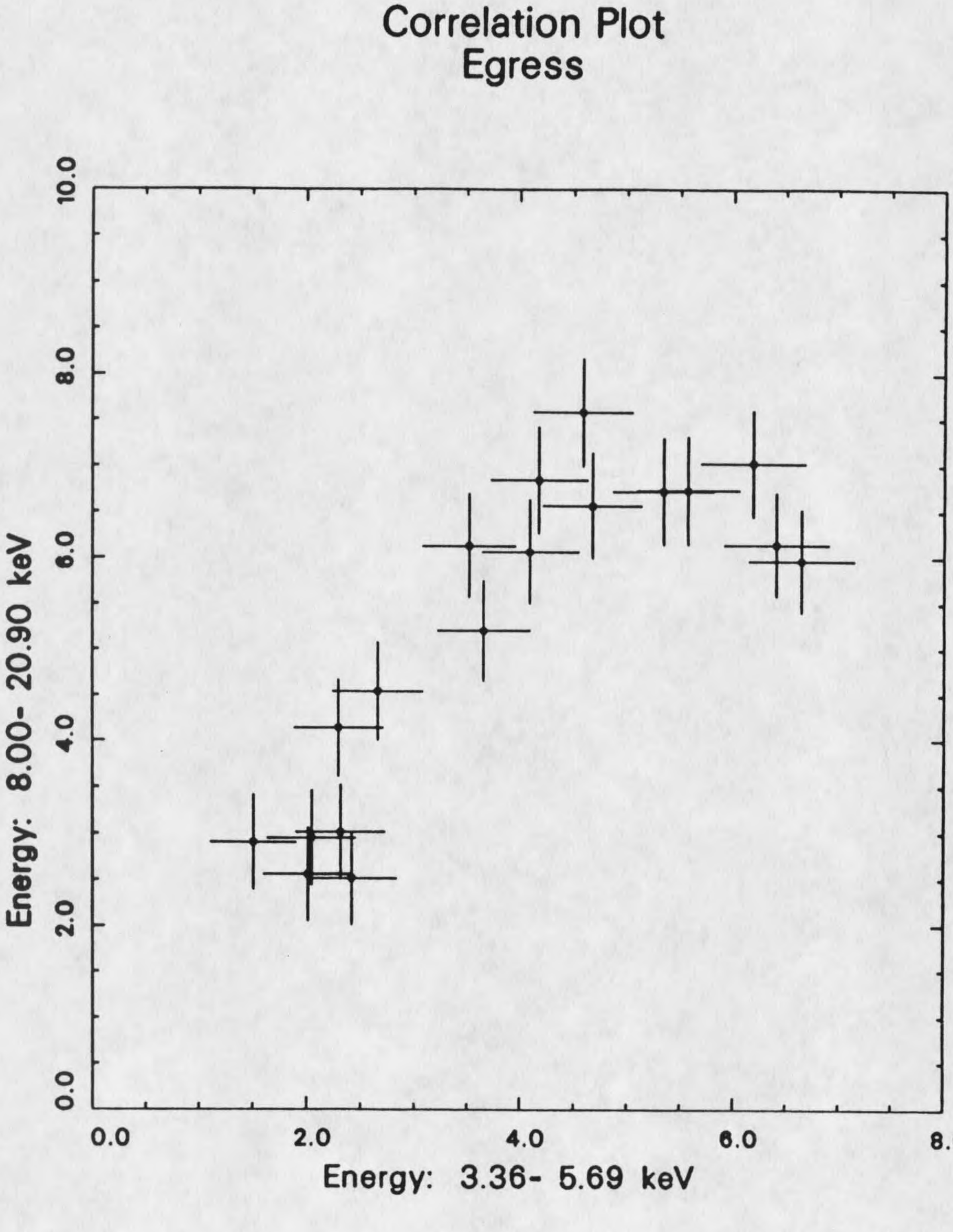

Figure 49. Hard versus medium energy flux correlation plot for the egress section of the October data. This shows the correlation between the hard band (8.00–20.9 keV) and the medium band (3.36–5.69 keV). Bin size is 64 seconds.

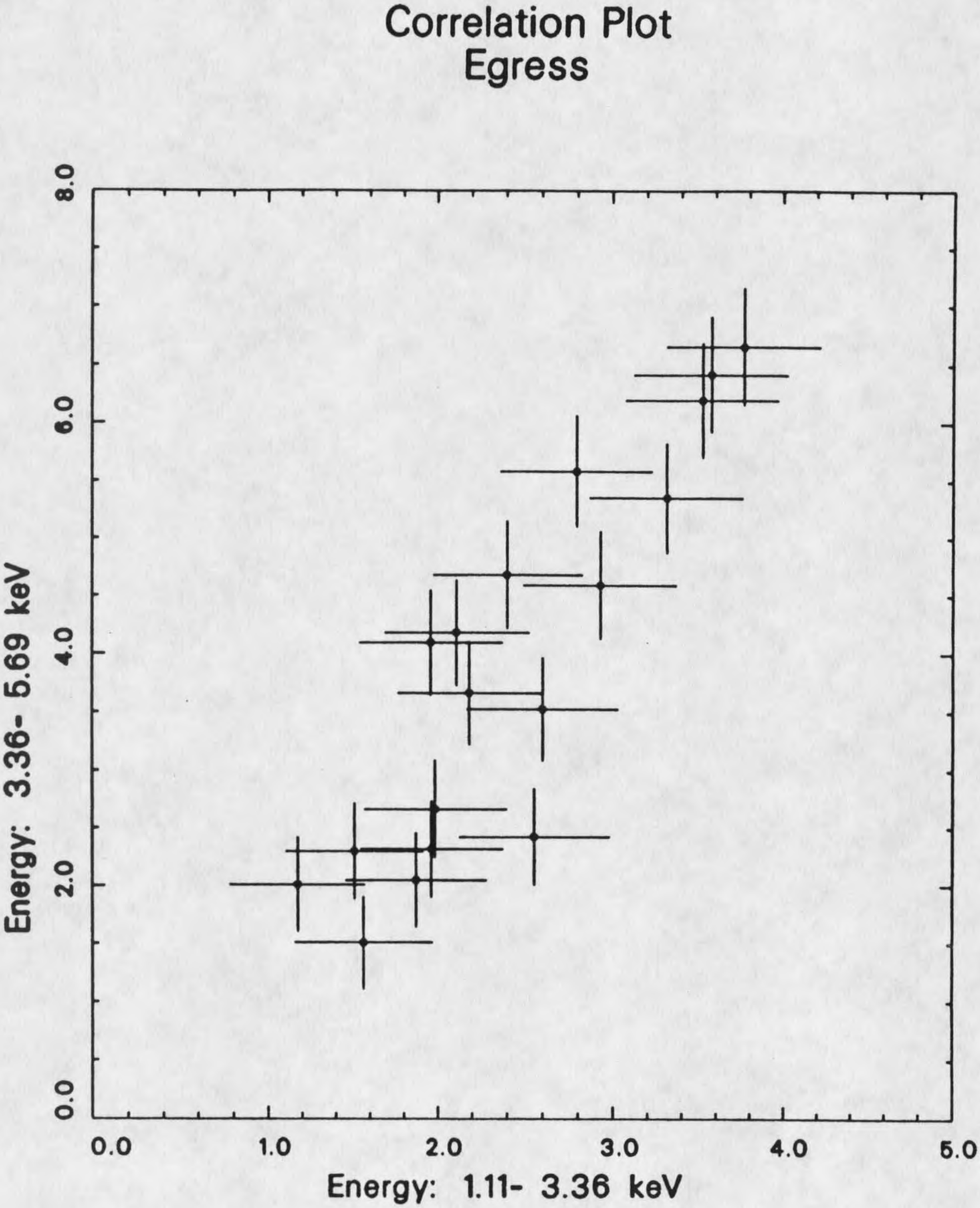

Figure 50. Medium versus soft energy flux correlation plot for the ingress section of the October data. This shows the correlation between the medium band (3.36–5.69 keV) and the soft band (1.11–3.36 keV). Bin size is 64 seconds.

flux horizontal branch. This implies that the hard and medium flux both increase for the first part of the egress, then the hard flux reaches a maximum while the medium flux continues to increase. This indicates a relatively longer time scale for variability of the medium flux compared with the hard flux. A spectral change and a lag are also again implied, this time in the sense that the medium lags the hard flux. Finally, Figure 50 shows the medium flux (3.36–5.69 keV) versus the soft flux (1.11–3.36 keV). This plot is again not linear; there is a slight bend in the lower flux region, indicating a lag of the medium energies over the soft. The fact that this bend is in the lower flux region, while Figure 49 shows the bend in the higher flux region indicate that the lag between these two bands occurs earlier in the data section, so the lag implied between the very soft flux and the hard flux is very large.

Cross correlation analysis. The qualitative results of the correlation plot analysis can be quantified by calculating the cross correlation of one energy band with respect to another. The algorithm used for calculation is that of Edelson and Krolik (1988) discussed in Chapter 6. However, since only one orbit of data is considered at a time, the cross correlation algorithm of Edelson and Krolik (1988) reduces to the classical discrete cross correlation. From this analysis, the possibility of any lags or leads of one energy band over another can be examined. Such lags are found, and offer very strong constraints on the nature of the modulation of the flux.

The cross correlation analysis of the April dip data was performed. The data in the following energy bands were accumulated, for before and after each dip separately, with 16 second time resolution: 1.11–3.36, 3.36–5.69, 5.69–6.84 (iron line energy band), 6.84–8.00 (iron absorption edge band), 8.00–10.32, and

10.32–20.9 keV. The cross correlation of the 10.32–20.9 keV data with each of the lower energy data with 16 second time resolution was calculated. The maximum lag considered depended on the length of the data section and the length of the decrease or increase. In general, the maximum lag was chosen by examining a plot of the cross correlation versus lag, and cutting the maximum lag where the cross correlation starts to turn up, due to edge effects. Next the cross correlation function was fit to a Gaussian function of the form

$$CCF = C\, e^{-(\frac{t-t_{lag}}{\sigma})^2} - 1 \tag{8.1}$$

where C is a constant describing the amplitude, t_{lag} is the lag, and σ is the width of the Gaussian. The spectral fitting routine used was a grid search from Bevington 1969. The uncertainties were evaluated assuming all parameters independent, and one parameter of interest. An example of the fit for the October data is shown in Figure 51. It is clear that the fits were over-determined.

The fit results for the April dip data are summarized in Table 11. The dips were split in two parts; the decrease to the lowest flux level, and the increase after the lowest flux level. In other words, the regions before and after the dip were analyzed separately. Because of the low flux level of the data, and because of another problem which will be discussed in the next section, many of the lags measured by the fit are consistent with zero. However, the data from the decrease of the third dip, all give lags different from 0 at greater than 3σ significance. The sense of the lag is that the hard data lags the soft data. In these data it is interesting that the iron line band has the greatest lag, and the iron absorption edge band has the least lag, although the difference between is only $\sim 5\sigma$. Another section in which there are lags different than 0 at greater than 3σ is after the

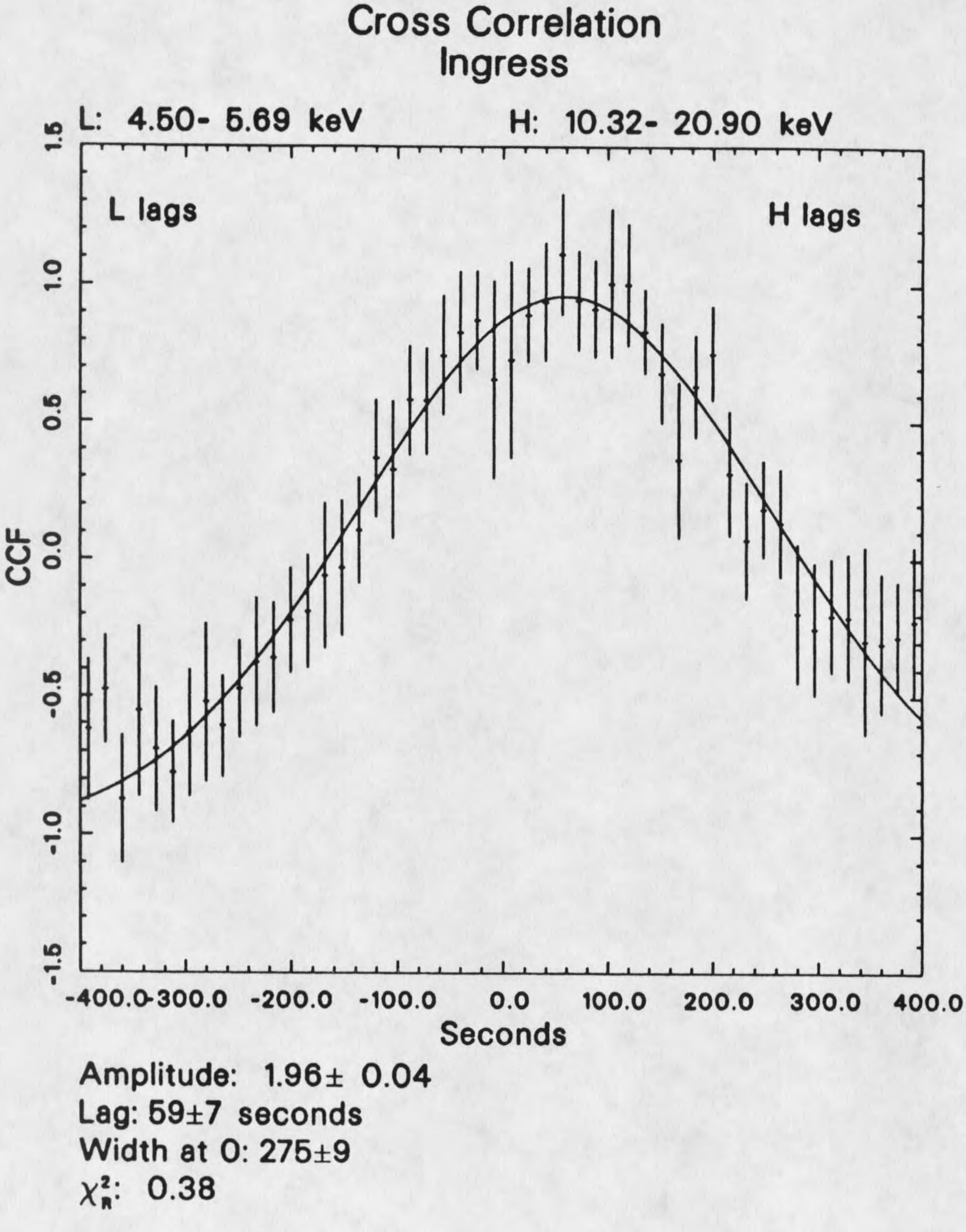

Figure 51. Example cross correlation from October ingress data. The hard band is (10.32–20.9 keV) and the soft band is in this case (4.50–5.69 keV). The peak to the right of 0 shows that the hard band lags. Best fit Gaussian is also shown, as well as the best fit parameter values and fit χ_R^2, below. Bin is 16 seconds.

Table 11. The results of fitting to the cross correlation of the April dip data. The correlations from before and after each dip are shown separately. The 10.32–20.9 keV data were correlated with the energy bands given in the first column. A positive lag indicates that the hard band lags the soft band. The uncertainties given are 1σ with one parameter of interest.

		Decrease		Increase	
	Energy Band (keV)	Time (s)	Lag (s)	Time (s)	Lag (s)
First dip	1.11 – 3.36	500	42 ± 11	400	-29 ± 22
	3.36 – 5.69		-13 ± 10		1 ± 12
	5.69 – 6.84		9 ± 11		17 ± 21
	6.84 – 8.00		19 ± 11		-48 ± 22
	8.00 – 10.32		-2 ± 14		-16 ± 18
Second dip	1.11 – 3.36	200	2 ± 6	300	-58 ± 12
	3.36 – 5.69		0 ± 6		-11 ± 7
	5.69 – 6.84		-6 ± 6		-32 ± 8
	6.84 – 8.00		-13 ± 7		-7 ± 8
	8.00 – 10.32		0 ± 7		4 ± 9
Third dip	1.11 – 3.36	300	45 ± 8	400	-9 ± 12
	3.36 – 5.69		43 ± 7		-10 ± 11
	5.69 – 6.84		67 ± 9		16 ± 18
	6.84 – 8.00		24 ± 8		-17 ± 13
	8.00 – 10.32		42 ± 8		4 ± 22

second dip where the 10.32–20.9 keV data lag the 1.11–3.36 keV data and also, the 5.69–6.84 keV data.

Partly because of the greater flux of the October data, the cross correlation from the ingress and egress data sections yields some interesting and important results. The data were divided into 7 energy bands for the ingress, and 6 energy bands for the egress. The energy bands and the cross correlation results are shown in the first two columns of Table 12. Again the cross correlation of the data was calculated as with the April data, with the cross correlation of the hardest band being taken with the lower bands. The cross correlation plot was fit with the same Gaussian function as the April data (Equation 8.1), and the lags measured by the fit are listed in Table 12. The errors listed are 1σ.

Table 12. Comparison of lags calculated using CCF and template fitting. In the first column is the energy band, in the second are the lags calculated by fitting the cross correlation function to a Gaussian, while in the third are the lags calculated by fitting the data to a template function. For the ingress data, the hard flux band is 10.32–20.9 keV, while for the egress data, the hard flux band is $\sim$ 9.0–20.9 keV. A negative sign indicates that the soft flux lags the hard, and the uncertainties are 1σ with one parameter of interest.

Energy (keV)	CCF Lag (s)	Template Lag (s)
Ingress:		
1.11 – 3.36	125 ± 9	186 ± 27
3.36 – 4.50	110 ± 7	106 ± 25
4.50 – 5.69	57 ± 7	83 ± 24
5.69 – 6.84	16 ± 6	51 ± 24
6.84 – 8.00	54 ± 8	64 ± 35
8.00 – 10.32	2 ± 6	7 ± 27
Egress:		
1.11 – 3.36	-142 ± 12	-268 ± 34
3.36 – 4.50	-110 ± 9	-196 ± 73
4.50 – 5.69	-96 ± 10	-50 ± 35
5.69 – 6.84	-61 ± 10	-104 ± 79
6.84 – $\sim$ 9.0	-38 ± 9	-15 ± 23

In contrast to the April dip data, large and significant lags are found for both the ingress and the egress of the October data. The sense of the lags is as understood qualitatively from the correlation plots; for the ingress, the hard flux lags, and for the egress the soft flux lags. Further, many of the energy bands show significant lags (1σ) with respect to those bands adjacent in energy.

The lags measured by the cross correlation technique are in general quite well determined. The Gaussian fit is generally quite good, as illustrated in Figure 51. However, these well determined lags may be somewhat misleading. Recall as discussed in Chapter 6, the uncertainty in the correlation function is in general underestimated. This underestimation in the uncertainty in cross correlation function points will propagate into the Gaussian fit parameters.

Nevertheless, examination of the lags in these tables shows some interesting patterns. First with respect to the ingress, it is noteworthy that the iron line band (5.68–6.84 keV) is not largely lagged with respect the highest band. In fact, the iron edge band (6.84–8.00 keV) shows a larger lag. Also, the iron edge band does not lead the 4.50–5.69 keV band significantly.

The egress data also yield interesting results. Many of the lower bands show no remarkable lag with respect to each other. The more significant lags occur between the $\sim$ 8.0–20.9 keV bands and those of lower energy. This implies that the hard energy band recovers to normal flux levels rapidly, and the soft bands recover nearly together, more slowly.

Another way to discover the lags and also the relative time scale for the flux change is through the transfer function. If the soft light curves from the ingress data truly have the same profile as the hard light curves, and if the soft light curves are viewed as a convolution of a transfer function and the hard light curve, then the shape of the transfer function would be approximately a delta function at the lag measured. If, on the other hand, as may be true for the egress data, the hard light curve recovers quickly and the soft light curves recover more slowly, then the transfer function will have a larger spread than a delta function, but still peaking at the same lag. These calculations have yet to be done, and may not yield these desired results because of the noise in the light curves.

Template fitting analysis. As mentioned in the last section, there is a problem with using the cross correlation analysis to find the lags. In this section, the problem is described as well as an alternate method to find the lags.

The data sections which contain the ingress and the egress are of course of finite duration. The length of the data section containing the ingress is 1008 seconds, while the length of the egress data section is 1136 seconds. If the lag between two energy bands is large compared with the length of the data section, the cross correlation function will be contaminated by effects due to the ends of the data.

Ideally, the cross correlation will peak at the value of the lag between the two energy bands considered. However, this is only true for data sections which have length much longer than the lag considered. In other cases, the peak of the CCF will be at a time less in magnitude than the true lag. Recall that the cross correlation function at a lag τ can be understood to be the sum of the products of the difference between adjacent pairs of points and the respective means when the data from different energy bands are shifted with respect to each other by an amount τ (Equations 6.6 and 6.7). The data an amount τ from the ends of the data section clearly do not contribute to this sum. Therefore, the CCF is smaller at large τ than it would be if the data were much longer in duration. This end effect causes the peak to decrease sooner, causing the lag which is measured to be smaller than the actual lag.

Note that this effect is only important for lags which are large compared to the length of the data section. How long is too long? The rule of thumb generally seems to be that lags can be reliably measured which are less than or equal to 10% of the length of the data section. For the ingress data, this becomes about 100 seconds, while for the egress data, it is about 110 seconds. Note that of the lags given in Table 12 for the ingress and the egress, six are at or near this limit. This is one reason to try to measure the lags in a different way.

Another way to quantify the behavior of the source during the ingress and egress is to fit the data to a template. This approach has the advantage that, though it is not elegant, it is direct. The template which was used to model the increase or decrease in flux was an arc tangent function

$$Flux = A \arctan\left(\frac{t - t_1}{B}\right) + y_1. \tag{8.2}$$

This is a four parameter model. The parameter y_1 is the distance that the average value of the flux is raised above the $Flux = 0$ line, and the parameter A is the amplitude of the arctangent curve. The two physically more interesting parameters are t_1 and B. The parameter t_1 is the time at which the flux drops half way from its original value to its final value, while B gives the extent of the increase or decrease. That is, if $B = 1$, the minimum value, the slope of the decrease or increase is infinite at t_1.

The data from seven energy bands from the ingress and six energy bands from the egress were fit to the arc tangent model. The results of the fittings are summarized in Table 13, along with the fit results from the entire energy range, (1.11–20.9 keV). However, in both the ingress and the egress, not all the data in the section were fit. This is because a satisfactory fit could not be obtained if all of the data were used, because the flux increase and decrease are not isolated in the egress and ingress data sections. A satisfactory fit was defined by two criteria: (1) the reduced χ^2 is low enough so that the probability is less than 10% that such a large value of χ_R^2 would be obtained from the correct fitting function (Bevington 1969), and (2) the best fit value obtained for B is not the minimum value of one. The reason for the first criterion was so that the change in flux would be correctly isolated. There is no reason to expect that the only change in flux in the data section should be due to just the presumed occultation of the source. Particularly, it was observed in the correlation plot in Figure 47 the spectrum hardens just before the ingress. Therefore, the light curve of the harder energy bands increases before it decreases. In this case, the fit is unsatisfactory, unless the first increase is removed. The second criterion is chosen for physical reasons, because it is not realistic to expect the flux change to occur in such a way that the slope should be infinite. This would be the case if the source were a point, and clearly, the source should have a finite size. In order to make the removal of data from the beginning and end of data sections consistent, the same amount of data was removed from each energy band, and the least amount was removed so that satisfactory fits would be obtained for all of the energy bands. For the ingress data, the first 10 points and the last point were removed, leaving 21 points to fit. For the egress data, only the first 2 points were removed, leaving 34 points to fit.

After trimming the data, the data were fit. The fitting in this case was done using the Statistical Analysis System, or SAS, available on the Vax node TREX. The weighted nonlinear regression NLIN procedure was used, and the method used was the modified Gauss-Newton method (SAS User's Guide: Statistics 1982). The best fit values were obtained with less than 50 iterations, and the results were stable with respect to starting value. The fitting results are listed in Table 13, and the data fits for the total flux (1.11–20.9 keV) as well as for the separate energy bands, are shown in Figures 52, 53 and 54 for the ingress, and Figures 55, 56 and 57 for the egress.

Table 13. Fit results for the arctangent template. All errors are 1σ.

Energy (keV)	t_1(seconds)	B(seconds)	$\chi^2/d.o.f.$
Ingress:			
1.11 – 3.36	23383 ± 14	*14 ± 16	17.2/17
3.36 – 4.50	23463 ± 10	10 ± 11	13.3/17
4.50 – 5.69	23486 ± 7	*7 ± 17	18.5/17
5.69 – 6.84	23518 ± 5	*7 ± 15	19.5/17
6.84 – 8.00	23505 ± 26	43 ± 39	24.8/17
8.00 – 10.32	23562 ± 15	*18 ± 17	19.7/17
10.32 – 20.90	23569 ± 23	*36 ± 32	22.2/17
1.11 – 20.90	23492 ± 7	33 ± 11	19.3/17
Egress:			
1.11 – 3.36	12159 ± 27	22 ± 39	31.8/30
3.36 – 4.50	12087 ± 70	212 ± 136	30.4/30
4.50 – 5.69	11941 ± 28	44 ± 40	36.7/30
5.69 – 6.84	11995 ± 76	256 ± 179	28.4/30
6.84 – ~ 9.0	11906 ± 9	*9 ± 22	34.4/30
~ 9.0 – 20.90	11891 ± 21	*20 ± 21	38.8/30
1.11 – 20.90	11928 ± 23	78 ± 37	62.9/30

* Those fits for which the parameter B was not statistically necessary.

A interesting feature of the data emerged from this fitting. All the data were fit twice; once with the parameter B being left free, and also with it being fixed to its minimum value of 1. In some cases, the reduced χ^2 was nearly the same for both fits, indicating that the additional parameter B was statistically not necessary. These cases are marked with an (*) in Table 13. However, in other fits, the χ^2 was substantially lower when B was left free, indicating that this parameter was necessary for a satisfactory fit. This result can be quantified by calculating the F statistic given in Equation 3.1 (see also Bevington 1969). In all the cases

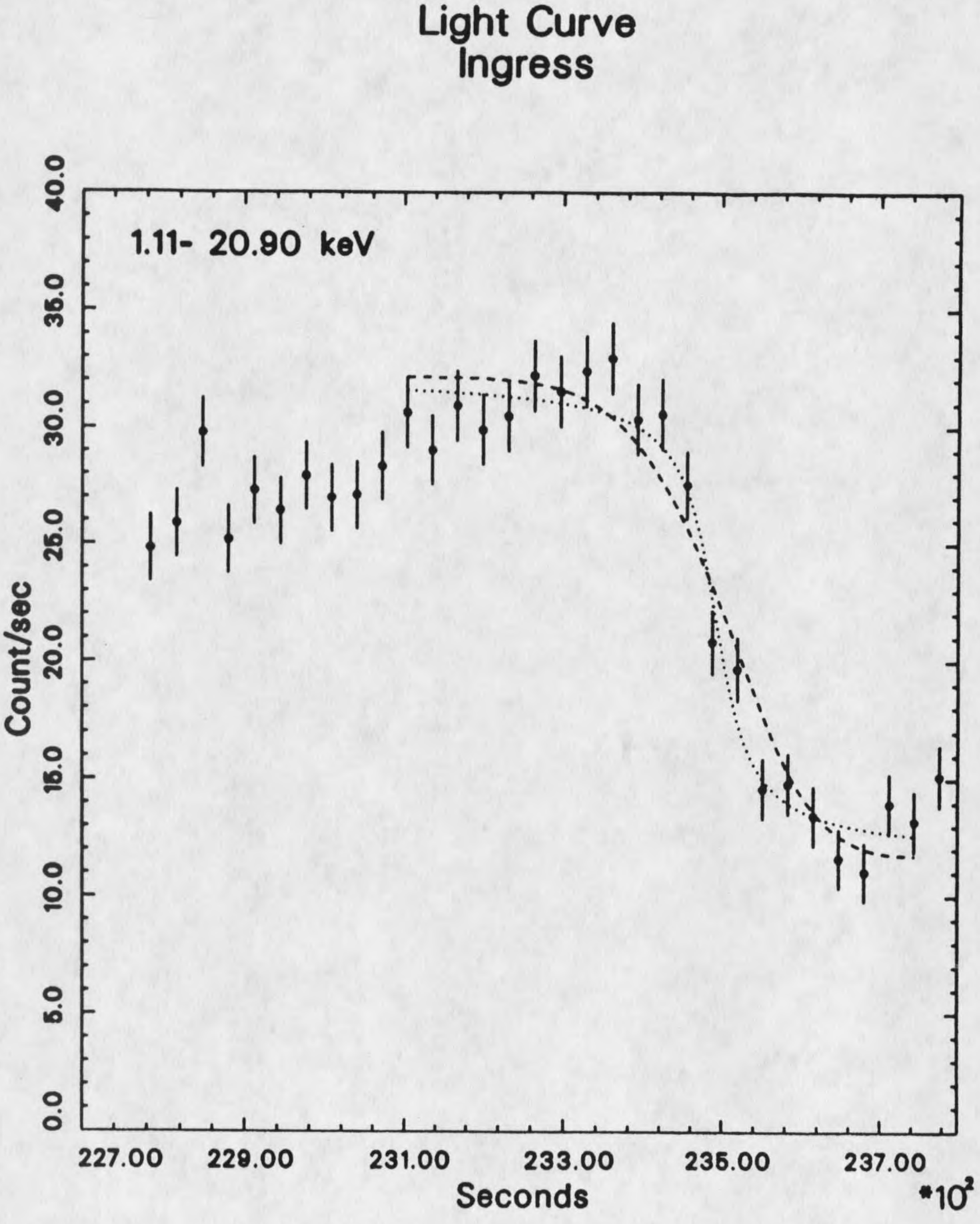

Figure 52. Template fitting to total ingress light curve. The dotted line shows the best fit from the arctangent template fitting, while the dashed line shows the predicted curve from the model calculation. Data bin size is 32 seconds.

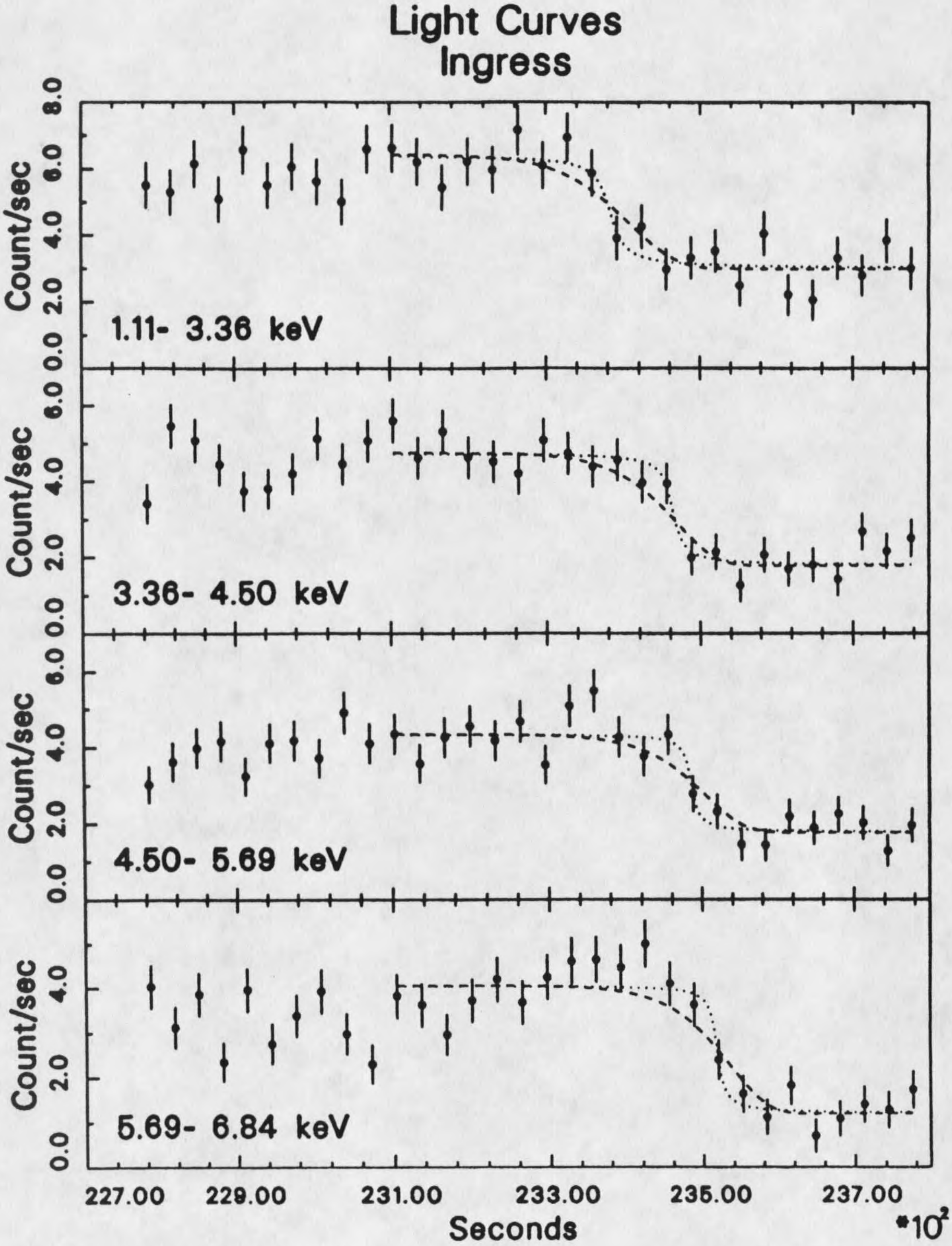

Figure 53. Template fitting to softer ingress light curves. The dotted line shows the best fit from the arctangent template fitting, while the dashed line shows the predicted curve from the model calculation. Data bin size is 32 seconds.

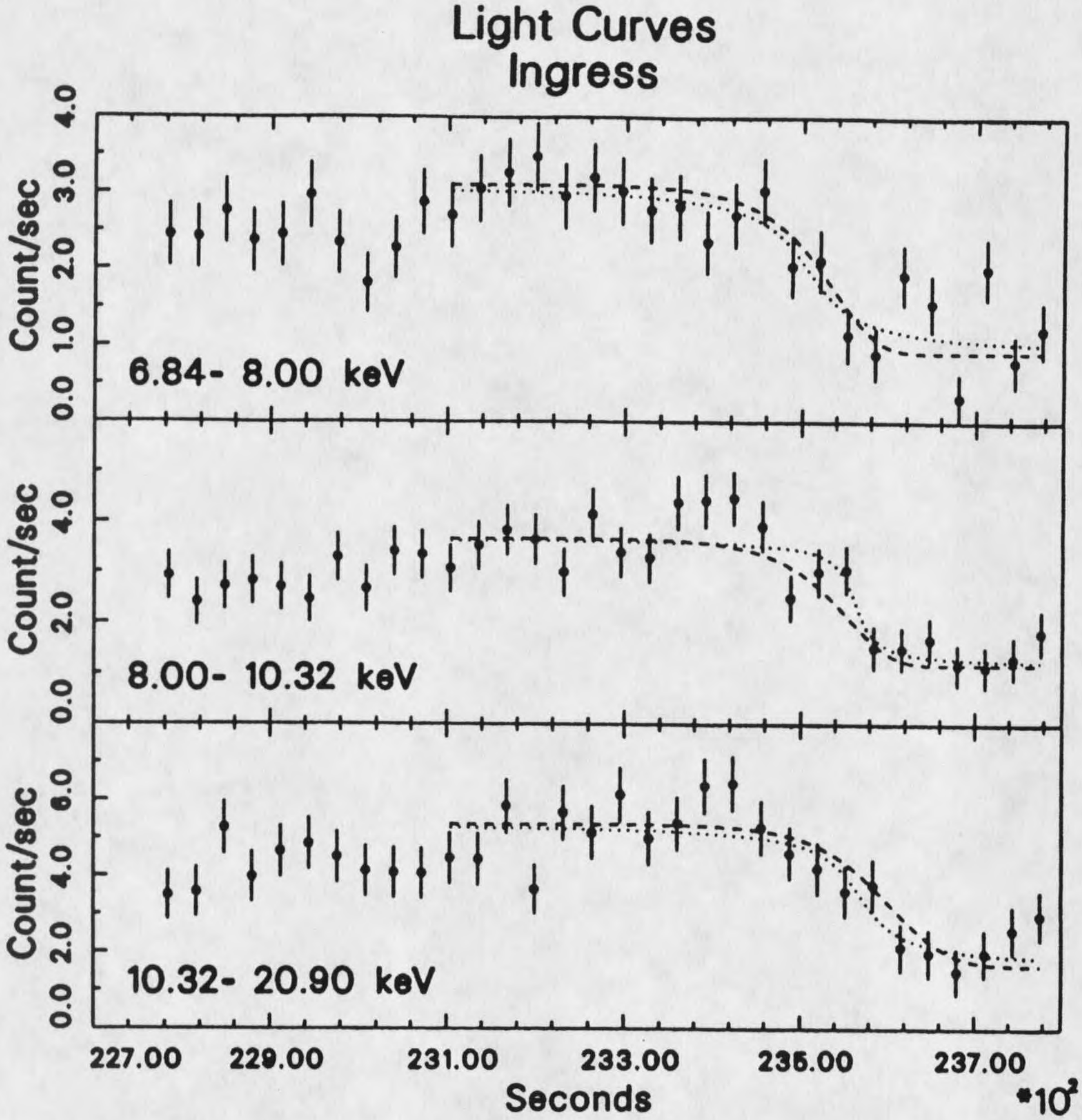

Figure 54. Template fitting to harder ingress light curves. The dotted line shows the best fit from the arctangent template fitting, while the dashed line shows the predicted curve from the model calculation. Data bin size is 32 seconds.

for which B was found to be statistically necessary, the F statistic indicated a confidence level of greater than 99%.

This result implies for those marked with an (*), the fitting program finds that the drop or rise in flux occurred nearly instantaneously. This is the case for

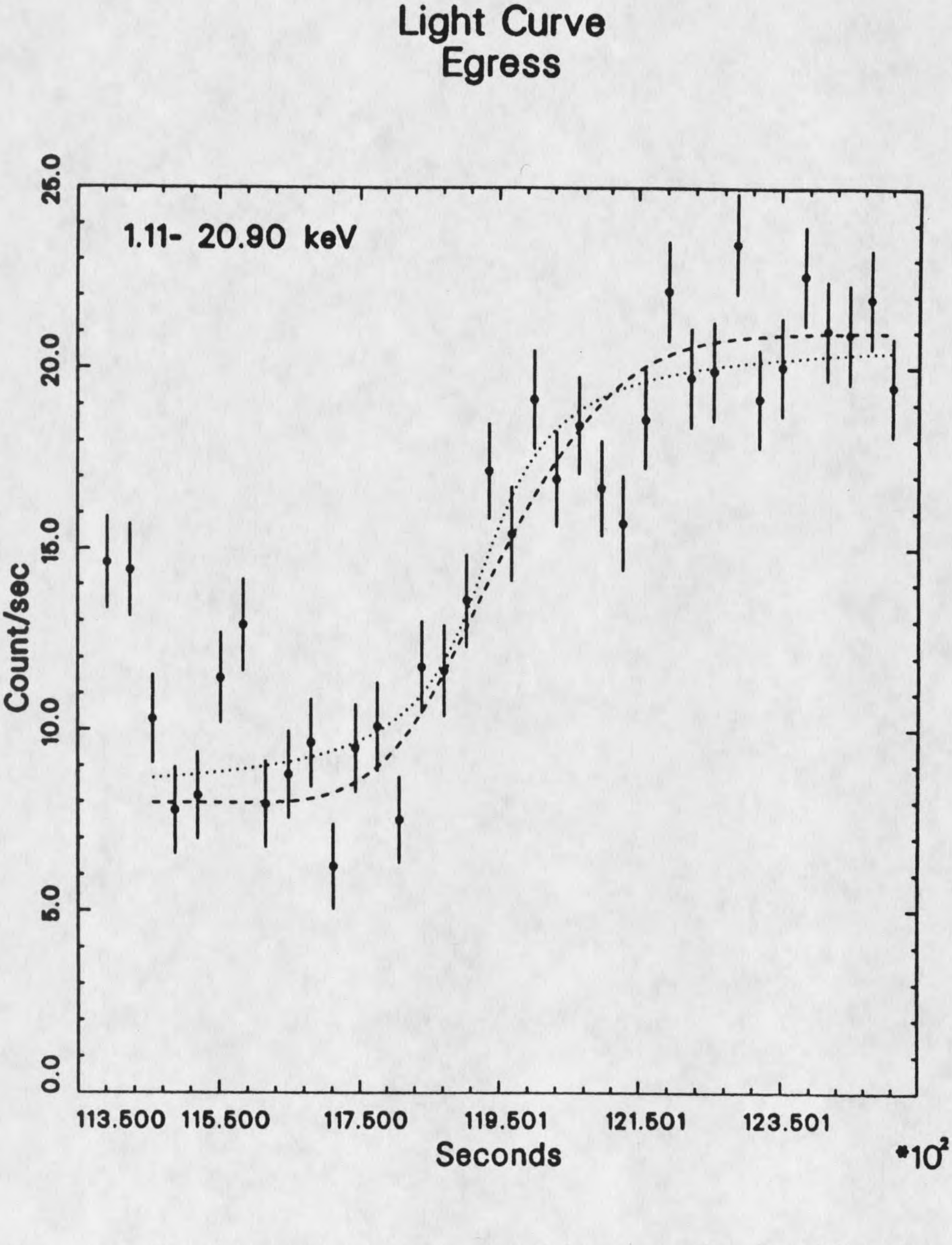

Figure 55. Template fitting to total egress light curve. The dotted line shows the best fit from the arctangent template fitting, while the dashed line shows the predicted curve from the model calculation. Data bin size is 32 seconds.

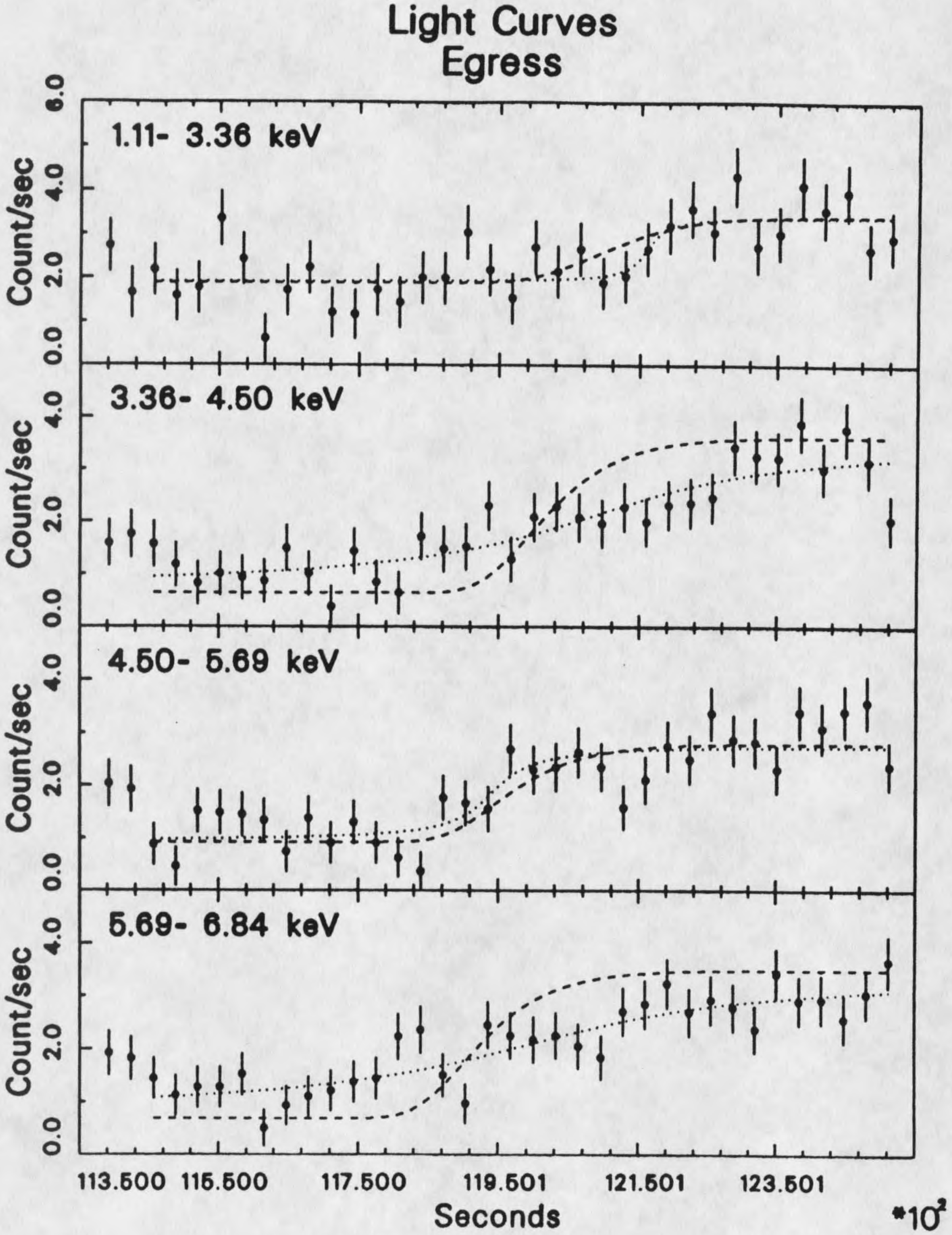

Figure 56. Template fitting to softer egress light curves. The dotted line shows the best fit from the arctangent template fitting, while the dashed line shows the predicted curve from the model calculation. Data bin size is 32 seconds.

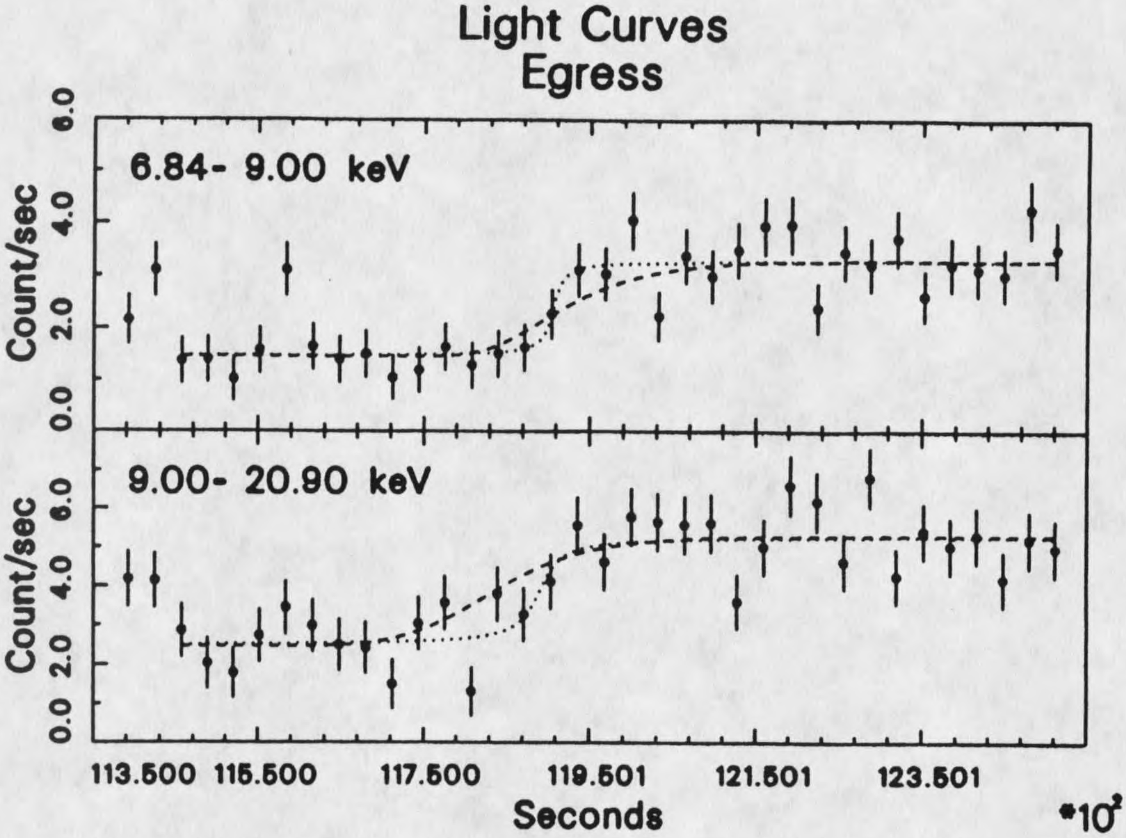

Figure 57. Template fitting to harder egress light curves. The dotted line shows the best fit from the arctangent template fitting, while the dashed line shows the predicted curve from the model calculation. Data bin size is 32 seconds.

nearly all of the ingress data, and for the hard flux energy bands of the egress. For those not marked, the fitting program could distinguish some rise time. This is true for the soft energy bands of the egress. Model implications of these facts will be discussed later, in the section on implications of realistic geometries; however, note that the best fit values for B are not well determined, except for the total flux cases, making a detailed model of the rate of flux decrease for the soft flux bands of the egress impossible. Determining the rise time from the transfer function would probably also be difficult. For the cases of the template fitting for the total flux range, from 1.11 to 20.9 keV, shown in Figures 52 and 55, the values for B are better determined. The ingress value of 33 ± 11 seconds is quite well determined, showing that B is different from 1 by 3σ. The egress value of 78 ± 37 seconds is not so well determined, but still shows B to be different from 1 by 2σ. These figures suggest that the rate of increase of the egress is slower than the rate of decrease of the ingress; however, the uncertainties are too large to confirm this idea.

With these data in hand, the lags can be calculated and compared to those measured using the Gaussian fit to the cross correlation function, as described in the previous section. These lags are given in Table 12.

In most cases the lags calculated from the two different methods are consistent with each other, the difference between them being smaller than the sum of the uncertainties. However, for the data from the lower flux bands, the difference in results is significant. Specifically, the lags from the 1.11–3.36 keV data for the ingress, and the 1.11–3.36 and 3.36–4.50 keV data for the egress are not consistent between the two methods. Note that the lags measured by the cross correlation function in these cases are equal to or larger than 10% of the data section length (100 seconds for the ingress and 110 seconds for the egress), and also the CCF lags are in these cases consistently smaller than those measured by the template method. This illustrates the effect of the ends in the cross correlation and shows the lags measured by the CCF method to be underestimated, as expected. Therefore, the lags are more reliably measured, for the softer fluxes, by the template method.

It is interesting to note that the lags of the ingress and the egress can be seen by examination of the light curves at different energies, shown in Figures 52 and 53 for the ingress and Figures 56 and 57 for the egress. In general, the maximum flux attained was larger for the ingress, and thus a different vertical scale was used. If these light curves are examined closely, the lags in the ingress can be easily seen.

The profile of the ingress light curves appears approximately the same, and the data are purely lagged. In contrast, for the egress, the data in the energy range 2.24–6.84 keV appear to have a long slow increase, while the 6.84–20.9 keV data have a sharper increase.

Finally, the template method should be applied to the April dip data, but has not yet been because of lack of time. As shown in Table 11, the cross correlation method does not find convincing evidence for lags in these data. However, the correlation plots suggest that they must be present. A likely reason that the cross correlation does not find significant lags is the end effect, since the dip data must be divided into regions before the dip and after the dip. Therefore, the sharpest decrease or increase occurs at the end or beginning of the data stream.

Spectral Analysis In this section, the regions of fastest variability are examined by spectral analysis, in order to further understand the nature of the fastest variability. The same data are examined as in the previous section; the data from the three dips from the April data, as well as the ingress and egress from the October data.

First we consider the April dip data. The results of the 256 second spectral fitting, as plotted in Figures 84, 85 and 86 in Appendix 1 were examined. Some of the spectral fitting results were consistent between adjacent spectra. In this case, these spectra could be combined, and fit, resulting in tighter parameter constraints. In the end, 11 spectra were found to describe the three dips. Spectral fitting results of these spectra are listed in Table 14.

Table 14 is divided into 4 sections vertically with the first 3 sections being from each of the three dips. The spectra names are listed in the first column. Along with the names are a designation (b), (a), or (d). This refers to the light

Table 14. The results of spectral fitting to the combined April dip data. Line energy fixed at 6.4 keV. All errors are 90% confidence.

Spectrum	Subframes	Photon Index	$\log(N_H)$ (cm^{-2})	Line Flux (count s^{-1})	Equivalent Width (eV)	χ^2_R /d.o.f.	Difference‡ in χ^2 Plot	Flux†
A1D10(b)	136–139	1.46 ± 0.17	22.70 ± 0.16	*1.52 ± 0.50	490 ± 160	0.96/25	$> 90\%$	*39.8
A1DB3(b)	140–142	1.97 ± 0.22	23.03 ± 0.12	*1.49 ± 0.66	440 ± 190	1.25/25	$> 99\%$	*56.3
A1DIP(d)	143–144	1.03 ± 0.58	22.54 ± 0.87	$<$ *0.59	< 630	1.61/26	—	*9.6
A1DA1(a)	145–147	1.40 ± 0.22	22.67 ± 0.22	*0.91 ± 0.56	360 ± 220	1.08/25	$> 1\sigma$	*31.5
A2DBFR(b)	157–158	1.51 ± 0.20	22.79 ± 0.16	1.55 ± 0.50	600 ± 190	0.73/25	$> 90\%$	34.4
A2DIP(d)	159–160	1.06 ± 0.49	22.32 ± 0.81	< 0.64	< 960	1.01/26	—	7.0
A2DA3(a)	161–166	1.20 ± 0.10	22.42 ± 0.18	1.11 ± 0.23	530 ± 110	1.52/25	$> 1\sigma$	23.8
A2D3(a)	167–168	1.71 ± 0.21	22.94 ± 0.14	0.93 ± 0.51	400 ± 240	1.44/25	$> 90\%$	32.4
A3DB2(b)	264–267	1.51 ± 0.13	22.70 ± 0.14	1.13 ± 0.35	440 ± 130	1.40/25	$> 99\%$	33.4
A3DIP(d)	268–269	1.10 ± 0.38	22.71 ± 0.46	< 0.39	< 390	0.53/26	—	10.6
A3DA1 (a)	270–272	1.27 ± 0.18	22.43 ± 0.32	0.77 ± 0.36	410 ± 190	0.48/25	$> 90\%$	22.1
ADIP(all dips)		1.03 ± 0.26	22.52 ± 0.41	$<$ *0.26	< 290	1.15/26	—	*9.1

(b)=before dip, (a)=after dip, (d)=dip spectrum.

†Continuum flux is from 2–10 keV, intrinsic, in count s^{-1}.

‡Smallest difference between the N_H versus photon index χ^2 contours for this spectrum and the ADIP spectrum.

*Corrected for aspect.

curve and shows whether the spectrum is from (b) before the dip, (d) during the dip, or (a) after the dip. As a group, the spectra with (b) or (a) are referred to as the 'non-dip' spectra, while those with (d) are referred to as the 'dip' spectra. All spectra were fit with a power law, line and absorption fit (Equation 4.2). However, notice that the dip spectra did not admit a line fit. That is, in these cases, the uncertainty in the line was found to be larger than the best fit parameter value. Therefore, for these, a line flux upper limit was measured.

In the third column of the table the photon index is listed. These show a dramatic decrease in the dips, indicating a hard spectrum at the point of lowest flux. The third column shows the column density. When tested against the constant hypothesis as a group, the column density is shown not to vary significantly, and any correlation would be positive with respect to flux. Therefore, the interesting question is whether the photon index varies significantly. Since the separate dip spectra are of such low flux level, as well as being composed of only 2 subframes, the parameter values in the dips are not well constrained. Examination of these parameter values shows that it cannot be concluded that the spectrum is significantly harder in each dip compared with the adjacent spectra. However, it can be seen that the dip spectra fit parameters are consistent from the three dips. Therefore, it is justified to combine the three dip spectra into one, in order to obtain better statistics. The spectral fitting results for this combined spectrum, called ADIP, are listed in the bottom line of the table. The photon index is found to be very low, indicating a very hard spectrum. The absorption column is moderate. No line was admitted in the fit, but the upper limit at the 90% confidence level is found to be small.

Then, it is interesting to investigate whether the ADIP spectrum is significantly different than the non-dip spectra from the three dips. Because of the uncertainties are calculated using 1 interesting parameter, the comparison cannot be done by examining the parameter values and uncertainties alone, but must be done by examination of the χ^2 contour plots. These are shown in Figures 58, 59 and 60, for each dip separately, along with the contours from ADIP. Only the 90% and 1σ contours are shown, although in a few cases, the difference between the ADIP contour and the non-dip contours is greater than 99%. The largest difference between the ADIP contours and the non-dip contours is listed in the 8th column of Table 14. In general, the spectra before the dips differs from the ADIP spectrum by at least 90%, while the spectra just after the dip differs from the ADIP spectrum by only at least 1σ. For the second dip, however, where a significant amount of data were available after the dip, the contours from a second spectrum after the dip differs from the ADIP spectrum contours by more than 90%. Comparison of the χ^2 contours shows a significant spectral change in the dips compared with the non-dip spectra.

In the fourth column of the table, the line flux is listed. As mentioned previously, the dip spectra do not admit a line fit. Note that the combined dip spectrum ADIP also did not admit a line fit, and also the upper limit for this spectrum at the 90% confidence level for one interesting parameter was only $0.26\,\mathrm{count\,s^{-1}}$. When the line flux parameter values of the non-dip spectra are compared with this upper limit, it can be seen that they are significantly larger at the 90% confidence level. Note that the line energy is coupled to the line flux; however, in this spectral fitting the line energy was fixed at 6.4 keV, assuming no line energy shift. Thus, it is valid just to compare the best fit values and uncertainties. Therefore, these spectral fittings show that the line flux decreases significantly in the dips, when compared with the non-dip spectra.

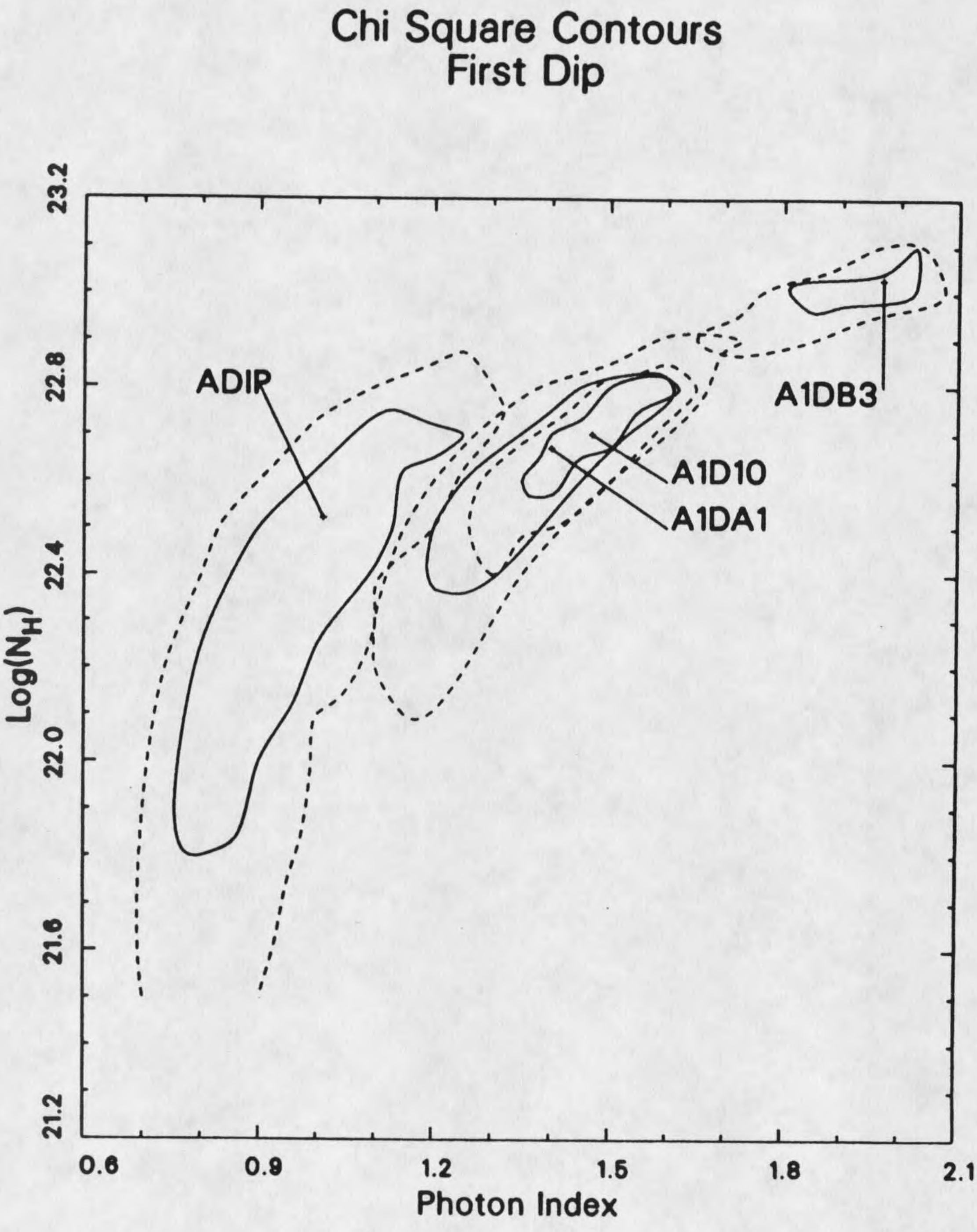

Figure 58. N_H versus photon index χ^2 contours from the first dip of the April data. The χ^2 contours for the non-dip spectra from the first dip of the April data are shown, as well as the contours from the ADIP spectrum. The solid line shows the 1σ contour, while the dashed line shows the 90% contour.

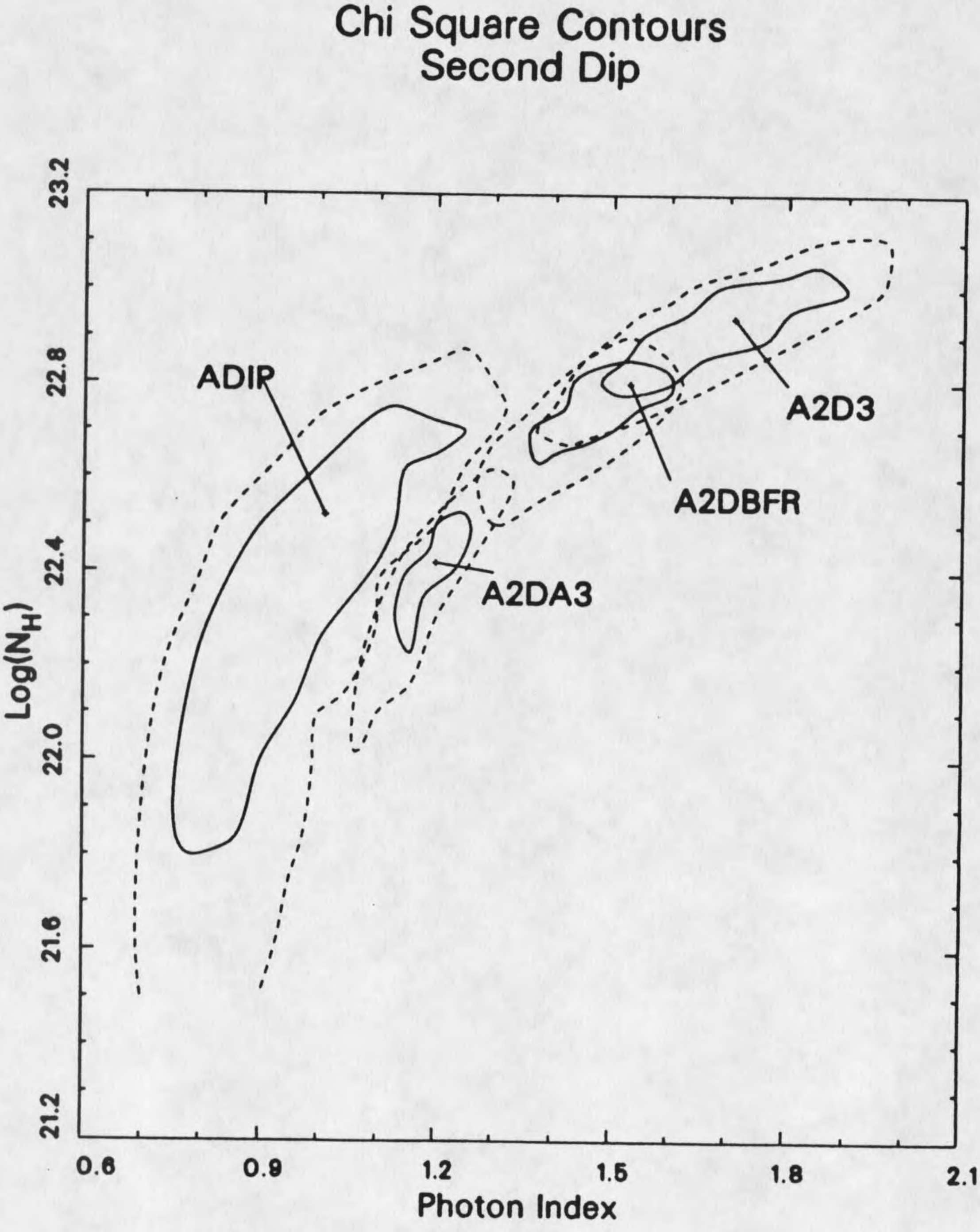

Figure 59. N_H versus photon index χ^2 contours from the second dip of the April data. The χ^2 contours for the non-dip spectra from the second dip of the April data are shown, as well as the contours from the ADIP spectrum. The solid line shows the 1σ contour, while the dashed line shows the 90% contour.

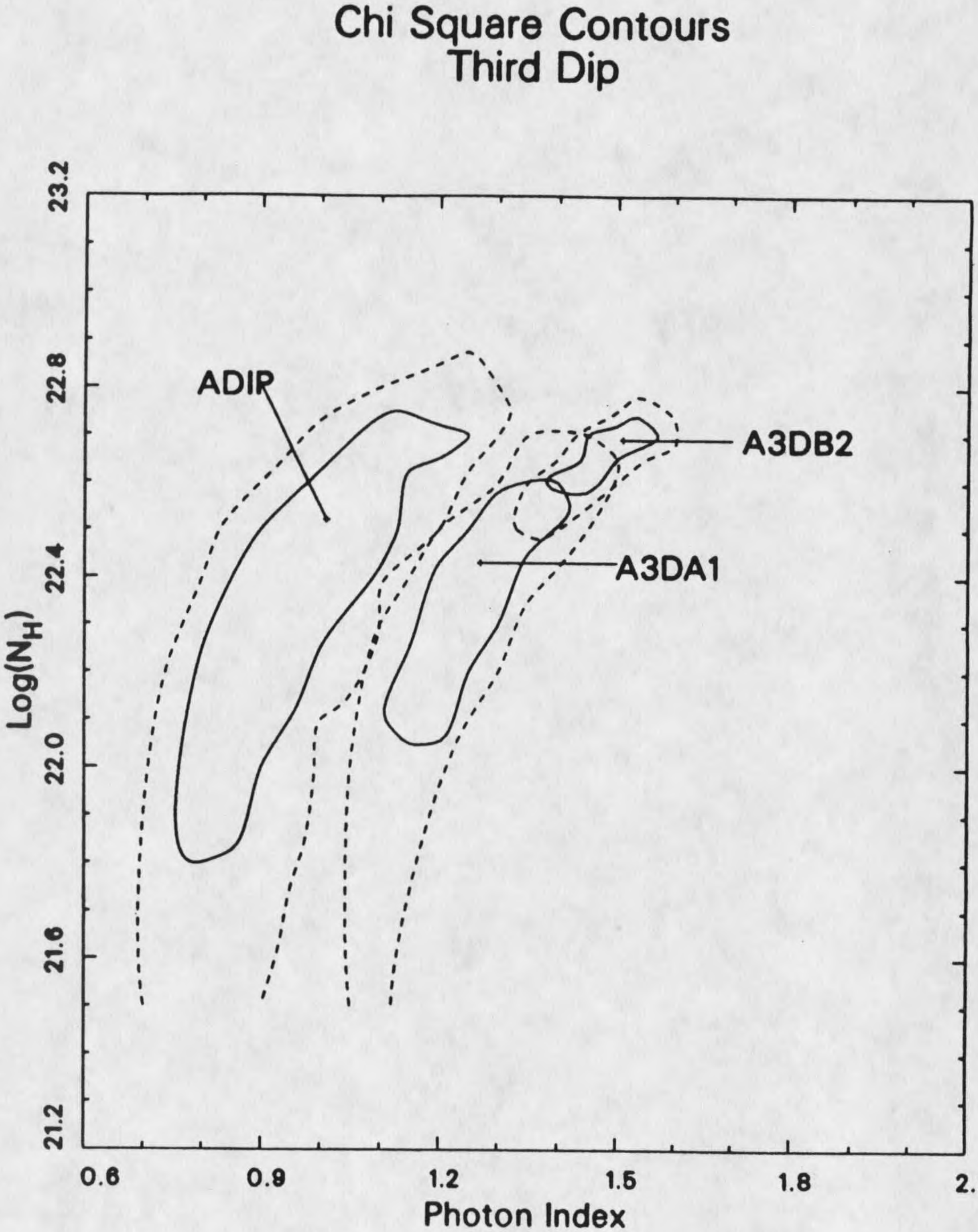

Figure 60. N_H versus photon index χ^2 contours from the third dip of the April data. The χ^2 contours for the non-dip spectra from the third dip of the April data are shown, as well the contours from the ADIP spectrum. The solid line shows the 1σ contour, while the dashed line shows the 90% contour.

The best fit spectra for ADIP and the eight non-dip spectra are shown in Appendix 2, Figures 95–103.

For the October ingress and egress data, the spectral fitting was carried out in the same way. First the results from fitting the 256 second spectra from these two data groups were examined in order to see which could be combined. For the ingress, the spectral change was too fast for any spectra to be combined. The results of spectral fitting to the combined spectra are found in Table 15.

In the first column of Table 15 are listed the names of the spectra. There are two groups of data corresponding to the ingress. The first four spectra correspond to all the data in the ingress data stream divided into equal parts. The OIHRD3 and OHLT5I spectra will be explained near the end of this section. The egress data were split into 3 spectra.

The results of spectral fitting to the October ingress and egress spectra are qualitatively similar to the results from spectral fitting of the April dip data. The spectral index is observed to drop as the flux decreases. Also, during some of the low flux spectra, the line model is not admitted. However, some of the details are different. First, for some of the low flux spectra, particularly O5E1, it was necessary to fix the absorption column at the Galactic value of $\log(N_H) = 21.2$. This is not an anomalous occurrence; many of the low flux 256 second spectra required this also. Also, some of the best fit spectral indices found were very hard, with photon indices below 1.0. Line equivalent widths seem to always be very large for this source, but they become even larger here, especially for the low flux egress spectra. Unfortunately, here it cannot be shown that spectra differ from adjacent spectra significantly, as was possible for the April data.

From the spectral fitting of the April and October data, at least one trend seems to be apparent. It seems that the spectral index is correlated with the

Table 15. The results of spectral fitting to the combined spectra from the October ingress and egress data. Line energy fixed at 6.4 keV. All errors are 90% confidence.

Spectrum	Subframes	Photon Index	$\log(N_H)$ (cm^{-2})	Line Flux ($count\,s^{-1}$)	Equivalent Width (eV)	χ^2_R /d.o.f.	Flux†
Ingress:							
OI1	245–246	1.46 ± 0.16	22.46 ± 0.29	0.58 ± 0.47	210 ± 170	0.89/25	35.2
OI3	247–248	1.54 ± 0.16	22.34 ± 0.28	0.95 ± 0.49	320 ± 170	1.69/25	38.6
OI5	249–250	1.28 ± 0.16	22.62 ± 0.20	1.42 ± 0.51	460 ± 170	0.72/25	36.6
OI7	251–252	1.27 ± 0.28	22.27 ± 0.70	< 0.41	< 310	0.67/26	15.0
OIHRD3	see text	0.85 ± 0.17	21.2(f)	0.89 ± 0.51	640 ± 370	0.59/26	14.5
OHLT5I	see text	1.54 ± 0.35	22.54 ± 0.43	< 0.41	< 320	0.76/26	16.6
Egress:							
O5E1	152–156	0.85 ± 0.11	21.2(f)	0.77 ± 0.23	770 ± 230	0.47/26	10.5
OE6	157–158	0.99 ± 0.21	22.31 ± 0.47	0.98 ± 0.44	530 ± 240	0.71/25	19.9
OE8	159–160	1.39 ± 0.20	22.61 ± 0.25	1.14 ± 0.47	500 ± 200	0.82/25	28.6

†Continuum flux is from 2–10 keV, intrinsic, in $count\,s^{-1}$.

flux. This result could be predicted by examining the hardness ratios at the dips for the April data, Figures 25 and 26, and the softness ratio for the ingress and egress for the October data, Figure 27. However, examination of the softness ratio for the October data suggests something else as well. The ingress data occur at about 23,000 seconds in this plot. The softness ratio is first observed to decrease. This is expected for a hardening spectrum; the soft flux becomes relatively smaller. However, the last 3 points of the softness ratio shows a sudden increase in softness, suggesting a softer spectrum.

To examine the possibility of the spectrum becoming softer again at low flux, the last three points were picked up, essentially. The actual data selection for this spectrum was that the count rate of the 8.00–20.9 keV band should be between 0 and 5 counts s^{-1}. This resulted in the spectrum called OHLT5I. For comparison, another spectrum was made, selected to be between 5 and 8.5 counts s^{-1} in the same energy band. This spectrum was called OIHRD3, and was composed of essentially the previous 2 points.

Recall that the binning of the softness ratio light curve was 64 seconds. This implies that OIHRD3 was comprised of only 128 seconds of data, while OHLT5I was comprised of only 192 seconds of data. Most of the spectra fit during this analysis were composed of at least 256 seconds of data. Because of the short time of accumulation of these spectra, the PHA spectra are shown in Figure 61 for OIHRD3, and Figure 62 for OHLT5I. These figures show that these spectra are acceptable, and not dominated by noise.

The spectral fitting results are listed in Table 15. The spectral indices are remarkably different between these two spectra. As predicted by the softness ratio, OIHRD3 had a hard spectrum having a photon index of 0.85 ± 0.11, while OHLT5I had a soft spectrum having a photon index of 1.54 ± 0.35. Again however, real

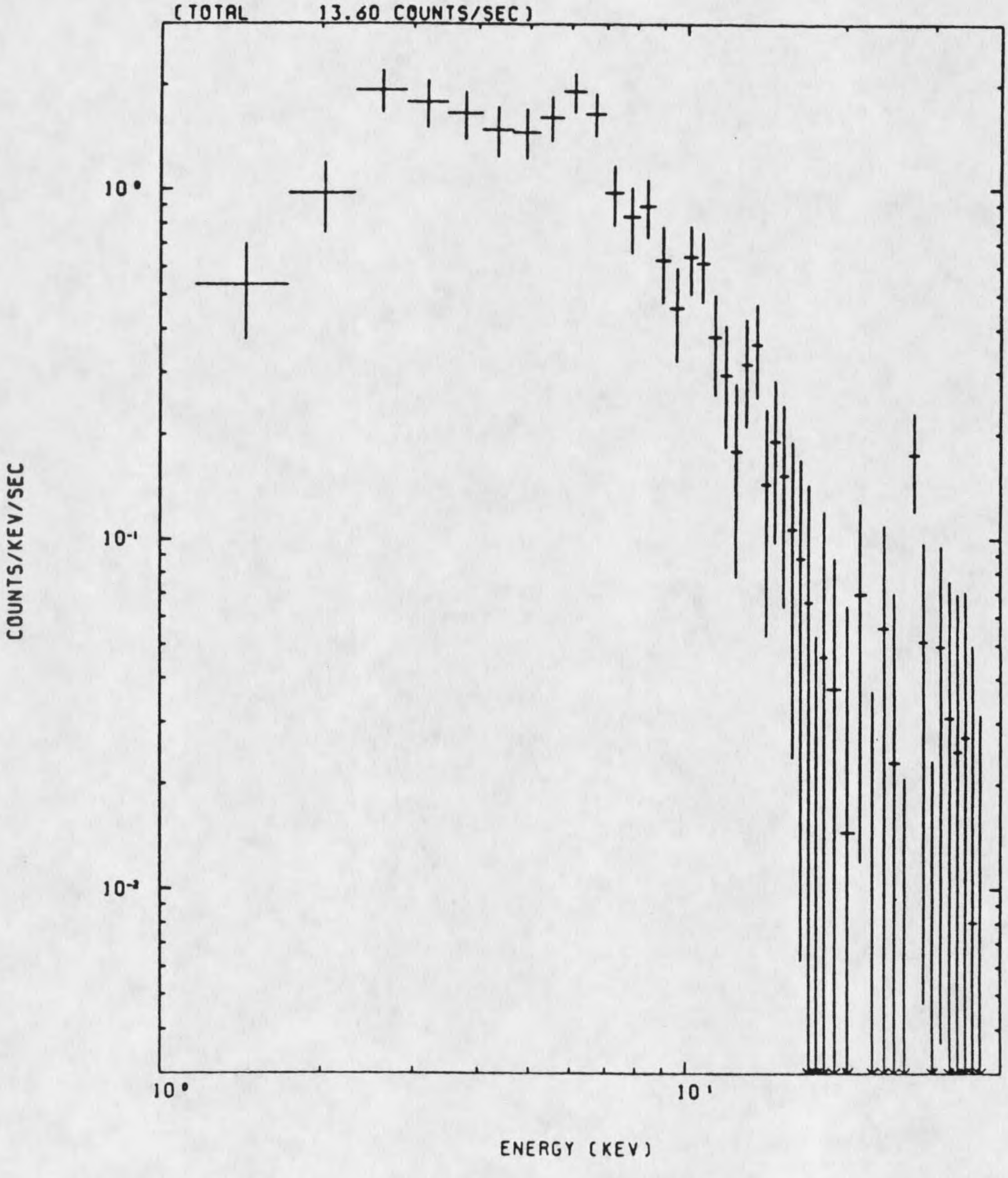

Figure 61. The ingress spectrum OIHRD3 from the October data. The data accumulation time is 128 seconds.

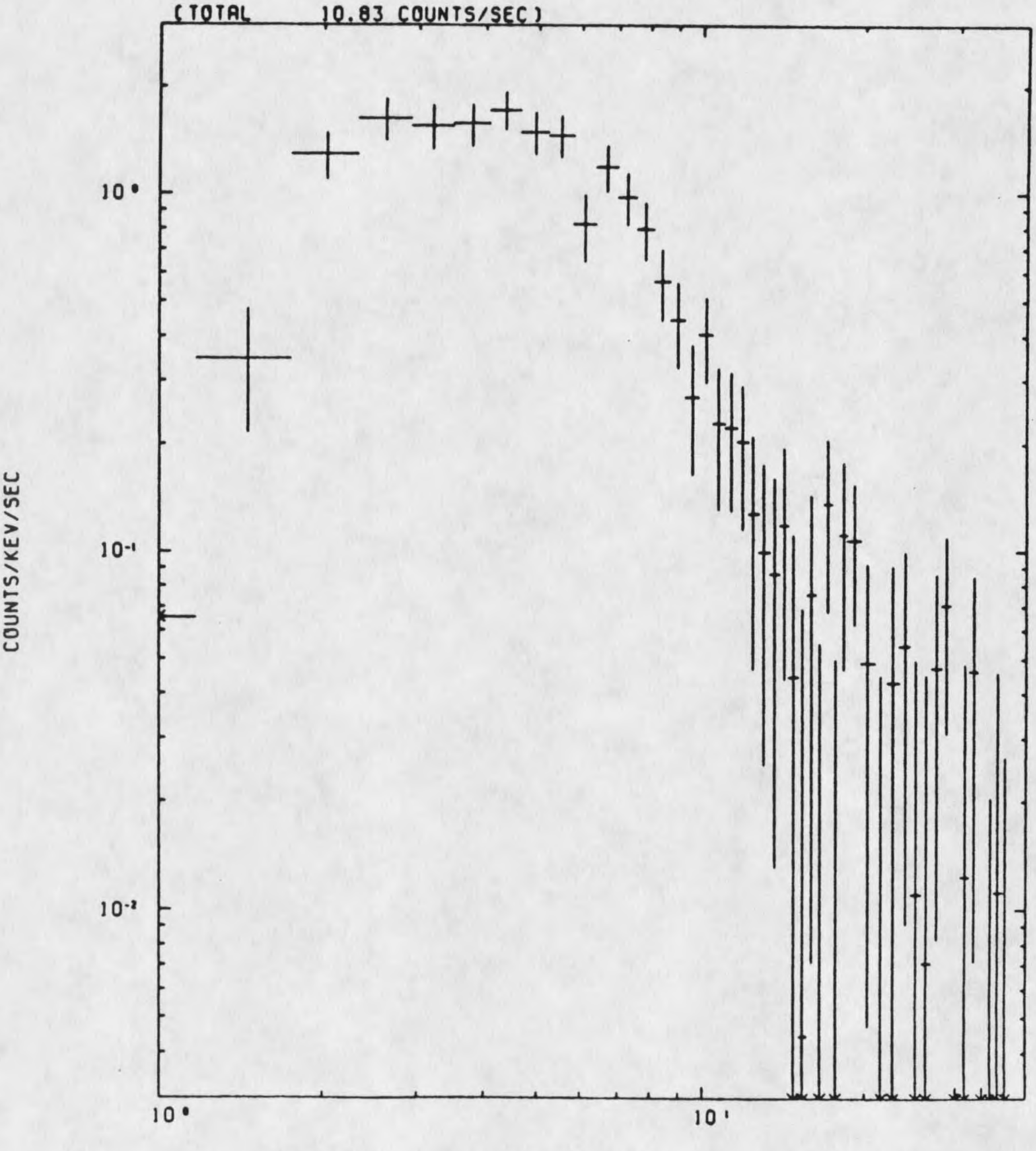

Figure 62. The ingress spectrum OHLT5I from the October data. The data accumulation time is 192 seconds.

spectral variability cannot be verified by just examining the uncertainties in the best fit parameter when only one parameter of interest is used; the χ^2 contour must be examined. Note that the χ^2 contour for OIHRD3 reduces to a line since the absorption column was fixed at the Galactic value. This is shown in Figure 63. From these contours, the spectra are seen to differ at the 90% confidence level.

There are some other interesting features in these spectra. For OIHRD3, the column density was required to be fixed at the Galactic value, as was the case for hard spectra of the egress. Also, the hard spectrum required a line. This line can clearly be seen in the spectrum shown in Figure 61. In contrast, the following soft spectrum did not require a line; Figure 62 shows that there was no evidence for one. However, probably because of the low flux and the small amount of data accumulated, the line fluxes are not quite significantly different at the 90% confidence level. Interestingly, though, the equivalent widths are different at the 90% confidence level. Thus spectral variability is verified on a time scale of ~ 128 seconds.

The four best fit spectra for the ingress are shown in Figures 104–107 of Appendix 2. The best fit spectra for OIHRD3 and OHLT5I are shown in Figures 108 and 109, respectively. Finally, the three best fit spectra for the egress are shown in Figures 110, 111 and 112.

Model Calculations

The appropriate model to explain the fastest variability is suggested from the light curve of the April dip data. Three dips were observed in which the flux drops nearly to 0 counts s^{-1}. A most obvious model to choose to describe this behavior is an absorption model, in which a block of material, optically thick to X-rays, comes between the observer and the source, temporarily blocking the X-ray flux. It is

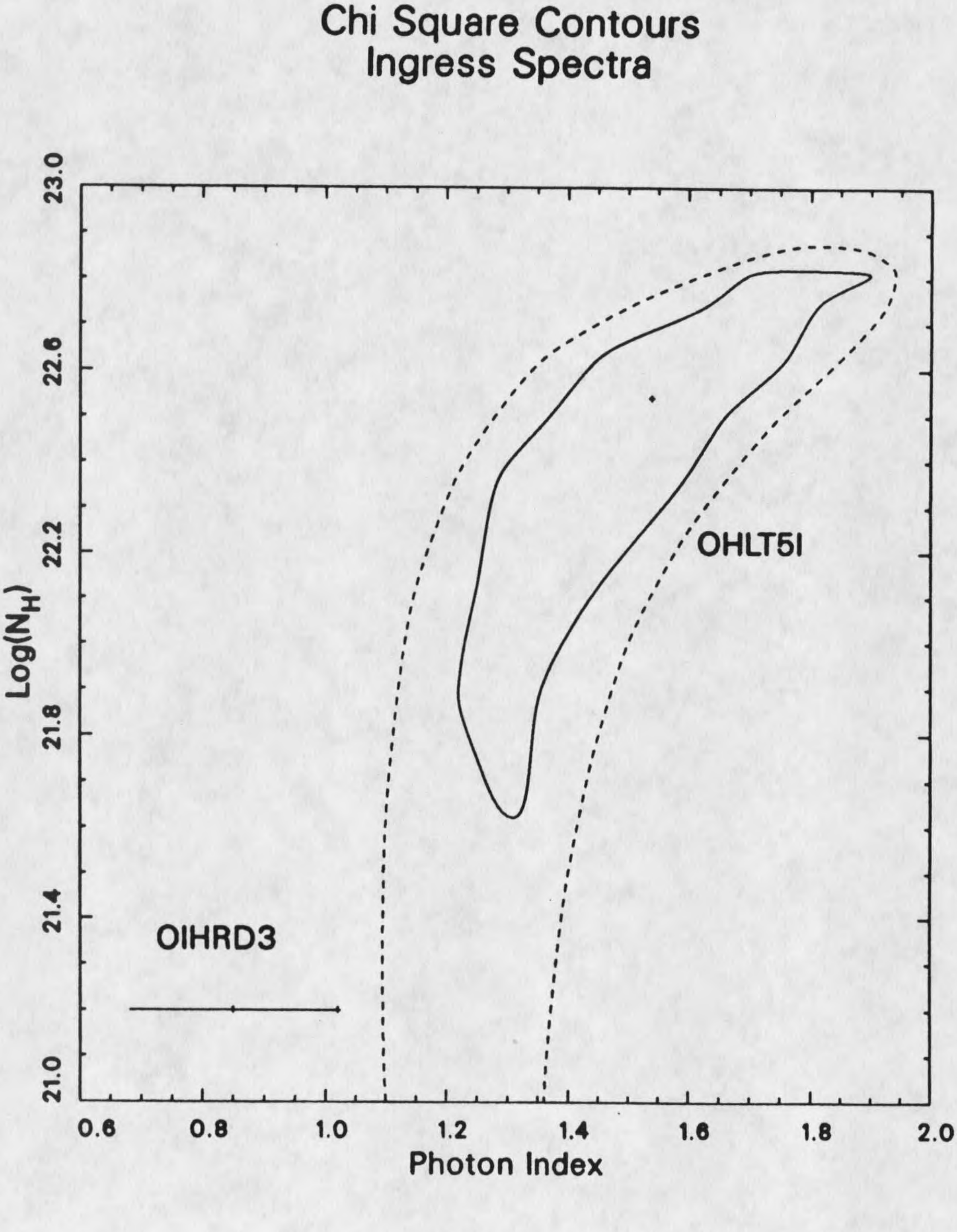

Figure 63. χ^2 contour for OHLT5I, and χ^2 line for OIHRD3. This shows that these spectra differ at the 90% confidence level.

difficult to imagine a model in which the dip in X-rays has an intrinsic origin; that would be equivalent to temporarily turning off the source. However, an absorption model does not obviously describe the ingress and egress region of the October data, since the flux level only falls to half of its original amount.

Therefore, we propose a modified absorption model to describe the fastest variability in NGC 6814. The model is built to explicitly explain the details of the ingress and egress data; in order to do this, we propose that the absorption column be variable. Detailed model calculations follow which demonstrate that the variable absorption model is consistent with the regions of fastest variability in the October observation. In the discussion section the implications of this model on the April dip data and on the variation of the spectral index over the entire October observation will be described. A motivation of the model is that the ingress and egress data are remnants of the decayed April dips.

The Variable Absorption Model

The model proposed is a variation of the partial covering model. In this model, the column covering the source is allowed to vary in time. Physically, the picture we have in mind is that a cloud with varying column density is moving across the source. This mechanism takes advantage of the fact that the X-ray absorption by neutral material with cosmic abundance is energy dependent. In this way, the lags observed can be explained if the column density increases as the time increases. So, during a flux decrease, first the soft flux is absorbed by a relatively small column density. Then harder and harder fluxes are absorbed by larger columns. The amount of lag measured directly implies the change of the column needed.

Fitting the Model. The template fit results can be used to fit models which describe the column density covering the source at a given time, $N_H(t)$. The fit parameter t_1 can be used, because it is the time at which the flux drops half way from its initial value to its final value. The time for this to happen can be easily found for any model of the column density, as follows.

Assuming no absorption by the host galaxy, the maximum flux

$$F_{Max} \propto e^{-\sigma(E)\, N_{H(Gal)}} \tag{8.3}$$

where $\sigma(E)$ is the energy dependent absorption cross section, and $N_{H(Gal)}$ is the absorption column due to the Galaxy. The values of the cross section for neutral material given by Morrison and McCammon (1983) were used. It is necessary to find the time $t_{1/2}$ at which the flux drops to half. This time obeys the equation

$$F(t_{1/2}) \propto e^{-\sigma(E)\,(N_{H(Gal)}+N_H(t_{1/2}))}. \tag{8.4}$$

Here $N_H(t)$ is the time dependent extra column covering the source. Note that it is assumed that the fraction of unabsorbed flux necessary to describe the ingress and egress data remains constant. Setting Equation 8.4 equal to 1/2 of Equation 8.3 results in the following equation:

$$N_H(t_{1/2}) = \frac{-\ln(0.5)}{\sigma(E)}. \tag{8.5}$$

For simple models of $N_H(t)$, this equation can be solved explicitly for $t_{1/2}$.

Two types of two-parameter models for the time dependent column density N_H were used. These models were devised by the author as possible descriptions of the time dependent column density. The first one is called the exponential model given by

$$N_H(t) = \pm 10^{\left(\frac{t-T}{P_1}\right)} \tag{8.6}$$

where the sign used was + for the ingress and − for egress. Here, T is the initial time and P_1 shows the extent of the decrease. The other model was called the power model

$$N_H(t) = \pm P1\,(t - T)^P \tag{8.7}$$

where T has a similar interpretation as above, while $P1$ is the initial column. Here P is an integer power, and was not left free. Powers from 1 to 12 were fit. The model fitting proceeded by a brute force grid search, in which the fit χ^2 was evaluated for a grid of possible parameter values. This was a practical method, since the model had only two parameters. The Statistical Analysis System software, used for the template fitting, could not be used in this case, because the absorption cross section is discontinuous at the iron absorption edge.

The power model, Equation 8.7, yielded formally acceptable fits for the ingress data for powers greater than 9. That is, the fit χ^2_R was smaller than the value such that the probability was less than 10% that the fitting function was appropriate. The best fit for this type of model was for $P = 12$, for both the ingress and the egress data. However, in both the ingress and the egress cases, the exponential model yielded a smaller χ^2_R. In no case was the fit over-determined. The fit results for the exponential model and the power model with $P = 12$ are given in Table 16, while the ingress and egress data along with the exponential fits are shown in Figure 64 for the ingress and in Figure 65 for the egress. Note that the energies chosen to correspond to the template fit data were found by calculating the mean of $E^{-\alpha}$, assuming $\alpha = 0.7$, weighting with the efficiency of detection, and folding in the Galactic absorption.

One interesting property of the ingress data that supports this model occurs around the discontinuity at the iron absorption edge. The iron line band data

Table 16. Fit results for the ingress and egress data. Parameter uncertainties are 90% for one parameter of interest.

Data	P_1	T	χ^2 /d.o.f
Exponential Model:			
Ingress	111.3 ± 0.3 seconds	20893 ± 7 seconds	6.24/5
Egress	157.2 ± 0.7 seconds	15631 ± 16 seconds	20.5/4
Power Model ($P = 12$):			
Ingress	1.39×10^{-10}cm^{-2}	22907 seconds	8.16/5
Egress	4.06×10^{-12}cm^{-2}	12748 seconds	25.6/4

point, at ~ 6 keV, shows less lag from the highest energy data than the iron edge band data. Therefore, the variable absorption model is fit well in this region.

Both fits are acceptable for the ingress data; however, the exponential model finds a smaller χ^2, and is more attractive, since the exponential function is a sum of powers, and so no single power need be singled out.

The fits are not satisfactory for the egress data, for either model, although the exponential model fit is better. The problems with this fit probably lie in both the model and the data. The data from the template fitting of the egress data are probably of poorer quality than the ingress data because of the low flux, and this fact may not be completely reflected by the larger error bars. The lower quality of these data is due to the fact that the combined flux in general was lower for egress data, and also, because most of the egress data statistically required $B \neq 1$, t_1 was less well determined. Note that the uncertainties were calculated assuming that B and t_1 were completely independent, and this assumption may not be completely justified. To examine this possibility, the χ^2 contours for these two parameters

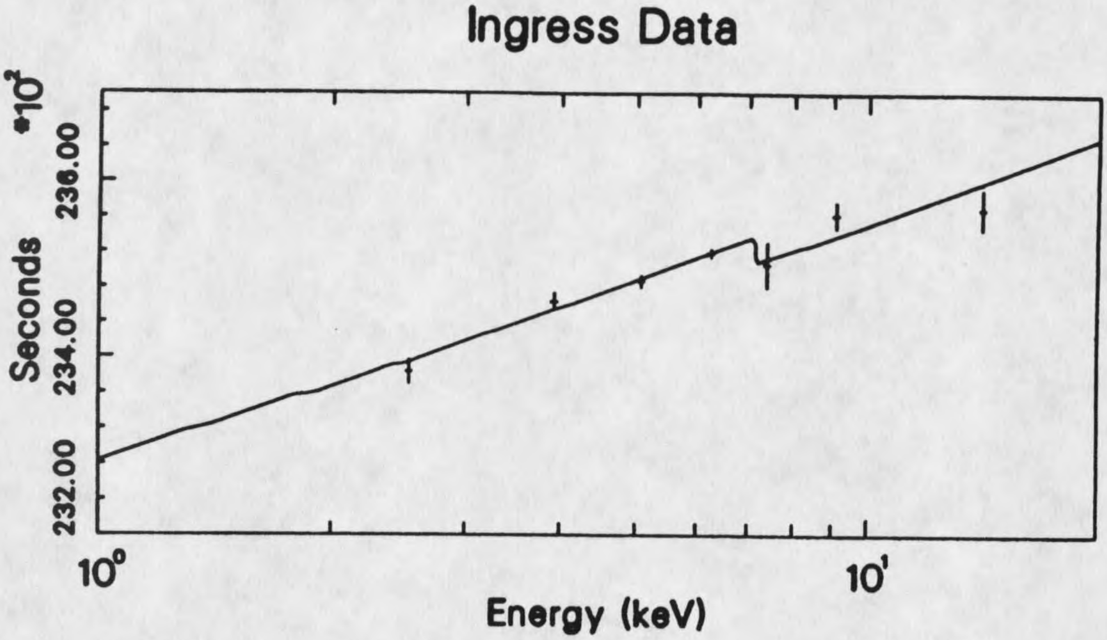

Figure 64. Best fit of exponential model to the ingress section of the October data. The fit χ^2 was 6.24 for 5 degrees of freedom.

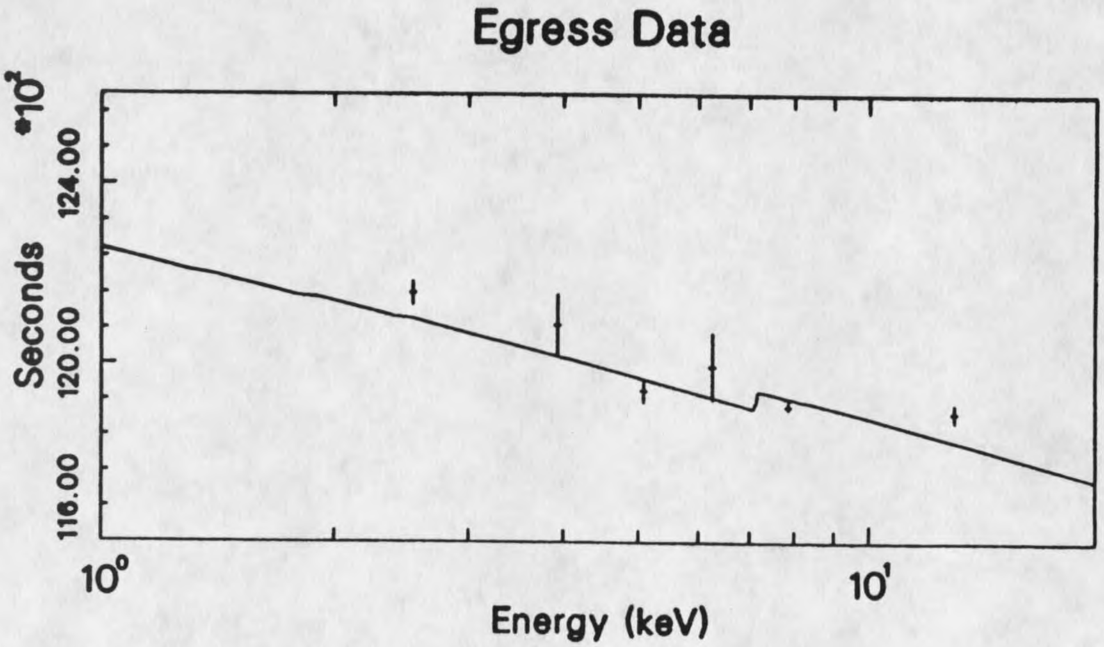

Figure 65. Best fit of exponential model to the egress section of the October data. The fit χ^2 was 20.5 for 4 degrees of freedom.

could be calculated and examined. However, probably the larger problem is that an exponential absorption model is not quite the best model to use. Examining Figure 65 shows that these data could be fit better by a function with curvature in order to fit the highest and lowest energy points. Perhaps one with a quadratic or some other power exponent might work better. It is important to understand that the problem most likely lies in the choice of fitting function and not in the model in general.

In general the model fits the data extremely well despite its simplicity. Of course such a simple model cannot explain all the details of the observation. However, a more complicated model with more fit parameters would not be justified, given the quality and quantity of the data to be fit.

Light Curves Predicted by the Model. As a comparison between the model and the data, the light curves predicted by the model were calculated. These were superimposed on the ingress data in Figures 53 and 54, and on the egress data in Figures 56 and 57. Also superimposed are the plots of the best fit for the arctangent template function. In addition, Figures 52 and 55 show the plots of the data from 1.11–20.9 keV, along with the template fit curves and model curves.

In order to calculate the light curves predicted from the model, it was necessary to normalize them to the asymptotic values of the best fit template parameter results. This is done because it is impossible to estimate the normalization completely theoretically. Too many assumptions would have to be made. For example, the power law index must be assumed, and the efficiency of photon detection must be folded in. Another factor is that the response matrix of the satellite precisely at the time of observation is not available in Montana. However, for qualitative comparison, the normalization carried out is certainly justified.

It is interesting to examine the time for the flux to fall halfway between its initial and final value and the amount of time for the decrease. The time for the flux to fall halfway between its initial and final value should correspond to the residuals of the model fits, shown in Figures 64 and 65. Comparing these figures shows this indeed to be the case.

The decrease and increase time is the real indication of the geometry of the situation. It is interesting to see from Figures 52–54 that for the ingress, the decrease time was smaller for the fits than for the model. Although the numerical values found for the decrease times given in Table 13 were not well determined, the idea is interesting to examine. The model calculation assumed a point source. Also, the model for the decrease in column density is 1-dimensional. In this model, a finite source size can only increase the decrease time. What could be modified to make the covering time faster?

For the entire energy range, from 1.11–20.9 keV, the comparison can be more quantitative. Table 13 gives the best fit decrease time for the ingress data to be 33 ± 11 seconds. A similar template fit to the model decrease finds the decrease time to be 81 ± 3 seconds, significantly larger than the measured decrease.

For the egress, Figures 55–57 shows the results to be more mixed. For several of the soft energy bands, the increase time for the model is smaller than the measured increase time from template fitting. However, for the harder bands, the model increase time is larger, as was the case for the egress data. For whole energy range, recall from Table 13 that the increase time was measured to be 78 ± 37 seconds from template fitting. Fitting the model, however, finds the increase time to be 106 ± 4 seconds, again longer than the measured decrease.

The explanation for the discrepancy could be that the model function, although adequate for qualitative comparison, is not completely appropriate. Recall that one cause of the discrepancy between model and fitting was that the hardest flux data values would require a function with curvature for a better fit. This implies that a better function would have the column, for very large values, increase faster as a function of time. Such a dependence on the time would cause a faster decrease for the model function, at least for the higher energy bands.

Spectra Predicted by the Model. As shown in the previous section, the variable absorption model can explain the nature of the lags found in the ingress and egress data sections from the October observation. The next question is, does the model produce spectra similar to those found in the ingress and egress data? In order to address this question, spectra from this model which correspond to ingress and egress data were accumulated and fit. However, the comparison must be qualitative, because of the many assumptions which must be made. For example, the power law index of incident spectrum cannot be known. Therefore, α is assumed to be 0.5.

The reason that α was chosen to be 0.5 is because of the interpretation of the OHLT5I spectrum. Recall that the best fit photon index for this spectrum was 1.54. This is assumed to be the intrinsic photon index. During the ingress and egress data sections, the flux does not drop to zero, but it appears that it may level out after it has dropped about half way. This is assumed to be due to a fraction of the incident spectrum not being absorbed. This assumption is also supported by the fast softening of the spectrum OHLT5I compared with OIHRD3. Assuming the variable absorption model, the soft spectrum would be due to the source being partially covered by a completely thick cloud, while the remainder of the flux is unabsorbed. Then the spectrum would be the unabsorbed, intrinsic spectrum reduced in flux. Therefore, model energy index was chosen to be 0.5.

However, there may be a way to discover the intrinsic index involving further spectral analysis. This will be discussed in the discussion section on implications of the absorption model on the hardness variability.

In order to make model spectra, the fraction of the incident spectrum not absorbed must be estimated. To find this fraction, the model for the source flux is assumed to be

$$F(E,t) = E^{-\alpha}\, e^{-\sigma(E) N_{H(Gal)}} (f_1\, e^{\sigma(E) N_H(t)} + f_2). \tag{8.8}$$

Therefore, the fraction of the source unabsorbed would be f_2/f_1. This equation neglects line emission, which would be negligible. In order to estimate f_1 and f_2, the template fits for the total 1.11–20.9 keV data were used. Using the ingress data as an example, it was assumed that, before ingress, there is no cloud absorption, and the only absorption was due to that of the Galaxy. Therefore

$$F(E, before) = E^{-\alpha}\, e^{-\sigma(E) N_{H(Gal)}} (f_1 + f_2). \tag{8.9}$$

The absorption column may be underestimated, since there is evidence of intrinsic absorption in this source. However, we cannot know the value of the intrinsic absorption, so the Galactic column provides the lower limit on the absorption column. Making this assumption, the asymptotic value of the arctangent template model is the total flux before ingress.

Next it was assumed that, after ingress, the cloud absorbed some fraction completely, and the flux remaining is only absorbed by the column due to our Galaxy. The appropriate relation is then

$$F(E, after) = E^{-\alpha}\, e^{-\sigma(E) N_{H(Gal)}} (f_2). \tag{8.10}$$

Similarly, the total flux after ingress can be found using the arctangent template fit results. Then these two equations can be solved for f_1 and f_2. For the ingress, they were found to be $f_1 = 4.31$ and $f_2 = 2.48$, while for the egress, the results were $f_1 = 2.75$ and $f_2 = 1.69$. Note that these are not equal, and they also do not yield the same ratio. Under ideal circumstances, they should. However, they may not because of several reasons. One is that the data sections are cut by the data selection process. In either the case of the ingress or egress, it cannot be known if the flux level at the end of the data section has reached its minimum or maximum, respectively. Similarly, it cannot be known if the flux level at the beginning of the data section is the maximum or minimum for the ingress and egress, respectively. However, this discrepancy again does not affect the qualitative comparison.

Once these normalizations are found, the spectra can be integrated. In order to simulate the measured spectra, the simulated spectra are accumulated over 256 seconds.

The model spectra are shown in Figure 66 for the ingress and Figure 67 for the egress. The number by the simulated spectrum corresponds to the number of actual spectrum which is being modeled. For example, the spectrum numbered with (3) on the ingress plot was accumulated over the same time interval as the actual measured spectrum OI3. The only exception to this is that for the ingress, spectrum number (8) corresponds to OHLT5I, which was essentially the last sub-frame of the ingress data section. Examination of these simulated spectra indicate significant spectral variability.

These model spectra were fit to a simple power law plus absorption model (Equation 4.1). The spectral fitting program used was a simple grid search program called GRIDLS from Bevington 1966. The spectra were accumulated every 0.5 keV, and uncertainty was simulated by a constant scaling factor times the flux divided by the square root of the energy dependent efficiency of detection. In this way, the fitting was weighted so that the high and low energies contribute

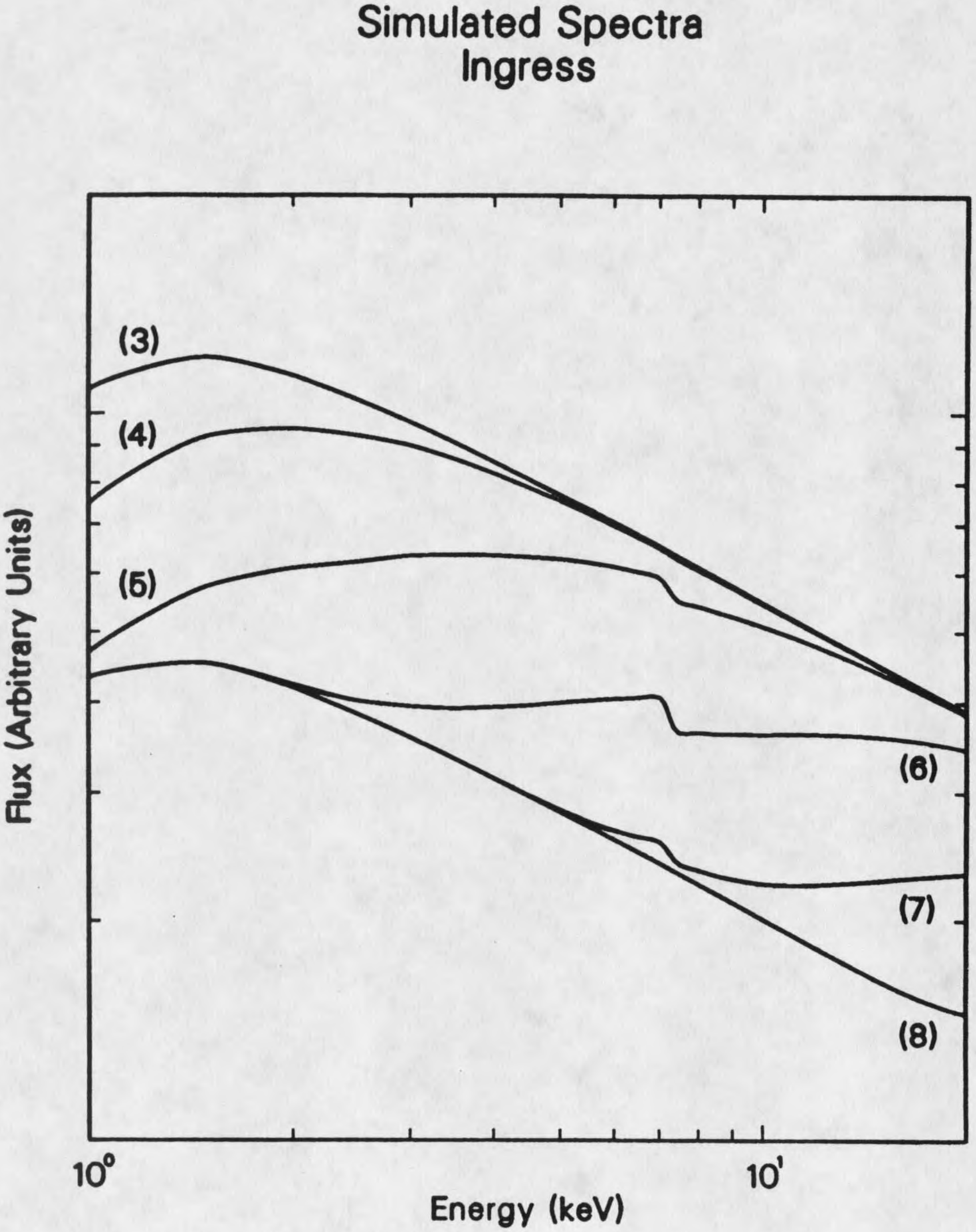

Figure 66. Model spectra of the ingress section of the October data. For the explanation of the numbers labeling each curve, see text.

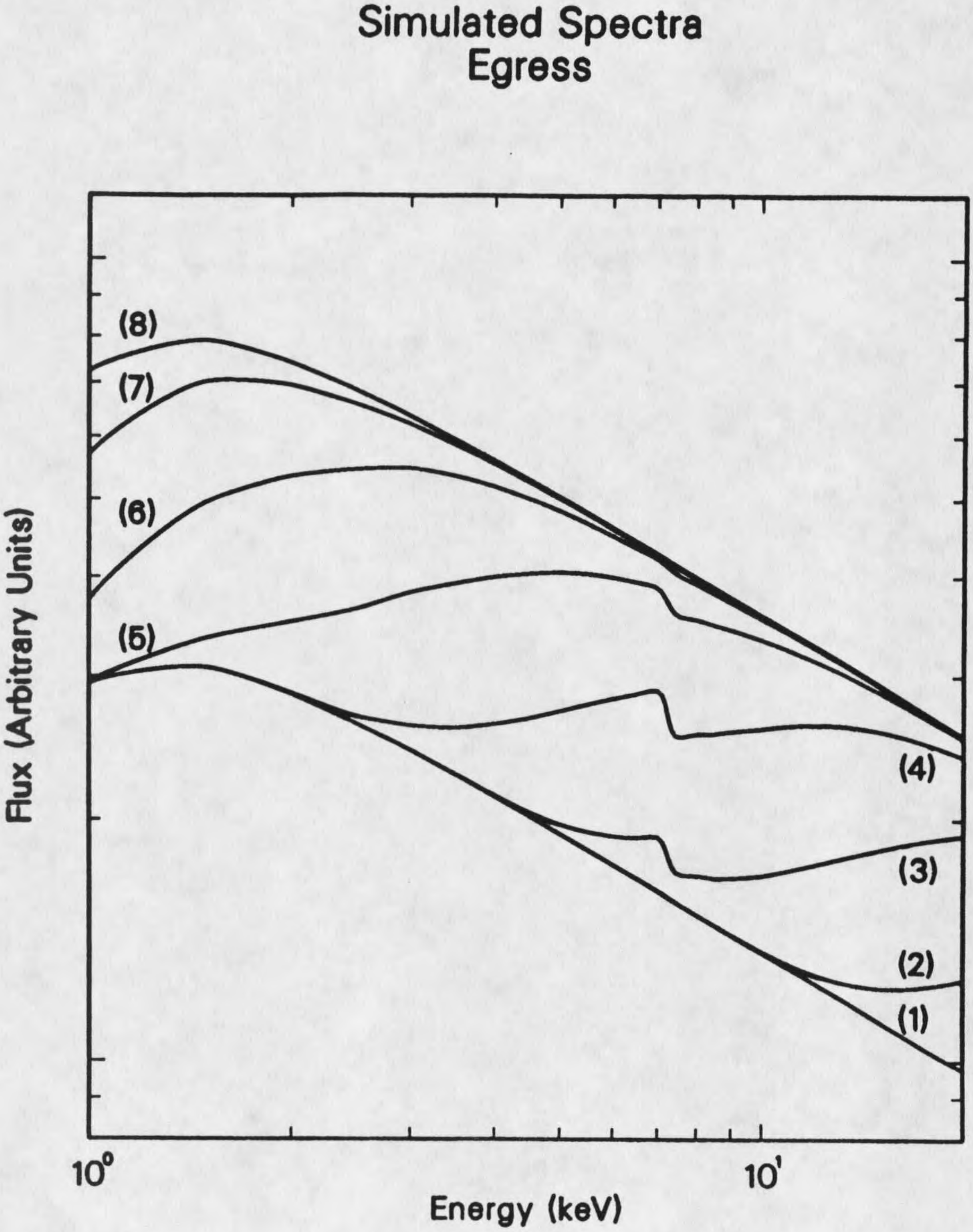

Figure 67. Model spectra of the egress section of the October data. For the explanation of the numbers labeling each curve, see text.

less to the determination of the best fit parameters, as is the case during spectral fitting of the real data. Since the constant scaling factor is chosen arbitrarily, the uncertainties of the parameters found in spectral fitting are also subject to normalization. Since the purpose of the uncertainties was only to weight the spectral fitting, the qualitative results will not be compromised by this choice. However, one improvement may be made, and probably will be done when time allows. That it, less points in the high energies should be fit, because *Ginga* spectra bin higher energy spectra into larger bins. Another improvement which will be made when time allows is to modify the energy band fit. The simulated data were fit in the energy band from 1–20 keV, while the real data were fit from 3.36–20.9 keV. The qualitative results would not be changed, however.

The spectral fitting results from the simulated spectra and the corresponding measured spectra are listed in Table 17. In the first column of the table are the the times over which the simulated spectrum was accumulated. In the second and third column are the index and absorption column found from spectral fitting of the simulated data. For comparison, in the second three columns are the results from the actual data fitting. In the fourth column is the name of the spectrum which was accumulated over the same time as the simulated spectrum, while in the fifth and sixth columns are the corresponding index and absorption column.

Qualitatively, two trends emerge. In the ingress data, the spectral index first falls and then rises, for both the simulated and measured data. A similar trend is observed also in the egress data.

Another trend is apparent, in the values for the absorption column. Although the model proposed is an absorption model, it is perhaps surprising that there is not a dramatic increase in column density as the proposed cloud covers the source. In fact, when the source is mostly covered, the column density is observed

Table 17. Fitting results to the measured and simulated data. For the simulated data the assumed incident energy index was 0.5 and the assumed uniform column density was the Galactic value, $\log(N_H) = 21.2$.

	Simulated		Measured		
Time	Index	$\log(N_H)$	Spectrum	Index	$\log(N_H)$
Ingress:					
23040–23296	0.500 ± 0.006	21.3 ± 21.0	OI3	0.57 ± 0.16	22.4 ± 0.4
23168–23424	0.480 ± 0.006	21.7 ± 19.3	OI4	0.36 ± 0.16	22.4 ± 0.3
23296–23552	0.320 ± 0.006	21.9 ± 21.0	OI5	0.25 ± 0.16	22.6 ± 0.2
23424–23680	0.101 ± 0.002	21.2*	OI6	0.25 ± 0.24	22.7 ± 0.3
23552–23808	0.320 ± 0.005	21.2*	OI7	0.27 ± 0.28	22.3 ± 0.7
23680–23936	0.494 ± 0.006	21.2 ± 21.0	OHLT5I	0.54 ± 0.35	22.5 ± 0.4
Egress:					
11392–11648	0.499 ± 0.006	21.2 ± 20.1	OE1	0.17 ± 0.37	22.3 ± 0.7
11520–11776	0.449 ± 0.006	21.2*	OE2	-0.02 ± 0.10	21.2 ± 2.0
11648–11904	0.221 ± 0.006	21.2*	OE3	-0.15 ± 0.20	21.2*
11776–11032	0.052 ± 0.005	21.2*	OE4	-0.24 ± 0.15	21.2*
11904–12160	0.292 ± 0.006	22.0 ± 21.0	OE5	-0.11 ± 0.22	22.1 ± 1.5
12032–12288	0.457 ± 0.006	21.8 ± 21.1	OE6	0.01 ± 0.21	22.4 ± 0.3
12160–12416	0.497 ± 0.005	21.5 ± 18.7	OE7	0.13 ± 0.20	22.3 ± 0.4
12288–12544	0.500 ± 0.007	21.3 ± 20.1	OE8	0.39 ± 0.20	22.6 ± 0.3

*Parameter fixed at value given for spectral fitting.

to decrease so much that the best fit value is below the Galactic value. In these cases, the absorption column was fixed at the Galactic value for spectral fitting. For the egress, in two cases, it was necessary to fix the column to the Galactic value both for the actual data fitting and for the simulated data fitting. The reason for this can be understood by examining the plot of the simulated egress spectra shown in Figure 67. For spectra (2), (3), and (4), there is significant upward curvature at the lower energies. Because of poor detection efficiency in the lowest energies, the column density is determined mostly by the curvature in the middle energy range, with large columns showing typically extreme downward curvature. Therefore, upward curvature as observed in these simulated spectra cause the spectral fitting program to find very small, or even negative column densities when the column density parameter is left free.

Thus the variable absorption model predicts qualitatively the rapid change in spectral index observed in the data during the fastest variable sections of the October data, as well as the very low absorption column measured in some of the low flux spectra.

Implications of the Model on Physical Parameters. In this section, some simple calculations are shown to illustrate what the variable absorption model for the fastest variability of this source implies for the physical parameters.

The unique characteristics of the dips and periodicity in the April data make possible a determination of source size and the position of the absorbing material. Historically, determination of source size relied on the use of the doubling time scale to estimate it. This is crude, because, in the case of occultation, for example, if the source is already more than half covered, the time to decrease the flux by half will be shorter than that to cover the entire source.

In the April observation of NGC 6814, we are lucky because we know considerably more than one knows just from examining the doubling time scale. Detailed spectral and time series analysis seems to favor the occultation model as being the cause of the fastest variability. Therefore, the time it takes for the hard flux to drop to zero from its previous level gives the lower limit of the source size. This is because the cloud blocking the hard X-rays must be nearly the same size as the source. If it were smaller, the flux would not go to zero. If it were larger, the flux would be at zero for a long time. However, as can be seen in the light curve of the dips in hard X-rays in Figures 84 and 85 of Appendix 1, the zero point is nearly a cusp. Therefore the occulting cloud in the April observation must be nearly the same size as the source.

Looking at the ingress light curve for the first dip, it can be seen that the time for the flux to decrease to zero is about 300 seconds. For the second dip it is harder to say because the dip occurs so close to the beginning of the data section, one cannot tell what the flux level was before the dip. However, it is again at least 300 seconds. Finally for the third dip, the decrease is also about 300 seconds or perhaps a little less.

Using the time for the flux to drop to zero to be 300 seconds, the estimate for the size of the source is $300 \times v$, where v must be the velocity of the cloud. The period for the cloud to orbit the source is 12000 seconds. Assuming the source of X-rays is within $5r_s$, where r_s is the Schwartzschild radius, and assuming the velocity to be Keplerian, then the distance to the cloud is found to be $\sim 7 \times 10^{12}$cm. The assumption that the emission comes from the region smaller than $5r_s$ also leads to the conclusion that the Schwartzschild radius is 2.3×10^{11}cm, corresponding to a black hole mass of nearly 10^6 solar masses. Then in this case, the cloud would be orbiting at a distance of $32r_s$.

What would be the condition of the gas at this radius in the cloud? The 2–20 keV luminosity of NGC 6814 is about $7 \times 10^{42} \mathrm{ergs\,s^{-1}}$ (Kunieda et al. 1990). However, the bolometric luminosity may be 10 times larger than that,

7×10^{43}ergs s^{-1} (Padovani and Rafanelli 1988). For the lags observed in the October data to be due to occultation by a cloud with variable optical depth, in order to observe the lags that are found, (i.e., the hard lags the soft for decreases and soft the lags the hard for increases), the cloud material must be relatively unionized, so that it is opaque to soft X-rays. This means that $\xi = L/nR^2$ (Equation 2.1; see also Kallman and McCray 1982) must be less than 100, for oxygen to retain some electrons. Using the above bolometric luminosity, and the distance to the cloud to be $32r_s$, the material of the cloud would have to be denser than 10^{16}cm^{-3}. If the X-ray luminosity is used, the density would have to be only about an order of magnitude smaller.

Can such dense material exist in this region? It has been hypothesized by Guilbert and Rees (1988) that such material could remain cool in the central region if confined to a high enough density. Rees (1987) asserts that a confining force for such material might be a tangled magnetic field at nearly the virial strength. Also, Ferland and Rees (1988) have found that material at such densities would be able to reprocess X-ray photons; the atoms would not yet be forced into local thermodynamic equilibrium.

Finally, if the black hole mass is 10^6 solar masses, then the associated Eddington luminosity is $L_{Edd} = 1.25 \times 10^{44}$ergs s^{-1}. For a bolometric luminosity of 7×10^{43}ergs s^{-1}, the source is radiating at a rate of $\sim 0.5 L_{Edd}$.

Discussion

The previous section described a model which is successful in describing the temporal and spectral variability of the ingress and egress sections of the October data. Previously we have mentioned that the absorption model is appropriate for the April dip data. Our idea then is that the ingress and egress data from the October observation are the decaying remnants of the April dip structures. In order to further motivate this conjecture, the major results are first briefly reviewed in order to display the similarities.

Similarities Between the April and October Results

The results from the analysis of two observations of NGC 6814, separated by about 6 months, were discussed in the results section. Though these two observations were from the same source, the light curves, Figures 23 and 24, are somewhat different. The April observation is characterized by sharp dips, in which the flux falls to nearly zero, while the flux level in the October observation never reaches 0, and the flux seems to be more continuously variable. Although there are some differences, the detailed analysis presented in the results section shows similarities implying that the physical processes modulating the source flux may be the same in these two observations.

Both sources show a periodic component in the light curve. The period of the April observation was clearly $\sim 12,000$ seconds. The $\sim 12,000$ second periodicity in the October observation was not quite as apparent; evidence for a 6,000 second periodic component was also found. However, in the October observation it was found that the hardness ratio varied with a $\sim 12,000$ second period, indicating spectral variability on that time scale.

Spectral fitting from the whole observation indicated evidence for variability of the iron line flux and the photon index in the April data and of the photon index of the October data. In the October data, the evidence for iron line flux variability was marginal. In the April data, the iron line flux was correlated with the continuum flux. There was only marginal evidence that the photon index was correlated with the continuum flux. For the October data, since the iron line was not observed to vary significantly over the whole observation, correlation between the line flux and the continuum flux was not verified, but was suggested. The photon index clearly did not vary in a correlated manner over the whole observation, since the light curve had a periodicity of $\sim$ 6000 seconds while the hardness ratio period was $\sim$ 12000 seconds.

In both observations, regions of fast variability were found, and detailed analysis showed that similar properties were found in both. A flux correlated significant spectral variability was found in the April dip data. This result was found through spectral fitting and was also inferred from the correlation plots. In addition, the spectral fitting showed that the line flux decreased significantly during the dips. In the ingress and egress sections of the October data, flux correlated spectral variability was implied but could not be confirmed. Interestingly, however, the comparison of two low flux spectra found that they differed significantly. Correlation plots also implied flux correlated spectral variability.

Flux lags were clearly demonstrated in the October data, both through conventional cross correlation calculations and through template fitting. These were in the sense that, during flux decreases, the hard flux lagged, while during flux increases, the soft flux lagged. Such an inference was available from examination of the correlation plots, as well. The cross correlation analysis of the April dip data did not yield clear evidence for lags. The correlation plots implied spectral variability which could be a result of lags. The template fitting of the April data has not yet been completed because of lack of time; however, preliminary results seem to indicate that this method can indeed demonstrate significant lags in these data, although the magnitude of the lags is certainly not as large as in the October data.

The similarities discussed here seem to indicate that the same mechanism is responsible for the behavior of the source in both observations. The success of the variable absorption model, described in the section on model calculations, in describing the details of the October ingress and egress data, shows that the investigation of the application of this model to the April data is important.

Implications of Model for April Data

The previous section illustrated that many similarities are present between the October ingress and egress data and the April dip data. The parameters of this model were derived using the data from the ingress and egress sections of the October observation. However, it is easy to see how such a model can be applied to the dips in the April observation.

In the April data, the cross correlation calculations did not yield conclusive evidence for lags in the dips. This is probably due to the end effects in the CCF calculation. Since the template fitting has not yet been completed, it is difficult to determine the value of the lags. Also, they cannot be as clearly seen in the light curves or in the hardness ratio as the October lags, though the low flux level is certainly partially responsible. The correlation plots show some evidence for lags, mostly between the low energy band and the medium. The evidence for lags between the medium and hard bands is not as conclusive. All this evidence points to the qualitative conclusion that the dip lags are not as big as in the October data. Another factor is the flux level during the dips. Here the flux drops to zero at the dips.

The model proposed above can explain these effects easily. First, for the flux level to drop to zero means that there is no unabsorbed intrinsic flux, indicating that the variable absorption column covers the entire source. Second, if the lags are not as large, it means that the variable column region is not so large; that is, the gradient of the column with respect to the time would be larger. Thus, for the exponential model given in Equation 8.6, the P_1 fit parameter, describing the extent of the column change would be smaller. This parameter would not be zero, however. If it were zero, a pure partial covering model would be described. Such a model could not explain both the change in hardness ratio during the dips, as well as the drop of the hard flux to zero.

Given that some extent of variation in column is appropriate to describe the April dip data, the spectral variability can be explained. The ADIP spectrum is flat because the data of which it is composed comes from a region in which the medium energy flux is low or zero for some time, while the hard flux quickly falls to zero, and just touches the zero point. This scenario is supported by the changing hardness ratio. The fact that the hard flux falls and recovers so quickly shows that the cloud implied by the variable absorption model must have only a small region which is completely optically thick to X-rays.

Using the variable absorption model to describe the fastest variable region of both observations implies that some evolution must have taken place in the 6 month period separating the observations. It appears that what is happening is that perhaps the large piece of material blocking the source during the April dips may be decaying. That is, its edges are thinning out.

Implications of Realistic Geometries

Such a simple and idealized model cannot explain all of the features of the observation qualitatively. However, to fit a more complicated model would not be justified due to the quality and quantity of the data. But it is interesting to predict the effect of more complicated model on the results.

Two major approximations were made in this model, in order to make it simple enough for fitting. First, the source was assumed to be a point source. Second, the variable absorption model was only variable in one direction; that is, the gradient of the column density only varied in the time direction.

It is clear that the source size can be no larger than the cloud size. Otherwise the flux could not be cut all the way to zero, as is the case in the April dip data. Theoretical arguments, outlined in the section on implications of the model on the physical parameters, show that the source cannot be much smaller than the cloud so that the luminosity will not be close to the Eddington luminosity.

The effect of the finite source size on the light curves would be to cause the decrease to be slower. This would be a problem for the ingress light curves, since the template fitting function found the decreases to be faster than the model curves when the point source is considered. However, as already stated in the section on the light curves from the model, this fact probably is due to a better model being one with more curvature. In contrast, much of the soft egress data shows a slower increase than is predicted by the model. A finite source size supports this result.

Recall from the section discussing the spectra from the model that the spectra were formed by integrating over 256 seconds in order to simulate the measured spectra. The effect of the finite source size on the spectra would be nearly the same as integrating over a longer time. This would result in a further smoothing of the spectra, so there would be less noticeable bends than those shown in Figures 66 and 67. This is true if the source is assumed to be square. However, if it is circular, the blending effects would be more complicated.

The effect of the variation in the vertical direction as well as the time direction is more difficult to predict. Of course in this case, a finite source size must be assumed. Recall that since the flux did not drop to zero during the ingress and egress data sections, an added unabsorbed component was required. If the column varied in the vertical direction, the added component should be an absorbed component instead. The effect of this on the resulting spectra would be to further decrease the index. This would help explain the larger change of the index found in the egress data.

There is some evidence in the light curves of the egress data that there is vertical variation of the column. Recall that the template fit data found a fast increase of the hard flux bands, but the softer bands were much better fit with a long slow increase. This result could be explained if the thicker column decreases suddenly, but the thinner column decreases more slowly.

As mentioned before, a more complicated model could not be constrained by our data; however, this discussion shows that when more realistic geometries are considered, some aspects of the data are explained better. In particular, the idea of a vertical gradient of column is promising. As will be seen in the next section, this idea of a vertical column gradient is also promising to explain the variation in index over the entire October observation.

Implications of the Model on the Hardness Variability

This model was derived to explain the behavior of NGC 6814 during the periods of fastest variability. In these regions this model successfully explained fast apparent spectral variability. However, recall that spectral variability was observed during the entire October observation, with 12000 second periodicity. The question is, can the absorption model be applied to understand this phenomenon?

Conceptually, it is easy to understand this spectral variability using the variable absorption model. As mentioned in the previous section, the variable absorption model applied to the ingress and egress data used a column variable in the time (horizontal) direction, and the column changed as as the inferred cloud moved across the point source. Now imagine some material in perhaps a torus in orbit with a 12000 second period around a source of finite size. If the column were variable in the vertical direction, the spectral index measured would depend on the extent of the variable region, described by parameter P_1 of the exponential model, discussed previously. If P_1 were low, the drop in column would occur suddenly, and the spectral index measured would be the intrinsic spectral index. If P_1 were larger, the spectrum would be modified by layers of variable absorption column, and appear flatter.

How could this idea be tested? The way is to measure the intrinsic spectral index. This can be done by fitting only the high energy band, from 10.32–20.9 keV. This energy band is least affected by absorption, so the spectrum would be least modified by the variable column. If the column is truly exponential, the fitting of this band may yet result in a variable index. However, from both the ingress and especially the egress data, the lags of the hardest band over those adjacent were usually smaller than would be expected for the exponential model. The fit residuals from the exponential model shown in Figures 64 and 65 also indicate this. Therefore, the decrease is faster than exponential for the hard flux, at least in these regions, so a constant spectral index should be measured.

An analysis program based on this idea designed by the author is currently being carried out by a Nagoya University graduate student Y. Tsusaka. In this analysis, first the spectra accumulated along the folded light curve are being fit in the high energy band, with the absorption column being fixed at the Galactic value. This analysis should find a series of spectral indices consistent with a constant. Then the 256 second spectra will be fit holding the index constant to the mean value. The results of this should be a series of column densities which vary significantly, and whose folded parameter light curve will show the average column varying as a function of the phase of the 12000 second period.

If this can be verified, further implications arise. It could be inferred perhaps that not only the fastest variability is due to absorption, but the bulk of the 12000 second periodicity would be due to absorption. Some of the variability could be due to intrinsic flux variability, but perhaps it need not be the bulk. Then changes in the light curve from observation to observation could be due to changes in the profile of the absorber.

Competing models

As seen in the model calculation section and the previous discussion section, the variable model successfully describes many aspects of these two observations. However, in Chapter 5, several models for flux correlated spectral variability were described and some diagnostics for these models were defined. The purpose of this final discussion is to show how these competing models fail to describe the data.

The first possible model was a cold absorption model. In this model recall that the uniform column density changes, and because of the tight coupling between the column and photon index, flux correlated spectral variability is sometimes inferred. This model does not work for several reasons. First, some modulation of column density would be expected in the spectral fits. Some is observed, but it is not inversely correlated with the flux. The trend even seems to be that the absorption column is larger when the flux is larger. Second, the flux modulation occurs at all energies, as shown in Figures 84–88 in Appendix 1. For the modulation to occur at high energies, the column density change would have to be to a very dense material, and if the column is uniform, the flux level would then have to drop to 0. This explanation works for the April observation. However, for the October observation, in the ingress and egress, the flux level drops only to about half of its original value at high energies, and this would not be possible for a uniform absorber.

Another model was that of the warm absorber. This model cannot be used here for many reasons. First, this model usually is used to explain spectral variability at low energies. To extend this to higher energies, very highly ionized material is needed. Then a deep iron absorption edge would be seen at a high energy. Such an absorption edge is not seen in these data, as seen from the spectral fits and residuals shown in Appendix 2. Another problem is the sense of the lags which would be observed. If a change in ionization produces the flux modulation, it would be expected that during a decrease, the hard should lead the soft, since the hard flux would be absorbed at relatively higher ionizations. Also, the warm absorber model shows flux correlated spectral variability. However, recall that significant spectral variability occurred in 128 seconds between spectra OIHRD3 and OHLT5I, with little change in flux.

Variability in the relative normalization of separate spectral components also does not adequately explain our observations. First of all, it can be seen from the spectral fits shown in Appendix 2 that there is no need or evidence for the presense of another component. There is a soft excess in this observation; however, the effect of the soft excess is eliminated by spectral fitting only above 3.93 keV. Second, the lags would be hard to produce. It would be difficult to describe a mechanism which would cause spectral components from presumably different regions to act in concert to produce such lags.

Thermal Compton models may also be ruled out. These models predict lags; however, the sense of the lags would always be so that the hard flux lags the soft flux. In the egress from the October data, evidence was found that the soft flux lagged the hard flux during this flux increase. Non-thermal models may be able to explain such lags, as well as rapid spectral change; however, usually when they are applied, a large change in flux accompanies the spectral variability. However, in the October ingress data section two adjacent spectra were examined; it was found that the photon index changed from 0.85 to 1.54 in 128 seconds, but the flux level of the two spectra were nearly the same. Also, it is difficult to apply such a model to explain the dips in flux occurring in the April dip data.

Finally, a simple partial covering model can in some cases explain the spectral variability. In fact, the variable absorption model proposed is a variant of the partial covering model. However, the simplest version of the model, in which fraction of the source is covered by a cloud characterized by a single column density, fails to describe the data. First of all, there was no evidence in the spectral fit residuals shown in Appendix 2 that a partial covering model is necessary to adequately fit the spectra. Second, if the column of the partial coverer is not totally optically thick to X-rays, the flux of the hard X-rays would not be modulated by the variation in the fraction covered. In contrast, in NGC 6814, the flux at all energy bands is modulated as shown in Figures 84–88 in Appendix 1. For this to be due to the partial coverer, the coverer would have to be totally optically thick to X-rays. Then, if this were the case, there would be no lags measured, because each energy band would be completely blocked.

Thus none of these models can completely explain the fastest variability in the April and October observation, singly. It may be possible that a combination of models could be found which would explain the data. However, a simple, easy to understand model like the variable absorption model which successfully describes qualitatively many aspects of these observations, is always preferred.

CHAPTER 9

SOME ASPECTS OF OPTICALLY THIN WINDS FROM AGN

Background

As discussed in the first chapter, intense radiation is observed from AGN. As discussed in the last chapter, the X-ray emission can vary very rapidly, and this fact indicates that much of the intense radiation originates very close to the supermassive black hole believed to power the AGN. The radiation observed is believed to be derived from the gravitational potential energy of material accreting onto the black hole. If this is the case, there will be material, protons and electrons, in the central region of the AGN. Therefore these particles must experience the intense radiation field, which can influence their motion by interacting via electron scattering. One question that could be asked is, what is the subsequent motion of such a particle?

There is a limit to the flux of radiation which a particle can experience, and still accrete. Parenthetically, the particle which is being discussed is usually the hydrogen atom; i.e., protons and electrons. The force per unit mass which the particle experiences is the radiation flux times the scattering cross section, divided by the speed of light, c. If the energy of the photon is small relative to the rest mass of the particle, the scattering cross section is the Thompson cross section, σ_T. The flux is the luminosity divided by $4\pi r^2$. If this force pushing out is equated to the gravitational force pulling in, the Eddington limit luminosity is derived:

$$L_{Edd} = 4\pi GMcm/\sigma_T. \tag{9.1}$$

Here, M is the mass of the black hole, and m is the mass of the particle involved, the mass of the hydrogen atom. If the Eddington luminosity is exceeded, then the particle will be accelerated outward from the AGN, giving rise to wind. Note that, since the simplest way to relate the accretion rate to the luminosity is by $L = \eta\dot{M}/c^2$, where η is the efficiency of converting accretion energy into radiation, an associated Eddington accretion rate, $\dot{M}_{Edd}$ is also defined.

The Eddington luminosity is the minimum required to accelerate an isolated hydrogen atom out. However, in the center of some AGN, because of the large luminosity in a small region, electron–positron pairs are expected to be formed, as discussed in Chapter 2. The pairs are approximately 1000 times less massive than the hydrogen atom, so they are much more easily accelerated by the radiation pressure. Therefore, winds can also in this case be formed for lower values of the luminosity.

The problem of winds, or more simply, the problem of the motion of the gas in the central region of AGN is complicated, and has many aspects and approaches. I consider only optically thin winds. Also, the energy dependence of the radiation is ignored. Two approaches have been taken. In the first approach, I consider the motion of an isolated particle in the radiation field. This is a very simple approach, since the relevant equation to be solved is only the equation of motion. However, because of the rapid acceleration, special relativity must be used, and also, because of the proximity to the black hole, general relativity, appropriate for a Schwartzschild black hole, is used. In the second approach, the particle is assumed to be magnetically coupled to its neighbors. In this case, the gas acts like a fluid. In both cases, the only acceleration mechanism is assumed to be electron scattering. However, in this thesis, only the first approach will be discussed.

The specific equations which must be used to find the solutions will be derived in the next section. However, here I present some of the background for the current understanding of this problem.

Much of the work done to derive optically thin winds from the particle approach has been done in order to explain the observed phenomenon of super-luminal jets. These are called super-luminal because they are observed to have high velocities and to travel nearly in the observer's line-of-sight, so their transverse velocity shows apparent faster-than-light motion (see, e.g., Abramowicz, Ellis and Lanza 1990). The collimation of some of the jet beams was also found to be quite good. One model that was proposed to explain these phenomena was the radiation torus. Many of the calculations exploring the acceleration of particles in an intense radiation field were done from this context.

On the face of it, it seems that a particle in a non-isotropic radiation field could be driven to an arbitrarily high velocity by radiation pressure. However, it turns out that besides gravity, there is an effective force retarding the motion. This is called the Compton Drag force, and arises from the fact that, as the particle is accelerated by the Thompson scattering flux incident from behind it, it will also be impeded by collisions with the radiation field in front of it. Therefore, the largest velocity a particle can reach in this situation is limited.

Results

In this section, I present the derivation and solution for two cases for a wind equation appropriate for the particle approach. One case has already been done by Abramowicz, Ellis and Lanza (1990), and is presented for comparison.

The sign convention used here is $-+++$ and in the derivation the speed of light, c, is set equal to 1.

Derivation of the Wind Equation

The appropriate equation to describe the motion of a particle in a radiation field is just a simple conservation of momentum equation. Note that much of the following derivation follows that of Jaroszyński, Abramowicz, and Paczyńsky (1980). Other sources include Abramowicz and Sharp (1983), and Abramowicz, Ellis, and Lanza (1990).

In this case, the momentum change of the particle is equal to the radiation force, and the radiation force equals the radiation flux times the cross section of interaction between radiation and the particle. In this treatment, the Thompson cross section is used because the energy of the incident radiation is not specified. Therefore the equation of motion is

$$\frac{dp^{\mu}}{d\tau} = -\sigma_T F^{\mu}, \tag{9.2}$$

where p^{μ} is the momentum 4-vector, τ is the proper time, and F^{μ} is the radiation flux. The radiation flux is defined to be $F^{\mu} = T^{\mu\beta}u_{\beta}$ where $T^{\mu\beta}$ is the stress energy tensor of the radiation field and u_{β} is the four velocity.

Only radial motion is assumed to be important. To find the explicit equation of motion from Equation 9.2, the projection tensor $P^{\mu}_{\alpha} = g^{\mu}_{\alpha} + u^{\mu}u_{\alpha}$. is used. Since the mass of the particle does not change, the change in momentum is just the mass times the acceleration. Therefore the equation of motion becomes

$$\begin{aligned} ma^{\mu} &= -\sigma_T\{P^{\mu}_{\alpha}T^{\alpha\beta}u_{\beta}\} \\ &= -\sigma_T\{T^{\mu\beta}u_{\beta} + [u_{\alpha}u_{\beta}T^{\alpha\beta}]u^{\mu}\}. \end{aligned} \tag{9.3}$$

The components of the radiation stress energy tensor which are relevant for finding the motion in the radial direction are T^{tt}, T^{rr}, and $T^{rt} = T^{tr}$, so the equation in the r direction becomes

$$ma^r = -\sigma_T\{u_t T^{tr} + u_r T^{rr} + [u_t T^{tt} u_t + 2T^{rt} u_r u_t + u_r T^{rr} u_r]u^r\}. \qquad (9.4)$$

The components of the stress energy tensor that will be calculated in the next section are found in terms of the basis vectors of the stationary tetrad. These are appropriate to use as basis vectors to describe the accelerated particle (e.g., Misner, Thorne, and Wheeler 1973). One property of such basis vectors is that the metric tensor, when written in terms of these basis vectors, reduces to $\eta_{\alpha\beta}$ along the observer's path. The t and r tetrad basis vectors appropriate for a Schwartzschild black hole are

$$\begin{aligned} e_t^{(t)} &= (1 - r_s/r)^{\frac{1}{2}} \\ e_r^{(r)} &= (1 - r_s/r)^{-\frac{1}{2}}. \end{aligned} \qquad (9.5)$$

Using these, and related 1-forms, the relevant components of the stress energy tensor can be written in terms of the stationary tetrad. They are

$$\begin{aligned} T^{(t)(t)} &= T^{tt} e_t^{(t)} e_t^{(t)} = (1 - r_s/r) T^{tt} \\ T^{(r)(t)} &= T^{rt} e_t^{(t)} e_r^{(r)} = T^{rt} \\ T^{(r)(r)} &= T^{rr} e_r^{(r)} e_r^{(r)} = (1 - r_s/r)^{-1} T^{rr}. \end{aligned} \qquad (9.6)$$

Similarly the velocity 4-vector must be written in terms of the stationary tetrad basis vectors. Explicitly, they become

$$\begin{aligned} u^{(t)} &= u^t e_t^{(t)} = u^t (1 - r_s/r)^{\frac{1}{2}} = (1 - \beta^2)^{-\frac{1}{2}} \\ u^{(r)} &= u^r e_r^{(r)} = u^r (1 - r_s/r)^{-\frac{1}{2}} = \beta(1 - \beta^2)^{-\frac{1}{2}} \end{aligned} \qquad (9.7)$$

where β is the dimensionless velocity.

Using these then the appropriate way to write the velocity vector is

$$u^{\mu} = \begin{pmatrix} (1 - r_s/r)^{-\frac{1}{2}}\gamma \\ (1 - r_s/r)^{\frac{1}{2}}\beta\gamma \\ 0 \\ 0 \end{pmatrix} \tag{9.8}$$

where $\gamma = (1 - \beta^2)^{-\frac{1}{2}}$. Using these constructions for the stress energy tensor and the velocity vector, the equation of motion finally becomes

$$ma^r = \sigma_T (1 - r_s/r)^{\frac{1}{2}} (1 - \beta^2)^{-\frac{3}{2}} [(1 + \beta^2) T^{(r)(t)} - \beta(T^{(t)(t)} + T^{(r)(r)})]. \tag{9.9}$$

From this equation the presence of the Compton drag force term can be recognized. $T^{(r)(t)}$ is the radiation flux, and classically it would be the only term in the brackets on the right hand side. This term can also be recognized because the other two tensor components are multiplied by β, and so for low velocities, are negligible. However, for larger velocities they provide an effective force opposing the particle motion, because that part is subtracted from the part containing the flux. Also, they must represent a drag force, since they are multiplied by β, and so cannot accelerate the particle on their own.

In general, the acceleration is

$$a^{\alpha} = u^{\alpha}{}_{;\beta} u^{\beta} = \frac{du^{\alpha}}{ds} + \Gamma^{\alpha}_{\beta\gamma} u^{\beta} u^{\gamma}. \tag{9.10}$$

The covariant derivative is appropriate. For the r component of the equation of motion, the only relevant non-zero components of the Christoffel symbol for the Schwartzschild black hole are Γ^r_{tt} and Γ^r_{rr}. Substituting these in, the right hand part of the sum on the right side of the equation becomes $r_s/(2r^2)$. For the left hand part of the sum, use the chain rule to find the value of the derivative in terms of r. This comes out to be

$$\frac{du^r}{ds} = \frac{1}{2}\beta^2\gamma^2\frac{r_s}{r^2} + (1 - r_s/r)\gamma^2\beta\frac{d\beta}{dr}. \tag{9.11}$$

Combining this with the result from the right hand part of the sum, multiplying by r_s and substituting into Equation 9.9, the wind equation becomes

$$(1 - r_s/r)\beta\frac{d\beta}{d(\frac{r}{r_s})} + \frac{1}{2}(\frac{r_s}{r})^2(1-\beta^2) =$$

$$\frac{\sigma_T r_s}{m}(1 - r_s/r)^{\frac{1}{2}}(1-\beta^2)^{\frac{1}{2}}[(1+\beta^2)T^{(r)(t)} - \beta(T^{(r)(r)} + T^{(t)(t)})]. \tag{9.12}$$

The Radiation Stress Energy Tensor

In this section we derive two forms of the radiation stress energy tensor which could be appropriate for AGN. The second case, called the shell case, has already been solved by Abramowicz, Ellis, and Lanza (1990), but it is presented here for comparison with the other case. In the shell case, all the radiation is assumed to emerge from a shell of radius r_{min}. No radiation is produced in the surrounding region. The first case is called the extended case. In this case the radiation source is assumed to be extended and radiation is assumed to be emitted isotropically from shells dR from r_{min} to ∞.

Extended Case. The extended case was chosen because it may be physically more realistic for AGN, particularly in the context of the blob model. As reviewed in Chapter 1, AGN are believed in some cases to be powered by the accretion of material onto a super-massive black hole. This accretion can occur in the form of a thin disk, but if the radiation pressure is too large, the thin disk is unstable, and may break up into blobs. A simple way to find the amount of radiation produced by this accretion is to assume it to be a fraction of the gravitational potential energy released by the accreting matter. This implies that, in the spherically symmetric approximation, the luminosity produced per unit radius is

$$\frac{dL}{dR} = \frac{\eta G M \dot{M}}{4\pi R^2}. \tag{9.13}$$

Here $\dot{M}$ is the accretion rate, M is the mass of the black hole and η is the efficiency for conversion of gravitational potential energy into radiation. The intensity at any radius due to the radiation produced at that radius is

$$\frac{dI(R)}{dR} = \frac{dL/dR}{4\pi R^2} = \frac{\eta G M \dot{M}}{16\pi^2 R^4}. \tag{9.14}$$

However, if general relativity is taken into account, the value of the intensity received by a particle at radius r is redshifted. The amount of redshift is easy to find, because $I/(p^\alpha u_\alpha)^4$, where p^α is the photon 4-momentum, is an invariant quantity. Using this, one finds that the intensity observed at a distance r when emitted at a distance R is

$$\frac{dI(r)}{dR} = \frac{(1 - r_s/R)^2}{(1 - r_s/r)^2} \frac{dI(R)}{dR}. \tag{9.15}$$

The next step is to find the relationship between the components of the stress energy tensor and the intensity. Intuitively, the relationship can be understood by recalling the physical interpretation of the components of the stress energy tensor and relating them to the moments of the intensity (Schutz 1985; Lindquist 1966; Rybicki and Lightman 1979). Recall that the T^{tt} component is the energy density of the radiation field, T^{rt} is the energy flux across the r surface and T^{rr} is the flux of radial momentum across the radial surface, or the pressure. Therefore, these three are the zeroth, first, and second moments of the intensity, J, H, and K where

$$\begin{aligned}
\frac{dT^{(t)(t)}}{dR} &= \frac{dJ}{dR} = \int \frac{dI}{dR} d\Omega \\
\frac{dT^{(r)(t)}}{dR} &= \frac{dH}{dR} = \int \frac{dI}{dR} \cos\phi d\Omega \\
\frac{dT^{(r)(r)}}{dR} &= \frac{dK}{dR} = \int \frac{dI}{dR} \cos^2\phi d\Omega
\end{aligned} \tag{9.16}$$

where $d\Omega$ is appropriate solid angle to be integrated over and ϕ is the polar angle, or the angle between the line connecting any R and the black hole and the line connecting the observer and the black hole.

The appropriate limits for the angle integral are the next question. The integral can be done two different ways. One way is to chose the origin to be the center of the radiation shell and integrate over the full 4π solid angle. However, it can be shown that this is equivalent to choosing the origin of coordinates to be at the observer, and performing the integral $2\int_0^{2\pi}\int_0^{\alpha}$ where α is the viewing angle, or the fraction of the sky that the shell of radiation occupies (Abramowicz, Ellis, Lanza 1990; Jaroszyński, Abramowicz, and Paczyńsky 1980). The factor of 2 comes from the fact that if the source of radiation is not solid and opaque, there is a contribution from the shell in the front as well as from the shell in the back.

The factor of 2 brings to attention an important approximation that has been made. Physically, if this is intended to model an AGN, the origin of coordinates should be occupied by a super-massive black hole. If this is the case, then some of the radiation from the far side of the shell of radiation will be lost down to the black hole. This will obviously reduce the magnitude of the components of the stress energy tensor. Also, if the minimum radius is very small, close to the Schwartzschild radius, some of the radiation from the larger ϕ will also be lost down the black hole, and will also reduce the components of the stress energy tensor. However, at the present the minimum radius is assumed to be $2r_s$ and so the magnitude of the viewing angle is not affected by this second approximation (Abramowicz, Ellis, and Lanza 1990).

The viewing angle α in this case, for $r_{min} = 2r_s$, is given by

$$\sin\alpha = \frac{R}{r}\frac{(1 - r_s/r)^{\frac{1}{2}}}{(1 - r_s/R)^{\frac{1}{2}}}. \qquad (9.17)$$

Note that using the viewing angle as the limit of the ϕ integration is appropriate for $R < r$, but for $R > r$, the integration must be performed over the entire 4π sterradians.

Performing the angle integrals, and substituting in the value of $\frac{dI(r)}{dR}$, the components of the stress energy tensor can be found to be

$$\frac{dT^{(t)(t)}}{dR} = \frac{\eta GM\dot{M}}{16\pi^2 R^4}\frac{(1-r_s/R)^2}{(1-r_s/r)^2}\begin{cases} 4\pi(1-\cos\alpha) & r_{min} < R < r \\ 4\pi & r < R < \infty \end{cases}$$

$$\frac{dT^{(r)(t)}}{dR} = \frac{\eta GM\dot{M}}{16\pi^2 R^4}\frac{(1-r_s/R)^2}{(1-r_s/r)^2}\begin{cases} 2\pi\sin^2\alpha & r_{min} < R < r \\ 0 & r < R < \infty \end{cases}$$

$$\frac{dT^{(r)(r)}}{dR} = \frac{\eta GM\dot{M}}{16\pi^2 R^4}\frac{(1-r_s/R)^2}{(1-r_s/r)^2}\begin{cases} \frac{4}{3}\pi(1-\cos^3\alpha) & r_{min} < R < r \\ \frac{4}{3}\pi & r < R < \infty \end{cases} \tag{9.18}$$

where α is the viewing angle.

Next the radial integral must be done. The T^{rt} integral can be done analytically. The solution is

$$T^{(r)(t)} = \frac{\eta GM\dot{M}}{4\pi^2 R_s}\frac{(r_s/r)^2}{(1-r_s/r)}\left[(1-r_s/r)^2 - (1-r_s/r_{min})^2\right]. \tag{9.19}$$

For the T^{tt} and the T^{rr} integrals, part of the integral can be done analytically. This is because, for these two parts, there is a 1 in the $r_{min} < R < r$ parts, so this can be combined with the $r < R < \infty$ parts, and the integral can be done analytically from r_{min} to ∞. The remaining parts of the integrals, containing $\cos\alpha$ terms, must be done numerically. Once these integrals have been done, the resulting components of the stress energy tensor can be substituted in the wind equation, Equation 9.12.

<u>Shell Case.</u> For the shell case the components of the stress energy tensor are easy to find, because no radial integral need be done. For comparison with the extended case the luminosity for the shell case is chosen to be the total luminosity

for the extended case, i.e., the integral of dL/dR from r_{min} to ∞ of the extended case. Therefore, $L = (\eta G M \dot{M})/(4\pi r_{min})$.

Following the same arguments as above, the components of the stress energy tensor for the shell case become

$$T^{(t)(t)} = \frac{\eta G M \dot{M}}{8\pi r_{min}^4} \frac{(1 - r_s/r_{min})^2}{(1 - r_s/r)^2} (1 - \cos\alpha)$$

$$T^{(r)(t)} = \frac{\eta G M \dot{M}}{8\pi r_{min}^4} \frac{(1 - r_s/r_{min})^2}{(1 - r_s/r)^2} \frac{1}{2} \sin^2\alpha$$

$$T^{(r)(r)} = \frac{\eta G M \dot{M}}{8\pi r_{min}^4} \frac{(1 - r_s/r_{min})^2}{(1 - r_s/r)^2} \frac{1}{3} (1 - \cos^3\alpha) \qquad (9.20)$$

In order to make the wind equation dimensionless, define a dimensionless parameter A to be

$$A = \frac{\eta G M \dot{M}}{4\pi c^3} \frac{\sigma_T}{m} \frac{1}{r_s^2}. \qquad (9.21)$$

Recall that the Eddington luminosity is defined to be

$$L_{edd} = \frac{4\pi G M c m_H}{\sigma_T} \qquad (9.22)$$

and the total luminosity is

$$L = \frac{\eta G M \dot{M}}{4\pi r_{min}}. \qquad (9.23)$$

Therefore the parameter A is related to the ratio of the total luminosity to the Eddington luminosity by

$$A = \begin{cases} 2\pi \frac{L}{L_{Edd}} \frac{r_{min}}{r_s}, & \text{for ions;} \\ 2\pi \frac{L}{L_{Edd}} \frac{r_{min}}{r_s} \frac{m_H}{2m_e}, & \text{for pairs.} \end{cases} \qquad (9.24)$$

Since r_{min} is assumed to be the $2r_s$, $A \approx 10$ is about the Eddington limit when accelerating ions, but $A \approx 10,000$ when accelerating pairs. Thus, if the accretion rate is required to be less than the Eddington limit accretion rate, a wider range of solutions is accessible when accelerating pairs.

Solutions

First, since the range of the r variable is from r_{min} to ∞, the solutions become easier to discuss if a change of variables is made. Let $y = 1 - r_s/r$. If this is true, and if r_{min} is chosen to be $2r_s$, then the range of y is from 0.5 to 1.0.

Before directly integrating the equation of motion, it is instructive to examine what is called the saturation velocity equation. This equation is the algebraic equation which results when $d\beta/dy$ is set equal to zero. The saturation velocity β_s is found by solving this equation as a function of y and the parameter A. This method has been used by several authors, including Abramowicz and Sharp (1983), who invented the term 'saturation velocity', and Sikora and Wilson (1981), who referred to this calculation as the 'zero-mass' approximation.

Note that the saturation velocity is not a solution of the wind equation, so a particle cannot travel at a velocity equal to the saturation velocity. The saturation velocity serves as a useful construct to divide the β–y space. Solutions of the wind equation behave as if they are drawn toward the saturation velocity solution, in that if a particle has velocity greater than β_s, then it will be decelerated, while if the velocity is less than β_s, then it will be accelerated.

Figure 68 shows the saturation velocity curves for the shell case for several representative values of A. For $A = 3$ the saturation velocity is everywhere negative. For $A = 5.7$, the saturation velocity is 0 at the minimum radius. For $A = 6.9$, the saturation velocity has a 'critical point', because this solution crosses the $\beta = 0$ line. The saturation velocity is 0 at $y = 1.0$ ($r = \infty$) when A is equal to 8. The solution of $A = 28$ is typical of those values of A for which there is a maximum in the saturation velocity curve. Note that the saturation velocity solutions are decreasing for larger values of y, except for the largest value of $A = 1000$, in which the saturation velocity increases for nearly all y. Note also that for A greater than

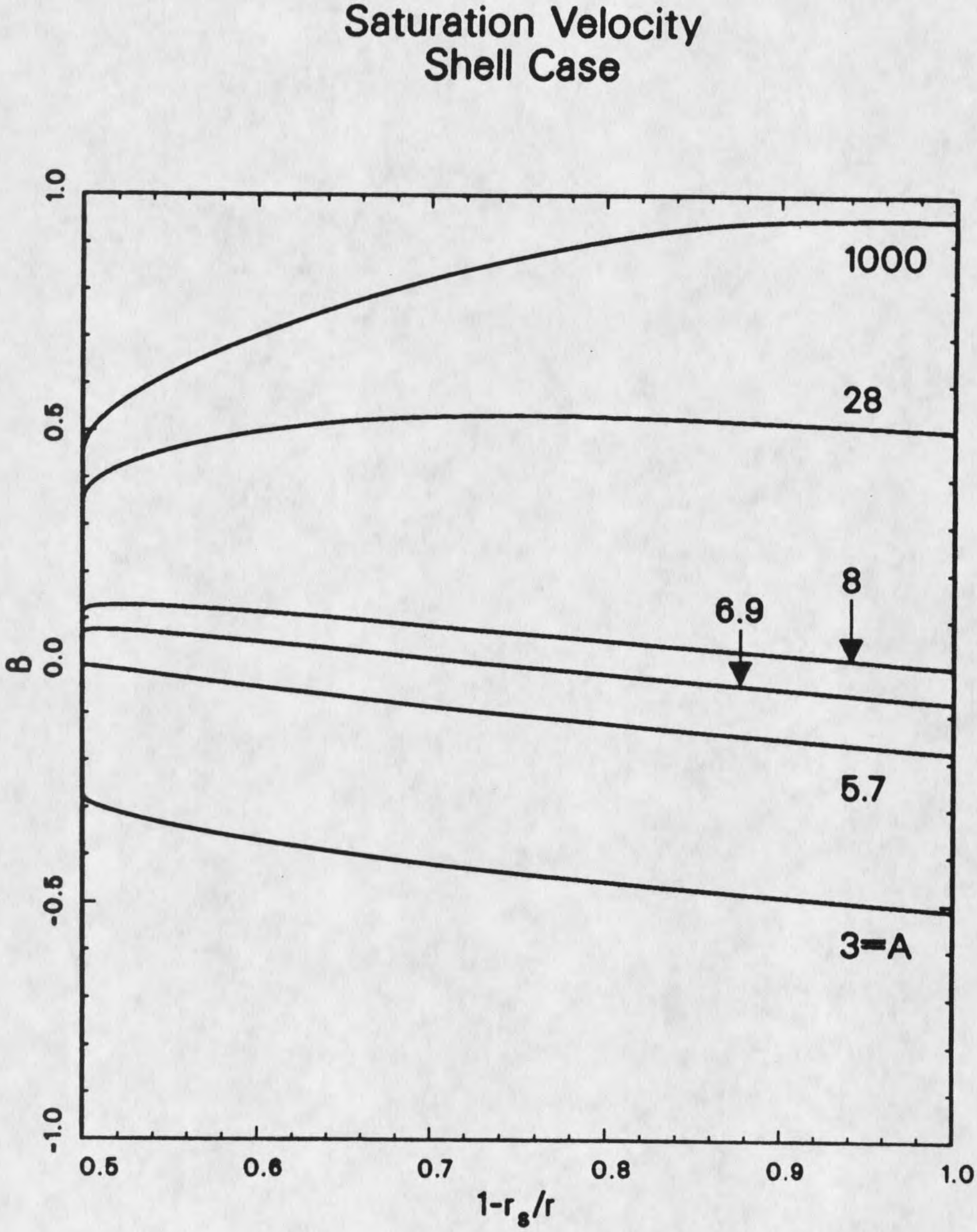

Figure 68. Saturation velocity profiles for the shell case. The numbers labeling each curve are the value of the parameter A.

5.7, the saturation velocity is positive at the minimum radius. This is because for the shell case, the flux, or $T^{(r)(t)}$, is maximum at the minimum radius, and for $A > 5.7$, the radiation flux is stronger than the gravitational pull force at the minimum radius.

In contrast, Figure 69 shows the saturation velocity curves for the extended case for several representative values of A. The values of A were chosen for similar reasons as for the shell case. The most interesting case is for $A = 5.5$, because here there is a critical point. These solutions are significantly different than those for the shell case. One difference is that, at the minimum radius, the saturation velocity is negative for all choices of A. The reason for this difference is that the flux, or the $T^{(r)(t)}$ component of the stress energy tensor, is equal to 0 at the minimum radius. Another obvious difference is that these are all monotonically increasing. The fact that the flux is 0 at the minimum radius partially explains this second difference, because if the flux is 0 at r_{min}, and it also must go to 0 as r approaches ∞, then it must be a maximum at some y not 0.

Next, the equation of motion can be integrated. A simple 4th order Runge-Kutta method was used. Many different starting values of β and y were chosen to fully investigate the nature of the solutions. First, however, Figure 70 shows the velocity profiles in the case of no radiation and only gravity is accelerating the particles. The saturation velocity for such a situation is -1, as pointed out by Abramowicz, Ellis, and Lanza (1990).

Figures 71–76 show the integrated solutions of the wind equation, for the shell case, for the different representative values of A, while Figures 77–80 show the integrated solutions for the extended case for the representative values of A. In both cases, the saturation velocity solution for the corresponding value of A is shown by the dashed line.

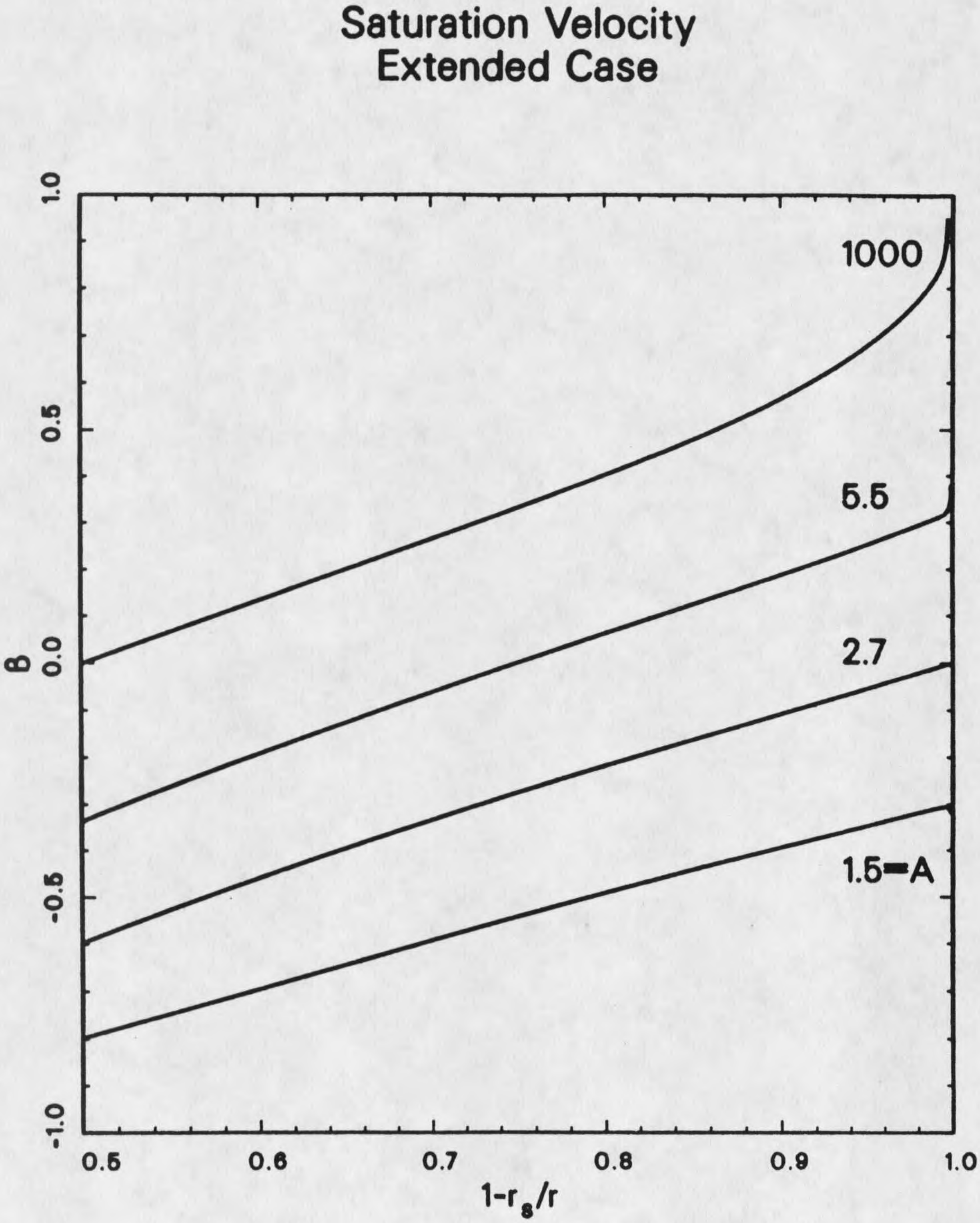

Figure 69. Saturation velocity profiles for the extended case. The numbers labeling each curve are the value of the parameter A.

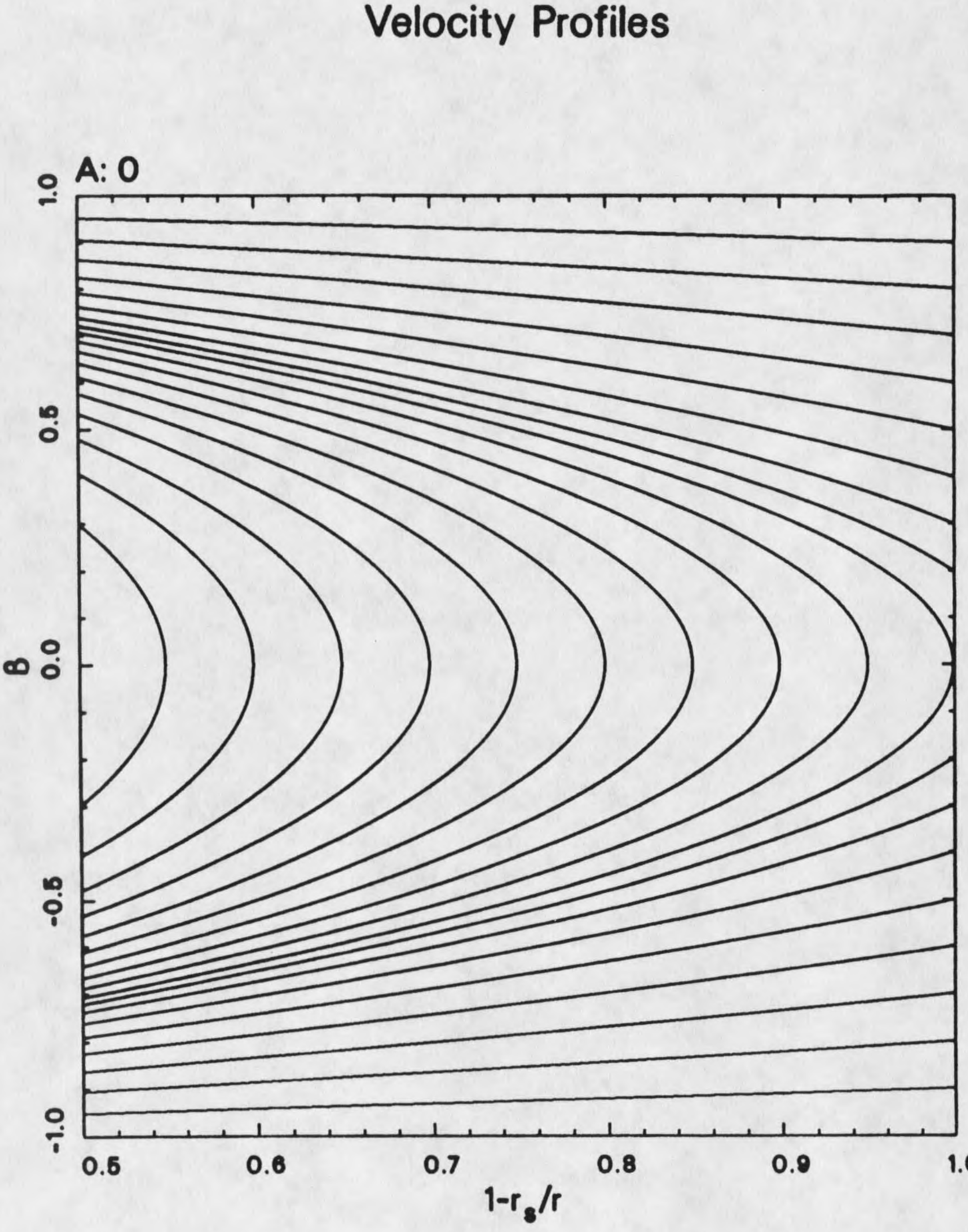

Figure 70. Integrated velocity profiles for the case $A = 0$, implying no radiation pressure. Saturation velocity solution is $\beta = -1$.

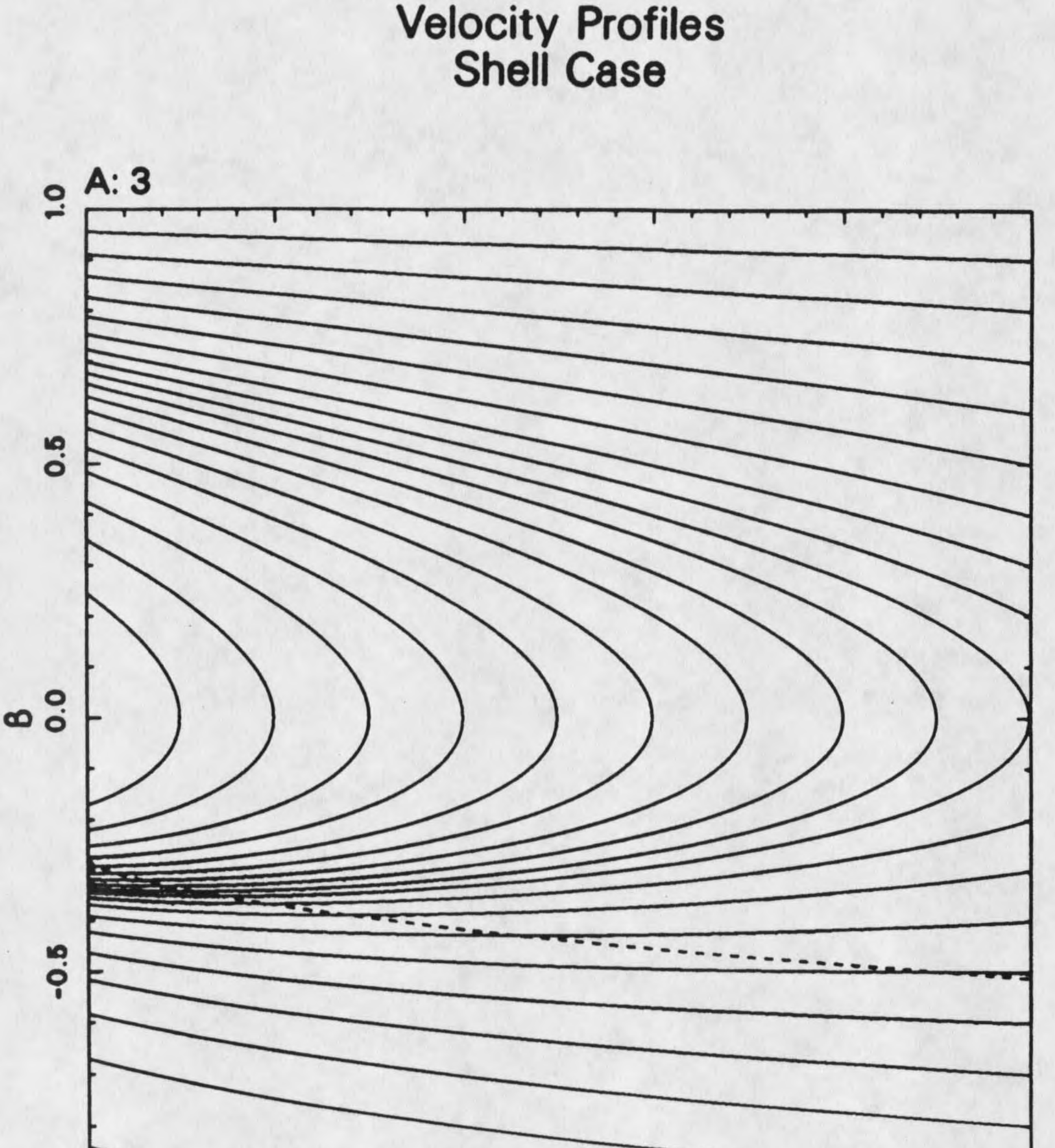

Figure 71. Integrated velocity profiles for the shell case with $A = 3$. The dashed line shows the saturation velocity solution.

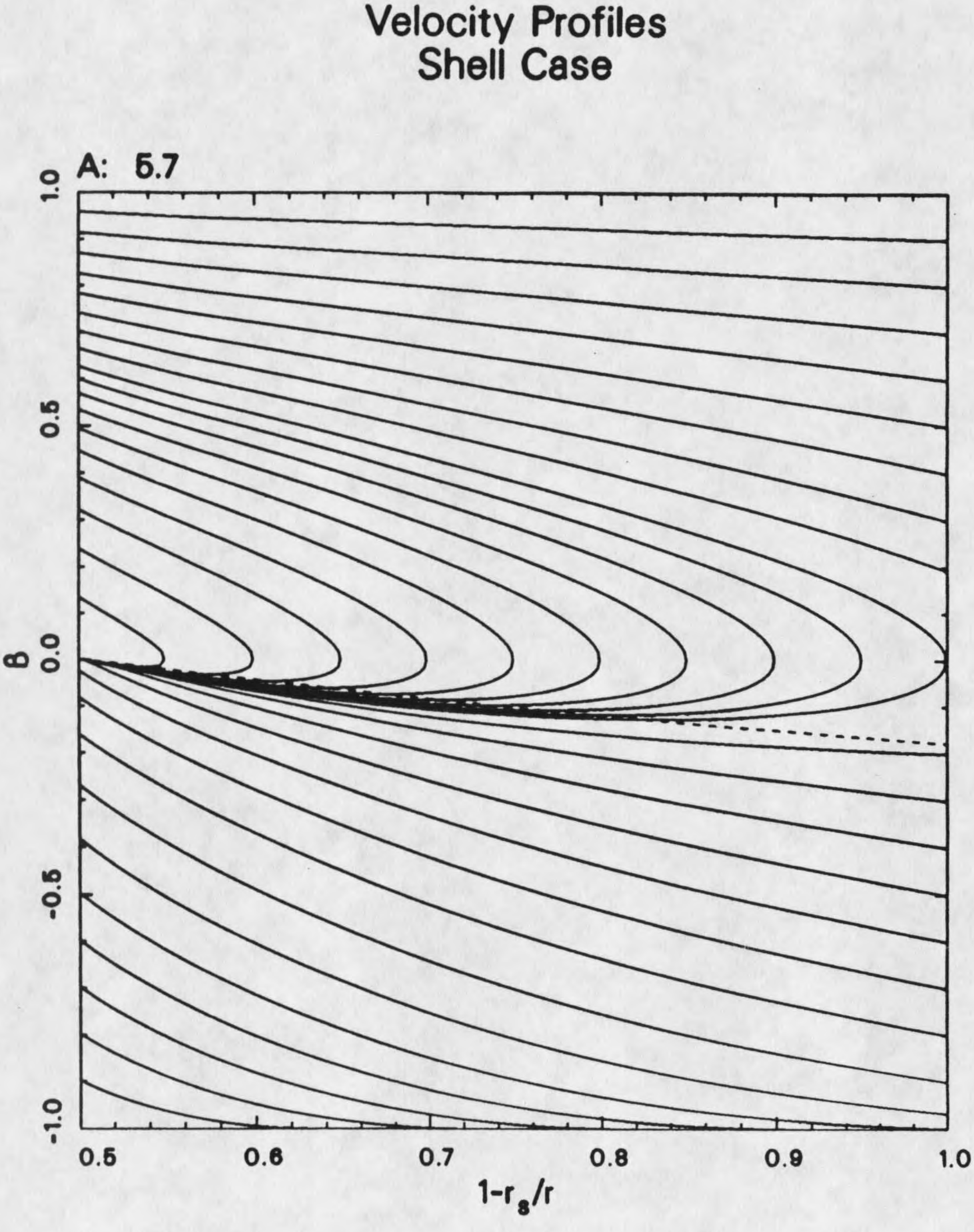

Figure 72. Integrated velocity profiles for the shell case with $A = 5.7$. The dashed line shows the saturation velocity solution.

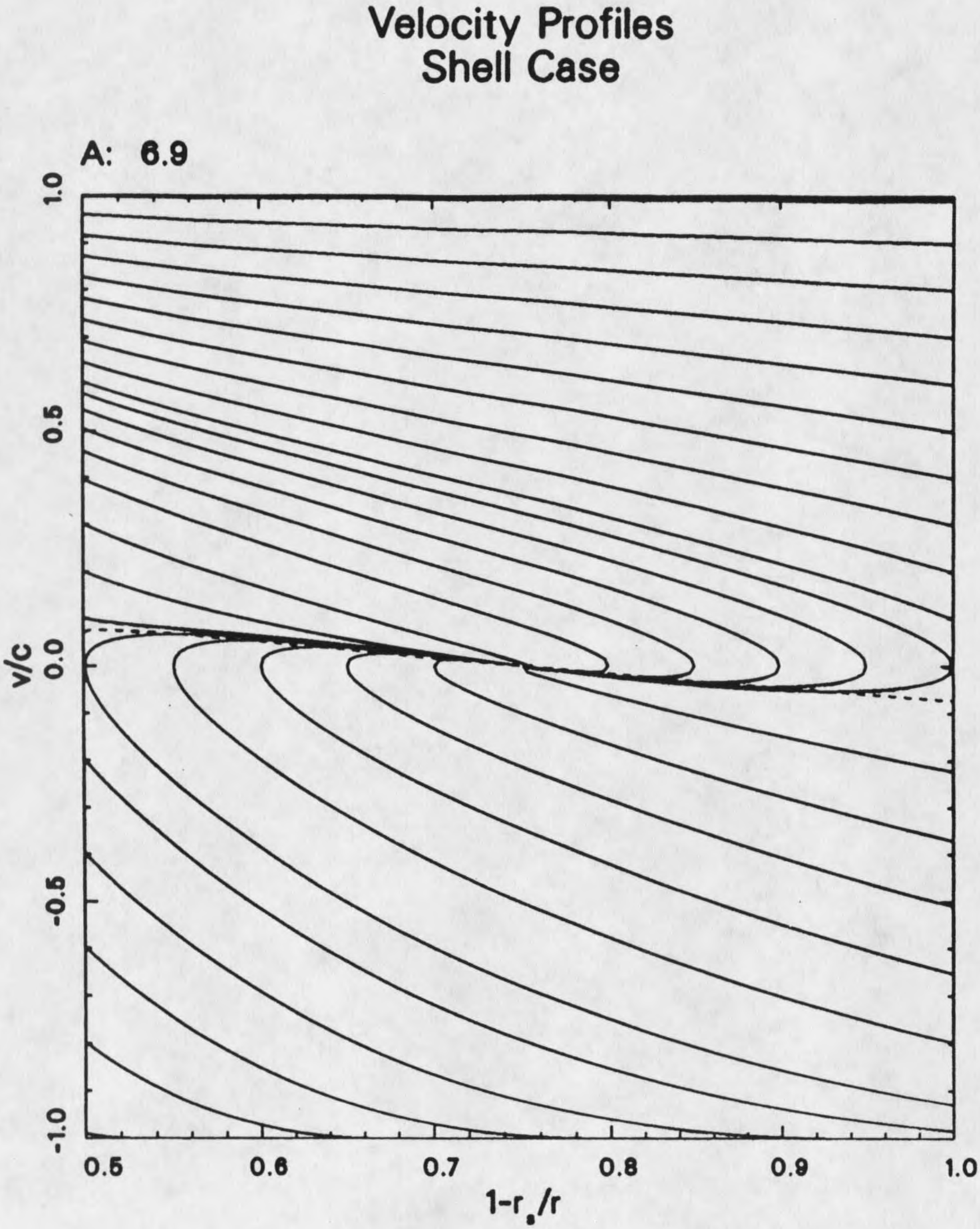

Figure 73. Integrated velocity profiles for the shell case with $A = 6.9$. The dashed line shows the saturation velocity solution.

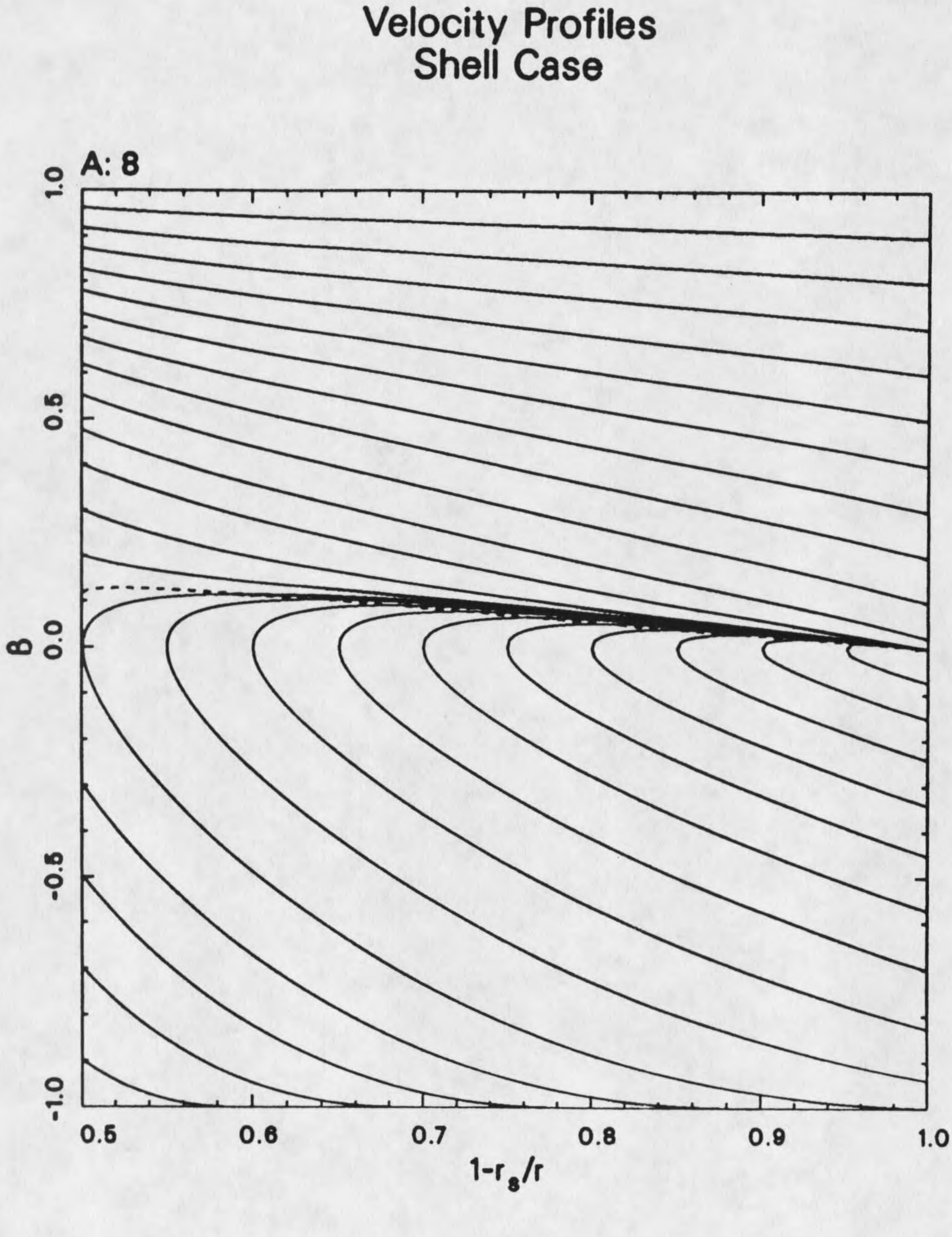

Figure 74. Integrated velocity profiles for the shell case with $A = 8$. The dashed line shows the saturation velocity solution.

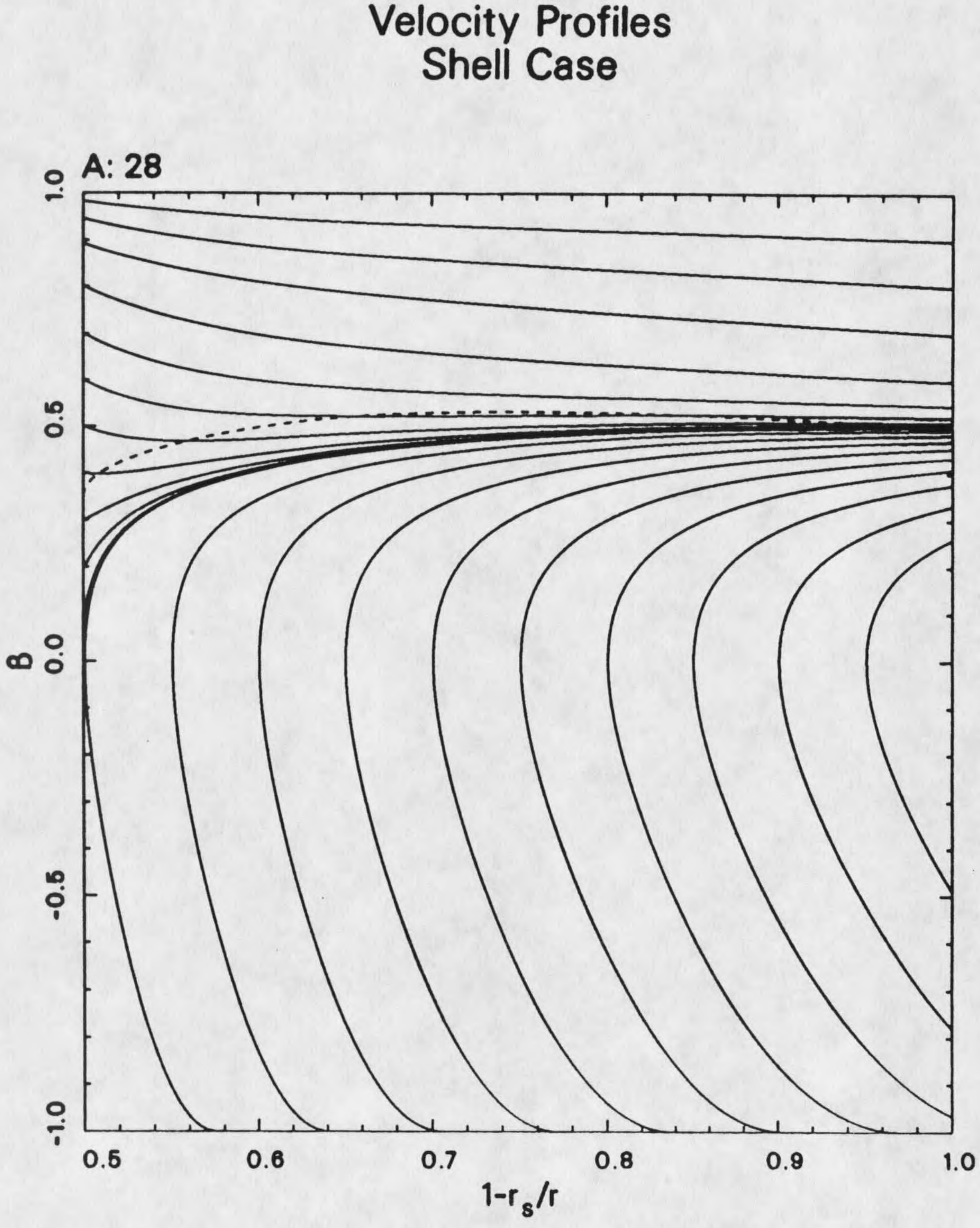

Figure 75. Integrated velocity profiles for the shell case with $A = 28$. The dashed line shows the saturation velocity solution.

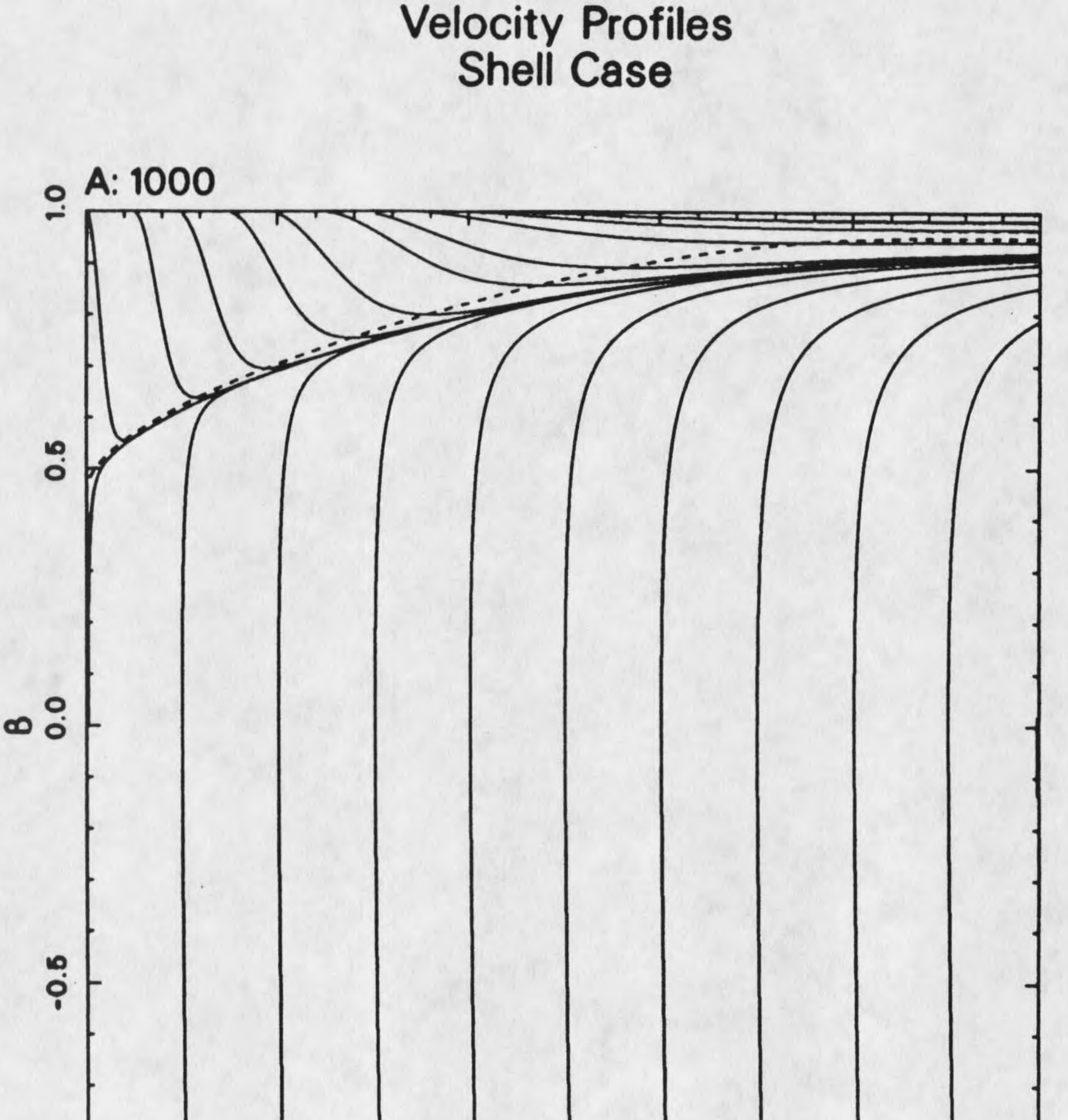

Figure 76. Integrated velocity profiles for the shell case with $A = 1000$. The dashed line shows the saturation velocity solution.

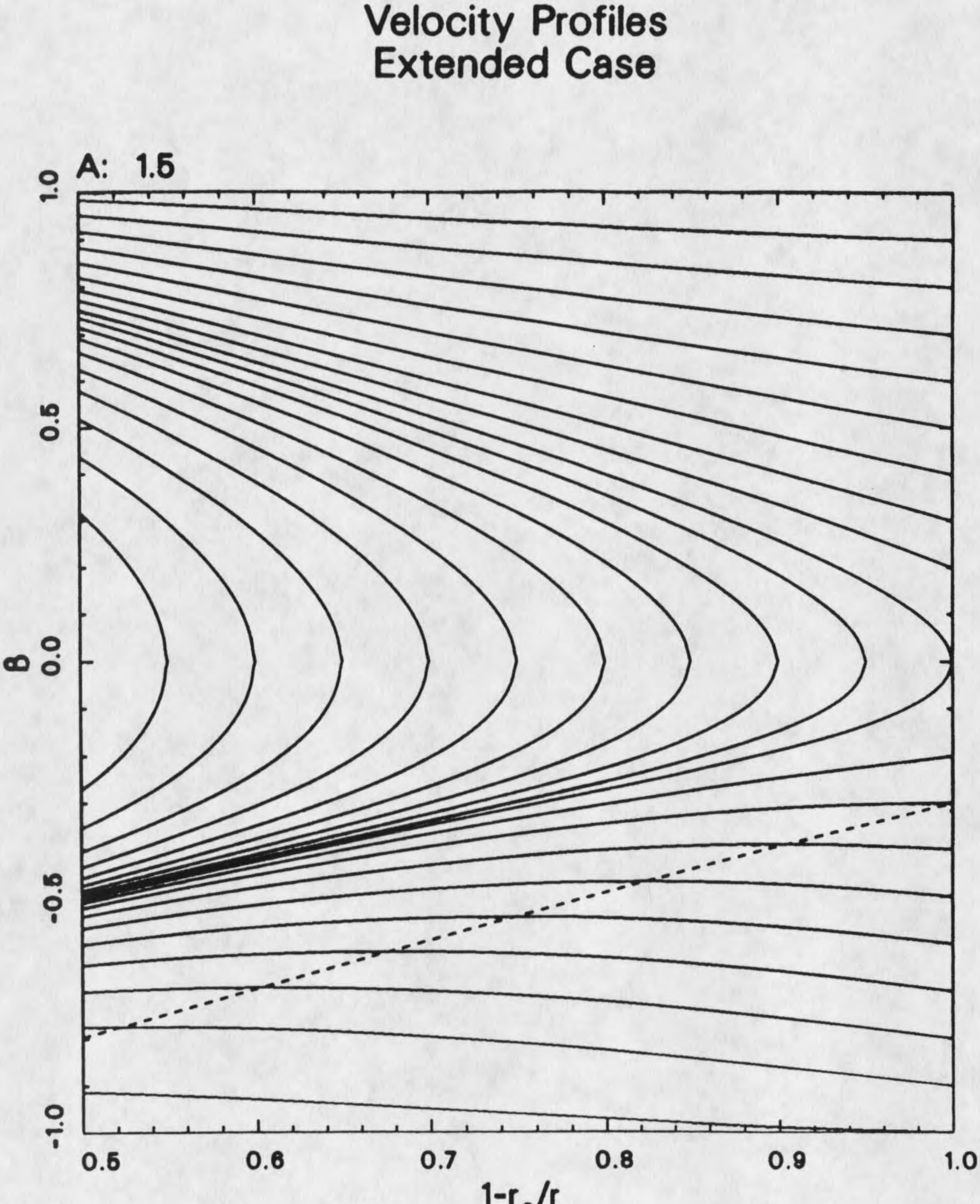

Figure 77. Integrated velocity profiles for the extended case with $A = 1.5$. The dashed line shows the saturation velocity solution.

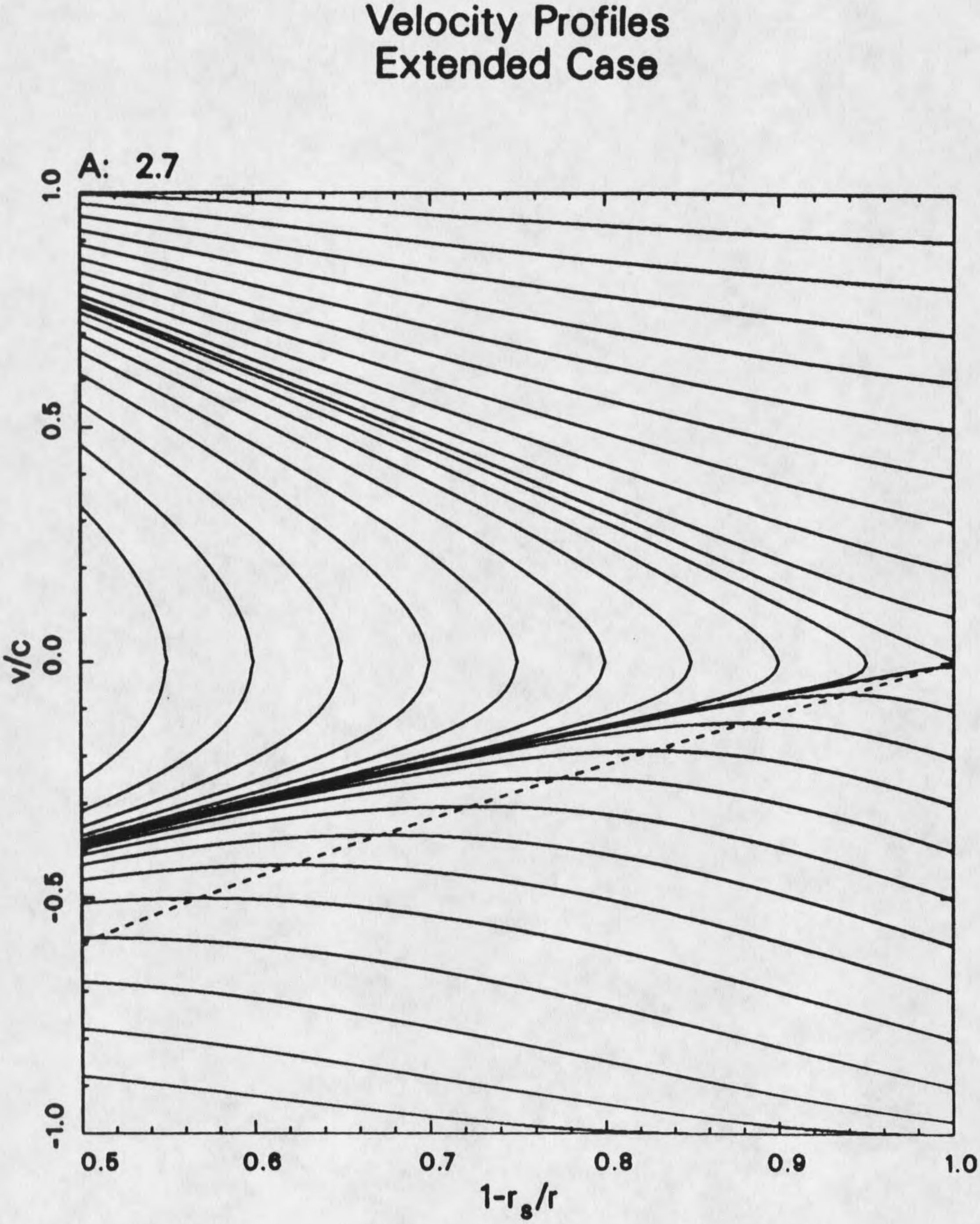

Figure 78. Integrated velocity profiles for the extended case with $A = 2.7$. The dashed line shows the saturation velocity solution.

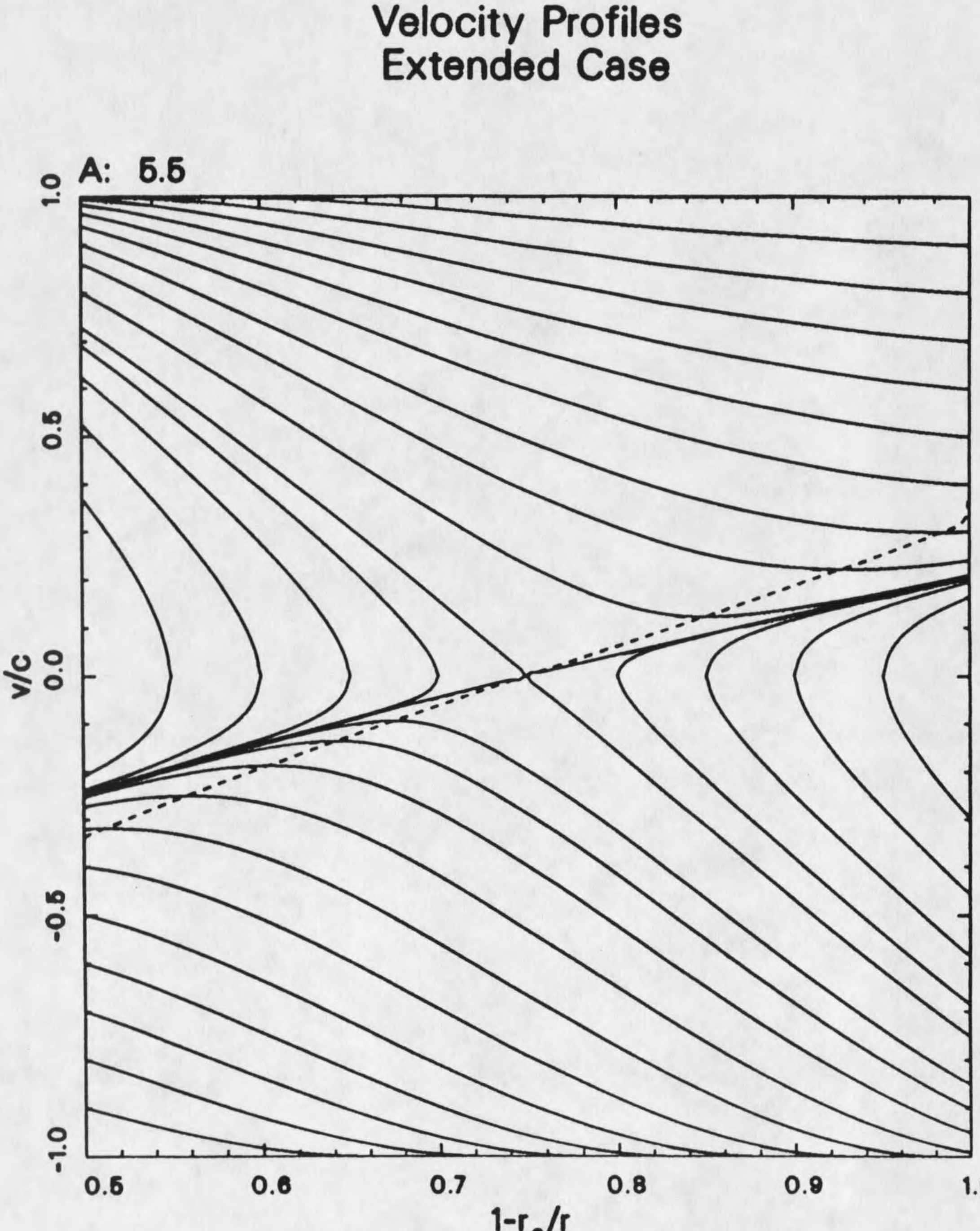

Figure 79. Integrated velocity profiles for the extended case with $A = 5.5$. The dashed line shows the saturation velocity solution.

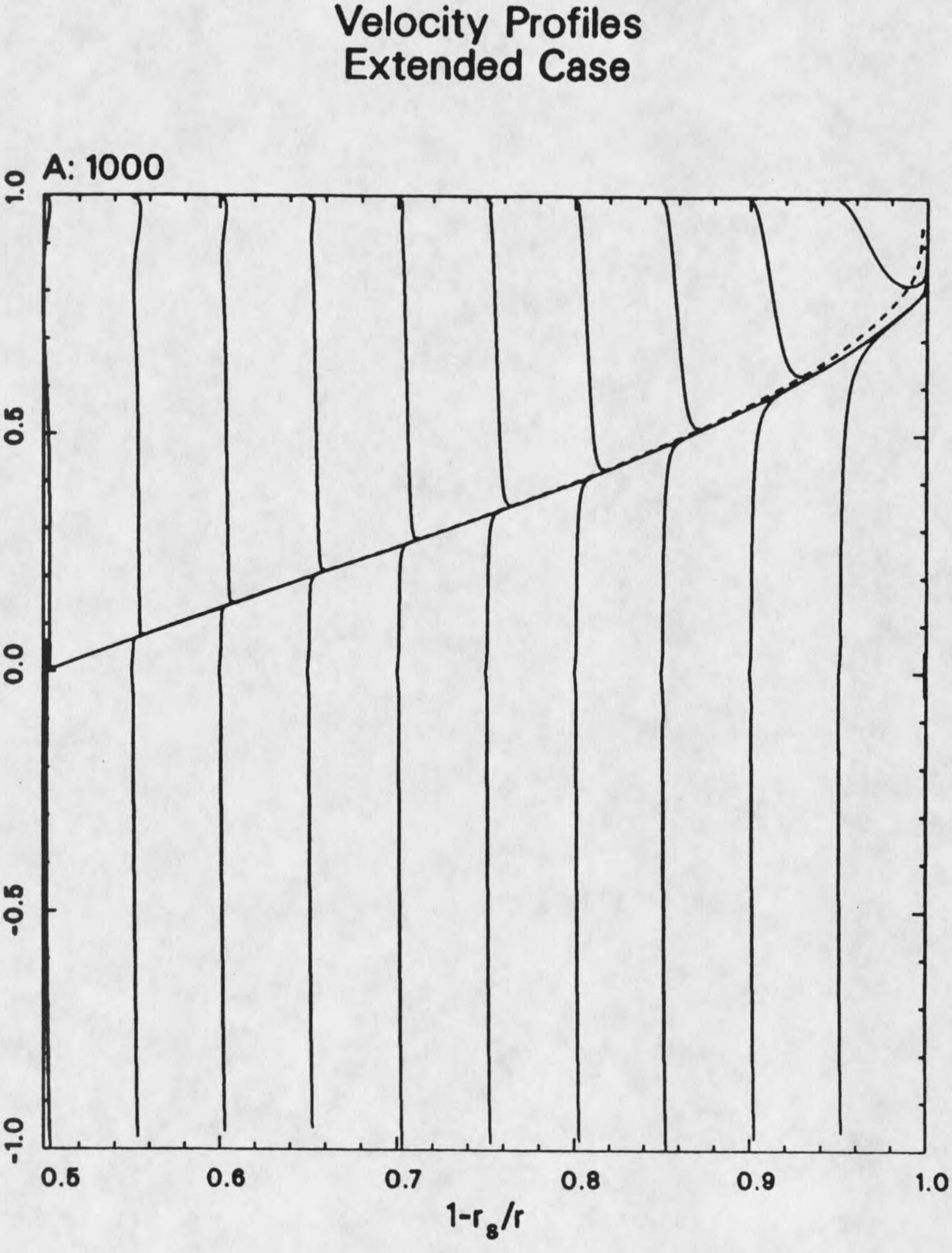

Figure 80. Integrated velocity profiles for the extended case with $A = 1000$. The dashed line shows the saturation velocity solution.

Figure 71 shows the solution $A = 3$ for the shell case, while Figure 77 shows the solution $A = 1.5$ for the extended case. These both have saturation velocity curves that are everywhere negative. For the positive velocities, the solutions are very similar. However, for negative velocities, or paths for infalling particles, the solutions are somewhat different, due mostly to the fact that for the shell case, the saturation velocity is monotonically decreasing, while for the extended case the saturation velocity is monotonically increasing. This causes some of the solutions for the shell case to have minima, while some of the solutions for the extended case have maxima. This means that, for the shell case, infalling particles are more impeded by the combination of radiation flux and Compton drag in the second part of their infall, or for small values of y, while for the extended case, infalling particles seem to be impeded more for large values of y.

Figure 72 shows the solution $A = 5.7$ for the shell case, while Figure 78 shows the solution $A = 2.7$ for the extended case. These both have saturation velocity curves that are negative for all y except for an extreme value of y. Again, solutions for positive A are similar. For the shell case, if a particle is released at any radius with 0 velocity, it will fall to the minimum radius and will arrive with 0 velocity. The situation for the extended case is very similar to the previous case.

Figure 73 shows the solution $A = 6.9$ for the shell case, while Figure 79 shows the solution $A = 5.5$ for the extended case. These both are examples of solutions for which the saturation velocity equals 0 for y not 0.5 or 1.0. Thus these solutions are representative of the values of A for which the solution is a critical point. These are critical points because $d\beta/dy = 0$ for some y. Solutions with critical points are interesting. Critical points can be classified. In order to do this, first note that a first order differential equation can be split into a system of first order equations

(Kaplan 1958). That is, if the equation is

$$-G(\beta, y)d\beta + F(\beta, y)dy = 0, \tag{9.25}$$

then

$$\frac{d\beta}{dt} = F(\beta, y), \frac{dy}{dt} = G(\beta, y). \tag{9.26}$$

After doing that, these equations can be expanded about the critical point (β_c, y_c). The simplest case is when the first derivatives of the functions are not 0. Then terms that are of higher order than linear are dropped, and this procedure produces two coupled linear first order differential equations. That is, for $u = \beta - \beta_c$ and $v = y - y_c$,

$$\frac{du}{dt} = a_1 u + b_1 v, \quad \frac{dv}{dt} = a_2 u + b_2 v, \tag{9.27}$$

where

$$\begin{aligned} a_1 &= F_\beta(\beta_c, y_c), \quad & b_1 &= F_y(\beta_c, y_c), \\ a_2 &= G_\beta(\beta_c, y_c), \quad & b_2 &= G_y(\beta_c, y_c). \end{aligned} \tag{9.28}$$

The nature of the solution around the critical point can be found by examining the characteristic equation

$$\det \begin{pmatrix} a_1 - \lambda & b_1 \\ a_2 & b_2 - \lambda \end{pmatrix} = 0. \tag{9.29}$$

Define $p = a_1 + b_2$, $q = a_1 b_2 - a_2 b_1$, and $\Delta = p^2 - 4q$. Then there are three major types of critical points. For $q < 0$, the critical point is a saddle point, and it is always unstable. For $q > 0$ and $\Delta > 0$ the critical point is a node which will be unstable if $p > 0$ 2 or stable if $p < 0$. For $\Delta < 0$ and $p \neq 0$, the critical point is a focus which also can be stable or unstable.

For the shell case, the solution at the critical point has been shown to be a stable node. This fact was found by Abramowicz, Ellis, and Lanza, 1990. However, the critical point for the extended case can be numerically shown to be a saddle point, for all relevant A ($A > 2.7$).

The physical interpretation of the type of critical point is very interesting. Since the critical point of the shell case is shown to be a stable node, as pointed out be Abramowicz, Ellis and Lanza (1990), this implies that, for many initial starting points for particles on the (β, y) plane, the particles will be decelerated to the critical point, and because it is a stable critical point, they will stay there. This implies that a shell of matter will be accumulated at the critical point radius. However, since the critical point for the extended case is a saddle point, and since all saddle points are unstable, even particles placed at the critical point will not remain there. So, far from having a build up of particles at the critical radius, there will be a void of particles. This is actually physically more familiar, because it shows the intuitive expectation that the boundary between infalling particles and out-flowing winds should be devoid of particles. It would be interesting to investigate the reason why these solutions are so different, but a possible reason is that it must be so because the saturation velocity curve has a negative slope at the critical point for the shell case, while it has a positive slope for the extended case.

Figure 74 shows the solution $A = 8$ for the shell case. For this choice of parameter, the saturation velocity is 0 at $y = 1.0$. Particles let go at rest will all escape. For the extended case, since the saturation velocity is always less than 0 at the minimum radius, there is no value of A where all particles let go at rest will all escape, except for the limit $A \rightarrow \infty$.

Figure 75 shows the solution $A = 1000$ for the shell case, while Figure 80 shows the same solution for the extended case. In both cases, the particles are all accelerated to ∞. However, for the extended case, since the saturation velocity solution is smaller than 0 at all y_{min}, then particles started with large positive velocities are drastically decelerated before being accelerated.

Discussion

The wind equation for two different radiation stress energy tensors was solved. An interesting physical implication was found. For the previously solved shell case, for certain parameter values for which there was a critical point of the equation, the solution implied that a shell of matter would be built up at the critical radius, around the source of radiation, because the critical point is a stable node. In contrast, for the extended case, the solution at the critical radius implies a void of particles at the critical radius.

Several interesting questions about this behavior remain unanswered. One is the question of why is the solution behavior different? Is it directly related to the slope of the saturation velocity curve at the critical point? If it is, what determines the saturation velocity slope? Is it the fact that the flux at the minimum radius is 0 for the extended case? Certainly this is a factor to cause the saturation velocity curve to increase for small y. However, does this fact determine the behavior for large y? For example, if a different distribution of radiation is chosen, for example, one with a faster decay, would the saturation velocity curve ever turn over? If so, could there be more than 1 critical point? These questions will be addressed in future work.

CHAPTER 10

CONCLUSIONS

In this chapter, the major results and conclusions of this thesis are discussed. In addition, the major unfinished work is also described. Finally, future prospects of X-ray astronomy are described.

Results, Conclusions and Unfinished Work

In Chapter 4 we described the results of the reanalysis of EXOSAT data carried out by the author in order to detect iron emission and absorption features. From the long observation of NGC 5506, an iron emission line and also an absorption edge were found. The size of the emission line was moderate. However, the iron absorption edge was found to be deep, corresponding to an over-abundance of iron by a factor of four. The iron edge fitting fixed the edge energy at a value appropriate for cold iron. However, a *Ginga* observation found the iron edge energy to be somewhat larger than the value appropriate for neutral iron. Therefore, assuming that a warm absorption edge would have been more appropriate, an ionization model was postulated. In this model, the absorbing screen consists of partially ionized gas, ionized to the extent that the low energy X-rays are not absorbed, but iron still retains enough K shell electrons to absorb X-rays above the iron K edge. In this way, the apparent overabundance of iron could be explained. This also lead to the conclusion that the iron line was produced in the material in the line-of-sight.

Also in Chapter 4 the results of the analysis for iron features of the EXOSAT spectral survey sources was described. A total of 47 spectra from 40 AGN were analyzed. Thirteen spectra from twelve sources showed evidence for an iron emission line, while five spectra from five sources showed evidence for additional absorption. Thus line emission is verified in a third of the AGN in this sample. The equivalent widths of the lines were not well determined. However, statistical analysis using the equivalent widths from the sample of detections show that there is some suggestion of inverse correlation between equivalent width and luminosity, as well as a correlation between the equivalent width and the host galaxy axial ratio. The first correlation perhaps suggests that the presense of cold material in the central region is more likely when the luminosity is lower. Such a conclusion is supported by the fact that intrinsic absorption is also found to be more common in low luminosity sources (Turner and Pounds 1990; Turner et al. 1991). The second correlation perhaps supports the theory of iron line emission in an accretion disk, because in such models, larger equivalent widths are predicted when the accretion disk is viewed face-on. No correlation could be established between the detected equivalent width and intrinsic absorption or soft excess emission.

The correlation calculation discussed above does not reflect the data well as a whole. Only 13 spectra from 12 sources produced line detection at the 90% level. Upper limits to line detection were found in 34 other spectra. It is more correct to use methods to calculate the correlations which take these upper limits into account (Avni et al. 1980; Schmitt 1985; Feigelson and Nelson 1985; Isobe, Feigelson and Nelson 1986). These calculations have not yet been done. However, the value of this calculation is in question. This is because, using *Ginga*, iron line emission has been shown to be common in AGN (Awaki 1991; Nandra 1991). Such work using the larger detector of *Ginga* found better constrained equivalent widths from the Seyfert 1 nuclei. These better constrained values are more appropriate for use in statistical analysis. However, it would be useful in the long run to have such computer programs available for other data with upper limits.

In Chapter 7 the analysis and results from a *Ginga* observation of NGC 7469 were discussed. Although the source was at a low flux level, inherently and because of satellite pointing problems, and although there were background subtraction problems, several results were found. In one section of the data the source was observed to decrease in flux with a halving time scale of 25,000 seconds, with no evidence for spectral change during this decrease. In another section of the data marginal evidence for spectral softening was found, with no significant change in flux. More interesting results were that there was no evidence in the low energy bands for the soft excess component which has been found previously in this source. This could not be due to a background subtraction systematic error, because such an error was estimated to enhance excess emission at low energies. Also, the photon index was found to be anomalously flat. A consistent but untestable model proposes that the soft excess component has become temporarily quiescent.

Further work on this source is planned during a visit to Nagoya University in November and December of 1991. First, the background subtraction problems of this observation will be resolved. Then, the analysis of another *Ginga* observation of NGC 7469 will be performed and the two will be compared. It may be possible, through this comparison, to derive a consistent model to describe the spectral changes in this source.

Chapter 8 described the most significant work in this thesis. The analysis of two observations of NGC 6814 was discussed. These observations proved exceptionally rich in data analysis opportunities. New results included the observation of 12,000 second periodicity of the hardness ratio from the October data, implying continuous variability of spectral index. The observation of periodic dips to nearly zero flux in the April data was also remarkable. Detailed spectral analysis of the dip data from the April observation showed that significant spectral variability was observed, with the photon index decreasing during the dips. Also, the iron line flux was found to decrease significantly during the dips. Detailed spectral analysis of the two sections of data from the October observation exhibiting the fastest change in flux also showed some evidence for spectral hardening during low flux states. In addition, comparison of two low flux spectra found significant spectral change within 128 seconds, in that the spectrum was suddenly found to soften. Time series analysis of two sections of the October data found that during the flux decrease (ingress), the hard flux was found to lag the soft flux. In contrast, during the increase (egress), the soft flux was found to lag the hard flux. Such lags were only marginally identified in the April dip data.

Armed with this abundance of observational results, a new variation of the partial covering model for the regions of the fastest variability of both observations was proposed. This model is called the variable absorption model and it proposes to explain both the spectral change and the lags observed by using an absorbing layer in the line of sight with a column density which is a function of time. An exponential column was proposed, and fit explicitly to the lag data from the October ingress and egress data sections. In the case of the ingress the fit was acceptable. However, for the egress the fit was not acceptable, and fit residuals imply that a better model function would result in faster decreases at high energies. Simulated spectra were derived using the model parameters found from the fitting. These spectra were then fit. The results quantitatively agreed with the actual spectral fitting results from the October ingress and egress, in that spectral hardening was found during flux decrease, followed by sudden softening. Also, the absorption column was found to be anomalously low in some cases, requiring it to be fixed at the Galactic value. Such a result was also found in the actual data. Finally, this model could be generalized to the April dip data, by assuming the gradient of the column density to be larger, causing lags which cannot easily be detected with the 16 second time resolution and low flux in the dips.

Work remaining in this project is of two types. First, some small details must be addressed. For example, template fitting of the April dip data needs to be done to find limits on the lags. Second, the applications of the variable absorption model to the whole October observation needs to be quantified. It is easy to see how such a model can explain the implied 12,000 periodicity of the photon index. If the column density gradient extends in the spatial direction as well as varying in time, and if the source is a finite size, comparable to the column gradient, then variability of the gradient would reflect the variation of the spectral index. However, detailed spectral fitting must be done to support this model. As mentioned before, part of this program is now being addressed by Y. Tsusaka at Nagoya University. Probably, the remainder will be addressed during the upcoming visit by the author to Nagoya University.

In general there are many interesting unsolved problems concerning this unusual source. One of the most puzzling is the problem of the large equivalent width yet fast variability of the iron line. The variable absorption model does not address this problem. Other models have been proposed to explain the large equivalent width (e.g. Hayakawa 1991), but in general these fail to explain the periodicity. This difficult problem is one of the most interesting problems confronting AGN research today.

Chapter 9 describes the results of a small theoretical calculation concerning the motion of particles in a strong radiation field near a black hole. The chief result of this calculation was that a small change in the stress energy tensor resulted in a change in the type of solution critical point. Specifically, in the case where all the radiation is emitted from a radius r_{min}, it is found that for those solutions exhibiting critical points, the critical point is the stable node type (Abramowicz, Ellis and Lanza 1990). This implies that a shell of material will be formed at this stable critical point. In contrast, if an extended source stress energy tensor, devised by the author, is used, which has the radiation flux being extended through the region, the critical point becomes a saddle type critical point. This type is unstable, and implies a void of material will be found at the critical point radius.

Much work remains to finish this project. Specifically, it must be determined why the difference in stress energy tensors results in a difference in critical point type.

Future Prospects of X-ray Astronomy

Future work in X-ray astronomy depends on what types of instruments will be available in the future. In this section, some of the present and future missions will be described. However, first it is important to know that even though large area proportional counters have been popularly used, as described in this thesis, in general nearly all of the new missions involve X-ray telescopes.

As Tennant points out in his thesis (Tennant 1983), the ideal detector has large area and low internal background. The advantage of proportional counters is that a large area can be achieved, but the disadvantage is that the internal background is high. X-ray telescopes are capable of low internal background, but in general because of the weight and expense of the telescope, the area is small.

Presently, the current X-ray telescope now available is *ROSAT*. This is a German/UK/USA mission, consisting of two imaging telescopes. The main one, provided by Germany, is an X-ray telescope (XRT) for imaging in the energy range 0.1–2 keV. The second telescope, called the Wide Field Camera (WFC) provides imaging in the EUV range from 0.02–0.2 keV. Thus the energy band of this mission is very soft. During the first year of operation *ROSAT* performed an all-sky survey. Early results from WFC all-sky survey increased the number of cosmic EUV sources by two orders of magnitude. Many of these objects are identified as active late-type stars and white dwarfs (Pounds 1991). In this energy band, the detection of AGN will be limited by absorption by interstellar hydrogen. Results from the XRT are not yet available; however, it is expected that using XRT, there is sufficient energy resolution (0.4 FWHM at 1 keV) to make progress on understanding soft spectral components in objects brighter than 10^{-12}ergs cm^{-2}s^{-1}, in exposures of 10^4 seconds (Mushotzky 1989).

A very short but significant mission was flown on the Space Shuttle in December 1990. One of the instruments was the Broad Band X-Ray Telescope (BBXRT). This instrument had a band pass 0.3 to 12 keV with quite good energy resolution of 0.15 keV at 6 keV. Such an instrument is known as a 'high through-put' instrument. This is because the optics consisted of many nested thin gold coated aluminum foil mirrors. In this way, the effective area was increased, but the image resolution was decreased. However, the internal background is quite low. Tennant (1983) suggests that the high through-put type of instrument may approach the ideal between the conventional X-ray telescope and the proportional counter. The detector at the focus was a solid state spectrometer.

Another high through-put mission will be soon flown. This is ASTRO D, a Japan/US collaboration, to be launched in 1993. There will be 100 nested layers of foil mirrors, but the telescope will only weigh 9.6 kg. CCD detectors will be used at the focus. This mission is expected to provide detailed spectral and variability studies at energies less than 10 keV.

One more proportional counter instrument is being planned by the US. This is the X-ray Timing Explorer (XTE) which will provide high quality spectra in the 2 to 60 keV range. It will have an area of 6250 cm^2. This is an important mission because of the high time resolution data which it will provide.

There are many other UK, European and Russian missions which are planned. However, the next primarily US mission will be The Advanced X-Ray Astrophysics Facility (AXAF), part of the quartet of Great Observatories. This observatory will be based on a conventional grazing incidence X-ray telescope with 6 nested pairs of elements. A variety of detectors will be available at the focal point, including transmission gratings, spectrometers, and CCD imagers. Also a X-ray Calorimeter is being developed, which will have 10 eV resolution and high detection efficiency (Weisskopf 1987). This combination of high energy resolution detectors and the polished X-ray telescope will make detection of very faint X-ray sources possible, compared with the high through-put instruments or the XTE.

This discussion shows that the future of X-ray observations of AGN is bright. Future missions will provide high energy resolution spectra. This will make the understanding of X-ray emission features possible. High through-put missions will also provide time resolved broad band spectroscopy. If XTE is flown, short time scale studies of variable AGN will be possible.

REFERENCES CITED

REFERENCES CITED

Abramowicz, M. A., Ellis, G. F. R., and Lanza, A., 1990. Ap. J., 361, 470.

Abramowicz, M. A., and Sharp, N. A., 1983. Astrophysics and Space Science, 96, 431.

Antonucci, R.R.J., and Miller, J.S., 1985. Ap. J., 297, 621.

Arnaud, K.A., Branduardi-Raymont, G., Culhane, J.L., Fabian, A.C., Hazard, C., McGlynn, T.A., Shafer, R.A., Tennant, A.F., and Ward, M.J., 1985. M. N. R. A. S., 217, 105.

Avni, Y., Soltan, A., Tananbaum, H., and Zamorani, 1980. Ap. J., 238, 800.

Awaki, H., 1991. Ph. D. thesis, Nagoya University.

Awaki, H., Koyama, K., Kunieda, H., and Tawara, Y., 1990. Nature, 346, 544.

Awaki, H., et al. 1991. Submitted to Ap. J.

Bak, P., Tang, C., and Wiesenfeld, K., 1987. Physical Review Letters, 59, 381.

Bak, P., Tang, C., and Wiesenfeld, K., 1988. Physical Review A, 38, 364.

Bambynek, W., 1972. Rev. Mod. Phys., 44, 716.

Barr, P., 1986. M.N.R.A.S., 223, 29P.

Barr, P., Clavel, J., Giommi, P., Mushotzky, R.F., Madejski, G., 1986. Proceedings of the Villa Olmo Meeting Ed. A. Treves (Milano: AADA) p. 43.

Barr, P., and Mushotzky, R.F., 1986. Nature, 320, 421.

Begelman, M.C., and De Kool, M., 1991. In Variability of Active Galactic Nuclei Eds. H.R. Miller and P.J. Wiita (Cambridge: Cambridge University Press) p. 198.

Bevington, P.R., 1969. Data Reduction and Error Analysis for the Physical Sciences (McGraw-Hill: New York).

Czerny, B., and Elvis, M., 1987. Ap. J., 321, 305.

de Korte, P.A.J., Bleeker, J.A.M., den Boggende, A.J.F., Branduardi-Raymont, G., Brinkman, A.C., Culhane, J.L., Gronenschild, E.H.B.M., Mason, I., and McKechnie, S.P., 1981. Space Science Reviews, 30, 495.

Dermer, C.D., 1989. In Proc. 23rd ESLAB Symp. Eds. J. Hunt and B. Battrick (Paris: European Space Agency) p. 925.

deZotti, G., and Gaskell, C.M., 1985. Astron. Astrophys., 147, 1.

Done, C., and Fabian, A.C., 1989. M.N.R.A.S., 240, 81.

Done, C., Koyama, K., Kunieda, H., Madejski, G., Mushotzky, R.F., Turner, T.J., 1990a. Proceedings of Paris Accretion Disk meeting.

Done, C., Ward, M.J., Fabian, A.C., Kunieda, H., Tsuruta, S., Lawrence, A., Smith, M.G., Wamsteker, W., 1990b. M.N.R.A.S., 243, 713.

Edelson, R.A., and Krolik, J.H., 1988. Ap. J., 333, 646.

Elvis, M., Czerny, G., and Wilkes, B.J., 1987. Physics of Accretion onto Compact Objects Eds. K.O. Mason, M.G. Watson, and N.E. White (Springer-Verlag: Berlin) p. 389.

Fabian, A.C., Blandford, R.D., Guilbert, P.W., Phinney, E.S., and Cueller, L., 1986. M.N.R.A.S., 221, 931.

Feigelson, E.D., and Nelson, P.I., 1985. Ap. J., 293, 192.

Ferland, G.J., and Rees, M.J., 1988. Ap. J., 332, 141.

Forman, W., Jones, C., Cominsky, L., Julien, P., Murray, S., Peters, G., Tananbaum, H., and Giacconi, R., 1978. Ap. J. Suppl., 38, 357.

Gaskell, C.M., and Sparke, L.S., 1986. Ap. J., 305, 175.

George, I.M. and Fabian, A.C., 1991. M.N.R.A.S., 249, 352.

George, I.M., Nandra, K. and Fabian, A.C., 1990. M.N.R.A.S., 242, 28P.

Ghisellini, G., 1991. In Variability of Active Galactic Nuclei Eds. H.R. Miller and P.J. Wiita (Cambridge: Cambridge University Press), p. 236.

Guilbert, P.W., Fabian, A.C., and Rees, M.J., 1983. M.N.R.A.S, 233, 475.

Guilbert, P.W. and Rees, M.J., 1988. M.N.R.A.S., 233, 475.

Halpern, J.P., 1984. Ap. J., 281, 90.

Hayakawa, S., 1991. Nature, 351, 214.

Hayashida, K., Inoue, H., Koyama, K., Awaki, H., Takano, S., Tawara, Y., Williams, O.R., Denby, M., Stewart, G.C., Turner, M.J.L., Makishima, K., and Ohashi, T., 1989. Publ. Astron. Soc. Japan, 41, 373.

Heiles, C., 1975. Astr. Astrophys. Suppl., 20, 37.

Holt, S. S., Mushotzky, R. F., Becker, R. H., Boldt, E. A., Serlemitsos, P. J., Szymkowiak, A. E., and White, N.E., 1980. Ap. J., 241, L13.

Inoue, H., 1985. Proceedings of US–Japan Seminar on Galactic and Extragalactic Compact X-ray Source Eds Y. Tanaka and W.H.G. Lewin (Tokyo: ISAS).

Isobe, T., Feigelson, E.D., Nelson, P.I., 1986. Ap. J., 306, 490.

Jaroszyński, M., Abramowicz, M. A., and Paczyńsky, B., 1980. Acta Astronomica, 30, 1.

Kallman, T.R. and McCray, R. 1982. Ap. J. Supp., 50, 263.

Kaplan, W. 1958. Ordinary Differential Equations (Reading, Massachusetts: Addison Wesley Publishing Company, Inc.).

Koyama, K., 1989. Publ. Astron. Soc. Japan, 41, 731.

Krolik, J.H., and Kallman, T.R., 1984. Ap. J., 286, 366.

Krolik, J.H., and Kallman, T.R., 1987. Ap. J. (Letters), 320, L5.

Kruper, J., Urry, C.M., and Canizares, C.R., 1990. Ap. J. Supp., 74, 347.

Kunieda, H., Hayakawa, S., Koyama, K., Tawara, Y., Tsuruta, S., and Leighly, K, 1991. Ap. J., in Press.

Kunieda, H., Turner, T.J., Awaki, H., Koyama, K., Mushotzky, R.F., and Tsusaka, Y., 1990. Nature, 345, 786.

Lampton, M., Margon, B., and Bower, S., 1976. Ap. J., 208, 177.

Lawrence, A., Pounds, K.A., Watson, M.G., and Elvis, M.S., 1987. Nature, 325, 692.

Lawrence, A., Watson, M.G., Pounds, K.A., and Elvis, M., 1985. M.N.R.A.S, 217, 685.

Lehto, H.J., 1989. In Proc. 23rd ESLAB Symp. Eds. J. Hunt and B. Battrick (Paris: European Space Agency) p. 499.

Lightman, A.P. and White, T.R., 1988. Ap. J., 335, 57.

Lightman, A.P., and Zdziarski, A.A., 1987. Ap. J., 319, 643.

Lindquist, R.W., 1966. Annals of Physics, 37, 487.

Makino, R., and the ASTRO-C team, 1987. Asrophys. Letters Commun., 25, 223.

Makishima, K., 1986. In The Physics of Accretion onto Compact Objects Eds. K.O. Mason, M.G. Watson, and N.E. White (Berlin: Springer-Verlag) p. 249.

Matsuoka, M., Yamauchi, M., Piro, L., and Murakami, T., 1990. Ap. J., 361, 440.

Marshall, F.E., Holt, S.S., Mushotzky, R.F., 1983. Ap. J., 269, L31.

Marshall, N., Warwick, R.S., and Pounds, K.A., 1981. M.N.R.A.S., 194, 987.

McHardy, I.M, 1989. In Proc. 23rd ESLAB Symp. Eds. J. Hunt and B. Battrick (Paris: European Space Agency) p. 111.

McHardy, I., and Czerny, B., 1987. Nature, 325,696.

Misner, C.W., Thorne, K.S, and Wheeler, J.A., 1973. Gravitation (New York: W.H. Freeman and Company).

Mittaz, J.P.D., and Branduardi-Raymont, G., 1989. M.N.R.A.S., 238, 1029.

Morrison, R., and McCammon, D., 1983. Ap. J., 270, 119.

Mushotzky, R., 1983. In Proceedings IAU/COSPAR Meeting on High Energy Astrophysics and Cosmology.

Mushotzky, R., 1984. In X-Ray and UV Emission from Active Galactic Nuclei Eds W. Brinkman and J. Trumper (MPE Rep. 184, Munich) p. 73.

Mushotzky, R., 1989. In Proc. 23rd ESLAB Symp. Eds. J. Hunt and B. Battrick (Paris: European Space Agency) p. 857.

Mushotzky, R.F., Marshall, F.E., Boldt, E.A., Holt, S.S., and Serlemitsos, P.J., 1980. Ap. J., 235, 377.

Mushotzky, R.F., Serlemitsos, P.J., Becker, R.H., Boldt, E.A., and Holt, S.S., 1978. Ap. J., 220, 790.

Nandra, K., 1991. Ph. D. Thesis, University of Leicester.

Nandra, K., Pounds, K.A., and Stewart, G.C., 1990. M.N.R.A.S., 242, 660.

Nandra, K., Pounds, K.A., Stewart, G.C., Fabian, A.C., and Rees, M.J., 1989. M.N.R.A.S., 236, 39P.

Nandra, K., Pounds, K.A., Stewart, G.C., George, I.M., Hayashida, K., Makino, F., and Ohashi, T., 1991. M.N.R.A.S., 248, 760.

Nolan, P.L., Gruber, D.E., Matteson, J.L., Peterson, L.E., Rothschild, R.E., Doty, J.P., Levine, A.M., Lewin, W.H.G., and Primini, F.A., 1981. Ap. J., 246, 494.

Padovani, P. and Rafanelli, P., 1988. Astr. Astrophys., 205, 53.

Pan, H.C., Stewart, G.C., and Pounds, K.A., 1990. M.N.R.A.S., 242, 177.

Petre, R., Mushotzky, R.F., Krolik, J.H., and Holt, S.S., 1984. Ap. J., 280, 499.

Piro, L., Yamauchi, M., and Matsuoka, M., 1990. Ap. J. Lett., 360, L35.

Pounds, K.A., 1991. Leicester University preprint XRA 91/05, to be published in the Proceedings of the 28th Yamada Conference on 'Frontiers of X-ray Astronomy', held in Nagoya, Japan, April 8–12, 1991.

Pounds, K.A., Nandra, K., and Stewart, G.C., 1991. Leicester University preprint XRA 91/04, to be published in the Proceedings of the 28th Yamada Conference on 'Frontiers of X-ray Astronomy', held in Nagoya, Japan, April 8–12, 1991.

Pounds, K.A., Nandra, K., Stewart, G.C., George, I.M., and Fabian, A.C., 1990. Nature, 344, 132.

Pounds, K.A., Nandra, K., and Stewart, G.C., and Leighly, K., 1989. M.N.R.A.S., 240, 769.

Pounds, K.A., Turner, T.J., Warwick, R.S., 1986. M.N.R.A.S., 211, 7P.

Press, W.H., 1978. Comments Astrophys., 7, 103.

Press, W.H., Flannery, B.P., Teukolsky, S.A., and Vetterling, W.T., 1986. Numerical Recipes (Cambridge: Cambridge University Press).

Press, W.H., and Teukolsky, S.A., 1988. Computers in Physics, Nov/Dec, 77.

Rees, M.J., 1984. Ann. Rev. Astr. Ap., 22, 471.

Rees, M.J., 1987. M.N.R.A.S., 228, 47p.

Reichert, G.A., Mushotzky, R.F., Petre, R., and Holt, S.S., 1985. Ap. J., 296, 69.

Rybicki, G.B., and Lightman, A.P., 1979. Radiative Processes in Astrophysics (New York: John Wiley and Sons).

SAS User's Guide: Statistics, 1982 Edition. (Cary, North Carolina: SAS Institute Inc.).

Scargle, J.D., 1982. Ap. J., 263, 835.

Schmitt, J.H.M.M., 1985. Ap. J., 293, 178.

Schutz, B.F., 1985. A First Course in General Relativity (Cambridge: Cambridge University Press).

Seyfert, C.K., 1943. Ap. J., 97, 28.

Shapiro, S.L., Lightman, A.P., and Eardley, D.M., 1976. Ap. J., 204, 187.

Sikora, M., and Wilson, D. B., 1981. M.N.R.A.S., 197, 529.

Sun, W.-H., and Malkan, M.A., 1987. New Insights in Astrophysics (Noordwijk: ESA).

Svensson, R., 1987. M.N.R.A.S., 227, 403.

Taylor, B.G., Andresen, R.D., Peacock, A., and Zobl, R., 1981. Space Science Reviews, 30, 479.

Tennant, A.F., 1983. NASA Technical Memorandum 85101.

Tennant, A.F., and Mushotzky, R.F., 1983. Ap. J., 264, 92.

Tennant, A.F., Mushotzky, R.F., Boldt, E.A., and Swank, J.H., 1981. Ap. J., 251, 15.

Tritz, B., and Tsuruta, S., 1991. In preparation.

Turner, M.J.L., and Smith, A., 1981. Space Science Reviews, 30, 513.

Turner, M.J.L., Thomas, H.D., Patchett, B.E., Reading, D.H., Makishima, K., Ohashi, T., Dotani, T., Hayashida, K., Inoue, H., Kondo, H., Koyama, K., Mitsuda, K., Ogawara, Y., Takano, S., Awaki, H., Tawara, Y., Nakamura, N., 1989. Publ. Astron. Soc. Japan, 41, 345.

Turner, M.J.L., Williams, O.R., Saxton, R., Stewart, G.C., Courvoisier, T.J-L., Ohashi, T., Makishima, K., Kii, T., Inoue, H., 1989. In Proc. 23rd ESLAB Symp. Eds. J. Hunt and B. Battrick (Paris: European Space Agency) p. 769.

Turner, T.J., 1987. M.N.R.A.S., 226, 9P.

Turner, T.J., 1988. Ph. D. Thesis, Leicester University.

Turner, T.J., and Pounds, K.A., 1988. M.N.R.A.S., 232, 463.

Turner, T.J., and Pounds, K.A., 1989. M.N.R.A.S., 240, 833.

Turner, T.J., Weaver, K.A., Mushotzky, R.F., Holt, S.S., and Madejski, G.M., 1991. Ap. J., in press.

Urry, C.M., Arnaud, K., Edelson, R.A., Kruper, J.S., and Mushotzky, R.F., 1989. In Proc. 23rd ESLAB Symp. Eds. J. Hunt and B. Battrick (Paris: European Space Agency) p. 789.

Urry, C.M. and Mushotzky, R.F., 1982. Ap. J. Lett., 306, L61.

Warwick, R.S., Pounds, K.A., and Turner, T.J., 1988. M.N.R.A.S., 231, 1145.

Warwick, R.S., Yaqoob, T., Jembay, S., and Barber, C., 1991. In 'Report for the period May 1989 to April 1991' Leicester University X-Ray Astronomy Group.

Warwick, R.S., Yaqoob, T., Pounds, K.A., Matsuoka, M., and Yamauchi, M., 1989. Publ. Astron. Soc. Japan, 41, 721.

Weast, R.C. (Ed.), 1975. Handbook of Chemistry and Physics (Cleveland: CRC Press).

Weisskopf, M.C., 1987. Astro. Lett. and Communications, 26, 1.

White, N.E., Fabian, A.C., and Mushotzky, R.F., 1984. Astron. Astrophys., 133, L9.

Yaqoob, T., and Warwick, R.S., 1991. M.N.R.A.S., 248, 773.

Yaqoob, T., Warwick, R.S., and Pounds, K.A., 1989. M.N.R.A.S., 236, 153.

Zamorani, G., Giommi, P., Maccacaro, T., and Tananbaum, H., 1984. Ap. J., 278, 28.

Zdziarski, A.A., Ghisellini, G., George, I.M, Svensson, R., Fabian, A.C., and Done, C., 1990. Ap. J. (Lett), 363, L1.

Zhang, X.-H., 1991. In Variability of Active Galactic Nuclei Eds. H.R. Miller and P.J. Wiita (Cambridge: Cambridge University Press) p. 253.

APPENDICES

APPENDIX A

SUPPLEMENTARY LIGHT CURVES FOR CHAPTER 8

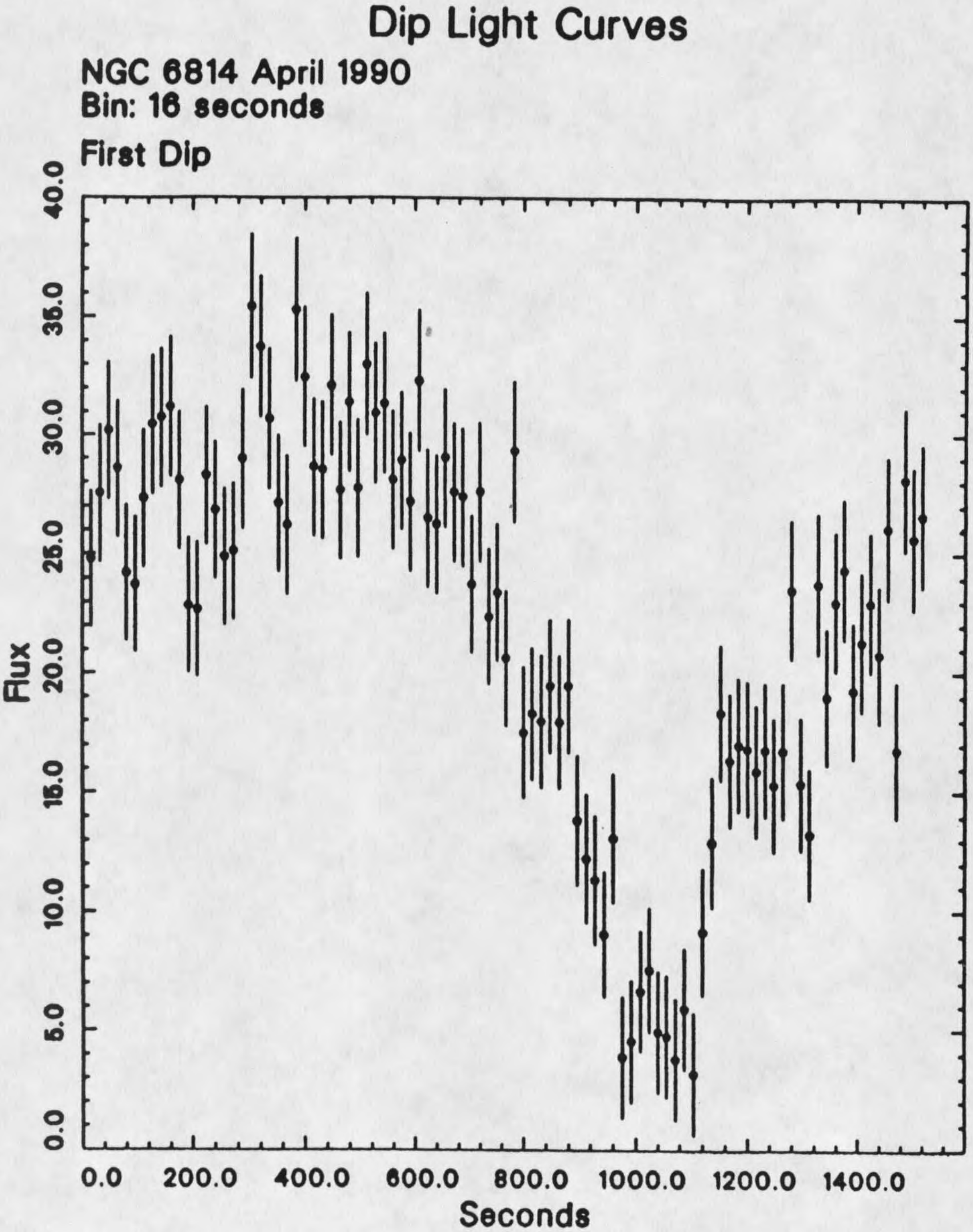

Figure 81. Light curve of first dip from the April observation. Bin size is 16 seconds, the intrinsic size.

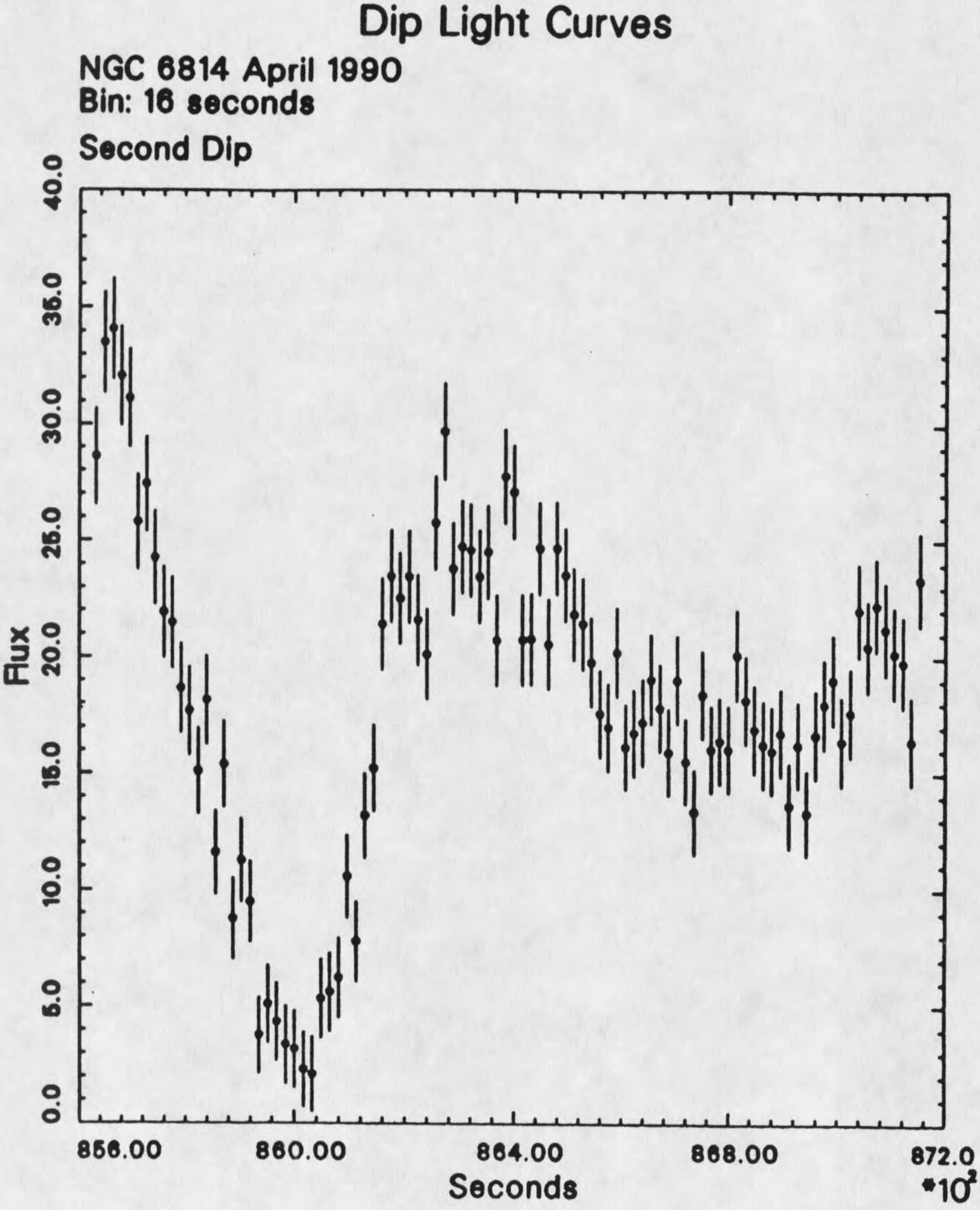

Figure 82. Light curve of second dip from the April observation. Bin size is 16 seconds, the intrinsic size.

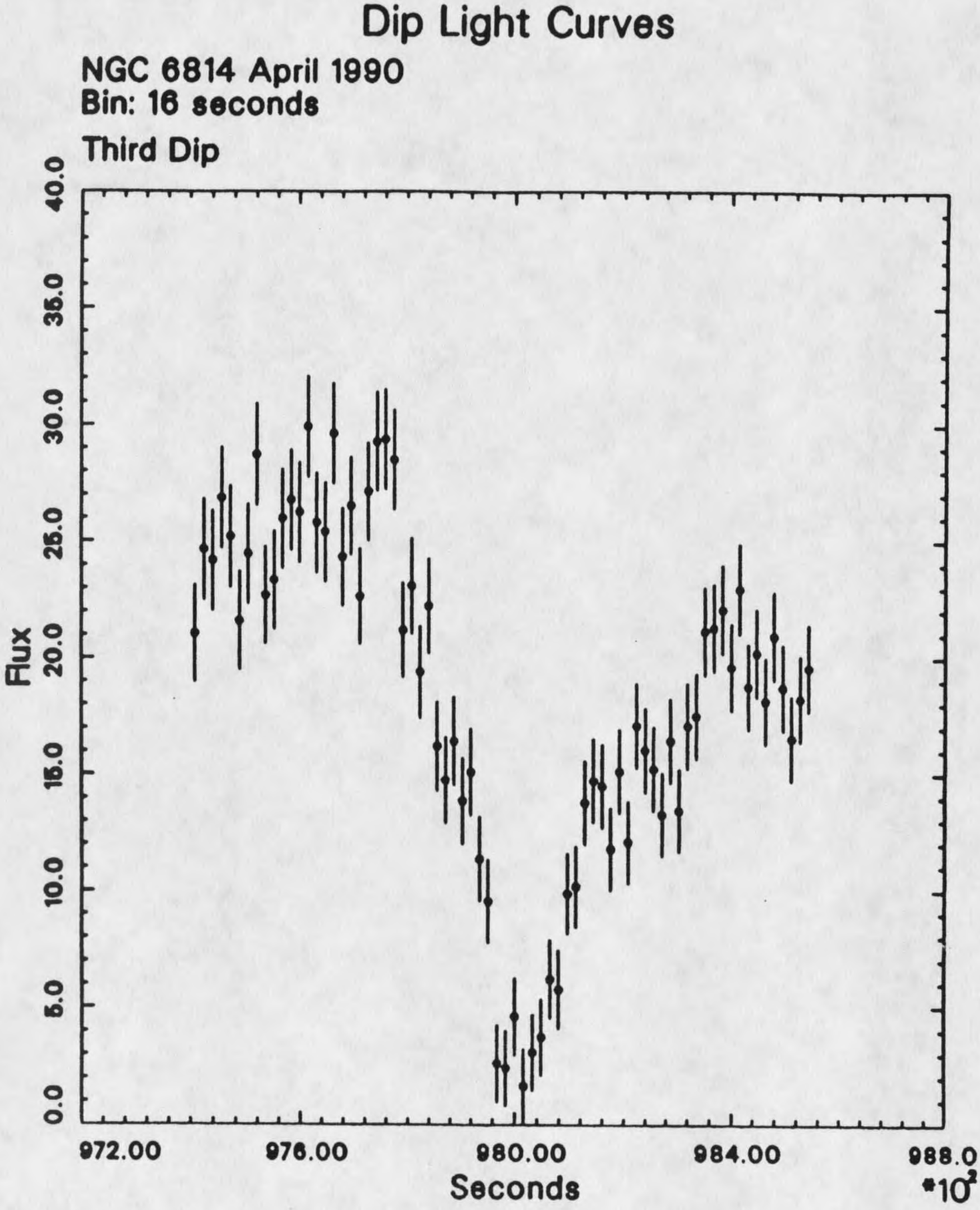

Figure 83. Light curve of third dip from the April observation. Bin size is 16 seconds, the intrinsic size.

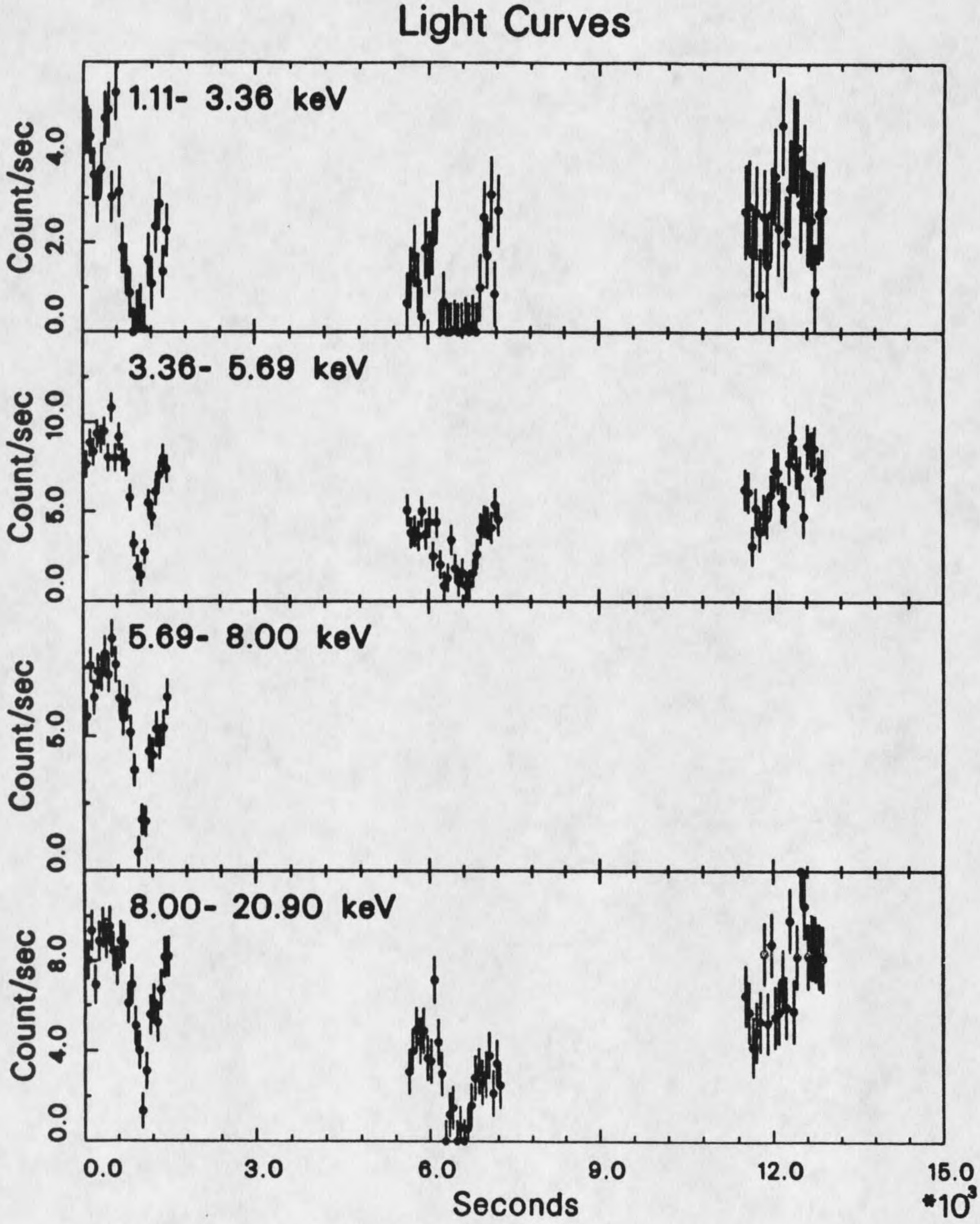

Figure 84. Light curve of April data from 0 to 15,000 seconds in four different energy bands. The bin size is 64 seconds.

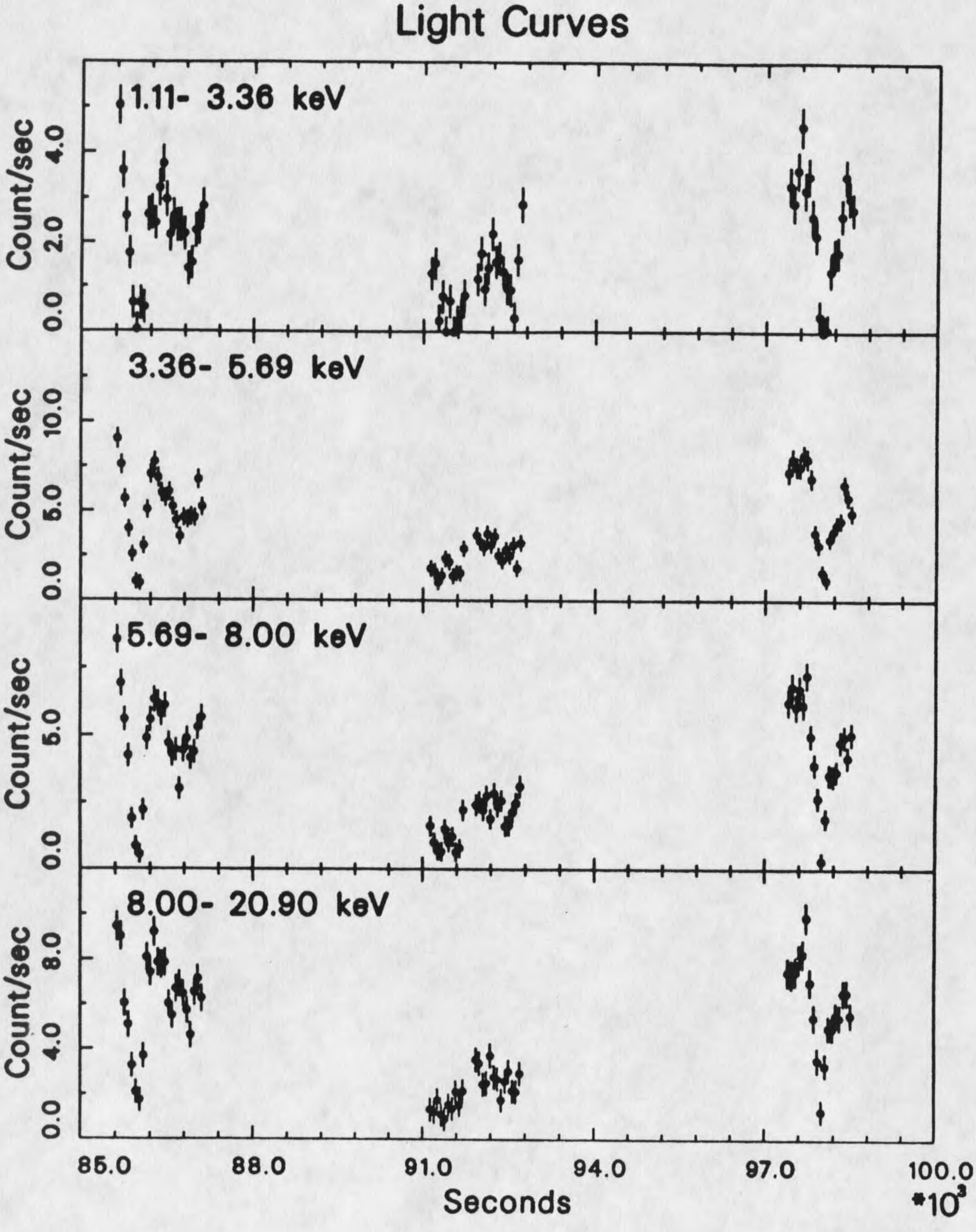

Figure 85. Light curve of April data from 85,000 to 100,000 seconds in four different energy bands. The bin size is 64 seconds.

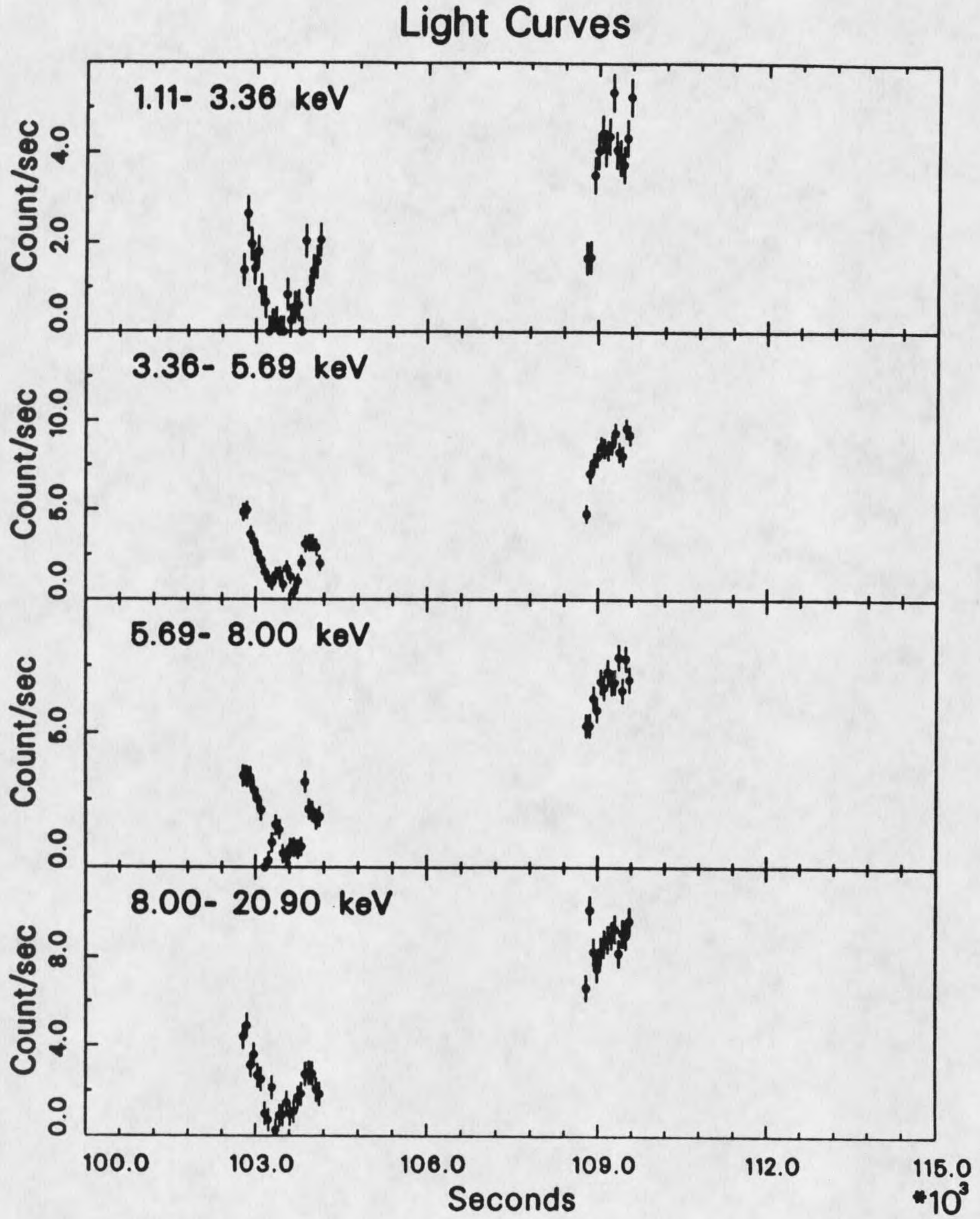

Figure 86. Light curve of April data from 100,000 to 115,000 seconds in four different energy bands. The bin size is 64 seconds.

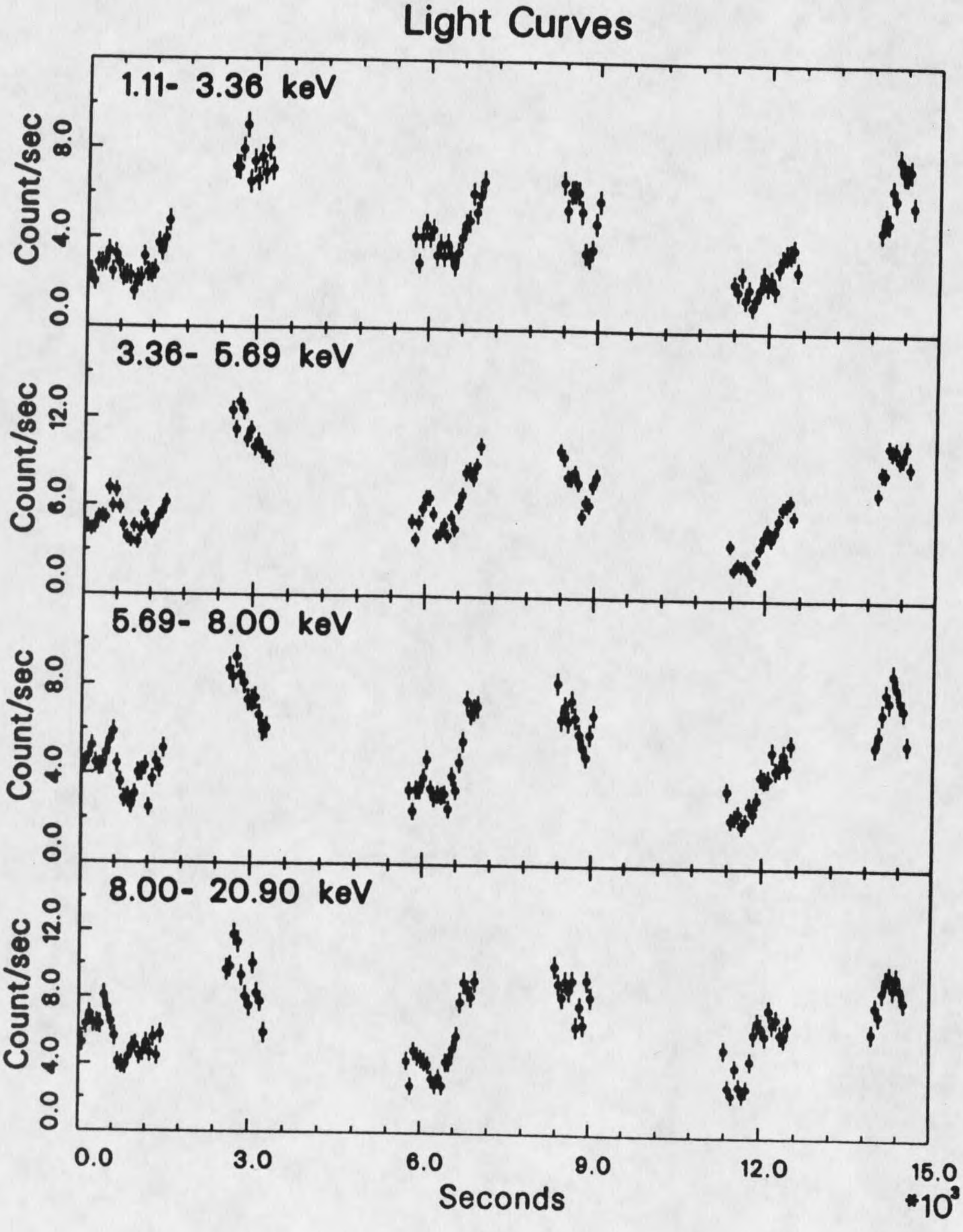

Figure 87. Light curve of October data from 0 to 15,000 seconds in four different energy bands. The bin size is 64 seconds.

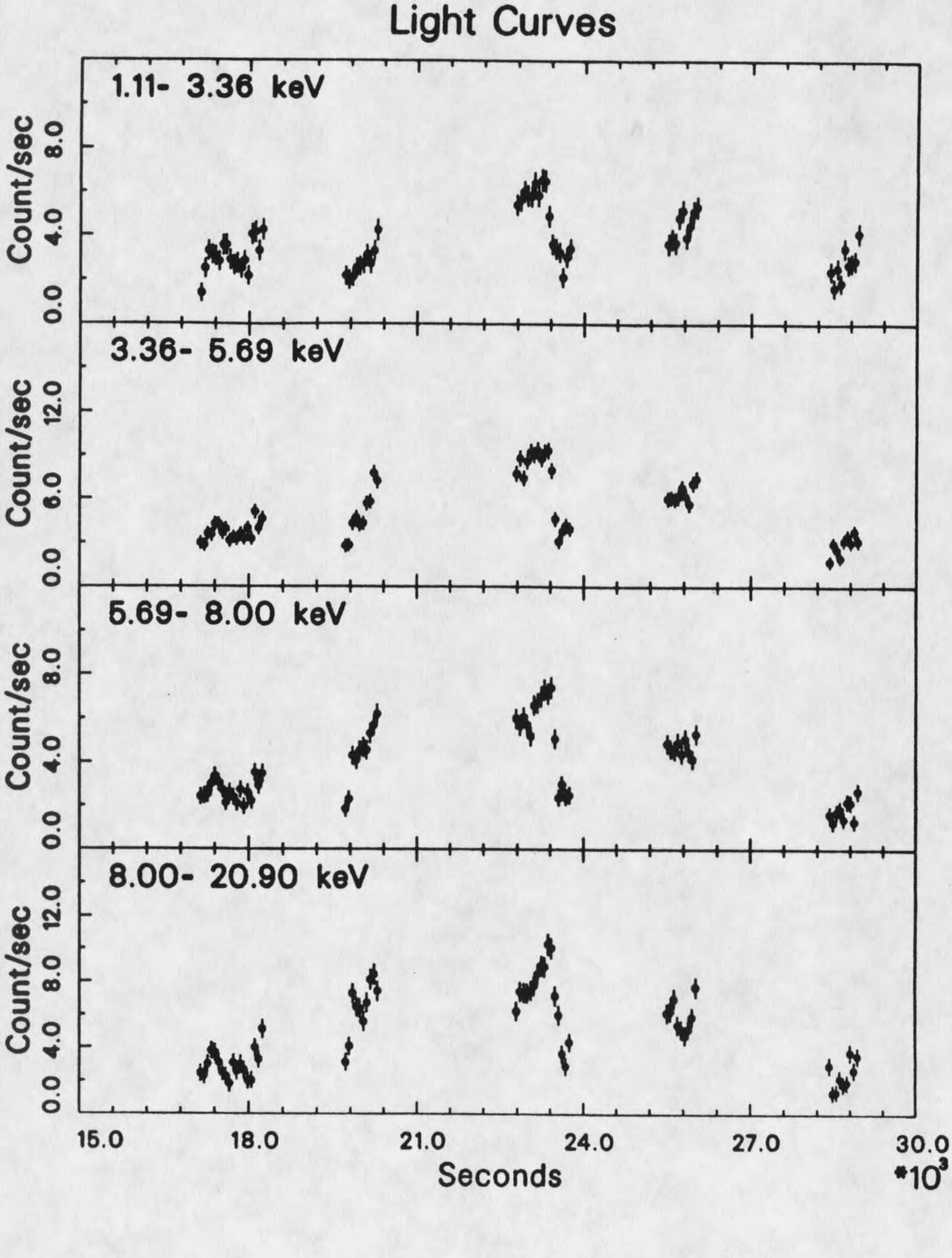

Figure 88. Light curve of October data from 15,000 to 30,000 seconds in four different energy bands. The bin size is 64 seconds.

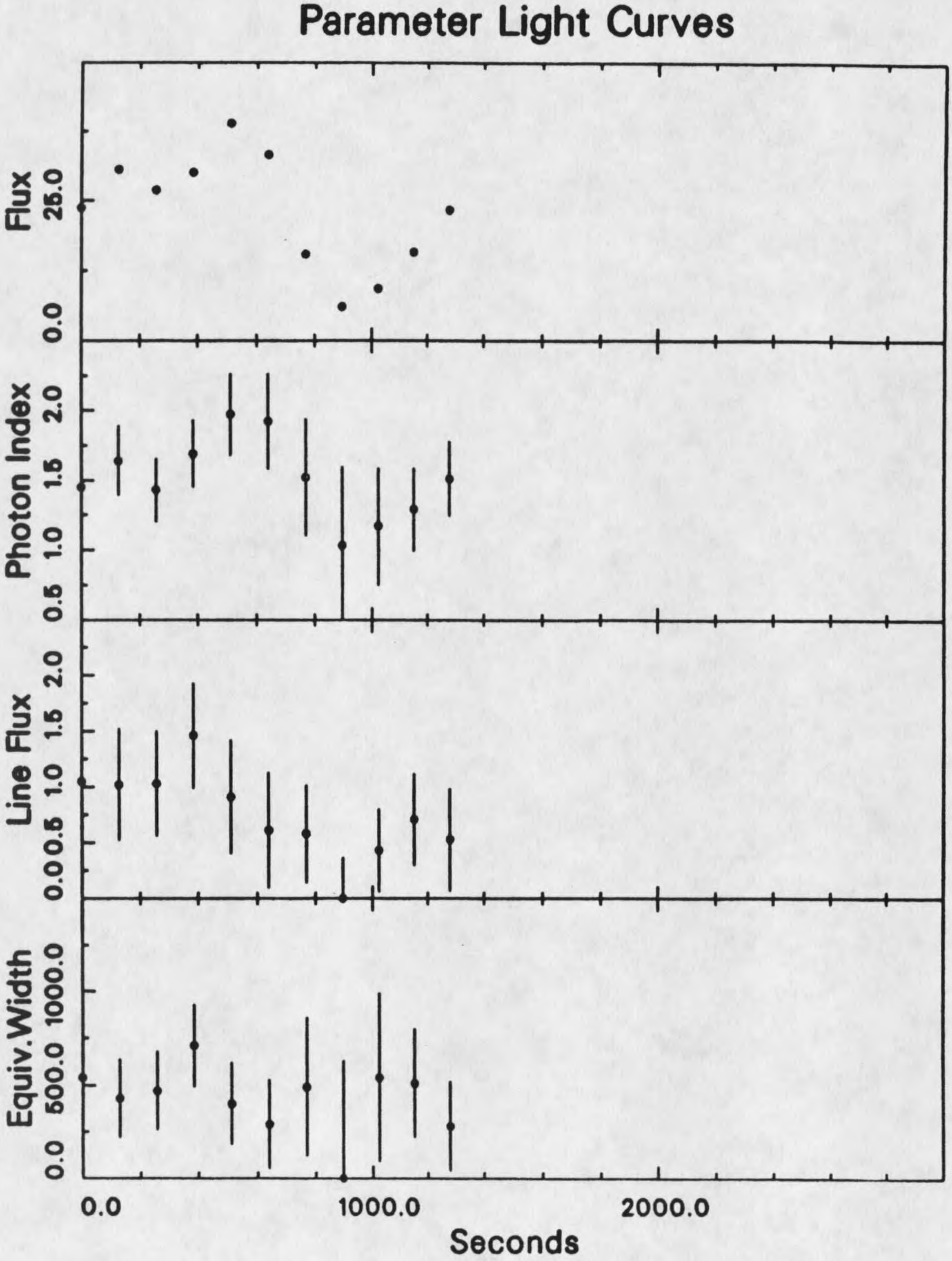

Figure 89. Parameter light curve for April data from 0 to 1400 seconds. The results from the first day with transmission coefficient greater than 0.5 are shown. Uncertainties are 90% for one interesting parameter.

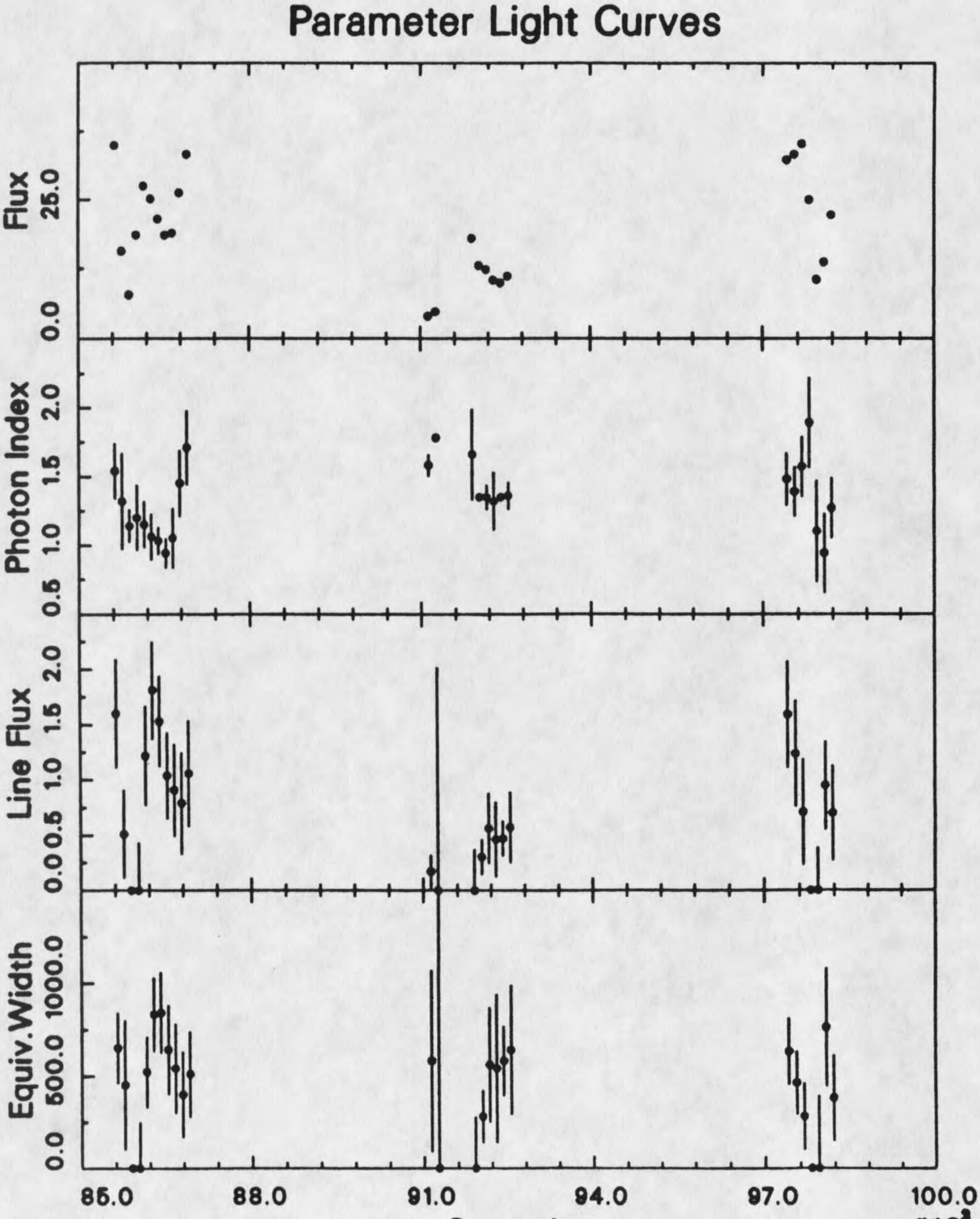

Figure 90. Parameter light curve for April data from 85,000 to 100,000 seconds. Uncertainties are 90% for one interesting parameter.

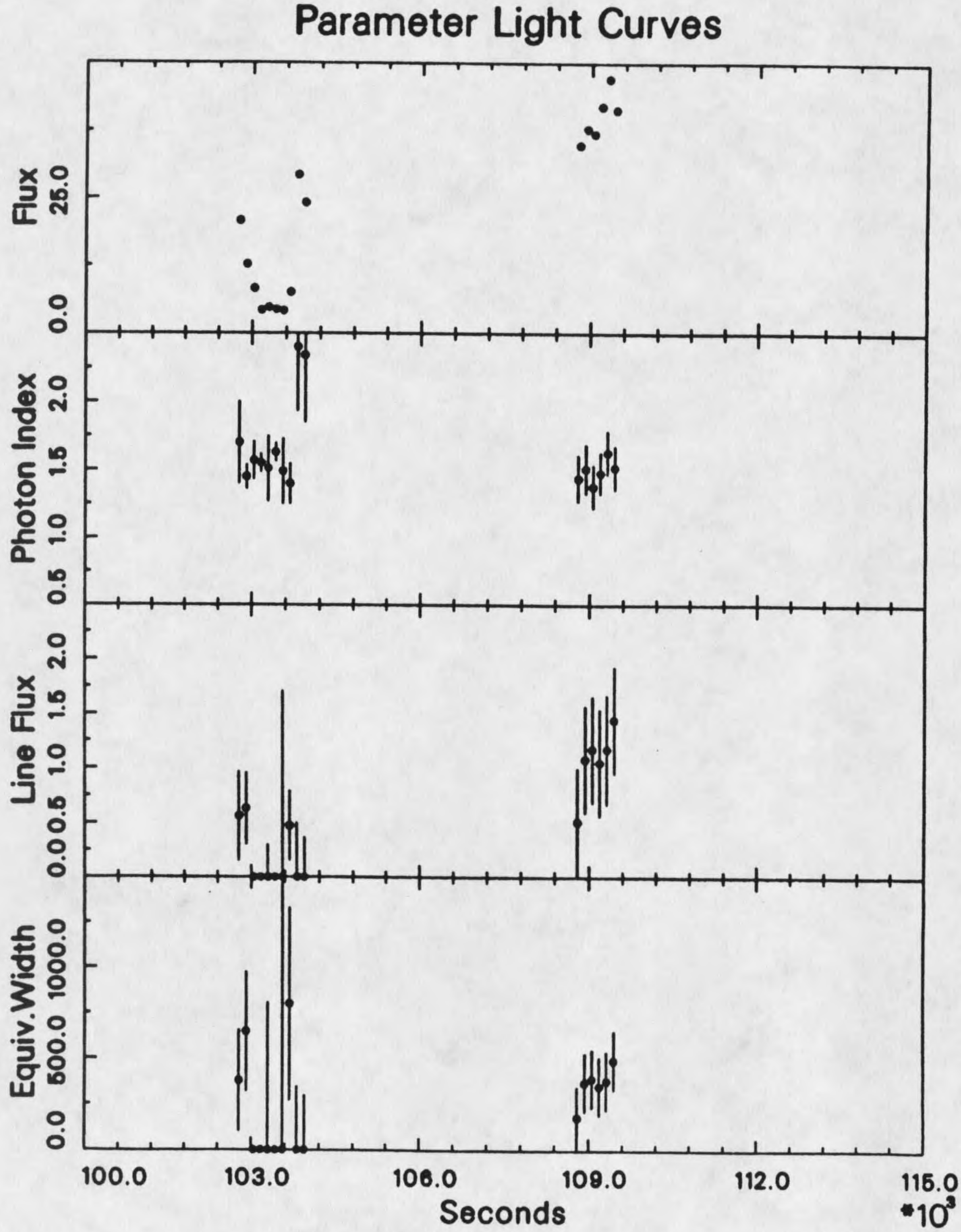

Figure 91. Parameter light curve for April data from 100,000 to 115,000 seconds past. Uncertainties are 90% for one interesting parameter.

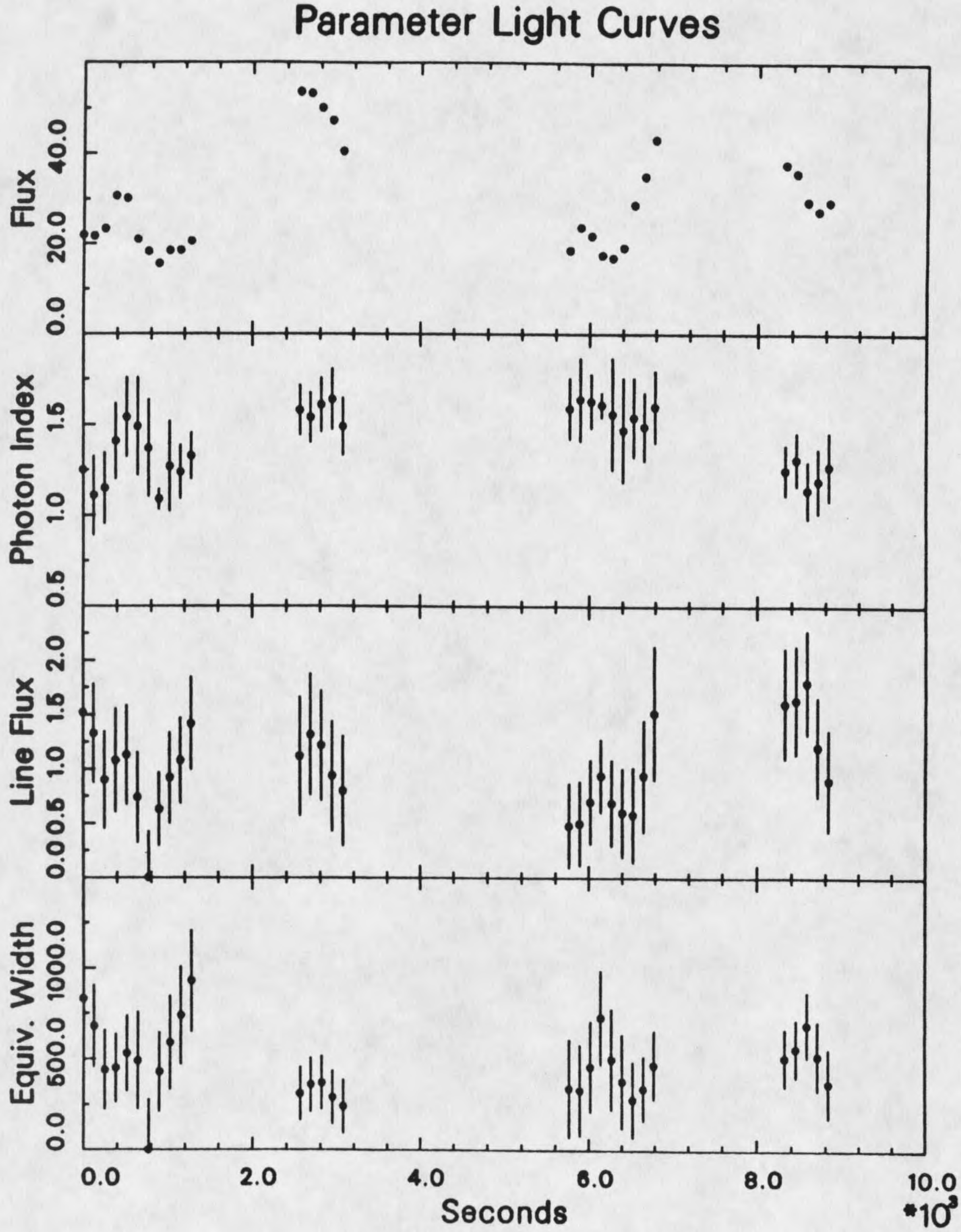

Figure 92. Parameter light curve for October data from 0 to 10,000 seconds. Uncertainties are 90% for one interesting parameter.

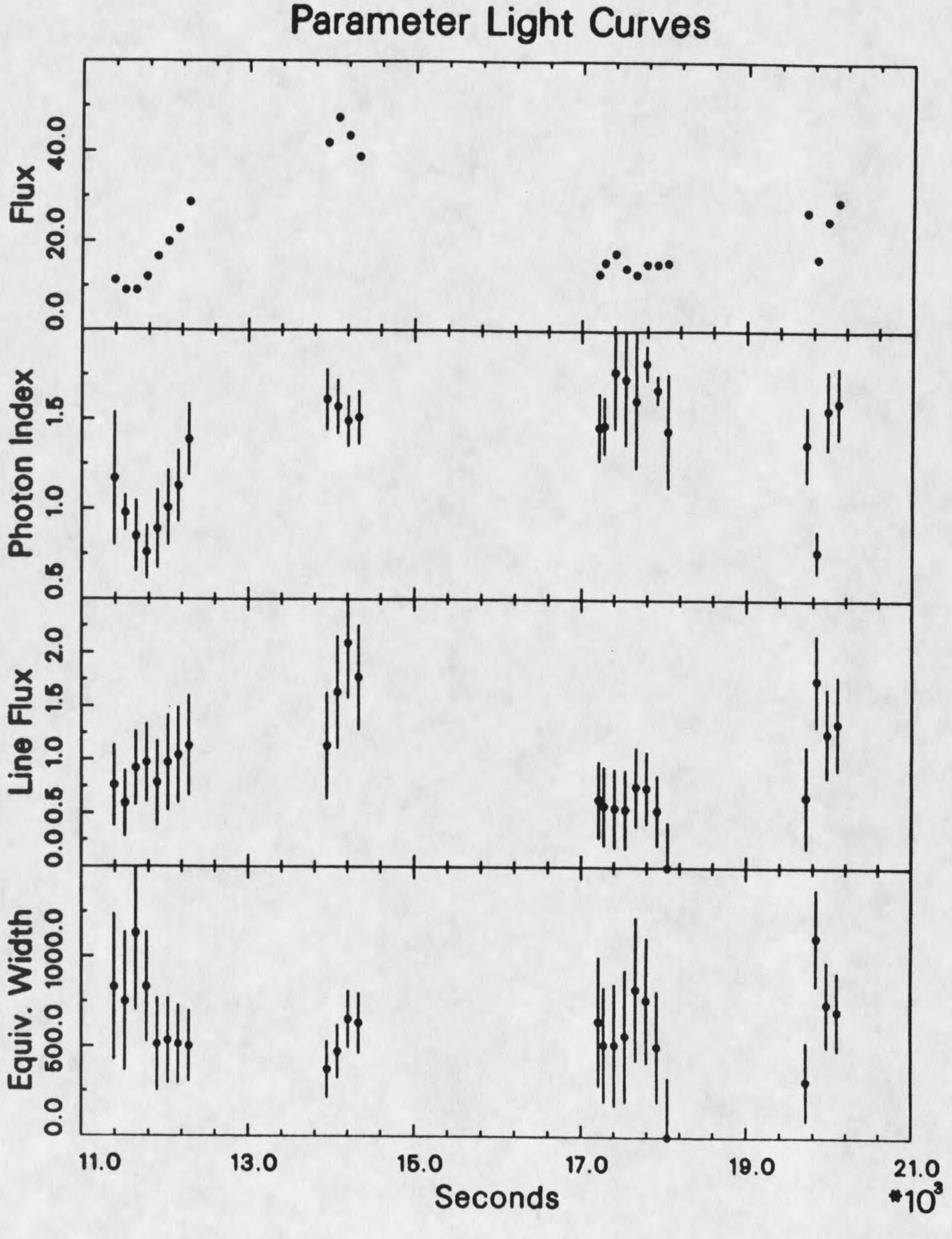

Figure 93. Parameter light curve for October data from 10,000 to 20,000 seconds. Uncertainties are 90% for one interesting parameter.

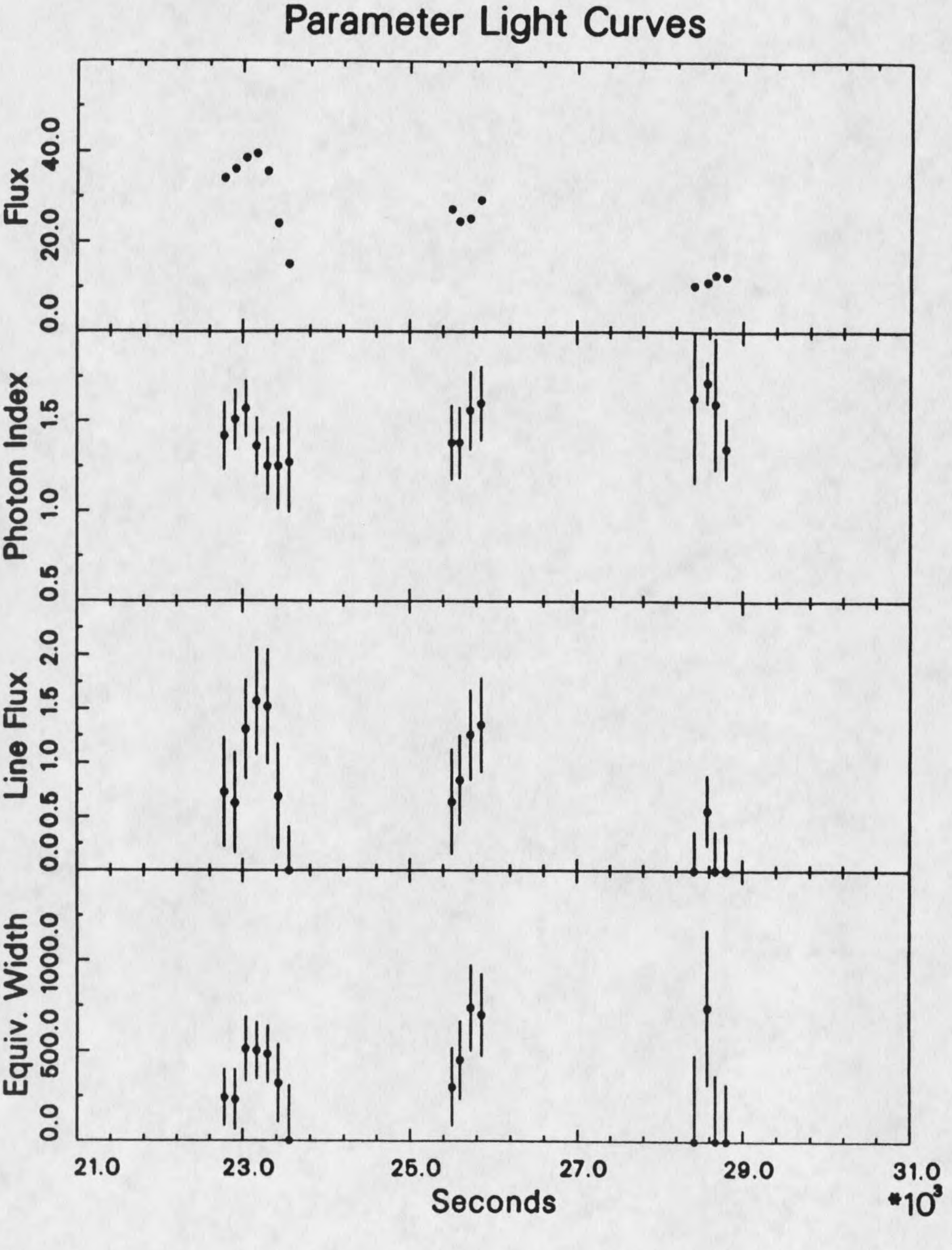

Figure 94. Parameter light curve for October data from 21,000 to 31,000 seconds. Uncertainties are 90% for one interesting parameter.

APPENDIX B

SPECTRAL FITS FOR CHAPTER 8

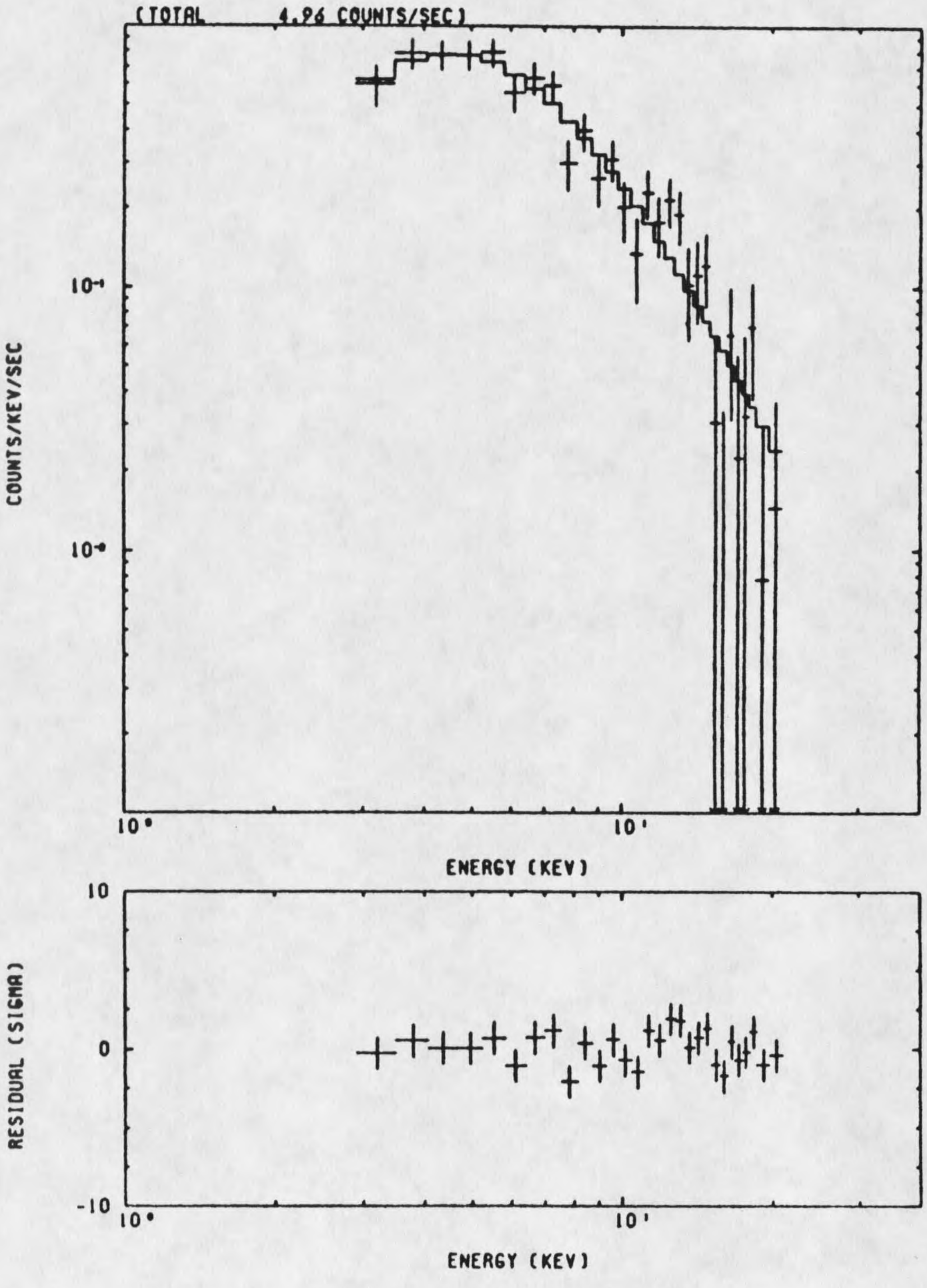

Figure 95. Spectral fit for ADIP, the combined dip spectrum. The power law plus absorption model was fit (Equation 4.1). Best fit parameters are $\Gamma = 1.03 \pm 0.26$, $\log(N_H) = 22.52 \pm 0.41$, $I_{Fe} < 0.26 \mathrm{count\,s^{-1}}$, equivalent width< 290eV, and $\chi^2_R = 1.15/26\, d.o.f.$

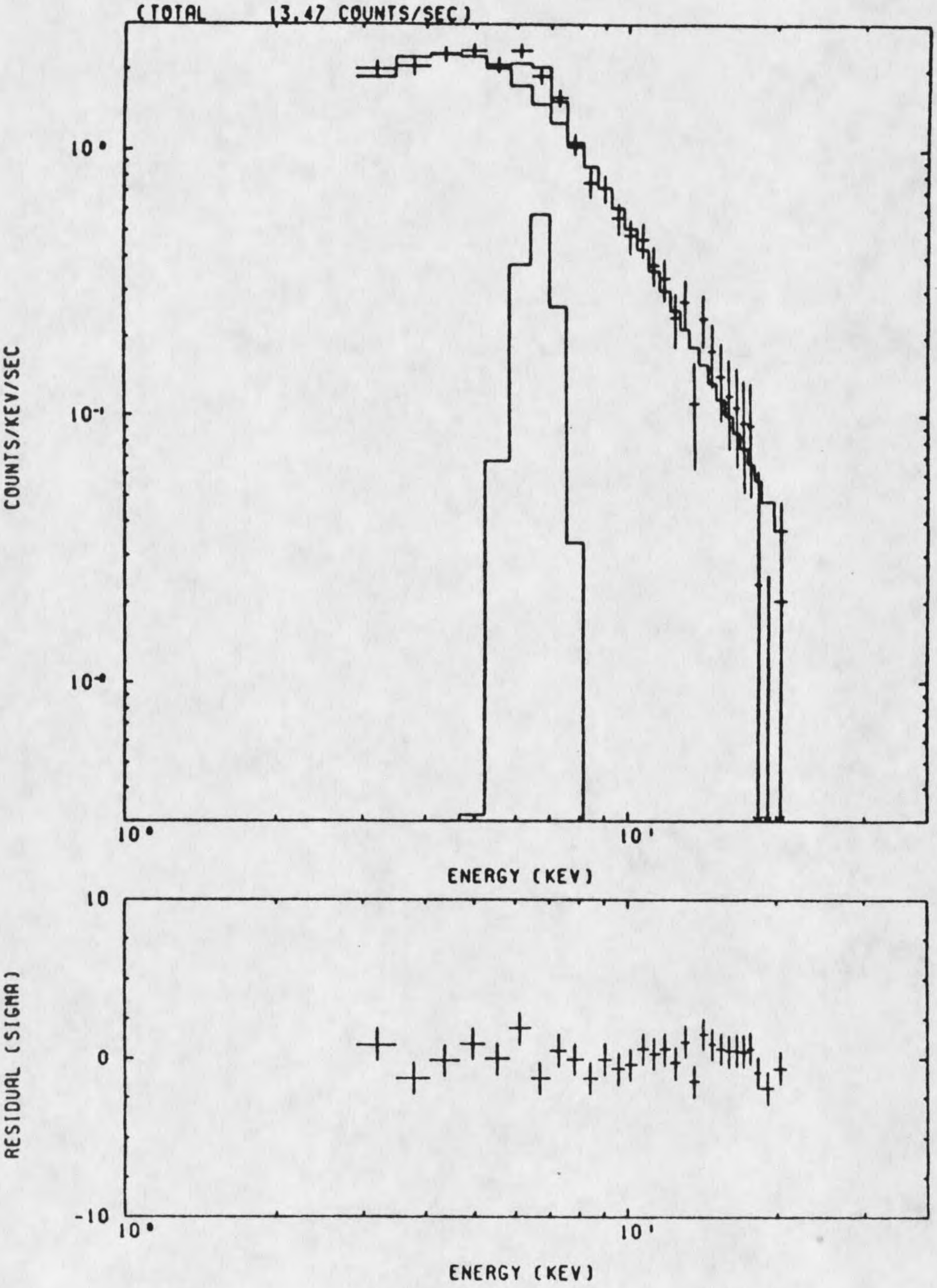

Figure 96. Spectral fit for A1D10, the first spectrum before the first dip. The power law and line plus absorption model was fit (Equation 4.2). Best fit parameters are $\Gamma = 1.46 \pm 0.17$, $\log(N_H) = 22.70 \pm 0.16$, $I_{Fe} = 1.52 \pm 0.50 \mathrm{count\,s^{-1}}$, equivalent width= $490 \pm 160\mathrm{eV}$, and $\chi^2_R = 0.96/25\, d.o.f.$

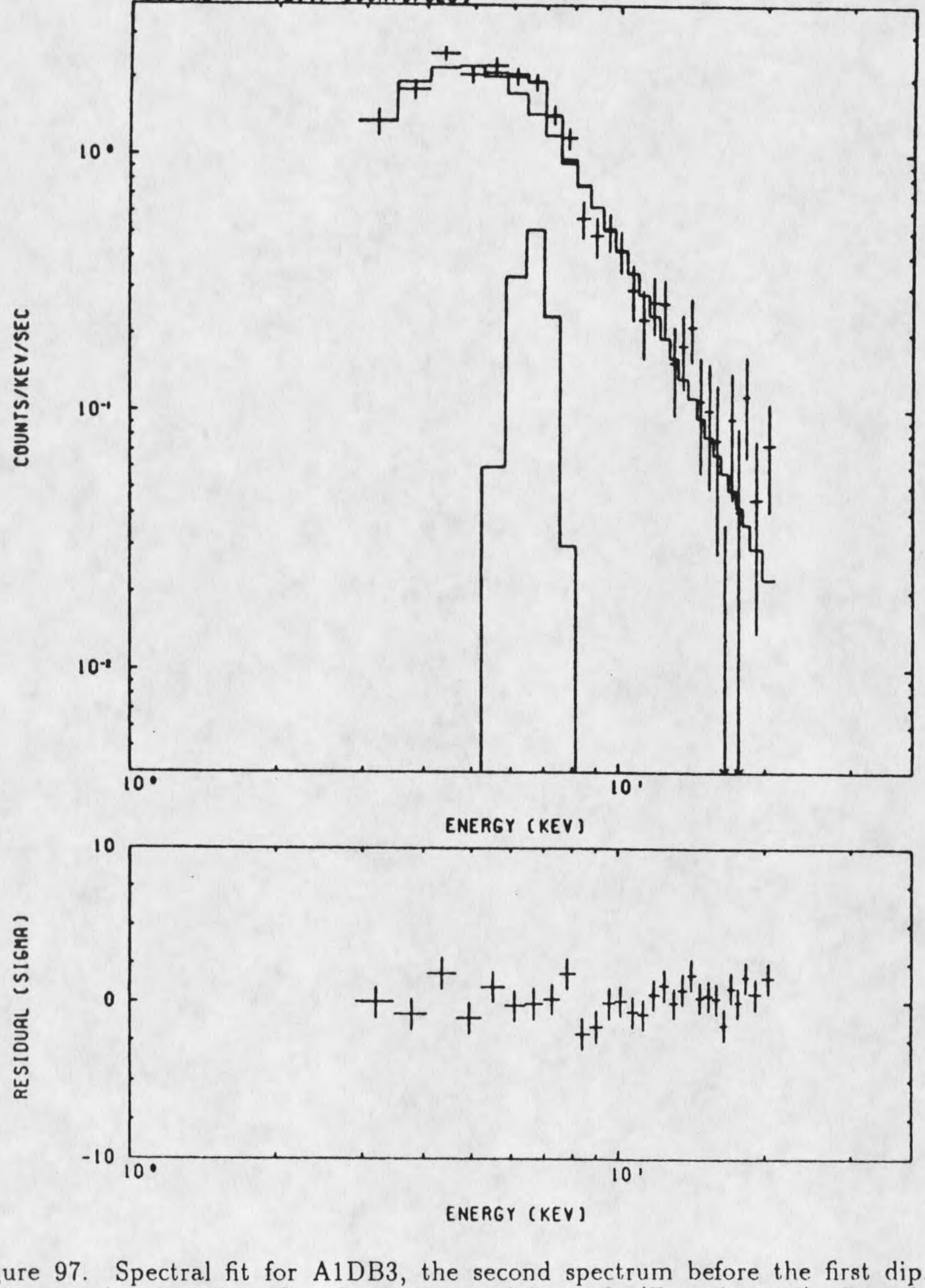

Figure 97. Spectral fit for A1DB3, the second spectrum before the first dip. The power law and line plus absorption model was fit (Equation 4.2). Best fit parameters are $\Gamma = 1.97 \pm 0.22$, $\log(N_H) = 23.03 \pm 0.12$, $I_{Fe} = 1.49 \pm 0.66 \mathrm{count\,s^{-1}}$, equivalent width= 440 ± 190eV, and $\chi^2_R = 1.25/25\, d.o.f.$

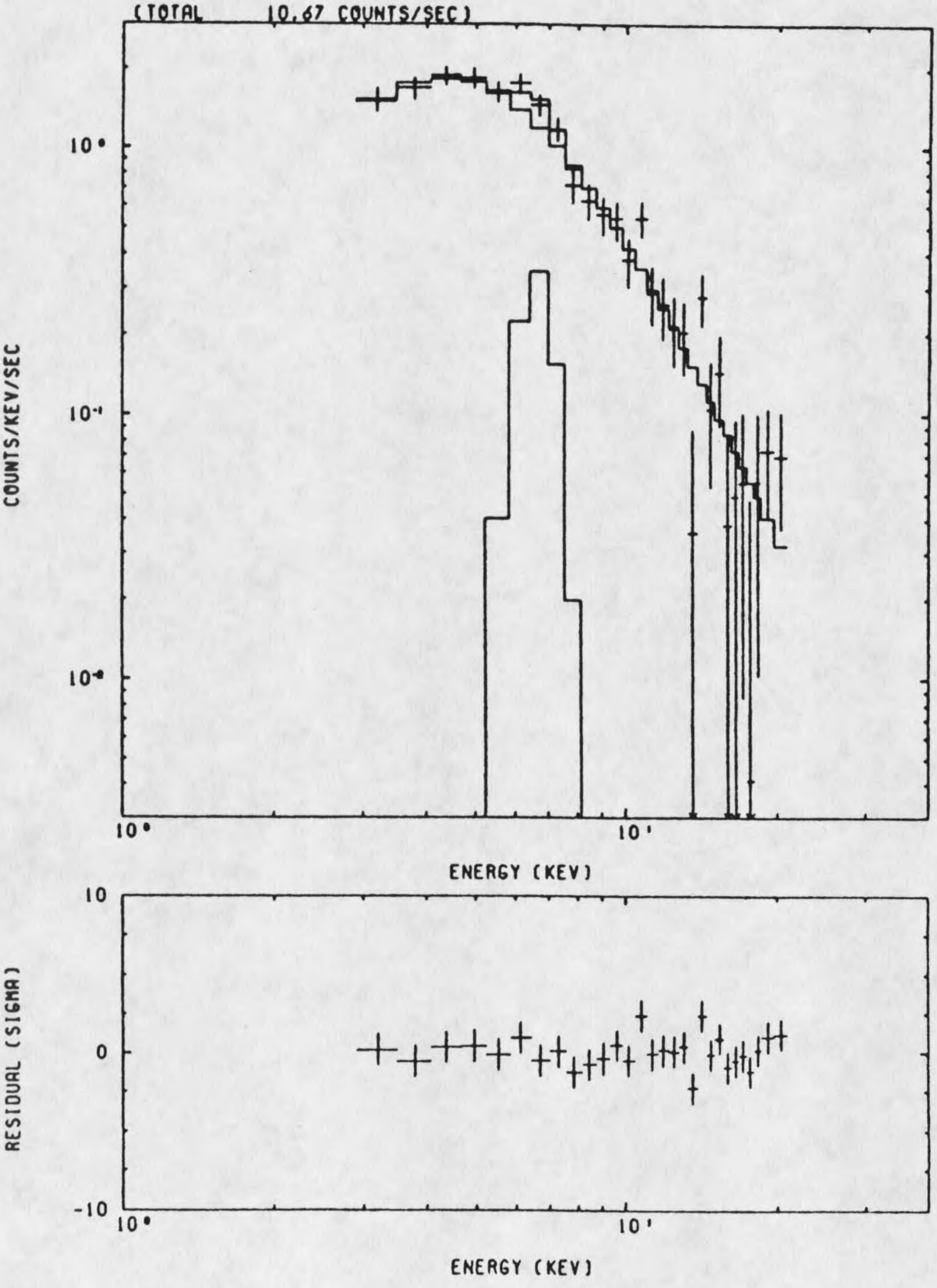

Figure 98. Spectral fit for A1DA1, the spectrum after the first dip. The power law and line plus absorption model was fit (Equation 4.2). Best fit parameters are $\Gamma = 1.40 \pm 0.22$, $\log(N_H) = 22.67 \pm 0.22$, $I_{Fe} = 0.91 \pm 0.56 \mathrm{count\,s}^{-1}$, equivalent width$= 360 \pm 220$eV, and $\chi^2_R = 1.08/25\, d.o.f.$

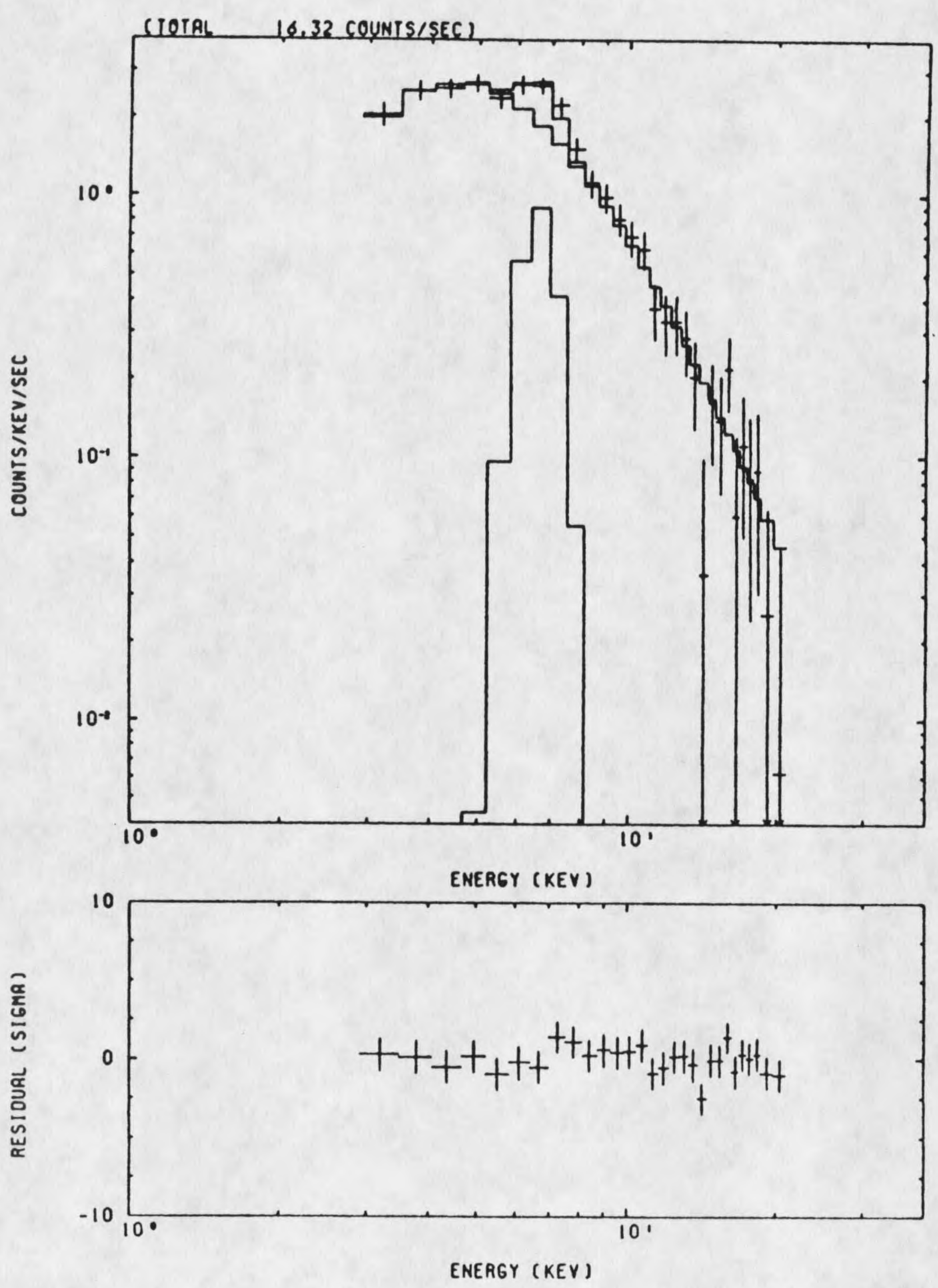

Figure 99. Spectral fit for A2DBFR, the spectrum before the second dip. The power law and line plus absorption model was fit (Equation 4.2). Best fit parameters are $\Gamma = 1.51 \pm 0.20$, $\log(N_H) = 22.79 \pm 0.16$, $I_{Fe} = 1.55 \pm 0.50 \mathrm{count\,s}^{-1}$, equivalent width$= 600 \pm 190$eV, and $\chi^2_R = 0.73/25\, d.o.f.$

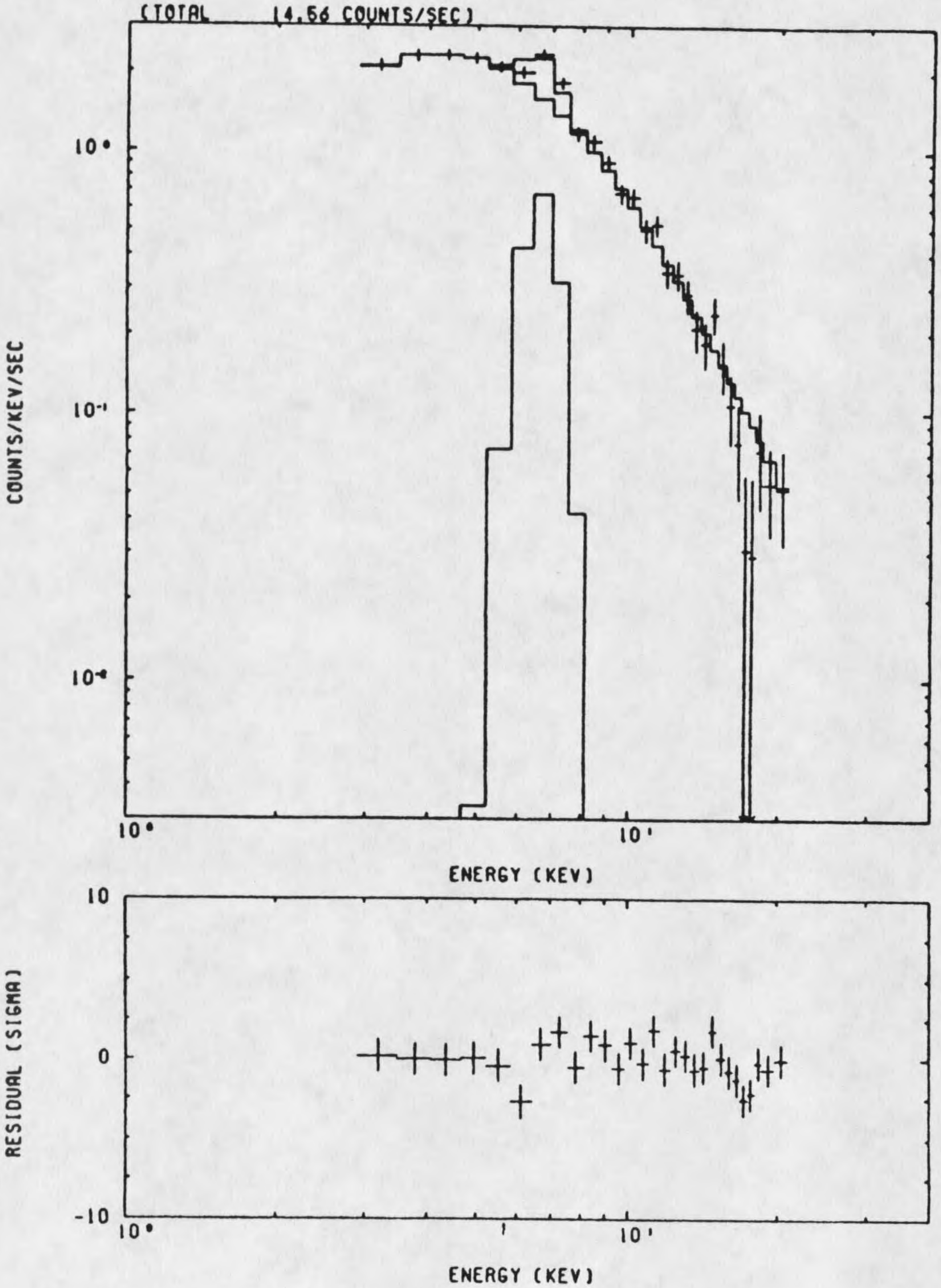

Figure 100. Spectral fit for A2DA3, the first spectrum after the second dip. The power law and line plus absorption model was fit (Equation 4.2). Best fit parameters are $\Gamma = 1.20 \pm 0.10$, $\log(N_H) = 22.42 \pm 0.18$, $I_{Fe} = 1.11 \pm 0.23 \mathrm{count\,s^{-1}}$, equivalent width$= 530 \pm 110$eV, and $\chi^2_R = 1.52/25\,d.o.f.$

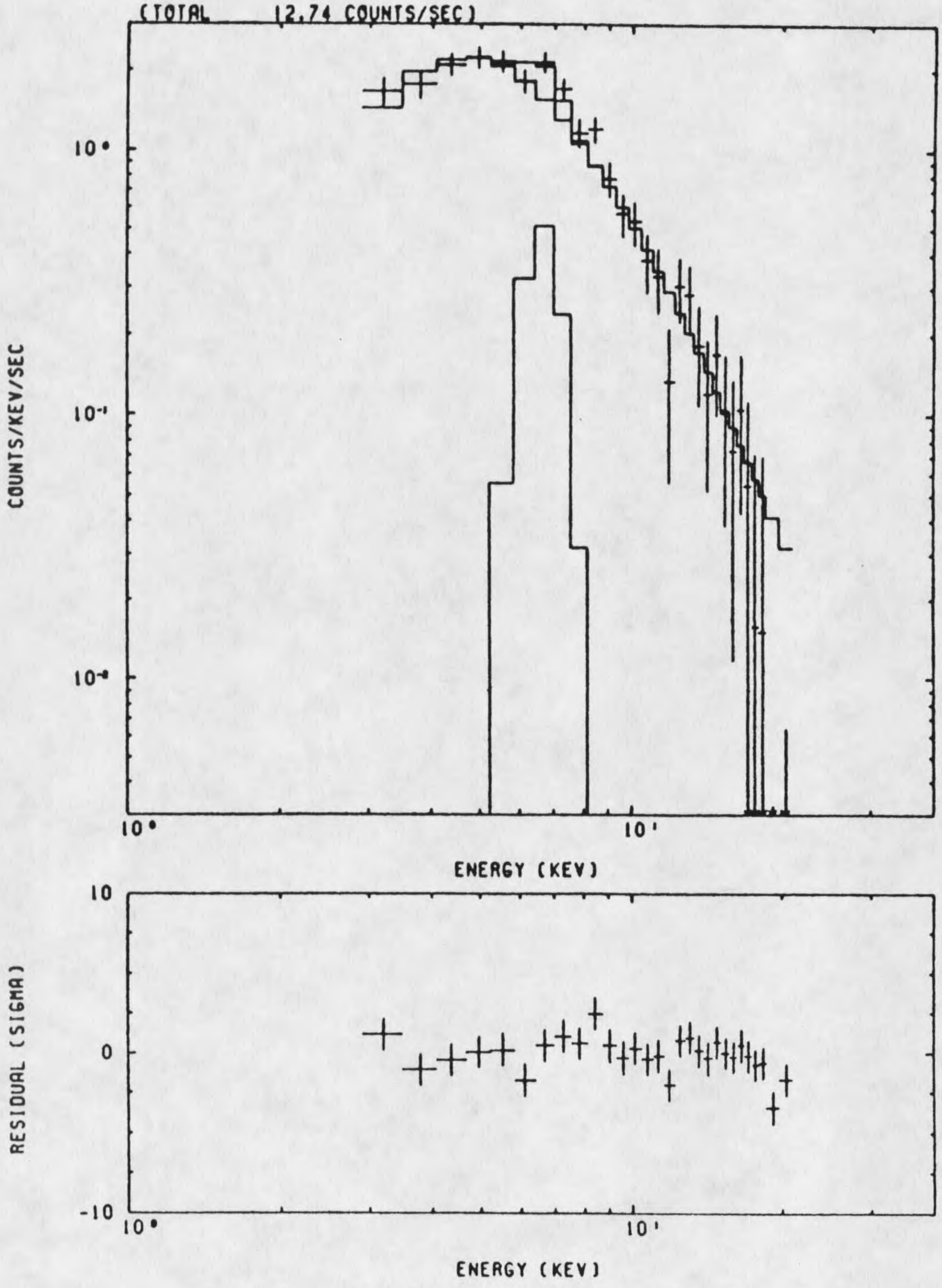

Figure 101. Spectral fit for A2D3, the second spectrum after the second dip. The power law and line plus absorption model was fit (Equation 4.2). Best fit parameters are $\Gamma = 1.71 \pm 0.21$, $\log(N_H) = 22.94 \pm 0.14$, $I_{Fe} = 0.93 \pm 0.51 \mathrm{count\,s^{-1}}$, equivalent width$= 400 \pm 240$eV, and $\chi^2_R = 1.44/25\, d.o.f.$

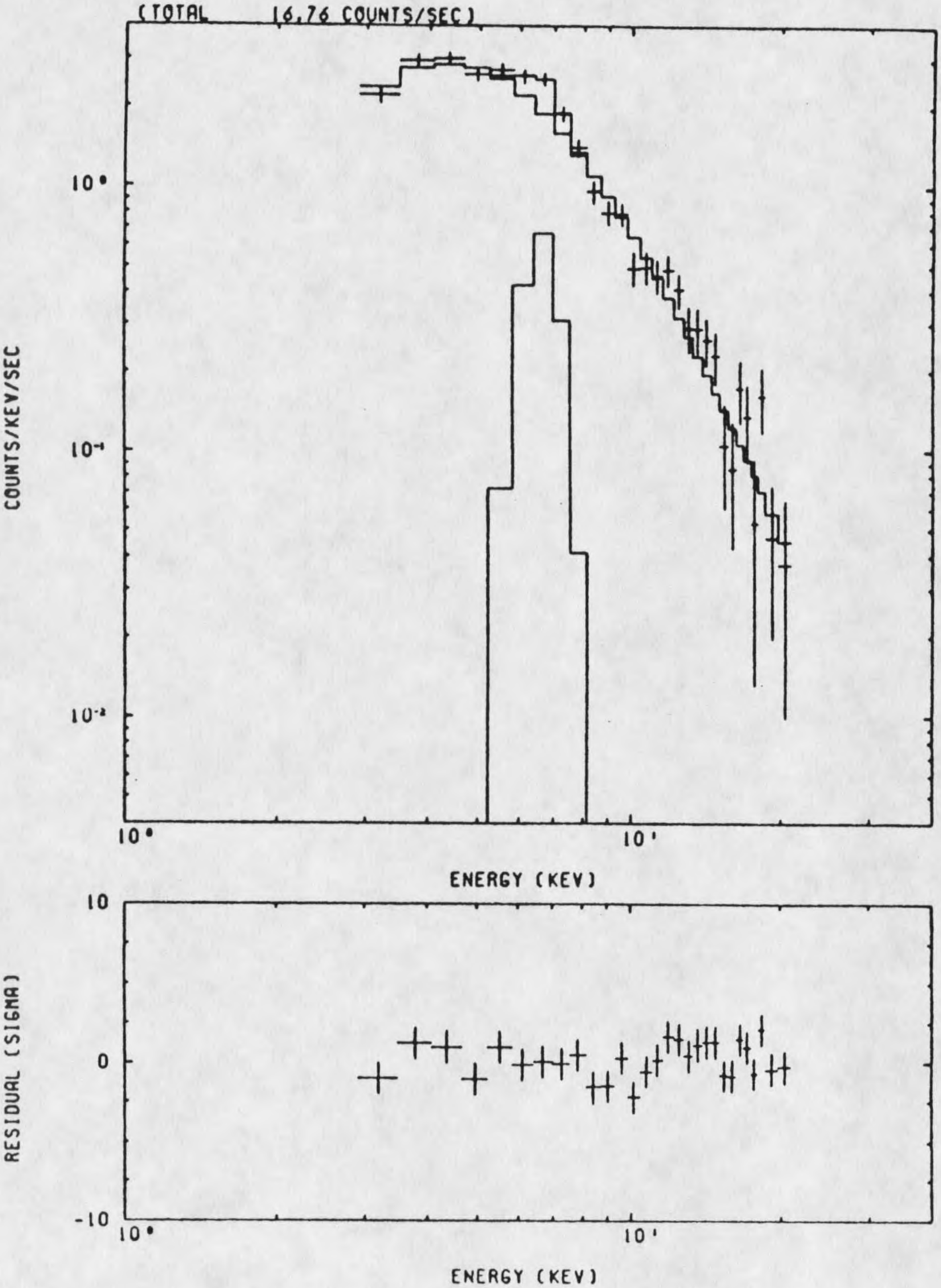

Figure 102. Spectral fit for A3DB2, the spectrum before the third dip. The power law and line plus absorption model was fit (Equation 4.2). Best fit parameters are $\Gamma = 1.51 \pm 0.13$, $\log(N_H) = 22.70 \pm 0.14$, $I_{Fe} = 1.13 \pm 0.35 \mathrm{count\,s^{-1}}$, equivalent width$= 440 \pm 130$eV, and $\chi^2_R = 1.40/25\, d.o.f.$

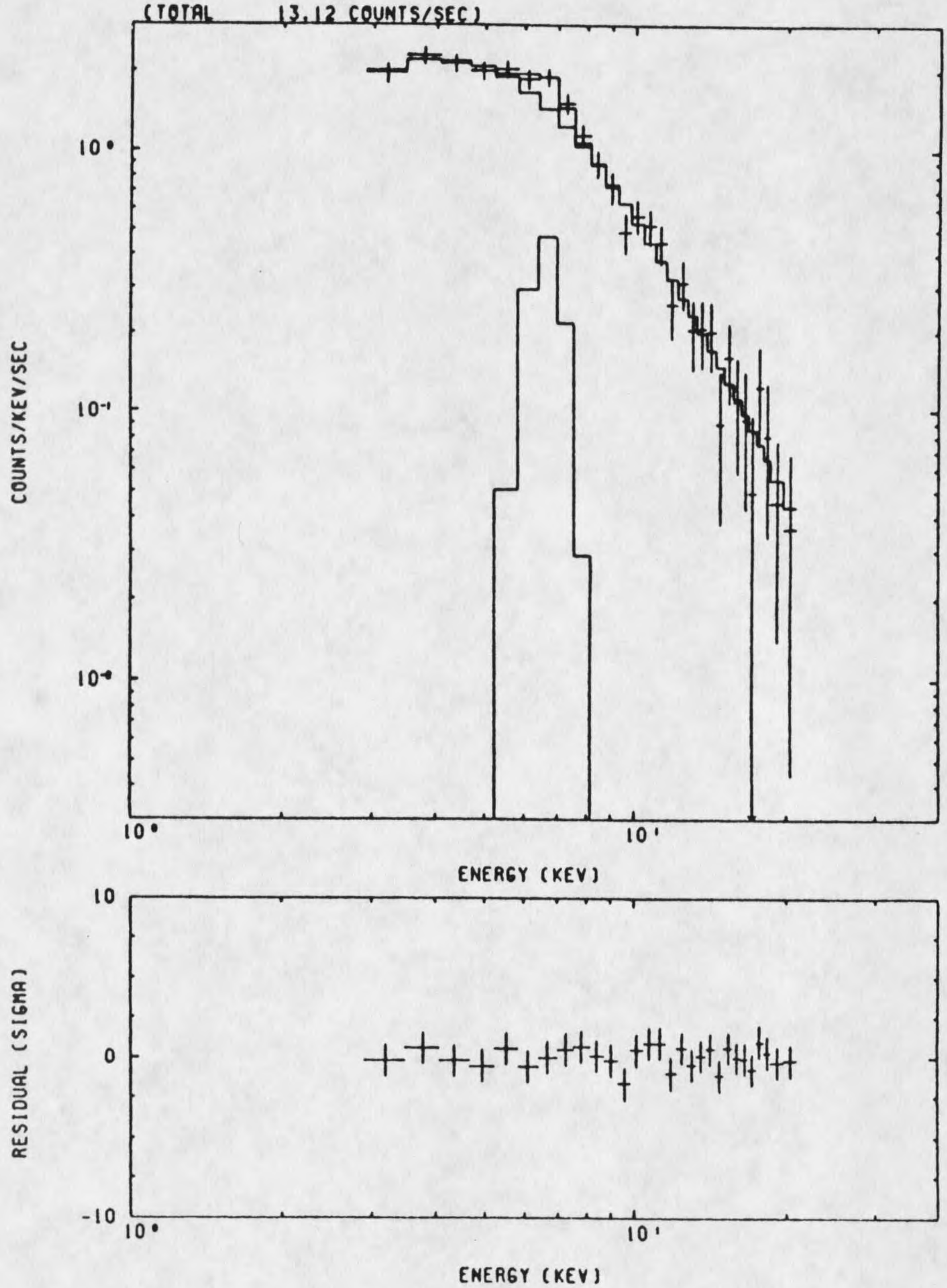

Figure 103. Spectral fit for A3DA1, the spectrum after the third dip. The power law and line plus absorption model was fit (Equation 4.2). Best fit parameters are $\Gamma = 1.27 \pm 0.18$, $\log(N_H) = 22.43 \pm 0.32$, $I_{Fe} = 0.77 \pm 0.36 \mathrm{count\,s^{-1}}$, equivalent width$= 410 \pm 190\mathrm{eV}$, and $\chi^2_R = 0.48/25\, d.o.f.$

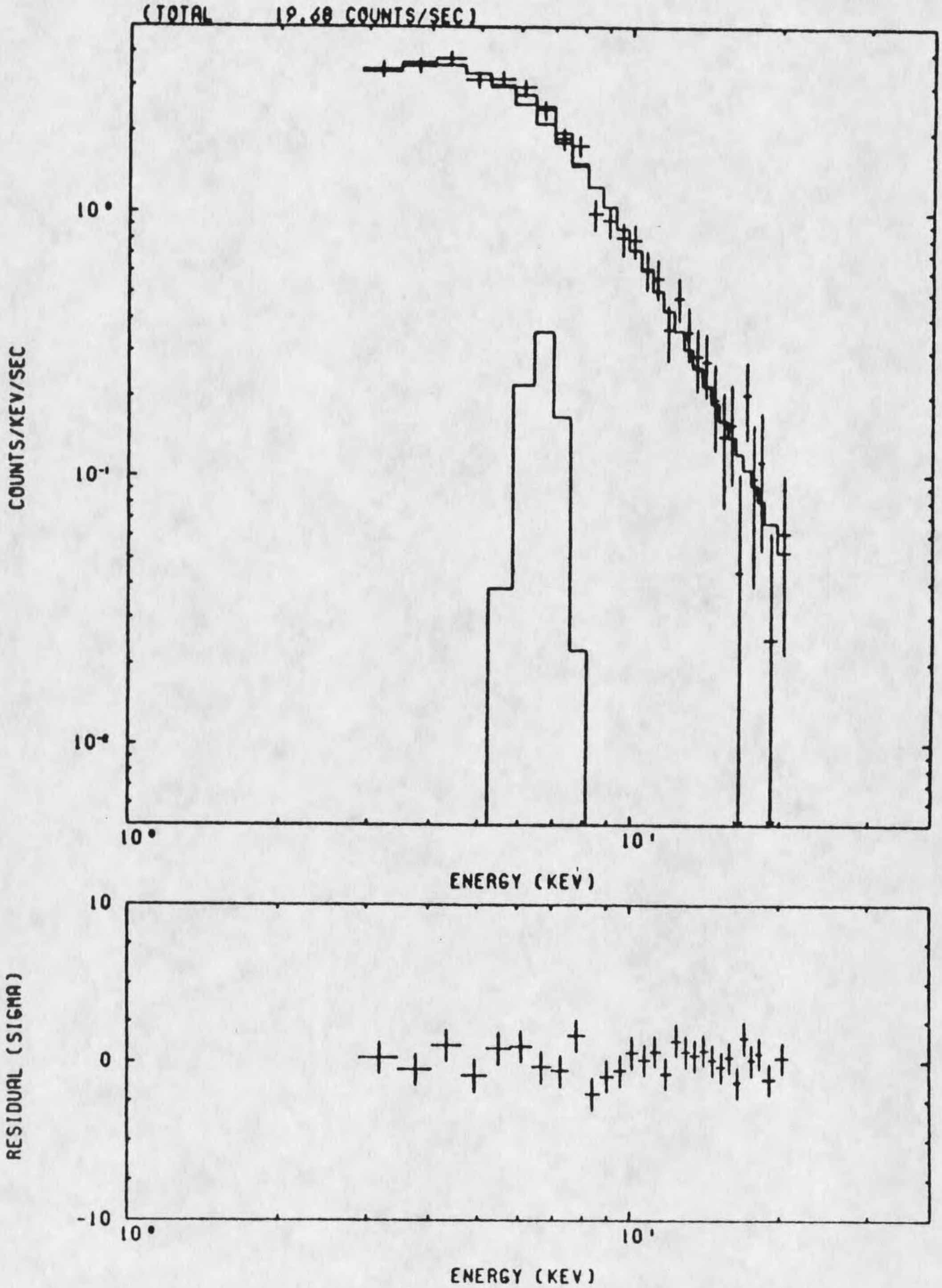

Figure 104. Spectral fit for OI1 from the October ingress data. The power law and line plus absorption model was fit (Equation 4.2). Best fit parameters are $\Gamma = 1.46 \pm 0.16$, $\log(N_H) = 22.46 \pm 0.29$, $I_{Fe} = 0.58 \pm 0.47 \mathrm{count\,s^{-1}}$, equivalent width$= 210 \pm 170$eV, and $\chi^2_R = 0.89/25\, d.o.f.$

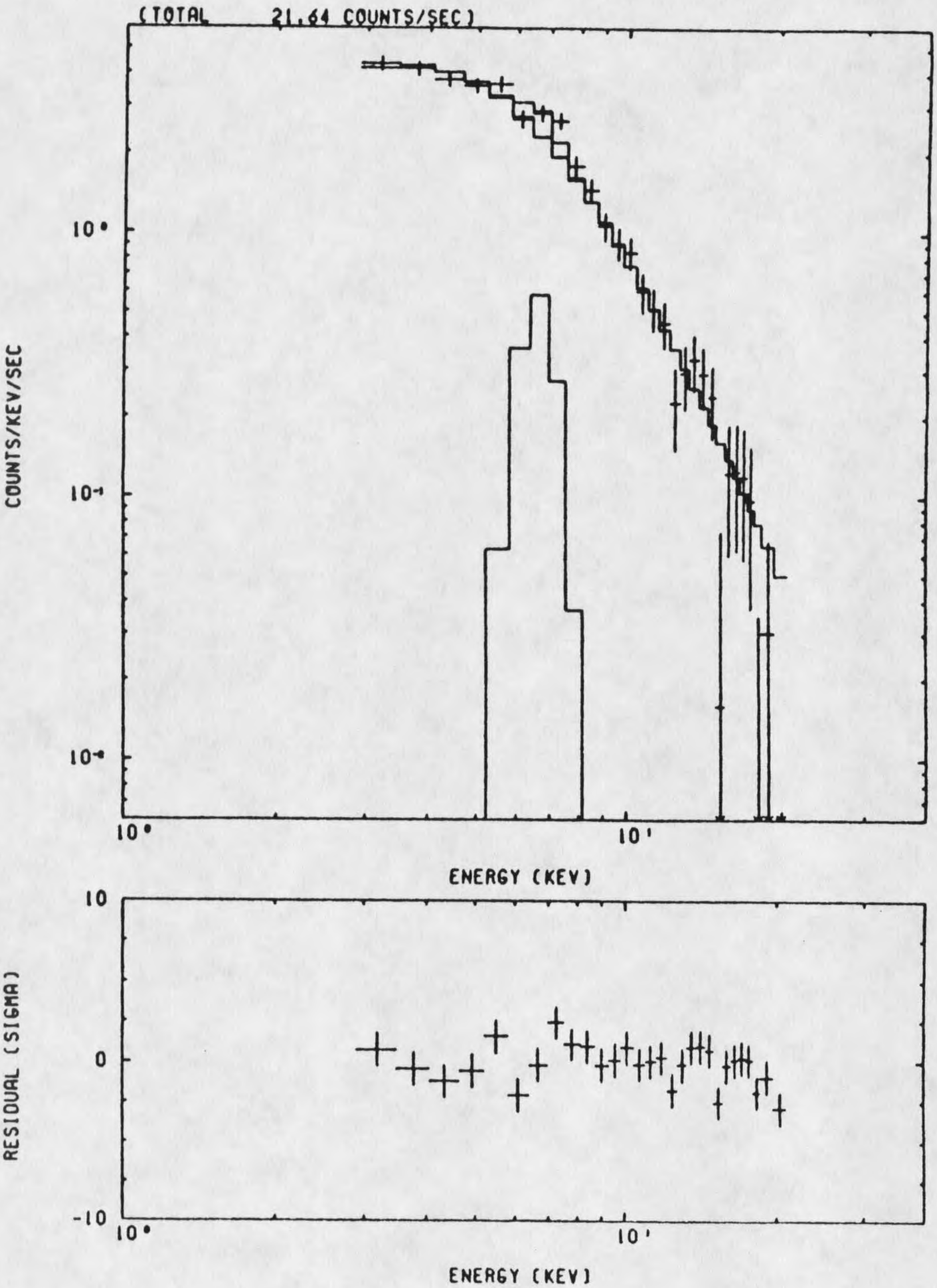

Figure 105. Spectral fit for OI3 from the October ingress data. The power law and line plus absorption model was fit (Equation 4.2). Best fit parameters are $\Gamma = 1.54 \pm 0.16$, $I_{Fe} = 0.95 \pm 0.49 \mathrm{counts\,s^{-1}}$, equivalent width= 320 ± 170eV, $\log(N_H) = 22.34 \pm 0.28$, and $\chi^2_R = 1.69/25\, d.o.f.$

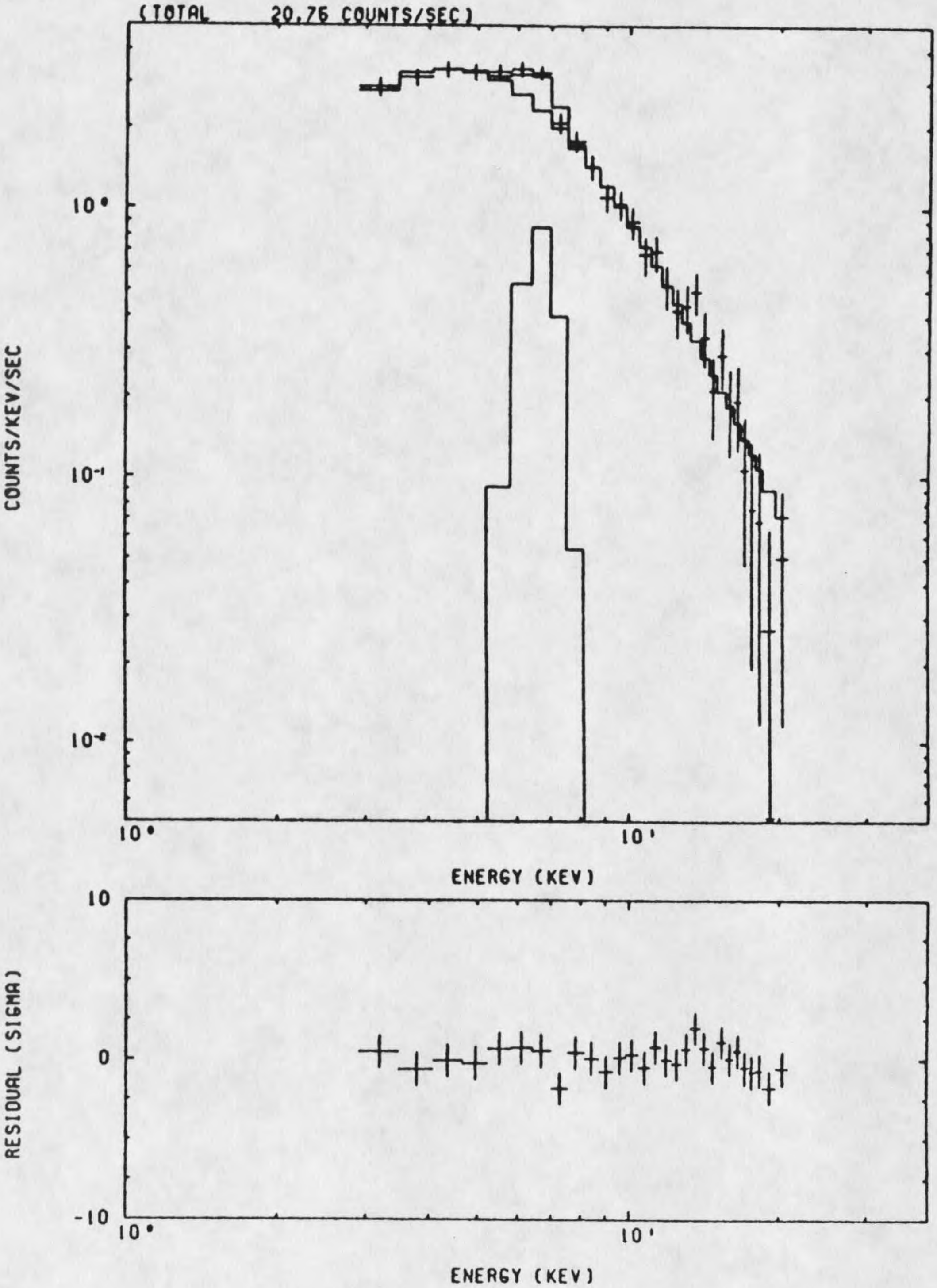

Figure 106. Spectral fit for OI5 from the October ingress data. The power law and line plus absorption model was fit (Equation 4.2). Best fit parameters are $\Gamma = 1.28 \pm 0.16$, $\log(N_H) = 22.62 \pm 0.20$, $I_{Fe} = 1.42 \pm 0.51 \mathrm{count\,s}^{-1}$, equivalent width$= 460 \pm 170$eV, and $\chi^2_R = 0.72/25\, d.o.f.$

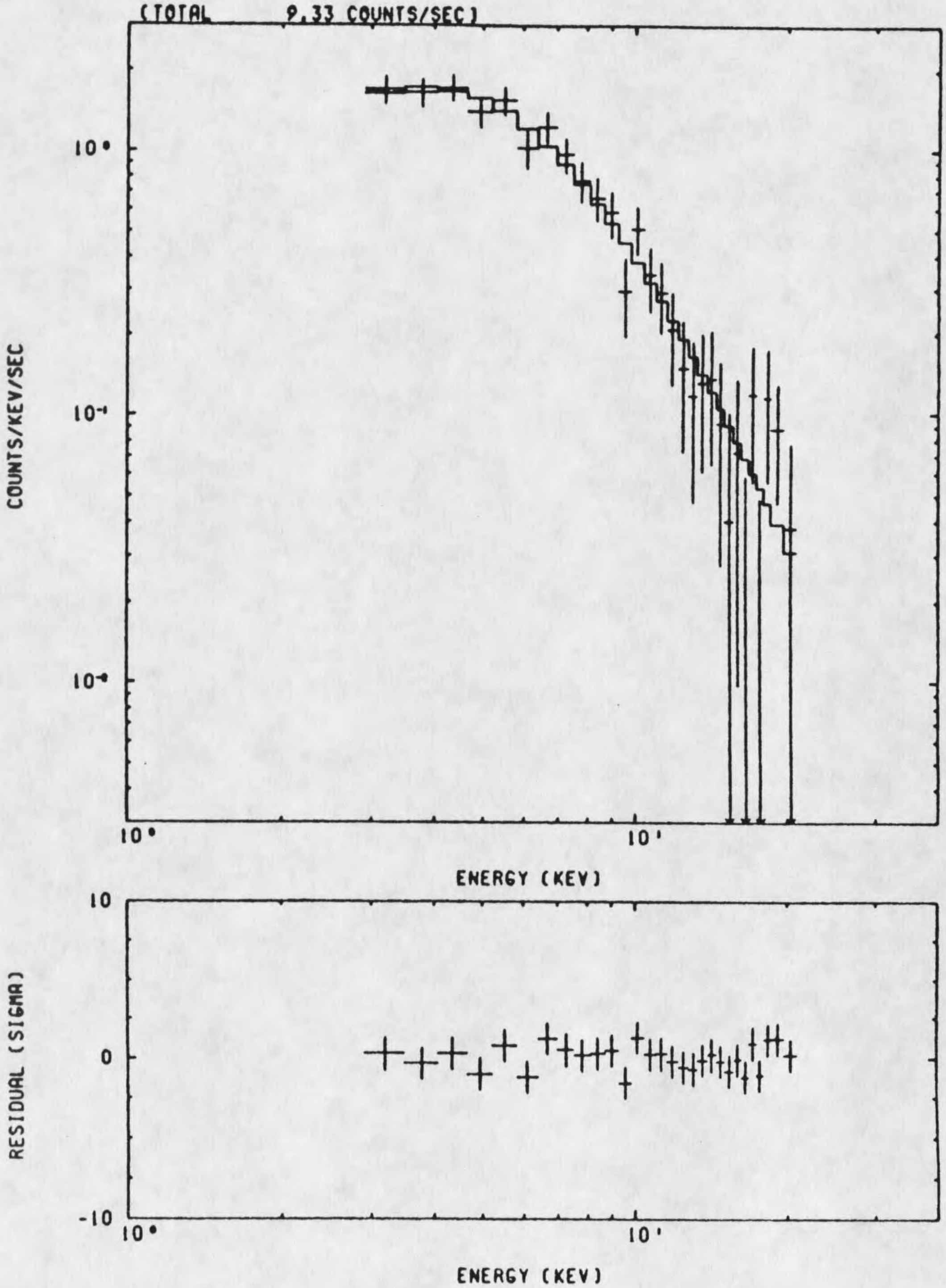

Figure 107. Spectral fit for OI7 from the October ingress data. The power law and line plus absorption model was fit (Equation 4.2). Best fit parameters are $\Gamma = 1.27 \pm 0.28$, $\log(N_H)$ was fixed at 21.2, the Galactic value, $I_{Fe} < 0.41 \mathrm{count\,s^{-1}}$, equivalent width$<$ 310eV, and $\chi^2_R = 0.65/26\ d.o.f.$

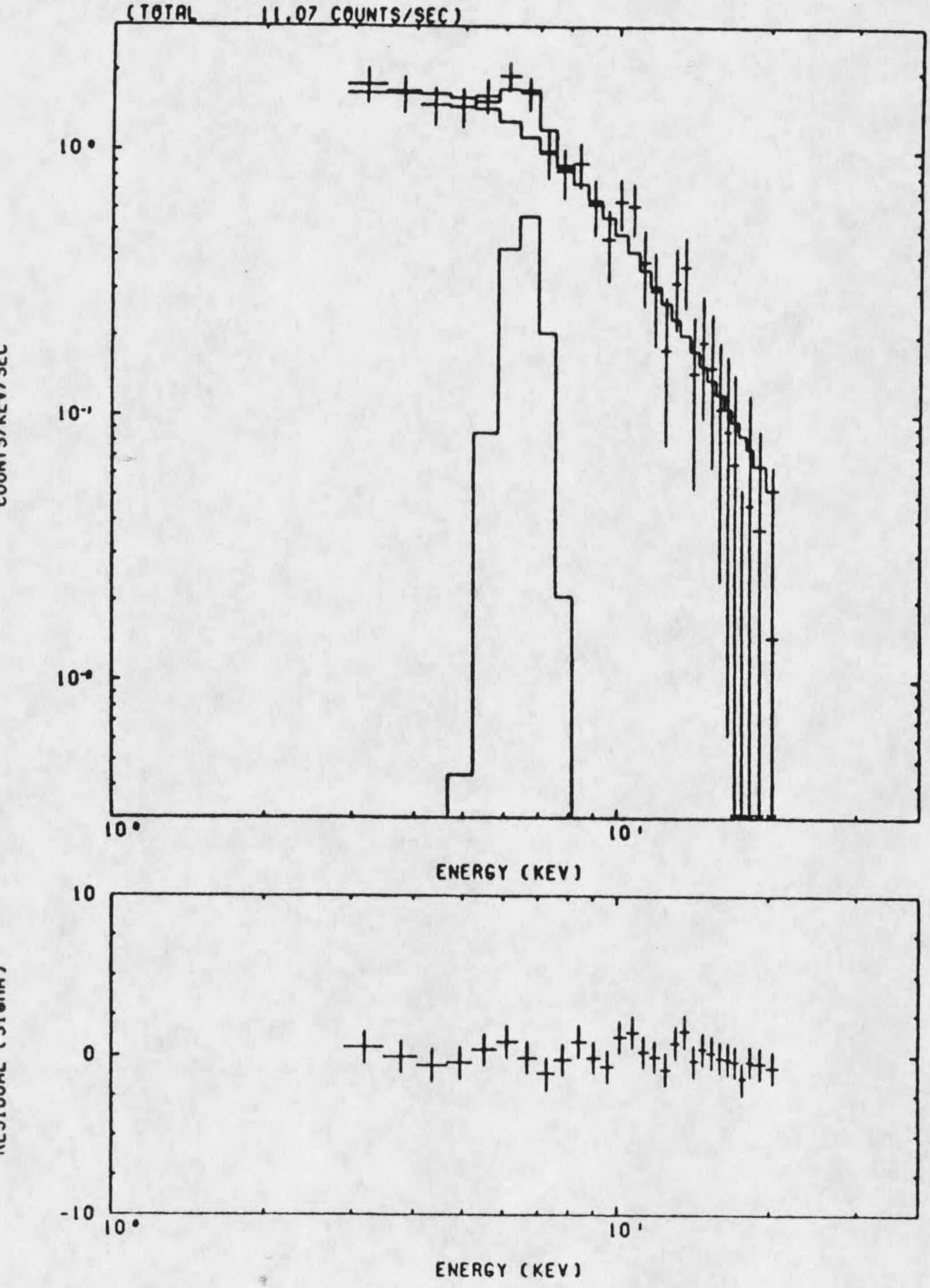

Figure 108. Spectral fit for OIHRD3 from the October ingress data. The power law and line plus absorption model was fit (Equation 4.2). Best fit parameters are $\Gamma = 0.85 \pm 0.17$, $\log(N_H)$ was fixed at 21.2, the Galactic value, $I_{Fe} = 0.89 \pm 0.51 \mathrm{count\,s^{-1}}$, equivalent width$= 640 \pm 370$eV, and $\chi^2_R = 0.59/26\, d.o.f.$

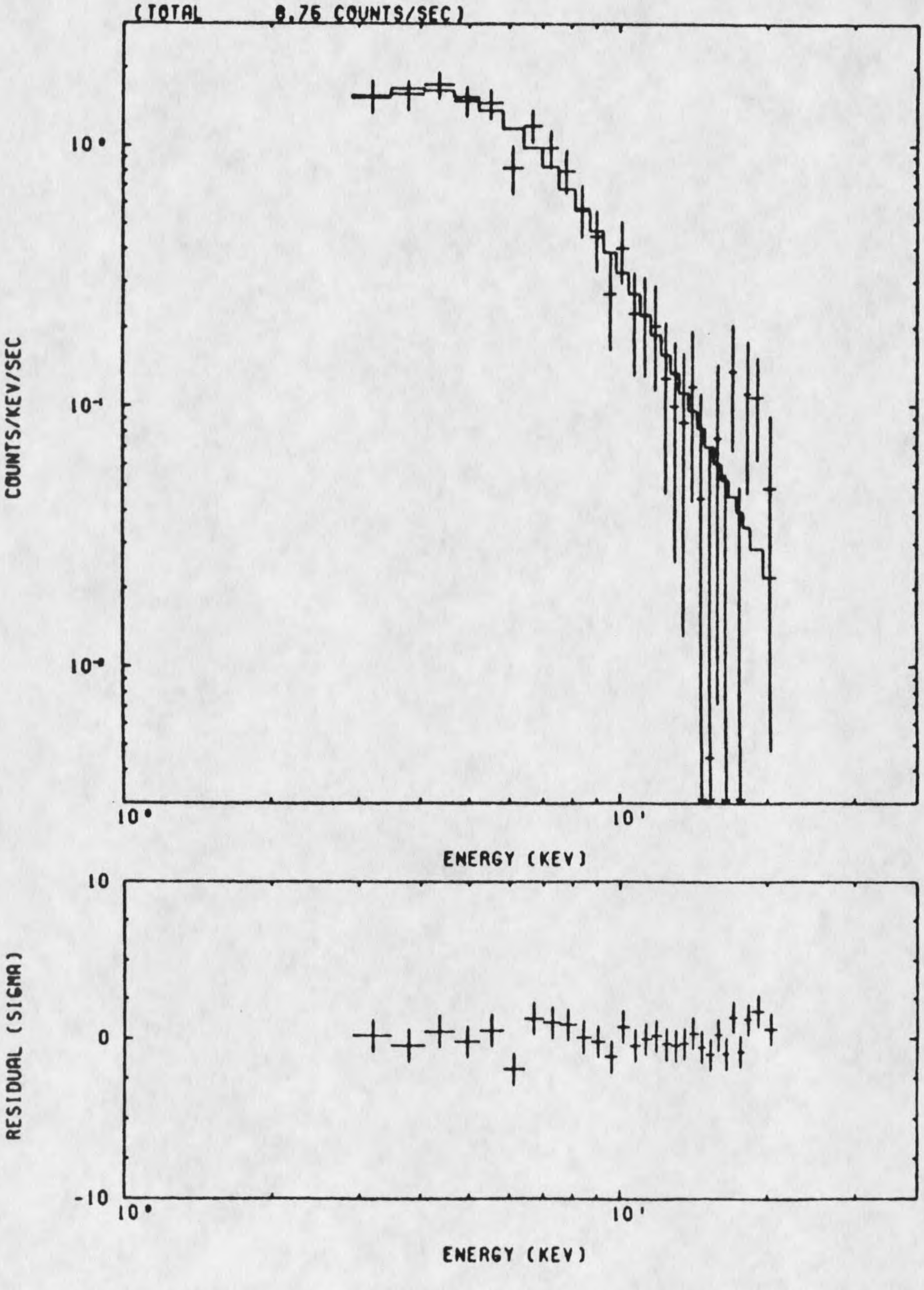

Figure 109. Spectral fit for OHLT5I from the October ingress data. The power law plus absorption model was fit (Equation 4.1). Best fit parameters are $\Gamma = 1.54 \pm 0.25$, $\log(N_H) = 22.54 \pm 0.43$, $I_{Fe} < 0.41 count\, s^{-1}$, equivalent width$<$ 320eV, and $\chi^2_R = 0.76/26\, d.o.f.$

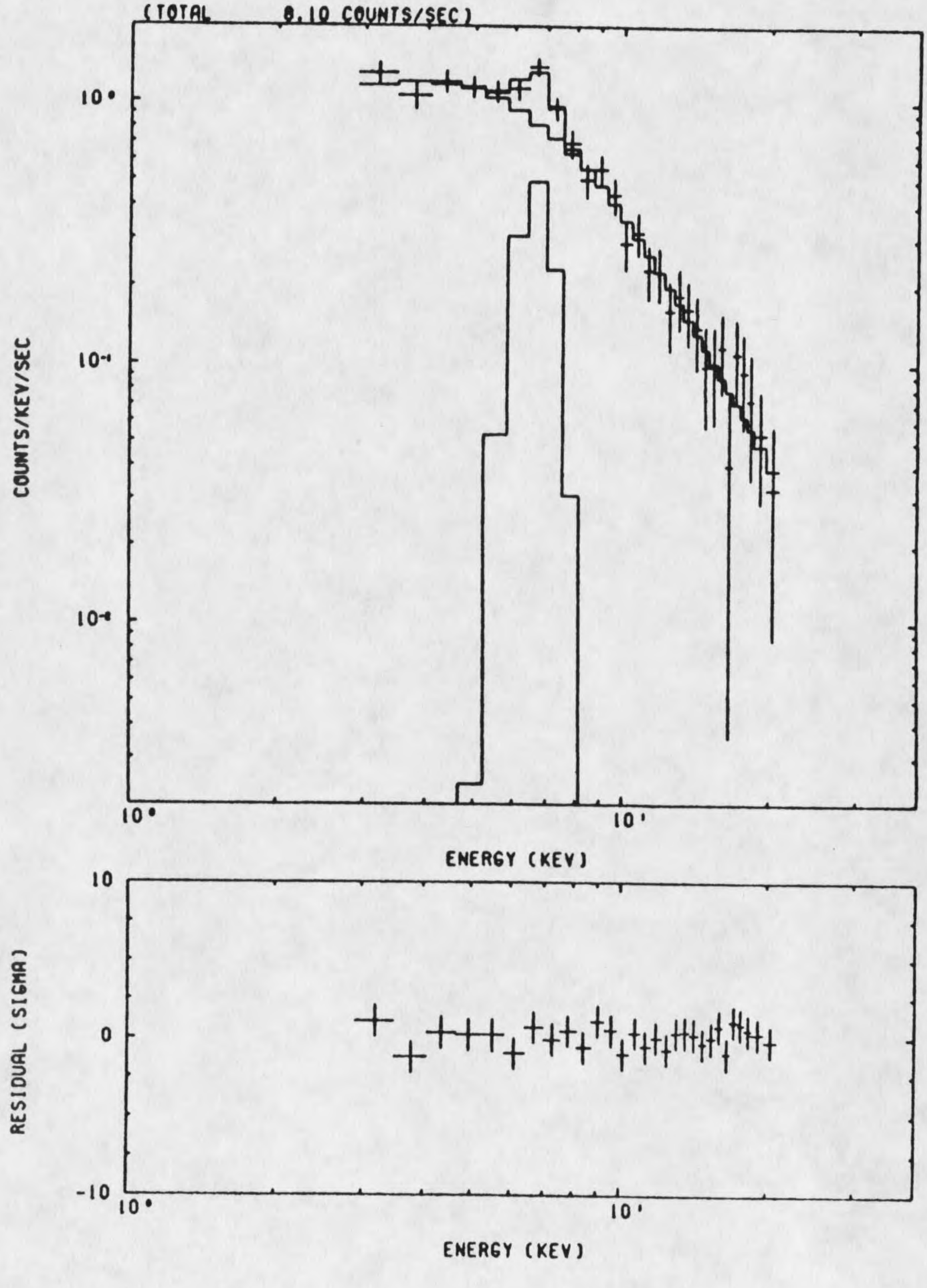

Figure 110. Spectral fit for O5E1 from the October egress data. The power law and line plus absorption model was fit (Equation 4.2). Best fit parameters are $\Gamma = 0.85 \pm 0.11$, $\log(N_H)$ was fixed at the 21.2, the Galactic value, $I_{Fe} = 0.77 \pm 0.23 \mathrm{count\,s}^{-1}$, equivalent width$= 770 \pm 230$eV, and $\chi^2_R = 0.47/26\, d.o.f.$

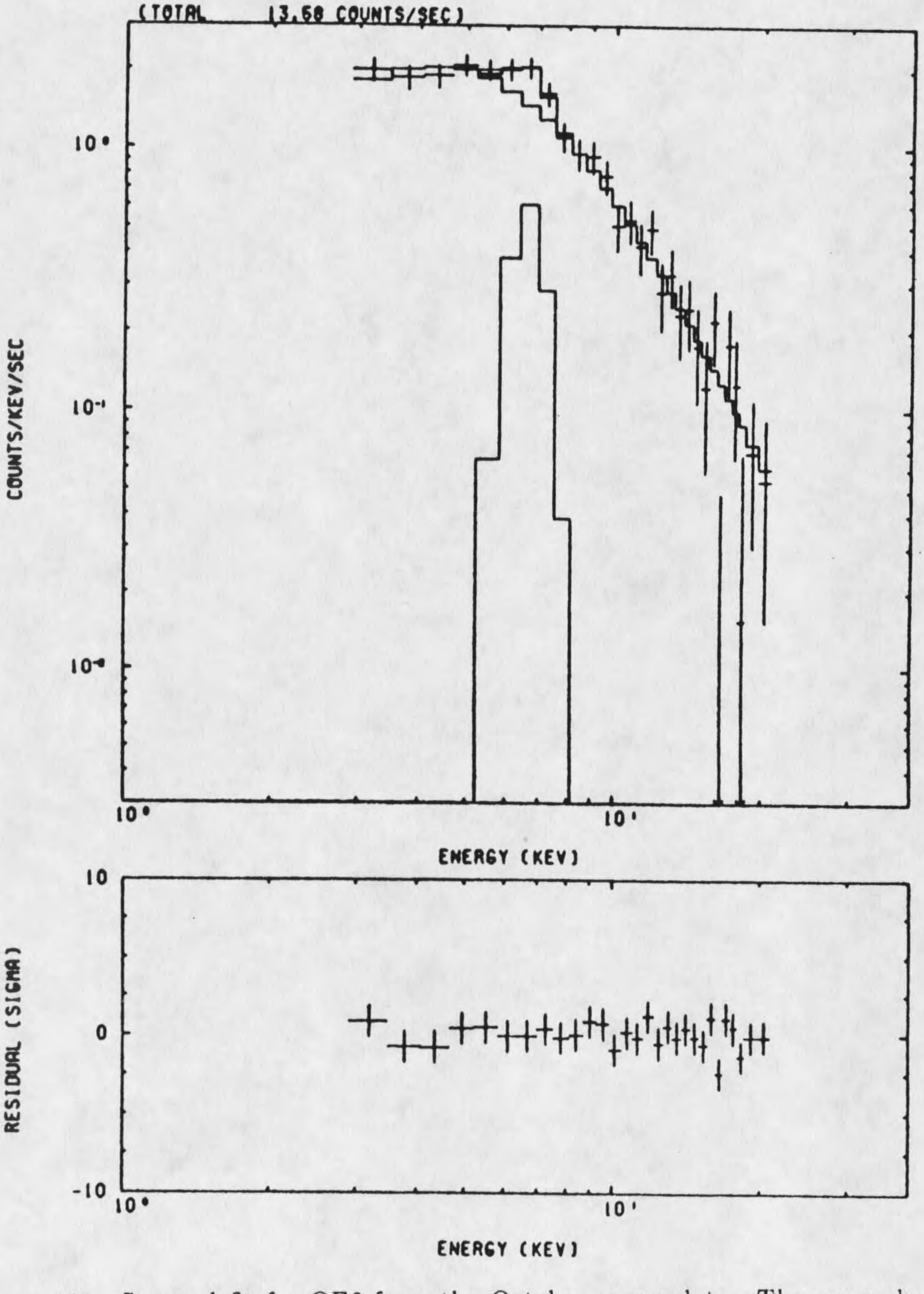

Figure 111. Spectral fit for OE6 from the October egress data. The power law and line plus absorption model was fit (Equation 4.2). Best fit parameters are $\Gamma = 0.99 \pm 0.21$, $\log(N_H) = 22.31 \pm 0.47$, $I_{Fe} = 0.98 \pm 0.44 \mathrm{count\,s^{-1}}$, equivalent width$= 530 \pm 240$eV, and $\chi^2_R = 0.71/25\, d.o.f.$

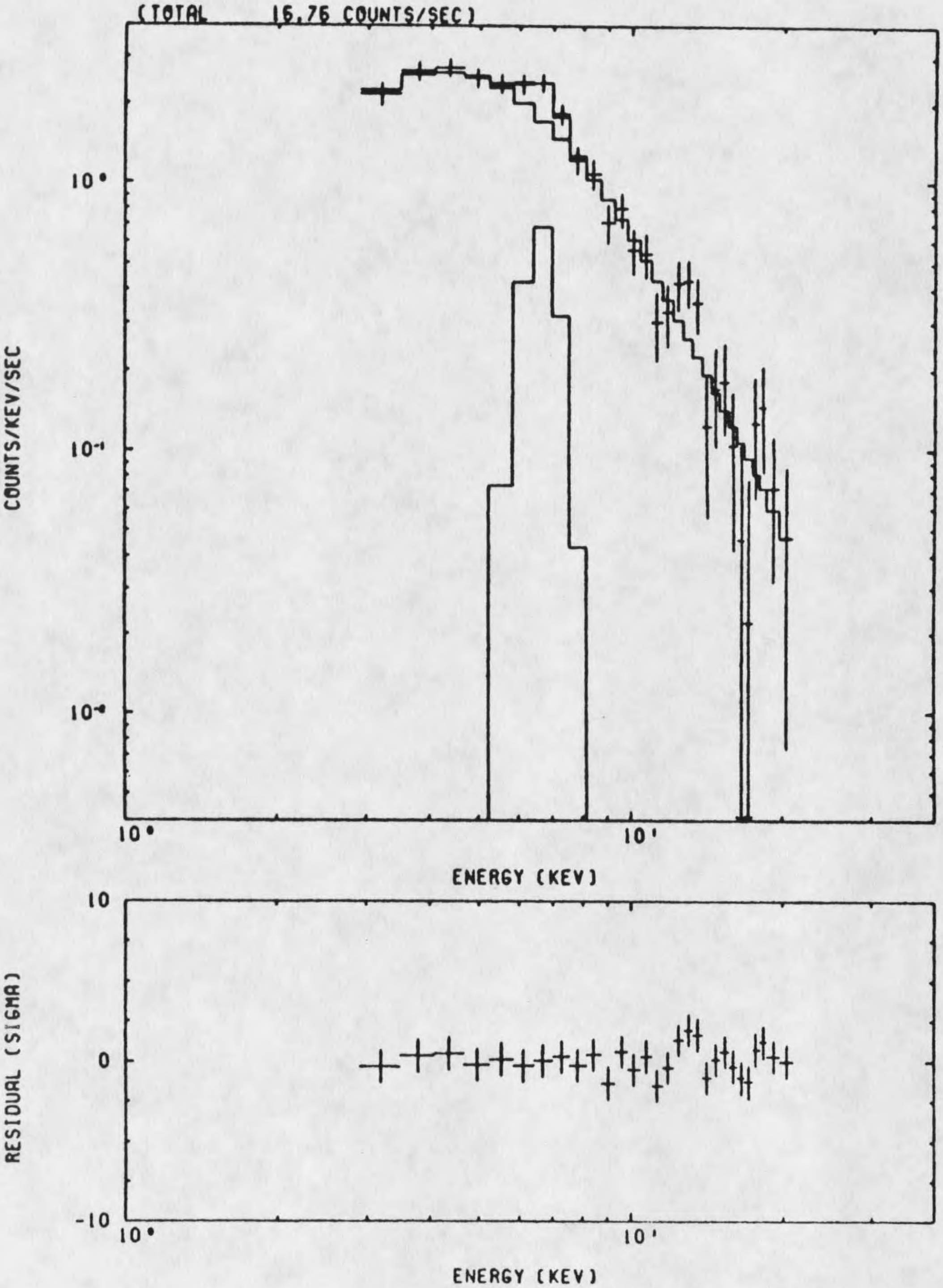

Figure 112. Spectral fit for OE8 from the October egress data. The power law and line plus absorption model was fit (Equation 4.2). Best fit parameters are $\Gamma = 1.39 \pm 0.20$, $\log(N_H) = 22.61 \pm 0.25$, $I_{Fe} = 1.14 \pm 0.47 \text{count s}^{-1}$, equivalent width$= 500 \pm 200$eV, and $\chi^2_R = 0.82/25\, d.o.f.$